Development of Polymeric Hydrogel Nanocomposites for Antibacterial Application

A thesis

submitted in partial fulfillment of the requirements for the award of degree of

DOCTOR OF PHILOSOPHY

IN

BIOTECHNOLOGY

THAPAR INSTITUTE
OF ENGINEERING & TECHNOLOGY
(Deemed to be University)

Submitted by

Navneet Kaur Dhiman

(Reg. No. 901600007)

Under the supervision of

Dr. Shekhar Agnihotri

Dr. M.S. Reddy

Department of Biotechnology

THAPAR INSTITUTE OF ENGINEERING AND TECHNOLOGY

(Deemed to be University)

Patiala – 147004, Punjab, India

January 2024

CERTIFICATE

Certified that the thesis entitled "Development of Polymeric Hydrogel Nanocomposites for Antibacterial Application" submitted by Ms. Navneet Kaur Dhiman, Reg. no. 901600007 in the partial fulfilment of the requirements for the award of the degree of Doctor of Philosophy in the Department of Biotechnology, Thapar Institute of Engineering and Technology, Patiala, Punjab is a record of candidate's own independent and original research work carried out by her under our supervision and guidance. The material embodied in this thesis has not been submitted in part or full to any other University or Institute for the award of any degree.

Dr. Shekhar Agnihotri
Assistant Professor
Department of Agriculture and Environmental Sciences,
National Institute of Food Technology Entrepreneurship and Management-Kundli, (NIFTEM-K),
Sonepat-131028, Haryana, India

Dr. M.S. Reddy
Professor
Department of Biotechnology,
Thapar Institute of Engineering and Technology (Deemed to be University),
Patiala-147004, Punjab, India

DECLARATION

I, hereby declare that the work presented in the thesis entitled "Development of Polymeric Hydrogel Nanocomposites for Antibacterial Application" in the partial fulfilment of the requirement for the award of the degree of Doctor of Philosophy in the Department of Biotechnology, Thapar Institute of Engineering and Technology (TIET), Patiala, Punjab is an authentic record of my work carried out under the supervision and guidance of Dr. Shekhar Agnihotri, Assistant Professor, Department of Agriculture and Environmental Sciences, NIFTEM, Sonepat, Haryana and Dr. M.S. Reddy, Professor, Department of Biotechnology, Thapar Institute of Engineering and Technology, Patiala, Punjab. This report has not been submitted for the award of any degree or certificate in any other university in India or abroad.

Navneet Kaur

Place: Patiala
Date: 15-01-2024

Navneet Kaur Dhiman
(Reg. No. 901600007)

ACKNOWLEDGEMENTS

"Gratitude is not only the greatest of virtues but the parent of all others."

-Marcus Tullius Cicero

While penning this expression of gratitude, which serves as the final brushstroke on my thesis, my heart brims with appreciation for those who have held pivotal roles in this unforgettable expedition. This transformative journey has been long and challenging and would not have been possible without the unwavering support, guidance, and encouragement of many individuals. Although, it is difficult to acknowledge everyone involved in the compilation of this PhD thesis. However, this writing piece fuelled by the thoughts and memories accumulated over the past several years, is a humble effort to remember all the people who have supported me throughout this research endeavour.

First and foremost, I would like to express my deepest gratitude to my reverent supervisor ***Dr. Shekhar Agnihotri***, Assistant Professor, Department of Agriculture and Environmental Sciences, National Institute of Food Technology Entrepreneurship and Management (NIFTEM), Sonepat. Dr. Agnihotri's unwavering guidance, invaluable advice, timely suggestions, and remarkable patience were indispensable for the successful culmination of my work and the attainment of my PhD. His genuine intellectual curiosity and positive attitude – even when results didn't go as expected – have been motivating. His recommendations and broad encyclopaedic knowledge across many fields have been instrumental in assisting me through numerous challenging situations. It was his consistent support at every step of my research endeavour that enabled me to embark on ventures in the field of nanotechnology and successfully complete them. From the very beginning and throughout this period, he encouraged me to explore new ideas and entrusted me with great independence to carry out my research work. Amidst the challenges that often accompany the pursuit of a PhD, at (many) times I was distracted and lost, these challenges would have been irreversible without my supervisor's kindness, sympathy and encouragements. I will continue to seek his blessings and cherish his valuable guidance throughout my life.

I consider myself exceptionally fortunate and privileged to have received the co-supervision from ***Prof. M.S. Reddy***, Head, Department of Biotechnology, Thapar Institute of Engineering and Technology, Patiala. His research philosophy, moral encouragement, open-door policy and willingness to engage in discussions at any time helped me overcome ups and downs and

smoothly sail through this journey. His constructive critiques challenged me to think critically, and his confidence in my abilities boosted my self-assurance. I also deeply appreciate his investment in my academic and administrative tasks in parallel with research works despite his busy schedule. I shall always remain indebted to him for his unending support, understanding, care and concern; his association with this endeavour will forever serve as a guiding light for me.

I wish to extend my special appreciation to the esteemed members of my doctoral committee: ***Dr. Moushumi Ghosh*** and ***Dr. Vikas Handa*** from the Department of Biotechnology at TIET, as well as ***Dr. Bhupendra Kumar Chudasama*** from the School of Physics & Materials Science at TIET. I sincerely thank them for evaluating my performance time to time, underscoring the gaps where I had to work hard, their critical comments and valuable suggestions which helped me to gain insight in the work I had undertaken.

My studies would not have been possible without the generous financial support received from **University Grants Commissions-Maulana Azad National Fellowship (UGC-MANF) (MANF-2017-18-PUN-83207)**. I have been fortunate enough to receive institutional support from **TIET, Patiala** in the form of **Teaching Assistantship** and **PhD contingency**. I am also indirectly grateful to the **TIET seed grant (TIET/DoRSP/57/474)** acquired by my research advisor Dr. Shekhar Agnihotri, which has immensely helped in obtaining necessary consumables for the research lab I worked in.

I am also thankful to the whole faculty and office staff at Department of Biotechnology and TIFAC-CORE for their constant help and cooperation. I am grateful to ***Mrs. Manjula Kamra*** for her timely help, moral support, and encouraging words. I owe my sincere thanks to ***Mr. Avinash Kumar*** for his consistent support, motivation and suggestions. Without the genuine assistance of our lab technicians, a significant portion of the work would have remained unfinished. I am thankful to ***Mr. Ram Newal (Babban ji)***, ***Mr. Soni Singh***, ***Mr. Prabhat***, ***Mr. Lallan***, ***Mr. Surinder Pal***, ***Mr. Mohinder*** and ***Mr. Phoolchand*** for their invaluable assistance during the lab and office paper work.

I would like to express my appreciation to my dedicated lab mates ***Dr. Devendra Sillu*** and ***Ms. Anjali Chauhan*** who have been an integral part of my research journey. Their collaborative spirit, shared insights, and willingness to exchange ideas without any hesitation have enriched my academic experience and significantly contributed to the success of this thesis. I am grateful for their *esprit de corps*, cosmic and otherwise. I will forever cherish our

discussions, professional and personal, about various facets of life that have undoubtedly contributed to my personal growth and development. It has been a privilege to work alongside such a talented and motivated group of individuals, and I look forward to witnessing their continued achievements in the future.

I would be remiss if I did not extend my most sincere gratitude to my loving friends and colleagues at TIET and beyond. I owe special thanks to ***Ms. Navneet Kaur Sidhu***, who consistently extended her support in countless ways, always available whenever needed. Our critical discussions that extended beyond microbiology, undoubtedly contributed to enhancing not only my scientific approach but also, my perspective on life. ***Dr. Ravneet Kaur***, ***Dr. Prerna***, ***Ms. Simarpreet***, and ***Ms. Jyotika***, as experienced seniors, warmly welcomed me into the department and nourished me intellectually and personally. The invaluable support offered by ***Dr. Jyoti Sharma***, ***Mr. Nirmalya Halder, Ms. Purnima Sharma*** and ***Mr. Jeon Jungkook (BTS)*** in most critical situations is also greatly acknowledged. I am also thankful to all the masters dissertation students, past and present, ***Ms. Tamanna Mahajan***, ***Ms. Suborna Chatterjee***, ***Ms. Darshdeep Kaur***, ***Ms. Garima Sharma***, ***Ms. Anjana Mittal*** and ***Ms. Pawandeep Kaur*** for providing me a very conducive environment in the lab. Their youthful enthusiasm and unwavering dedication consistently pushed me to match their energy levels.

I am grateful to **SAI Lab at TIET** and **SAIF & CIL at Punjab University** for the instrument facilities used during this work. I gratefully acknowledge the guidance and assistance of ***Dr. Priyankar Dey***, DBT, TIET for cytotoxicity analysis. I am immensely thankful to ***Mr. Ajeet Singh***, Electron Microscopy Lab, TIET for providing timely assistance in FEG-SEM analysis. I am also grateful to ***Mr. Pardeep Bhatia*** and ***Mr. Ghanshyam Mourya***, SAI lab TIET for helping me with SEM and XRD analyses.

Behind every successful endeavour lies the unwavering support of loved ones, and in my case, it is my parents ***Sr. Parvinder Singh*** and ***Mrs. Malkeet Kaur*** who have been the bedrock of my academic journey. Their sacrifices, both big and small, have enabled me to pursue my dreams. When my experiments yielded positive results, I celebrated my joy with them. Conversely, during moments of experiment setbacks, their support and encouragement were my solace. I would also like to extend my deepest gratitude to my younger brother ***Sr. Shivreet Singh,*** who always offered a listening ear when challenges seemed insurmountable. My brother, wise beyond his age, has provided emotional, psychological, and spiritual

support during all difficult times. I would like to dedicate a special place in this acknowledgment to my faithful pet companion, ***Trigger***, who was a source of unfaltering comfort and companionship throughout the journey of my higher education. Trigger was my anti-depressant pill, who brought immense joy to my life with his loyalty, affection, and cheerful presence. His absence is deeply felt and his role in my life and PhD is forever cherished. The unconditional love showered by my family upon me has resulted in this incredible achievement.

This thesis is a testament to the collective efforts and the culmination of years of hard work, dedication, and perseverance. While I have attempted to acknowledge everyone who played a role in this journey, I sincerely apologize if I have inadvertently omitted anyone. As I conclude this phase, I am filled with gratitude for the privilege of learning, growing, and contributing to my field. Thank you all for being instrumental in making this Ph.D. thesis a reality.

Navneet Kaur Dhiman

List of Publications

Publications

1. **Dhiman, N. K**., Reddy, M. S., & Agnihotri, S.* (2023). Graphene oxide reinforced chitosan/polyvinyl alcohol antibacterial coatings on stainless steel surfaces exhibit superior bioactivity without human cell cytotoxicity. *Colloids and Surfaces B: Biointerfaces*, 113362. https://doi.org/10.1016/j.colsurfb.2023.113362. (**I.F. 5.8**)

2. **Dhiman, N. K**., & Agnihotri, S.* (2020). Hierarchically aligned nano silver/chitosan–PVA hydrogel for point-of-use water disinfection: contact-active mechanism revealed. *Environmental Science: Nano*, *7*(8), 2337-2350. **(I.F. 7.3)**

Book chapters

1. Agnihotri, S., & **Dhiman, N. K**. (2017). Development of nano-antimicrobial biomaterials for biomedical applications. *Advances in biomaterials for biomedical applications*, 479-545.

2. Agnihotri, S., **Dhiman, N. K.**, & Tripathi, A. (2018). Antimicrobial surface modification of polymeric biomaterials. *Handbook of antimicrobial coatings*, 435-486.

3. **Dhiman, N. K.**, Agnihotri, S., & Shukla, R. (2019). Silver-based polymeric nanocomposites as antimicrobial coatings for biomedical applications. *Nanotechnology in Modern Animal Biotechnology: Recent Trends and Future Perspectives*, 115-171.

4. **Dhiman, N. K.***, Sidhu, N.*, Agnihotri, S., Mukherjee, A., & Reddy, M. S. (2022). Role of nanomaterials in protecting building materials from degradation and deterioration. In *Biodegradation and Biodeterioration At the Nanoscale* (pp. 405-475). Elsevier.

5. Chauhan, A., Sillu, D., **Dhiman, N. K.**, & Agnihotri, S. (2022). Silver-Based Nano-formulations for Treating Antibiotic-Resistant Microbial Strains. In *Nano-Strategies for Addressing Antimicrobial Resistance: Nano-Diagnostics, Nano-Carriers, and Nano-Antimicrobials* (pp. 279-309). Cham: Springer International Publishing.

List of Papers in conferences (National/International)

1. **Navneet Kaur Dhiman**, Dinesh Goyal, and Shekhar Agnihotri (2017). Contact-killing mediated antimicrobial efficacy of chitosan/pva hydrogels loaded with silver nanoparticles. *4th International Conference on Nanostructured Materials and*

Nanocomposites (ICNM), Mahatma Gandhi University, Kottayam, Kerala (India) (short invited lecture).

2. **Navneet Kaur Dhiman** and Shekhar Agnihotri (2018). Comparative Biocidal Efficacy of Nano-Silver Reinforced Chitosan based Hydrogels. *International Conference on "Drug Discovery: Biotechnology & Pharma at Cross Roads*, TIET, Patiala, Punjab (India) (Oral).

3. **Navneet Kaur Dhiman**, Yeshaswi Kaushik, and Shekhar Agnihotri (2018). Silver nanoparticles- microcarrier system in chitosan based antimicrobial films for food packaging. *International Conference on Food Security: Challenges and Opportunities*, TIET, Patiala, Punjab (India) (Poster).

TABLE OF CONTENTS

LIST OF TABLES

LIST OF FIGURES

LIST OF SYMBOLS

%	Percentage
°	Degree
°C	Degree Celsius
L	Litre
µL	Microlitre
Kg	Kilogram
g	Gram
µg	Microgram
µg mL^{-1}	Microgram per millilitre
g kg^{-1}	Gram per Kilogram
×g	g-force
M	Molar
mM	Millimolar
µM	Micromolar
Å	Angstrom
cm^{-1}	Reciprocal centimetres
K min^{-1}	Kelvin per minute
CFU mL^{-1}	Colony Forming Units per millilitre
m^2 g^{-1}	Square metres per gram
cm^3 g^{-1}	Cubic centimetres per gram
g cm^{-3}	Gram per cubic centimetres
eV	Electron-volt
KeV	Kiloelectron-Volt
g L^{-1}	Gram per litre
h	Hour
mg	Milligram
mg g^{-1}	Milligram per gram
mg L^{-1}	Milligram per litre
mg mL^{-1}	Milligram per millilitre
s	Seconds
s^{-1}	Reciprocal seconds
min	Minute

min^{-1}	Reciprocal minute
mm min^{-1}	Millimetre per minute
mL	Millilitre
mL min^{-1}	Millilitre per minute
mm	Millimetre
µm	Micrometre
nm	Nanometre
ppb	Parts per billion
MPa	Mega Pascal
Pa.s	Pascal-second
Kgf	Kilogram force
Psi	Pounds per square inch
R^2	Correlation coefficients
rpm	Rotations per minute
v/v	Volume by volume
w/v	Weight by volume
w/w	Weight by weight
wt.%	Weight percentage
θ	Theta
λ	Lambda
γ	Gamma
σ	Sigma
OD	Optical density

LIST OF ABBREVIATIONS

Ag^+	Silver ions
Ag^0	Elemental Silver
$AgNO_3$	Silver nitrate
AgNPs	Silver nanoparticles
ANOVA	Analysis of Variance
APTES	3-Aminopropyl-Triethoxysilane
Aq.	Aqueous
ASTM	American Society of Testing and Materials
ATCC	American Type Culture Collection
ATP	Adenosine triphosphate
BET	Brunauer-Emmett-Teller
BOD	Biochemical Oxygen Demand
BSA	Bovine serum albumin
Ca	Calcium
$CaCO_3$	Calcium carbonate
Cl	Chlorine
CO_2	Carbon dioxide
COD	Chemical Oxygen Demand
Conc.	Concentrated
Cr	Chromium
CS	Chitosan
DMEM	Dulbecco's Modified Eagle Medium
DNA	Deoxyribonucleic acid
DSC	Differential Scanning Colorimetry
DWS	Drinking water system
EDS/EDX	Energy-Dispersive X-Ray Spectroscopy
EDTA	Ethylenediamine tetraacetic acid
ELISA	Enzyme-linked immunosorbent assay
FCC	Face-Centred Cubic
Fe	Iron
FEG-SEM	Field Emission Gun Scanning Electron Microscopy
FTIR	Fourier-Transform Infrared Spectroscopy
GO	Graphene oxide
GSH	Glutathione
HepG2	Human Hepatocellular Carcinoma
ICP-AES	Inductively Coupled Plasma-Atomic Emission spectrometer
ISO	International Organization for Standardization
K^+	Potassium ion
KBr	Potassium bromide
KH_2PO_4	Monopotassium phosphate
LB	Luria Broth
LDH	Lactate Dehydrogenase

Mg^{+2}	Magnesium ion
$MgSO_4$	Magnesium sulphate
Mn	Manganese
MP-AES	Microwave Plasma-Atomic Emission spectrometer
MTCC	Microbial Type Culture Collection
MTT	3-4,5-Dimethyl-thiazol-2-yl)-2,5-diphenyl tetrazolium bromide
N^+	Nitrogen ion
N_2	Nitrogen
NA	Nutrient agar
Na	Sodium
$NaBH_4$	Sodium borohydride
NaOH	Sodium hydroxide
NB	Nutrient broth
NCIM	National Collection of Industrial Microorganisms
Ni	Nickel
OH	Hydroxyl group/bond
P	Phosphorous
PBMCs	Peripheral Blood Mononuclear Cells
PBS	Phosphate buffer saline
PVA	Poly (vinyl-alcohol)
RBCs	Red Blood Cells
RMSE	Root mean square errors
ROS	Reactive oxygen species
RPMI-1640	Roswell Park Memorial Institute (RPMI) 1640 Medium
SBF	Simulated body fluid
SEM	Scanning Electron Microscope
SS	Stainless steel
TDS	Total Dissolved Solids
TEM	Transmission Electron Microscopy
TGA	Thermogravimetric Analysis
TSS	Total Suspended Solids
USEPA	United States Environmental Protection Agency
UV	Ultraviolet
UV-Vis	Ultraviolet-Visible
W	Weight
WHO	World Health Organization
XPS	X-Ray Photoelectron Spectroscopy
XRD	X-Ray Powder Diffraction
ZoI	Zone of Inhibition

ABSTRACT

The invasion of bacterial pathogens has becoming a pervasive and challenging issue for public health and environmental well-being with far-reaching implications. The survival and success of all such pathogens share a common requirement: a conducive niche that allows initial attachment, colonization, and replication. Once established, they become resilient to eradicate, develop multi drug-resistance capacity and facilitate further spread. Drinking water and biomedical implants serve as prominent examples of such niches that grapple with bacterial contamination, bearing huge socioeconomic burdens with a high mortality rate. Inherent limitations in conventional disinfection technologies necessitate novel strategies in these two sectors to counteract the challenges posed by such 'smart' enemies. The present work, thus is an attempt to develop polymer-based antimicrobial therapeutics aimed at disrupting the 'niche-resistance' feature of bacteria, utilizing nanotechnology as a tool with multimodal functionalities. Polymeric nanocomposites, in the form of hydrogels and thin films, were fabricated for biocidal applications in both water disinfection and biomedical implants. All such chitosan-based polymeric nanocomposites were synthesized using eco-friendly and straightforward protocols. These materials served as a template for immobilizing nano-antimicrobials, specifically silver nanoparticles (AgNPs) or graphene oxide (GO), with the primary objective of enhancing their antibacterial efficacy while limiting their release into the surrounding environment. The research includes a comprehensive analysis of material characteristics, antibacterial performance against environmentally and clinically relevant strains, elucidation of antibacterial mechanisms, modelling disinfection kinetics, *in vitro* cytotoxicity assessment, hemocompatibility testing, and evaluation of soil biodegradability.

Under environmentally relevant conditions, the improper disposal of biomedical waste presents hazardous consequences for natural water resources, as contamination can occur through various leakage pathways into waterways. This study successfully demonstrates the disinfection potential of nano-silver loaded chitosan-PVA (CS/PVA/Ag) hydrogel to completely eradicate biomedical contaminants (*S. aureus*; *S. epidermidis*) coexisting with natural contaminants (*E. aerogenes*; *E. coli*) in environmental samples for the first time. The polymeric networks of hydrogel served dual role for *in situ* synthesis and immobilization of silver nanoparticles (AgNPs) simultaneously. Porous Ag-loaded hydrogels elicited a temperature-dependent swelling behaviour and exhibited an improved mechanical strength (Young's modulus, 12.36±0.29 MPa; elongation at break, 180%) by effectively distributing

the external stress and restored its structural integrity. A complete disinfection (100% killing) could be achieved within 4 h against all four tested contaminants, demonstrating a distinct strain-specific biocidal activity. Being a diffusion-controlled process, the oxidative dissolution of AgNPs, deeply buried in interiors of hydrogel architectures was adversely affected on repeated use and restricted a maximum silver release of 38.8±5.6 μg g^{-1} hydrogel in aqueous suspension over seven days. Correlating reusability and silver release kinetics, a predominant contact-active role of hydrogel was envisaged via 'capture and kill' over silver ions leaching for rapid water disinfection. The Ag-loaded hydrogels also severely inhibited biofilm formation of *Escherichia coli* and *Staphylococcus aureus* till 48 h. Finally, hydrogels could completely disinfect the natural water samples i.e., river, ground and tap water with inherited microbiota and biomedical contaminants in 2 h under real test conditions.

Another nanocomposite hydrogel, consisting of chitosan-graphene oxide loaded with silver nanoparticles (CS/GO/Ag) was evaluated for on-demand disinfection ability against natural contaminants and biomedical pathogens in natural waters. *In situ* synthesized silver nanoparticles (AgNPs) with fine-size of ~4.2 nm were subsequently immobilized within 3D polymeric hydrogel network. The hydrogel nanocomposites displayed time & temperature swelling behaviour with low AgNPs release concentration (87.4 ppb) and rate (0.07%) over 96 h. A definite species-specific biocidal activity exhibiting 100% kill rate could be achieved within 2 h against *E. aerogenes*, *E. coli*, *S. aureus*, and *S. epidermidis*. Nano-silver loaded hydrogels were equally effective with ≥87.8% growth inhibition at higher bacterial loads of ~10^4-10^6 CFU mL^{-1}. CS/GO/Ag hydrogels fabricated in a continuous-flow reactor (bed height, 8cm; flow-rate, 2.6 mL min^{-1}) disinfected river and rain water within 20 minutes with >90% reusability over five cycles. The modelling kinetics demonstrated that bacterial inactivation followed the non-linear Weibull model. Comprehensive analysis of the disinfection mechanism revealed that membrane destruction and elevated oxidative stress play pivotal roles in initiating the bactericidal process. The CS/GO/Ag nanocomposite indicated superior mechanical strength, soil biodegradability (30.2% wt. loss) and significant biocompatibility towards various mammalian cells including peripheral blood mononuclear cells (PBMCs), Vero, and human hepatocellular carcinoma (HepG2).

In healthcare, Biomaterial-associated infections (BAIs) pose a major hindrance to the successful integration of biomedical implants during regenerative surgeries. An alternative antimicrobial therapeutics to diminish bacterial attachment by modifying implant surface via

passive coatings is proposed here. A uniform, thin-film of chitosan/polyvinyl alcohol/graphene oxide (CS/PVA/GO) was coated on 316L stainless steel (SS) surface through spread casting followed by solvent evaporation. The abundant anchoring sites available at macromolecular interfaces of chitosan/PVA matrix facilitated a smooth, dense loading of GO. The effect of GO content on drying process parameters, physicochemical features, antibacterial potential, and biocompatibility of coatings was thoroughly studied. The residual solvent at drying equilibrium increased with GO content and by altering the initial coating thickness from 700 to 1400 µm. The hybrid films displayed good adhesion behavior, and UV-protection ability with desired mechanical and thermal stability when coated on SS surface. Coatings manifested a 1.5-1.7 fold rise in antibacterial efficacy against *Staphylococcus epidermidis* and *Staphylococcus aureus* while exhibiting a permanent biocidal response after 6 h. We investigated excessive ROS generation as the predominant antibacterial mechanism, which diminishes bacterial integrity by inducing membrane permeability and suppressing respiratory chain activity as secondary mechanisms. All coatings with varying GO content appeared non-hemolytic (<2%) with ultra-low cytotoxicity (<29.08%) against human hepatocellular carcinoma (HepG2) and peripheral blood mononuclear cells (PBMCs). The degradation rate of coatings in simulated body fluid exhibited a higher stability, indicated by a lower weight loss (69-78%) and a decrease in pH values as the GO content in coatings increased from 0.05 to 0.15 wt.%. Such an anti-infective coating could be a step forward in inhibiting bacterial colonization on SS surfaces to extend its lifespan.

In conclusion, the use of polymeric nanocomposites featuring silver nanoparticles and graphene oxide holds immense promise for point-of-use water disinfection and as protective coatings for stainless steel biomedical implants. The cost-effectiveness, accessibility to materials, and straightforward fabrication process, all without posing any toxicological concerns, make these nanocomposites an exceptionally practical and impactful solution for various antimicrobial applications.

Chapter 1

Introduction

1.1 Scientific Background

Bacteria are omnipresent. The majority of bacteria pose no harm, as we continually inhale and ingest them without experiencing illness. In fact, our association with them is so crucial that our survival would be challenging in their absence (Rook et al. 2017; Zeng et al. 2022). On contrary, the persistence and prevalence of pathogenic bacteria, even in small numbers, have posed significant challenges to global economy and hindered progress towards achieving healthier lifestyles worldwide (Peters et al. 2012; Váradi et al. 2017; WHO 2022). Bacteria know no borders and have the capacity to interact with any solid substrate, liquid or even air to grow and proliferate (Zhang et al. 2020).

Two critical sectors, constantly struggling with bacterial invasion and present a major source of mortality/morbidity in humans are drinking water and biomedical devices. Major species of bacterial pathogens commonly recognized in these domains include *Escherichia coli, Staphylococcus aureus, Enterobacter aerogenes, Vibrio cholerae*, *Pseudomonas aeruginosa*, *Staphylococcus epidermidis,* and *Klebsiella spp*. (Amin Yavari et al. 2020; Arciola et al. 2018; Ashbolt 2015; Baker-Austin et al. 2018). In case of potable water, resources like aquifers, ponds, and lakes have consistently suffered contamination by these microorganisms due to unhygienic anthropogenic activities, unsafe waste disposal practices and inadequate sanitation, leading to the emergence of various waterborne diseases (Bain et al. 2020). To name a few, cholera, dysentery, and typhoid are among the leading causes of over 829,000 annual deaths globally, attributed to unsafe drinking water, as reported by the World Health Organization (Palansooriya et al. 2020; WHO 2019). On a similar note, biomedical implants, aim to restore mobility and function of damaged tissues are prone to bacterial colonization causing biomaterial associated infections (BAIs). Indwelling medical devices account for 50-70% of all healthcare-related infections, and prior to the Covid-19 pandemic, they were responsible for a million deaths per year in the United States alone (Filipović et al. 2020; WHO 2015).

The above two domains though present distinct challenges, they share a common apprehension to health professionals, i.e., cross-contamination of bacterial pathogens. The improper disposal of biomedical waste and wastewater into our water systems, along with the aging infrastructure of water distribution networks, has facilitated the infiltration of nosocomial pathogens into our drinking water supply—a concern frequently overlooked (Parida et al. 2022; WHO 2018; Zhang et al. 2020). Similarly, within healthcare settings, such as dental unit waterlines (Ricci

et al. 2012; Zhang et al. 2018) or during the production and handling of biomaterials, infections related to waterborne pathogens have been witnessed (Park et al. 2012; WHO 2016). Hence, it is imperative to devise a comprehensive strategy to mitigate the proliferation of bacterial pathogens, spanning both the biomedical sector and drinking water, underscores the pressing need in our current context.

The current research carry profound implications for the realization of the United Nations' 6th Sustainable Development Goal, which aims to ensure access to safe and clean drinking water, particularly in regions, like India with inadequate infrastructures (United-Nations 2015). Conventional water disinfection methods, including chlorination and UV irradiation, as well as advanced technologies like membrane filtration, ozonation often prove ineffective over large scales. These methods introduce additional challenges through to the generation of carcinogenic disinfection by products, necessitate continuous monitoring, and demands high energy and resource inputs (Bahcelioglu et al. 2021; Li and Mitch 2018; Zhang et al. 2020). Conversely, to control biomaterial associated infections, existing treatments often rely on broad-spectrum antibiotics and chemical biocides. Such approaches come with inherent drawbacks beyond the development of resistance against host defences, culminating to surgical removal of the biomedical implant, carrying post-operative complications, and imposing huge economic burdens (Chae et al. 2020; Koo et al. 2017; Maillard and Pascoe 2023). Moreover, both sectors encounter similar issues pertaining to biofilm formation and the inadequacy of existing antimicrobial solutions (Cámara et al. 2022). Thus, the correlation and potential hazards involved emphasize the urgent need for developing new-generation antimicrobial materials capable of effectively treating microbial contamination in water bodies and inhibiting the colonization of microorganisms on biomedical implants together. By addressing this shared narrative, advancements in antimicrobial materials hold the potential to make a significant impact on public health and foster sustainability in both sectors.

Recent advancements in nanoscience and technology have unlocked immense opportunities for manipulating materials at nanoscale, altering their physicochemical attributes and transforming them into promising antimicrobial agents (Agnihotri et al. 2015; Agnihotri et al. 2013; Xing et al. 2023). Due to their extremely small size, nanomaterials possess a high surface area-to-volume ratio, rendering them remarkably effective against bacteria even at relatively lower concentrations than their bulk counterparts (Agnihotri et al. 2014; Wang et al. 2020). Several nanostructures such as silver, copper, zinc-oxide, carbon nanotubes, graphene and its

derivatives are being widely adopted across various disciplines including environmental (air filtration, water purification and disinfection) (Lyu et al. 2021; Mauter et al. 2018), biomedical (wound dressing, biomaterial coatings, sutures, catheters) (Gaur et al. 2021; Makvandi et al. 2020) and consumer products (cosmetics, textiles, food packaging) (Dubey et al. 2022; Huang et al. 2020; Kim et al. 2022). Furthermore, nanomaterials exhibit a multi-modal mechanism of antibacterial action, preventing microorganisms from developing resistance against them (Munir et al. 2020; Xie et al. 2023). A recent few reports claiming direct, contact-active role of nano-silver based composites appear to be more efficacious on bacterial species (Agnihotri et al. 2019; Bondarenko et al. 2013). This mechanism does not require either a continuous release of nanomaterials or their subsequent internationalization inside bacterial cells to elicit the bactericidal effect.

Despite their benefits, the practical application of as-synthesized nanomaterials for antibacterial purposes faces three significant challenges. Firstly, nanomaterials, in colloidal state are susceptible to coalescence, leading to the formation of larger aggregates and lose their original efficacy during application (Bharti et al. 2015; Tang et al. 2014). Secondly, retrieving colloidal nanoparticles after their intended use is exceedingly challenging, discouraging their reuse and rendering the strategy economically unviable (Duval et al. 2019). Thirdly, the continuous release of nanoparticles after each use can inevitably impact our ecosystems, primarily affecting aquatic life forms before potentially affecting humans (Agnihotri et al. 2013; Mukherji et al. 2011).

Over the past few years, substantial efforts have been directed towards minimizing these limitations, either by immobilizing or incorporating nanoparticles onto suitable support matrices to enhance their antibacterial activities and promote reusability (Agnihotri et al. 2012; Matsumoto et al. 2021; Moritz and Geszke-Moritz 2013; Zakia et al. 2020). In general, various immobilization approaches can be categorized into three main categories:

1. Incorporation and entrapment of segregated nanoparticles inside a porous matrix
2. Simultaneous *in-situ* generation and immobilization of nanoparticles onto a support matrix
3. Immobilization of nanoparticles on a surface-functionalized solid support

The key factor in achieving a stable association between nanoparticles and the support matrix lies in the selection of appropriate surface modification methods. The choice of immobilization protocol though is dictated through several parameters including the type of solid support used,

size/shape, morphology, surface functionalization, and stability of nanoparticles, as well as specific application for which they are intended (Atmianlu et al. 2021; Bhatia et al. 2017).

Among the various choices of support matrices, polymers have garnered considerable attention for immobilizing nanomaterials due to their flexibility, relatively low density, and cost-effectiveness (Ghazzy et al. 2023). Polymers of both natural and synthetic origin, including chitosan, alginate, polyvinyl alcohol, and polylactic acid, have been extensively employed to anchor nanoparticles using *in situ* or *ex situ* approaches (Porter et al. 2021; Shi et al. 2020; Xie et al. 2020; Zhang et al. 2019). Polymeric nanocomposite, thus emerge as an advanced group of materials offering numerous advantages over conventional composites, such as enhanced mechanical, thermal, and biological characteristics. Polymer nanocomposites also offer versatility in creating diverse structures tailored for specific antibacterial purposes. These structures include hydrogels, porous membranes for water treatment (Das et al. 2020; Marjani et al. 2020), fibres for wound dressing (Jatoi 2020), thin-film coatings for biomedical implants (Rikhari et al. 2020), and scaffolds for tissue regeneration (Shanmugam et al. 2020).

Hydrogels are porous, hierarchical polymeric microstructures with high water absorption capacity due to large surface area and swelling capabilities. They have emerged as a paradigm in myriad of water purification applications not limited to disinfection, clean-up of oil-spill regions, removing emerging contaminants, and water desalination (Li et al. 2019; Salazar et al. 2020; Sultan et al. 2022; Zhou et al. 2018). The semi-interpenetrating networks of hydrogel act as miniature reactors, offering numerous sites for synthesizing and subsequently immobilizing nanomaterials through surface functionalization (Mohan et al. 2007). Besides inherent antimicrobial and biodegradable, chitosan (CS)-based hydrogel displays a well-defined porous structure with the necessary elasticity to facilitate optimal interactions between AgNPs and water within their semi-interpenetrating networks, allowing for better control over silver release (Guo et al. 2021). The presence of electrostatic and covalent interactions in tailorable chitosan-based hydrogels offers numerous sites for AgNPs immobilization, which offers numerous benefits in water disinfection purposes. One of primary limitations of chitosan-based hydrogels i.e., poor mechanical strength can also be minimized by introducing specific crosslinker(s), compatible polymers, and carbon-based fillers. Incorporating a water-soluble polymer, such as polyvinyl alcohol (Alfuraydi et al. 2022), or another nano-antimicrobial, i.e., graphene oxide (GO) (Chen et al. 2013) may augment to achieve the desired physicochemical and mechanical properties of hydrogel nanocomposites too. Such hydrogel composites can

effectively eliminate bacterial pathogens, not only in simulated laboratory conditions but also when treating water with diverse background chemistry conditions. They are equally suitable for operation under continuous flow-through conditions, if installed within a reactor assembly (Taka et al. 2021). A comprehensive evaluation of AgNPs-based hydrogel nanocomposites under various situation will establish them as a robust choice for concurrent water disinfection approaches.

In biomedical sector, our limited understanding towards microbial interactions at implant's interface significantly hinders the long-term utilization of prophylactic coatings. There is a constant need for the development of facile methods to create biomedical coatings without the use of toxic ingredients. Considering these crucial aspects, graphene oxide (GO) emerges as a highly relevant nanomaterial. GO possesses characteristics such as easy functionalization, impressive mechanical strength, and minimal cytotoxicity, making it amenable for producing durable and bactericidal coatings for biomedical surfaces (Grant et al. 2021; Panda et al. 2018; Zhao et al. 2016). The 2D structure of GO, composed of hexagonally packed carbon atoms and featuring various functional groups like hydroxyl, epoxy, and carboxyl, lends itself well to antibacterial applications (Su et al. 2021). GO is a polymer-friendly nanomaterials which can integrate well in coating formulation composed of chitosan, polyethylene glycol, polyvinyl pyrrolidone, and polyvinyl alcohol (Jena et al. 2021; Silva-Leyton et al. 2019; Tamayo Marín et al. 2019). These formulations exhibits the desired surface functionalities of a coating without compromising the mechanical properties of the underlying substrate (Sadeghi and Seo 2022). GO-based polymer nanocomposites have proven to enhance substrate adhesion, prevent crack formation, and significantly improve the overall antibacterial performance of coatings (Muthuchamy et al. 2020; Ruiz et al. 2019). Thus, by utilizing chitosan and PVA, each with its film-forming capability and adjustable plasticity, a robust support matrix can be formed for GO, serving as an antimicrobial nanofiller. The resulting nanocomposite films provide implants with a coveted antimicrobial interface, effectively preventing bacterial adhesion, proliferation, and biomaterial-associated infections.

1.2 Scope of Work and Objectives

The thesis focuses on the application of polymeric nanocomposites to combat bacterial pathogens within two domains, i.e. drinking water and biomedical implants. Specifically, hydrogel nanocomposites, derived from chitosan-based polymers, were employed,

incorporating silver nanoparticles and graphene oxide. These materials were then transformed into hierarchical structures or surface coatings for subsequent utilization. To establish defect-free biopolymeric coatings on stainless steel implants, an extensive analysis of drying processes was conducted, considering various parameters. The research also explored the impact of graphene oxide content on physicochemical and antimicrobial properties to develop resilient and bactericidal coatings for medical surfaces. A strategy for enhancing the antibacterial performance of stainless steel-based implants was devised.

For disinfection purposes, the antibacterial effectiveness of polymer nanocomposites was evaluated against both natural and biomedical contaminants coexisting in potable water due to unsafe biomedical waste disposal. The hydrogels' ability to eliminate pathogens was assessed across diverse global water quality parameters, allowing for the correlation of disinfection kinetics with corresponding silver release profiles, providing insights into the mechanism of bactericidal action by immobilized nanoparticles. This disinfection approach is distinguished by its eco-friendliness, with silver release levels well below EPA standards, minimizing the associated risks of silver leaching into the ecosystem. Finally, the hydrogel nanocomposite was deployed in a fixed-bed reactor to disinfect large volumes of water continuously. It is noteworthy that the hydrogel poses no toxic effects on humans and is biodegradable in soil. This research is particularly significant given the growing use of AgNPs-based disinfection systems, where the leaching of colloidal AgNPs into natural surface and groundwater could have severe ecological repercussions.

The fundamental questions that were attempted to address in this research work are:

Research Question-1: *Can polymeric nanocomposites be synthesized to effectively eliminate both water-borne and biomedical pathogens together under practically relevant conditions?*

Research Question-2: *Is it feasible to develop a strategy for immobilizing silver nanoparticles onto a support matrix just sufficient to elicit biocidal response without causing much release in the surrounding environment?*

Research Question-3: *What are the underlying mechanisms explaining the antibacterial activity of polymeric nanocomposites, while minimizing the release of loaded nano-silver? Are there synergistic effects contributing to enhanced antibacterial activity?*

Research Question-4: *How do the continuous flow-through operations, biocompatibility and biodegradation characteristics of the resulting polymeric nanocomposites ensure their safety and suitability for applications in both biomedical and water disinfection contexts?*

Building upon the questions posed and an extensive review of existing literature, the research objectives were formulated as follows:

1. Synthesis and characterization of nano-silver immobilized polymeric nanocomposite based on chitosan hydrogel
2. Evaluation of the antibacterial activity of nano-silver loaded hydrogels against environmental and/or clinically relevant bacterial strains under various test conditions
3. Determining the cytotoxic effects of polymeric nanocomposites under *in vitro* conditions

1.3 Organization of the Thesis

The doctoral research work in current thesis is systematically organized in five successive chapters. A sequential overview of these chapters ensues

Chapter 1 acknowledges the pervasive issue of bacterial contamination in both potable water sources and biomedical implants, emphasizing the adverse consequences for global public health. The chapter underscores the shared challenges posed by microbial intrusion in these diverse applications and the inadequacies of existing technologies/infrastructure in effectively addressing these issues. It delves into a comprehensive discussion of how nanotechnology can serve as a valuable tool to combat microbial infections, highlighting current limitations and potential remedies. Furthermore, the chapter advocates for the use of immobilized nanomaterials on suitable support systems, the development of contact-driven polymeric nanocomposites, and the creation of hydrogel-based nano-antimicrobials that are adaptable for both water disinfection and coating biomedical implants. These solutions are designed to exhibit synergistic responses, while minimizing human cytotoxicity and ensuring good biodegradability.

Chapter-2 provides a thorough literature review, encompassing an in-depth examination of polymer nanocomposites. It covers various aspects, including properties and composition in terms of polymer matrices and nano fillers, as well as synthesis methods. The chapter explores the versatility of polymer nanocomposites when applied as hydrogels for water treatment and as thin-film coatings for biomedical implants, highlighting their specific characteristics and the

associated fabrication strategies. The chapter compiles and summarizes recent research studies conducted over the past five years, elucidating the antibacterial performance of hydrogels and coatings in their respective domains. Finally, the chapter addresses the remaining challenges within the current research landscape and outlines potential areas for future studies.

Chapter-3 elaborates on the experimental procedures employed for the fabrication, optimization and characterization of chitosan-based hydrogels and coatings. Protocols adopted for investigating antibacterial activity with underlying mechanisms of developed nanocomposites and their real-time applications are presented as well. Methods for *in vitro* biocompatibility evaluation with different types of mammalian cells and biodegradability of coatings under simulated body fluid are also thoroughly described.

Chapter 4 presents the results obtained through the methodologies outlined in Chapter 3, offering scientific explanations, plausible mechanisms, and discussing their future implications.

Chapter-5 offers a concise summary of the key findings and significant conclusions derived from this research. It also provides recommendations for potential future investigations. The thesis concludes with a bibliography listing the sources and references used throughout the work.

Chapter 2

Review of Literature

2.1 Polymer Nanocomposites (PNCs)

Polymer nanocomposites (PNCs) are a class of high-performance materials that combine polymer matrices with organic or inorganic fillers, while possessing at least one of their dimension in nanoscale (10–100 nm) (Sun et al. 2021). Despite their relatively early birth when Theng (1970) first introduced the term "nanocomposites", PNCs did not garner significant attention in their infancy. Hess and Parker Jr (1966) pioneering work showcased one of the earliest instances where metallic cobalt particles, approximately 100 nm in size, were effectively and uniformly dispersed within a polymer matrix. Although, in late 1980s, PNCs started to develop in both academic laboratories and commercial research organizations. However, the polymer nanocomposites commenced their true journey in 1988 when Toyota Company of Japan utilized polymer/layered silicate nanocomposites in the production of their innovative car models. In the early 1990s, resurgence in use of PNCs was observed when it was discovered that incorporating such fillers could profoundly reinforce the material, leading to improved properties and performance (Balazs et al. 2006; Usuki et al. 1993). At present according to SciFinder Scholar, number of publications on search term “nanocomposites” and polymer nanocomposites” has increased to >20,000 and >4000, respectively in the year 2020 alone. Thus, PNCs have experienced significant advancements in various domains over the last decade, as evident from the exponential growth of publications on the subject since their inception.

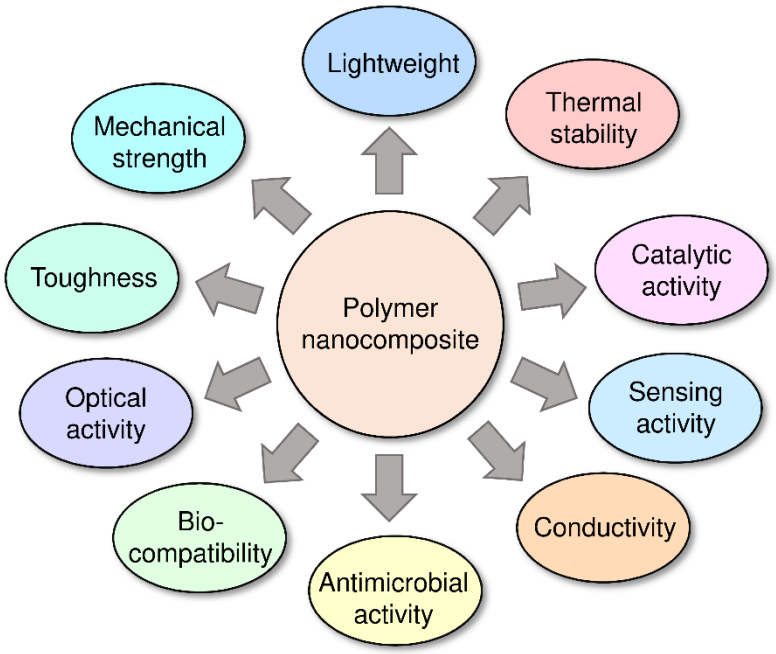

Figure 2.1 Significant properties of polymer nanocomposites.

The existence of nanomaterials (even low wt.%) in polymer matrix leads to a remarkable improvement in the desired properties of pristine polymers, including mechanical, thermal, barrier, flame retardancy, antimicrobial, biodegradability, and biocompatibility (Bitinis et al. 2011; Müller et al. 2017), without affecting their processability (Figure 2.1). Moreover, depending on the specific nanomaterials employed, it may also give rise to entirely novel intrinsic properties in the resulting polymer nanocomposites. Through integration of nanomaterials into polymer matrices, the surface chemistry is transformed, and the physicochemical properties are finely tuned, leading to a direct impact on the performance of the resultant systems. The surface chemistry, aspect ratio, size, geometrical shape, and orientation of nanomaterials are the critical parameters which invariably dictate the regulation of these performances (Zaïri et al. 2011). The optimal nanocomposite design also entails uniformly dispersing individual nanofillers within a polymer matrix. Achieving a well-dispersed state of nanofillers is crucial to fully harness the potential for enhancing the material's properties. This uniform distribution results in significant interfacial interactions at the interfaces between nanomaterials and polymer matrices while, the nanoscopic scale of these domains combined with cost to performance ratio fundamentally sets PNCs apart from conventional composites and doped polymer systems. Thus, the crossover of polymer science with nanotechnology has unlocked diverse application-oriented possibilities for polymer nanocomposites, which expand to various fields including aerospace, automotive, biomaterials, biomedical implant coatings, energy storage and dielectrics, photocatalysis, sensing, packaging, flame retardancy, antimicrobial materials, water treatment & disinfection, drug delivery system, etc. in addition to the high-performing materials (Gao 2012; Koo 2019; Ray and Bousmina 2007) (Table 2.1). Consequently, PNCs have carved out a unique and unparalleled position in the realm of advanced materials.

Table 2.1 Properties and Applications of Polymer Nanocomposites in Various Fields.

Type of polymer nanocomposites	Features	Potential application(s)	Reference
Polyvinyl pyrrolidone/carboxymethyl cellulose/ multi-walled CNTs/AgNPs films	• Improvement in electrical conductivity due to nanofiller making charge carrier transfer easier • Improved dielectric properties with increased quantity of parallel aligned dipoles in polymer matrix	Antireflection coatings, integral thin film capacitors, energy storage and flexible nanodielectric for microelectronic devices	Morsi et al. (2023)
Nano-silica modified MXene/Poly (vinyl) alcohol	• Peak heat release rate (pHRR) 34.9% lower than pure PVA • Tensile strength increased by 32.9% due to addition of 2% m-MXene	Flame-retardant materials	Ning et al. (2021)
Polyaniline/ZnO	• 63 times higher degradation rate of metronidazole by ZnO/PANI than pure ZnO	Photocatalyst; photocatalytic degradation	Asgari et al. (2019)
plasma polyaniline-modified tin oxide/ reduced graphene oxide	• Improved lower detection limit of 0.047 ng mL^{-1} (0.26 nM) (S/N = 3)	Electrochemical biosensor for glucose, biological diagnosis	Wu et al. (2017)
Sodium alginate/cellulose nanowhiskers/CuO films	• Strong antibacterial activity against *S. aureus, E. coli, Salmonella sp., C. albicans, Trichoderma spp.* • High antioxidant activity	Antibacterial active food packaging	Saravanakumar et al. (2020)

UiO-67-Zirconium nanocrystals/Polyurethane films	• 60-fold improvement in the adsorption capacity of ocular drug due to UiO-67 nanocrystals incorporation	Drug delivery in ocular therapeutics	Gandara-Loe et al. (2020)
ZnO modified natural rubber/graphene oxide (ZnO m-NR/GO)	• Mechanical and dielectric properties from neat NR and NR-GO nanocomposites significantly improved	Coating in automotive and aerospace	Jose and Athikalam Paulose (2020)
Natural rubber/multi-walled CNTs (NR/MWCNTs)	• Lower filler concentration reinforced NR with improved geometrical stability	Prosthetic foot (biomaterial)	Medupin et al. (2019)
Functionalized boron nitride nanosheets/graphene oxide/silver/polyether sulfone (FBN/GO-Ag/PES) membrane	• 21% and 22% increment of hydrophilicity and porosity with 1 wt.% FBN-GO-Ag • 40% increase in permeability • Improvement in dye removal and fouling resistance, antibacterial performance	Dye removal and disinfection of wastewater	Vatanpour et al. (2022)
Poly-L-lactic acid/ Graphene oxide/AgNPs/ (PLLA/GO/Ag)	• Superior corrosion resistance and cytocompatibility than uncoated Mg alloy • Improved antibacterial performance against *E. coli* and *S. aureus*	Anti-corrosion and antibacterial coatings for Mg alloy implants	Bakhsheshi-Rad et al. (2020)

2.2 Composition of PNCs

2.2.1 Polymer/Host Matrices

Polymers are macromolecules composed of organic and inorganic constituents that are formed by covalent linkages of a large number of small and simple repeating units called monomers, through polymerization process (Karak 2009). A wide range of polymers, including fibers, rubbers, and plastics, serve as matrices for manufacturing polymer nanocomposites with various nanomaterials. Both *in situ*-generated polymers (simultaneously with nanomaterials) and preformed polymers are utilized as matrices for these composite materials. Although, the choice of the suitable polymer is primarily influenced by its physicochemical (mechanical, thermal etc.) properties. However, the functionalities of the polymer backbone such as hydrophobic/hydrophilic balance, bio-compatibility and biodegradability etc. are also taken into consideration during the selection process in relation to the intended use of the PNCs (Jeon and Baek 2010). Additionally, for the fabrication of PNCs, polymer matrices can be utilized individually or in combination with two or more polymers. Moreover, as for the manufacturing process, polymers are known for their cost-effectiveness and ease of being readily fabricated into various complex conformations such as gels, films, fibres, and solids. In essence, polymers provide exceptional versatility, processability, and stability, whether used as homogenous systems, copolymers, or graft polymers in the synthesis of PNCs (Lofrano et al. 2016).

Antimicrobial polymers which contain functional groups that can kill bacteria and other polymers that may have been modified by attaching a mimicking protein to reduce toxicity are also employed for PNC synthesis intended for antibacterial applications (Palza 2015). The research in this field first commenced in 1965 with the synthesis of 2-methacryloxytroponones related antimicrobial polymers with broad-spectrum activity (Cornell and Donaruma 1965). Since then, a variety of polymers have been extensively tested to address the limitations of conventional antibiotics and highly biocidal chemicals. These polymers have the potential to offer extended effectiveness, reduced toxicity, combat antibiotic resistance, and lower production costs simultaneously (Timofeeva and Kleshcheva 2011). Utilizing such polymers to create nanocomposites not only serves as a supporting function for nanoparticles but also enhances the antibacterial performance of these PNCs. This behaviour is attributed to the synergy between the polymer and nanomaterials, and

polymer's capability for long-term ion release (Bogdanovic et al. 2015) thereby, effectively extending the antibacterial activity of the nanocomposite.

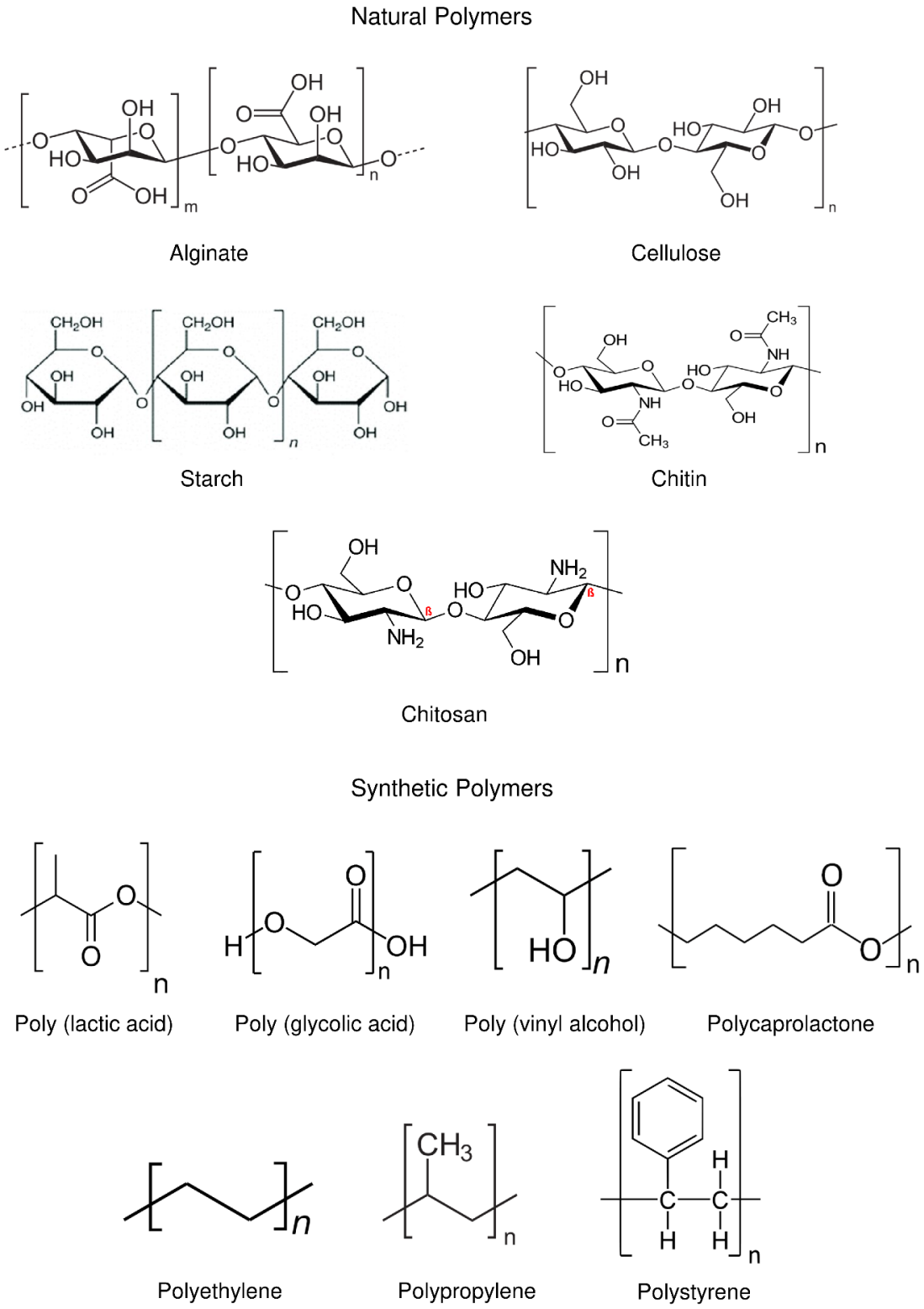

Figure 2.2 General structure of a few polymer matrices for designing antimicrobial materials.

Polymer matrices are of different categories and those mostly utilized for PNCs fabrication can broadly be divided into two major groups called natural or synthetic, based on their origin. The natural or biopolymers, which are made up of renewable resources characterized by their easy biodegradability, non-toxicity, and abundance include lignin, alginate, cellulose, starch, chitin, and chitosan. While synthetic or man-made polymers yet biodegradable are comprised of poly (lactic acid) (PLA), poly-(glycolic acid) (PGA), poly (lactic-co-glycolic acid) (PLGA), poly (vinyl alcohol) (PVA), polycaprolactone (PCL), and their copolymers (Panchal and Vasava 2022; Rodrigues and Vieira 2019; Wypij et al. 2023). In addition, some non-biodegradable synthetic polymers such as polyethylene terephthalate (PET), polyethylene (PE), polypropylene (PP) and polystyrene (PS) (Mathew and Radhakrishnan 2019) have also been utilized for PNC synthesis. However, their use is much debated nowadays due to rising micro- and nano-plastics causing environmental damage and therefore biodegradable polymers are gaining ground (Sani et al. 2022). The general structures of most commonly employed and important polymer matrices are given in Figure 2.2 and a very brief overview is presented below.

Chitosan (CS)

Chitosan is a linear biopolymer derived from chitin, which is a natural mucopolysaccharide and a major structural component that forms the exoskeleton of shellfish, crustaceans, beaks of cephalopods, insects, and fungi cell walls (Escudero-Oñate and Martínez-Francés 2018; Kumar et al. 2019; Shukla et al. 2013). It is synthesized via chitin hydrolysis (by removing the acetyl group from chitin) under alkaline conditions in a process called deacetylation. Chemically, chitosan consists of randomly distributed N-acetyl-D-glucosamine and D-glucosamine units linked together through β-(1,4)- glycosidic bond (Rizeq et al. 2019). The ratio of these units determines the degree of deacetylation (DD), a crucial factor that affects the physicochemical and biological properties of chitosan, including solubility, viscosity, antimicrobial activity, and quality grade. Thus, chitosan with DD of >55% is often soluble in dil. acidic solutions of ascorbic acid and acetic acid (Wang and Chen 2014). Chitosan is non-toxic, antioxidant, biocompatible, biodegradable, adsorbent, antibacterial, and antifungal polymer (Kumar 2000; Wan et al. 2013; Ziani et al. 2009). However, it is the chitosan's inherent broad-spectrum antimicrobial activity against various microorganisms that has garnered significant interest across the globe (El Knidri et al. 2020).

The antimicrobial action of chitosan involves several mechanisms, which can be summarized as cell membrane disruption, chelation of essential nutrients, interference with microbial gene expression, and reactive oxygen species (ROS) generation. The antimicrobial activity of chitosan is influenced by various factors, including molecular weight, degree of deacetylation, pH, and the ionic strength of the environment. Molecular weight is a critical determinant, with lower molecular weight chitosan generally demonstrates higher antimicrobial activity due to increased solubility, allowing for better penetration of bacterial cell walls (Minh et al. 2020). Additionally, higher DD chitosan (100%, obtained by enzymatic deacetylation) often exhibits enhanced antimicrobial activity, attributed to the increased density of protonated amino groups that interact with bacterial cell surfaces (Akpan et al. 2020). Additionally, chitosan is both a polycationic and semi-crystalline polymer with hydrophobic characteristics. It also features hydrophilic functional groups, specifically one amino (NH_2) group and two hydroxyl groups (OH) in each glucosidic unit. The remarkable chemical and biological properties of chitosan are attributed to the presence of these functional groups, which significantly influence its reactivity (Shukla et al. 2013; Wang and Chen 2014). For instance, the active primary amino group in chitosan demonstrates efficient reactivity under mild reaction conditions, serving as a specific platform for attaching side groups. The hydroxyl and amino groups in chitosan also provide flexibility for customizing chitosan materials with specific functionalities, enabling adjustments in their physical and biological properties (Kumar et al. 2019; Wang and Chen 2014). By subjecting chitosan to physical and chemical functionalization, it becomes possible to incorporate desired chemical, mechanical, and physical properties, which are crucial for enhancing its reactivity with nanomaterials in subsequent PNCs formation (Negm et al. 2020; Zhao et al. 2020).

Physical (UV irradiation, ultrasounds, plasma irradiation, sputtering) or chemical (cross-polymerization, surface grafting, phosphorylation, carboxymethylation, surface-active agents) methods can be used to accomplish the functionalization of chitosan (Fiorani et al. 2014; Shukla et al. 2013). Phosphorylated chitosan-based materials have been shown to exhibit exceptional antibacterial and chelating characteristics, making them highly valuable for applications as biosorbents in water treatment (Morsy 2015; Song et al. 2018; Wang and Liu 2013; Wu et al. 2019). Further, OH and NH_2 groups of chitosan can form a variety of chemical bonds with metals, leading to the creation of stable chelate complexes capable of withstanding washing with organic solvents. This chelating property of chitosan makes it an ideal material for the synthesis of metal nanoparticles during *in situ* PNC synthesis

(Muzzarelli 2011). Chitosan reacts with H^+ ions to produce protonized chitosan with $–NH_3^+$ functional groups in an acetic acid medium. The zeta potential of nanoparticles incorporated in polymers increases with chitosan concentration due to greater availability of protonized $–NH_3^+$ on nanoparticle surfaces, which increases electrostatic repulsion among the particles and therefore reduces the incidence of agglomeration, resulting in more stable nanoparticle dispersion (Zain et al. 2014).

Cellulose

Cellulose is one of the most abundantly available, relatively cheap, renewable and versatile biopolymers on earth, which is widely distributed over a variety of sources, including plants, algae, tunicates, and some bacteria such as *Acetobacter xylinum* (Chen et al. 2008; Joseph et al. 2020). It is a linear polysaccharide composed of repeating units of D-glucose, linked through β-(1,4)-glycosidic bonds (Bezerra et al. 2015). Cellulose is tasteless and water-insoluble for which binary mixtures of organic or inorganic liquids and organic electrolytes are used as preferred solvents. It exhibits a robust affinity for self-association and the formation of extended structures through the creation of intramolecular and intermolecular hydrogen bonds due to the presence of strongly interacting hydroxyl groups (Jorfi and Foster 2015). The significant traits of cellulose, such as chirality, degradability, chemical variability, and hydrophilicity can be attributed to its molecular structure and the presence of hydroxyl groups that are accessible for chemical modifications and superior hydrogen bonding (Padalkar et al. 2010). The mechanical properties of cellulose are determined by both its crystalline and amorphous regions, which contribute to its superior tensile strength and stiffness owing to their uniform distribution. Cellulose is also non-toxic, broadly inert biocompatible polymer and although non-biodegradable *in vivo* however, studies have shown that oxidized cellulose is potentially degradable (Li et al. 2009; Luo et al. 2013). The impressive properties of cellulose makes it a promising candidate for fabrication of cellulose nanocomposites (Pandey et al. 2013) which are widely applicable in diverse fields of biomedical devices, packaging, and textiles. Cellulose polymer does not possess intrinsic antibacterial activity however, by combining appropriate nanoparticles with cellulose, the preparation of hybrid composites has resulted in a plethora of materials exhibiting significant antibacterial activity. Furthermore, in cellulose based nanocomposites the antibacterial activity is also dependent upon the type and structure of the polymer. For instance, bacterial cellulose based copper nanocomposite shows better antibacterial activity because its 3D

internal organization functions as a protective cage for copper nanoparticles (CuNPs), resulting in reduced copper ion release compared to the more open structure of vegetal cellulose (Pinto et al. 2013).

Poly(vinyl alcohol) (PVA)

PVA is a linear and semi-crystalline synthetic polymer, which is tasteless, odourless, non-toxic, biocompatible, easily processible, and thermostable (Abdullah et al. 2017; Saini et al. 2017; Ye et al. 2014). PVA is commercially produced by polymerization of vinyl acetate as monomer since its structural monomer (i.e., vinyl alcohol) is unstable in nature. PVA is formed as a reaction precipitate of controlled partial alkaline hydrolysis (saponification) where, in an aq. sodium hydroxide environment, the ester group of vinyl acetate is partially substituted with a hydroxyl group. The length (time period) of the saponification reaction determines the degree of hydrolysis of PVA which in turn dictates its various physical attributes such as water solubility, degree of polymerization, film formation density, and crystallinity (Gaaz et al. 2015; Saunders 2012). Additionally, by altering the length of monomer and the degree of hydrolysis under acidic or alkaline conditions, various forms of PVA with distinct flexibility, tensile strength, dispersing power, emulsification index, adhesiveness, and solubility can be obtained (Halima 2016). In commercially available bulk form, the abundance of hydroxyl groups attached to the carbon backbone creates a significant source of hydrogen bonding, which exerts a major influence on its physicochemical (such as high melting point) and mechanical attributes.

Throughout the exploration of PVA matrix, diverse morphologies have been discovered, paving the way for a wide range of applications including biomedical, water treatment, pharmaceutical and others (Hassan and Peppas 2000). For instance, certain water filtration systems may employ PVA gel beads while PVA films due to their high optical quality are useful in optical sensors and devices (Surkatti and El-Naas 2014). Further, PVA based hydrogels are being fabricated through crosslinkers by exploiting its hydrophilic nature for water disinfection applications (Hassan and Peppas 2000). PVA is also utilized in the synthesis of controlled and interconnected micro-porous 3D biomedical scaffolds, catering to tissue engineering applications (Itoh et al. 2016). Some aforementioned areas work well with native PVA matrix while others depend on its modified composition and advancement of novel polymeric materials primarily relies on compounding, blending, and modification

rather than the chemical synthesis of entirely new polymers. Therefore, modifying the properties of PVA becomes crucial for achieving specific targeted applications. Chemical modification of PVA could be achieved by conventional reactions involving carbamation, acetalization, etherification, or esterification of its hydroxyl groups (Awada and Daneault 2015), while a more modern approach to chemical modification comprises of click chemistry. Thus, modified and pristine versions of PVA allow other materials to be incorporated via hydrogen bonding and is employed as an embedding mat or matrix for metal/inorganic nanofillers for PNC synthesis (Moulay 2015).

Table 2.2 Summary of Nanomaterials grouped according to their Nanoscale Dimensions

0D	1D	2D
		
• Nano-silver (AgNPs) • Nano-zinc oxide (ZnO NPs) • Nano-copper (CuNPs) • Nano-titanium dioxide (TiO_2NPs) • Nano-silica (SiNPs)	• Carbon nanotubes (CNTs) • Halloysite nanotubes (HNTs) • Carbon nanofibers (CNFs) • Nickel nanostrands (NiNs) • Aluminium oxide nanofibers (Nafen)	• Nanographene platelets (NGPs) • Graphene oxide (GO) • Montmorillonite clays (MMT) • Reduced graphene oxide (rGO) • Layered double hydroxide (LDHs)

2.2.2 Nanomaterial Fillers

Nanofillers or nanomaterials are typically materials with at least one dimension below 100 nm with fascinating intrinsic and in often cases, enhanced nanoscale physicochemical and biological properties that differ from their bulk counterparts (Hanemann and Szabó 2010). Up until now, diverse types of nanomaterials have been discovered to possess the capability to create PNCs. The inherent specific surface area of nanoparticles facilitates the development of a substantial interphase within the composite, characterized by outstanding interactions between the nanofillers and the polymer matrix (Naffakh and Díez-Pascual 2014). The inclusion of finely dispersed nanomaterials within polymeric matrices has been noted for its significant utility in enhancing the resulting composites used for diverse applications such as

water treatment and remediation purposes, ranging from its photocatalysis (Ali et al. 2016; Hir et al. 2017) to disinfection (Yuan et al. 2016), biomedical implant coatings (Morselli et al. 2023) and sensing and monitoring (Östergren et al. 2021) functionalities. The selection of nanoparticles to utilize in the fabrication of PNCs is primarily dictated by the intended purpose while thermal, mechanical, biological, and tribological characteristics of nanoparticles become deciding variables during design of PNCs (Naffakh and Díez-Pascual 2014).

A vast array of nanomaterials in the form of bulk materials, films or hybrid powders have been employed in PNCs fabrication. Based on the composition, nanomaterials can be sorted into different classes such as metal/metal-oxide NPs, ceramic NPs, carbon-based NPs, mixed-metals NPs, organic NPs (polymeric, micelles, dendrimers), and clay/silicate-based NPs etc (Akharame et al. 2018). Categorized according to their dimensions, nanoparticles can also be classified into zero-dimensional (0D), one-dimensional (1D), and two-dimensional (2D) structures (Tiwari et al. 2012) (Table 2.2). Various forms of spherical nanoparticles fall within the category of 0D nanomaterials, encompassing metals like gold (Au), silver (Ag), copper (Cu), and iron (Fe). Additionally, metal oxides such as iron oxide (Fe_2O_3 or Fe_3O_4), copper oxide (CuO or Cu_2O), zinc oxide (ZnO), titanium dioxide (TiO_2), silica (SiO_2), serve as notable examples. While the most prevalent form is spherical, 0D nanomaterials exhibit diverse shapes, ranging from nanospheres to nanoclusters and even nanocrystals (Fahlman 2023). Nanotubes, nanorods, nanowires, and nanofibers constitute crucial specimens of 1D nanomaterials and contribute to the formation of extended structures in PNCs (Fahlman 2023). Carbon nanotubes (CNTs), cellulose nanofibers, carbon nanofibers (CNFs), polyaniline nanofibers, and nanowhiskers are commonly used 1D nanomaterials. 2D nanomaterials are available in the form of sheets, discs, plates, films, layers or ribbons and prove to be the most advantageous out of all the varieties of nanomaterials. In this class, nanoclay or layered silicates have been investigated extensively and being hydrophilic in nature, these are often modified with organic cationic surfactants via an ion-exchange reactions. For instance, organically modified montmorillonite nanoclays (OMMT) incorporate better than their pristine counterpart in polymers, which are relatively hydrophobic and organic (Ray and Okamoto 2003). Besides silicate nanomaterials, carbon-based 2D nanomaterials such as graphene, graphene oxide (GO), and reduced graphene oxide (rGO) are becoming extremely important in the field of PNCs. Depending upon the structure, shape, crystallinity, and chemical nature of these nanomaterials, mechanical and thermal

stability as well as new biological functionalities such as antimicrobial activity are provided to the polymer matrix (Jeon and Baek 2010). Several antimicrobial nanomaterials possess inherent ability to kill bacteria and are classified into oligodynamic metals, including Ag, Cu, Zn, Ti, and Co (Nangmenyi and Economy 2009); photocatalytic semi-conductors, such as TiO_2 and ZnO (Chong et al. 2010; Gondal et al. 2009); and carbon nanomaterials, including CNTs and fullerenes (Kang et al. 2007; Lee et al. 2009; Magrez et al. 2006). These nanomaterials can potentially be used as alternative disinfectants or coupled with current technologies to enhance the bacterial inactivation efficacy.

Two primary methodologies exist for creating nanostructured materials: the top-down and bottom-up approaches. The top-down method includes the systematic breakdown of the bulk materials into smaller fragments with nanoscale dimension by following grinding mechanism involved in physical processes such as mechanical milling, nanolithography, laser ablation, repeated quenching, attrition, arc discharge and so on. This approach is directed by the interplay of physicochemical interactions among adjacent atoms, self-assembly principles, and the surface chemistry. The nanomaterials generated by aforementioned approaches exhibit structural anomalies such as irregular shapes, wide size distribution, low particle surface areas, and crystallographic alterations to the processed patterns, which substantially influence the physicochemical characteristics of the nanostructures (Abid et al. 2022). The bottom-up approach employs a concept of controlled assembly of basic building blocks such as atoms or molecules obtained from the precursors into larger nanoparticles by chemical transformations. The bottom up strategies include sol-gel, spinning, chemical vapour deposition, pyrolysis etc., where chemical reduction or decomposition of precursors (metal salts/ organometallic complexes) takes place resulting in particle nucleation and growth. These methods involves the use of chemical reducing agents such as $NaBH_4$, alcohol, citrate, hydrazine etc. along with stabilizing agents while biogenic green technologies leverage the redox properties of plant extracts, microorganisms, vitamins to form nanoparticles. The energy for these reactions is provided in the form of photoenergy (UV and visible light), γ rays, electricity, and sonochemical energy. The bottom up approach produces nanoparticles with fewer defects, homogeneous composition, better short- & long-range ordering, and a narrow size distribution which is a result of decrease in the Gibbs free energy during their formation in a state closer to the thermodynamic equilibrium. The applicability of bottom-up strategies appeals to a wide range of end products as many of these techniques can be adapted to be performed in gas, liquid, solid or even supercritical states (Cunningham and Bürgi

2013). Now, providing a detailed description of all the current and historical bottom up synthesis methods of nanoparticles is beyond the scope of this thesis, as there are a great number of variations. Instead, different methods to synthesise PNCs will be described in a later section of this literature review with relevant examples to provide a suitable overview. In direct context of polymer nanocomposites for antibacterial applications, a brief overview of a few important and commonly used nanofillers such as metal nanoparticles, graphene oxide, CNTs along with antibacterial mechanism is presented below.

Silver (Ag)

Silver, a naturally occurring oligodynamic, zero-valent transition metal has been extensively utilized over millennia for its broad-spectrum antimicrobial effect, ease of operation and low toxicity to humans (Nangmenyi and Economy 2009). Its historical systemic use traces back to ancient Greek civilizations (Melaiye and Youngs 2005; White 2001) where, Alexander III of Macedon is said to have utilized silver vials to store and treat water during his expeditions (Alexander 2009; Dhanalakshmi et al. 2013; Melaiye and Youngs 2005). This concept translated into the 21st century, exemplified by silver's role in preserving and purifying water on spacecraft like Apollo, the MIR space station, and NASA shuttles. The medicinal significance of silver dates to 69 B.C.E. when the Romans employed silver nitrate to prevent infection in burns and wounds (Alexander 2009; Barillo and Marx 2014). While the advent of antibiotics shifted attention away from silver's applications, its clinical use was revived in the 1960s by Moyer, who employed silver nitrate in treating severe burns and demonstrated its antibacterial efficacy against *S. aureus*, *E. coli*, and *P. aeruginosa* (Moyer et al. 1965). This spurred the development of various silver-based composites in the wake of the increase of antibiotic-resistant microbial organisms and the restrictions of the utilization of antibiotics. This also catalysed the creation of diverse silver-based composites as antibiotic-resistant microbial organisms became more prevalent and the usage of antibiotics faced limitations.

The synthesis of AgNPs can be achieved through a wide array of chemical, physical, and bio-based procedures (Abbasi et al. 2016; Paladini et al. 2015) which result in AgNPs of varying shapes, sizes, and functionalities. Particularly, in the academic domain, the reduction of stable silver salt (e.g., $AgNO_3$) utilizing a reducing agent (e.g., sodium borohydride, ascorbic acid) is a common approach. The silver ion ($Ag^{+)}$ acquires an electron from the reducing agent during chemical reduction to transform into its metallic form (Ag^0), thus forming

AgNPs. Occasionally, a capping agent like poly(N-vinyl-2-pyrrolidone) (PVP) is employed during chemical reduction to stabilize the nanoparticles and prevent agglomeration (Murphy et al. 2015). Silver nanoparticles possess significant properties such as antimicrobial activity, electrical conductivity, optical activity (due to surface plasmon resonance), catalytic activity, chemical sensing, and biocompatibility.

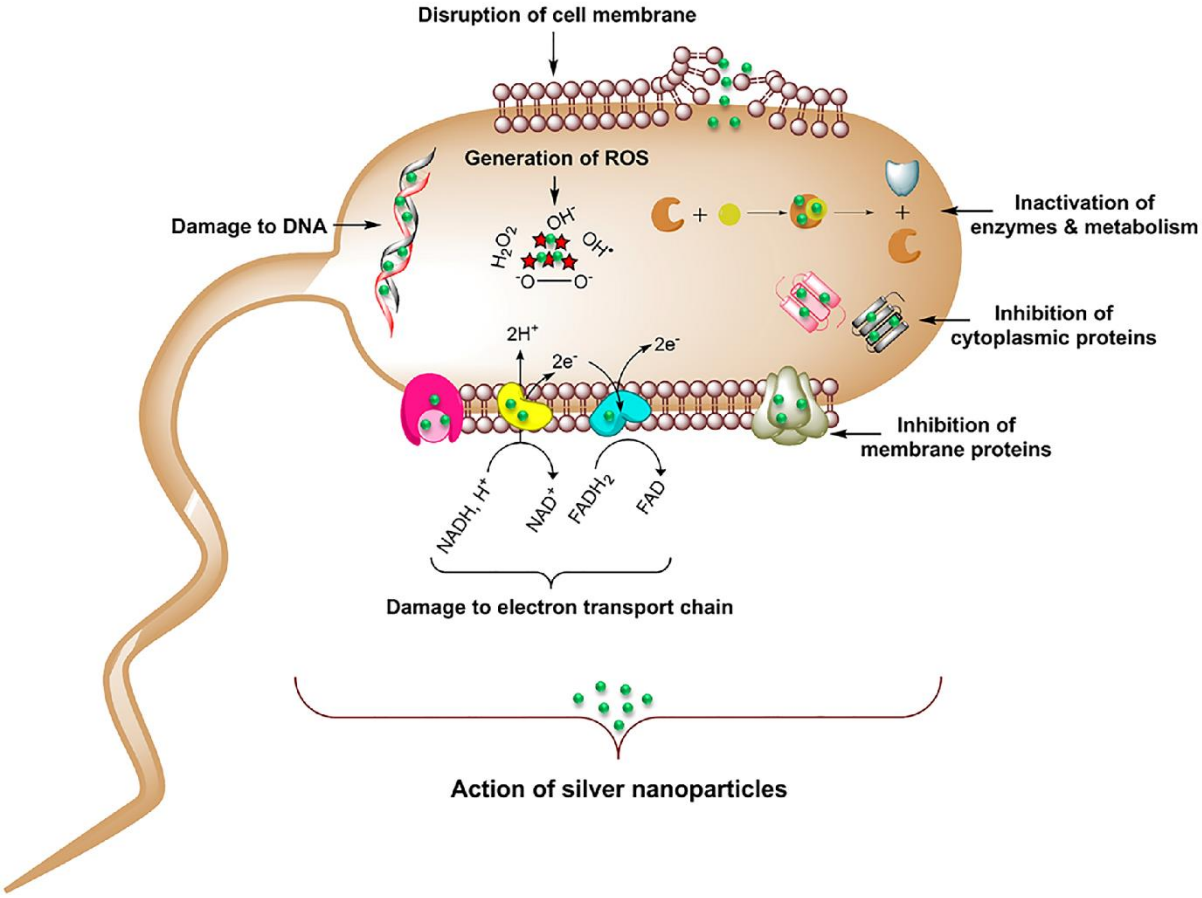

Figure 2.3 Mechanism for antibacterial behaviour of silver nanoparticles (Reprinted with permission from Singh et al. (2021). Copyright (2021) Springer Nature).

The exact mechanism behind the antimicrobial effect of AgNPs is not clearly known despite the extensive amount of data published in the literature. However, several mechanisms have been proposed to explain the biocidal action of AgNPs on bacteria (Figure 2.3) and may include the following. AgNPs have the ability to anchor and aggregate on the bacterial cell wall to subsequently penetrate its surface via formation of "pits", inducing structural alterations such as enhanced membrane permeability, ultimately leading to the demise of the cell (Prabhu and Poulose 2012; Sondi and Salopek-Sondi 2004). AgNPs has been linked to catalyse the reactive oxygen species (ROS) generation in the cytoplasm thereby, inciting

elevated oxidative stress and consequent cell death and some researchers regard this as the primary action mechanism (Reidy et al. 2013; Zare and Shabani 2016). Another prevailing perspective leans towards the liberation of Ag^+ ions from AgNPs, achieved through either the oxidative dissolution of AgNPs or the release of chemisorbed Ag^+ ions situated on the surfaces of AgNPs. Silver ions then can bind to proteins and enzymes and react with their sulphur, thiol or cysteine residues, leading to modifications in the structural integrity of the cell wall on account of inactivation of important enzymes and protein chain synthesis (Durán et al. 2016; Rawashdeh et al. 2020). Certain investigations have documented that AgNPs induce the denaturation of bacterial ribosomes, resulting in the inhibition of protein synthesis and bridge the linkages between thiols to form irreversible aggregations inside cell. Moreover, AgNPs possess the capability to interact with phosphates and amines in DNA, which interrupts DNA replication, disrupting cell biological functions (Chaloupka et al. 2010; Chappell and Greville 1954; Domènech et al. 2013). Thus, the combined effects of AgNPs and Ag^+ ions may be the reason for broad spectrum antimicrobial activity of nano-silver. However, the bactericidal activity of AgNPs varies with the particle size, shape and concentration. Small sized AgNPs, particularly $\leq$10 nm, contribute to more bacterial cell toxicity as a consequence of higher degree of interaction on account of its high aspect ratio. Additionally, in a study, truncated triangular AgNPs were observed to have the highest biocidal efficacy against *E. coli* than its rod or sphere shaped counterparts (Gogoi et al. 2006; Morones et al. 2005; Pal et al. 2007). AgNPs are deemed to be extremely potent and can induce higher biological activity at relatively low concentrations as minimum inhibitory concentration (MIC) of 1.35 mg mL^{-1} in a study was found to be enough to inhibit both methicillin resistant *S. aureus* (MRSA) and *S. aureus* cells (Ayala-Núñez et al. 2009). Therefore, with highly tunable biocidal activity along with important physiochemical characteristics, AgNPs have established a prestigious place as a nanofiller for PNCs synthesis. Many researchers driven by the desire to establish a synergistic nanocomposite, have endeavoured to synthesise silver based antimicrobial hybrids targeted for antimicrobial applications in water treatment, wound dressing, packaging, food preservation (Table 2.3).

Table 2.3 Polymer Nanocomposites for Microbial Control in Environmental and Biomedical Applications.

Type of polymer nanocomposite	Synthesis	Test microorganism(s)	Antibacterial performance	Cytotoxicity	Potential application(s)	Reference
Chitosan/Poly vinyl alcohol/AgNPs hydrogel	Chemical crosslinking- *in situ* NPs formation	*S. aureus*, *E. coli*, *P. aeruginosa*, *K. pneumonia*	ZOI: 15-45 mm	MTT: 68-85% dermal fibroblast cells viability	Biomedical devices	Suflet et al. (2021)
Calcium alginate gels-functionalized polyurethane foam/AgNPs	Crosslinking-*in situ* NPs formation	*E. coli*	ZOI: 20.3-22.8 mm OD_{600}: <0.04 after 72 h	NR	Water disinfection	Xu et al. (2023)
Carboxymethyl-hexanoyl chitosan-/graphene oxide/cellulose nanocrystals hydrogel	Solution casting	*S. aureus*, *E. coli*, *C. albicans*	Bacteriostatic ratio: 94.1-99.99%	MTT: 98-100% 3T3 fibroblast cells viability	Wound dressing and plastic masks	Yang et al. (2019)
Starch/nanofibrillated cellulose/AgNPs cryogel	Chemical crosslinking-*ex situ* formed NPs integration	*S. aureus*, *E. coli*	0 CFU mL^{-1} (100% inhibition)	NR	Dye and bacteria removal from wastewater	Radwan et al. (2021)
Chitosan/ Poly vinyl alcohol/AgNPs nanofibrous membranes	Electrospinning	*E. coli*	1.8-2.3 log reduction (10^5 CFU mL^{-1}, 30 minutes)	NR	Active food packaging	Adibzadeh et al. (2014)
Chitosan/ Poly vinyl alcohol/Copper sulphide NPs	Ultrasonic irradiation	*E. coli*, *P. syringae*, *S. aureus*, *S. pneumoniae*	ZOI: 13.5-27.1 mm	NR	Photocatalytic water disinfection	Wang and Fakhri (2020)
Chitosan/graphene oxide/AgNPs	RT-atmospheric pressure microplasma	*S. aureus*, *E. coli*	ZOI: 0.8-0.9 cm	NR	Water treatment	Su et al. (2021)

Chitosan/graphene oxide/AgNPs	*ex situ* formed NPs integration-agitation	*S. aureus, S. mutans, E. coli, K. pneumoniae, P. aeruginosa, S. typhi*	ZOI: 19-22 mm MIC: 7-10 μg mL^{-1}	NR	Biomaterials and food packaging	Khawaja et al. (2018)
Chitosan/ Poly vinyl alcohol/graphene oxide hydrogel films	Solution casting	*E. coli, S.aureus*	ZOI: 28.6-32.4 mm	MTT: pre-osteoblast (MC3T3-E1) >70% cell viability	Biomaterial	Khan et al. (2021)
Chitosan/ Poly vinyl alcohol/graphene oxide scaffold	Electrospinning	*B. cereus, S. aureus, S. enterica, E. coli*	ZOI: Weak inhibition	*In vivo* Wistar rats: low inflammation response at 0.5 wt.% (GO)	Bone tissue engineering	Tamayo Marín et al. (2019)
Chitosan/AgNPs	*In situ* NPs formation-electrospinning	*S. aureus, P. aeruginosa*	Colony count: 30-99% inhibition	NR	Filters in water disinfection	Cortés et al. (2021)
Chitosan/silver-loaded biochar	High-temperature carbonization	*E. coli*	Antibacterial rate >90%, bacteriostatic time, 7h	NR	Drinking water purification, heavy metal ions removal	Hu et al. (2019)
Chitosan/graphene oxide/AgNPs hydrogel beads	Chemical crosslinking-*ex situ* formed NPs integration	*S. aureus, E. coli*	ZOI: 8.5-18.5 mm	NR	Smart drug delivery	Rasoulzadehzali and Namazi (2018)

*ZOI: Zone of inhibition; NR: Not Reported

Copper (Cu)

Since the 5th millennium B.C., copper metal and its alloys have been employed by human civilizations for their inherent antimicrobial properties (Grass et al. 2011). The earliest documented usage of copper can be traced to the 1501 B.C.in Edwin Smith Papyrus, which details the use of copper for disinfecting thoracic injuries and drinking water. Roman Empire utilized copper cooking utensils as a measure to halt disease transmission and Japanese soldiers during World War II, placed copper pieces inside their water bottles to safeguard against dysentery (Borkow and Gabbay 2009). The application of copper and its alloys as antimicrobial agents, encompassing both micro- and nano-scale formulations have persisted throughout the recent years in the form of commercially available products. Copper-based materials with their multi-toxicity, hold the distinction of being the sole metal touch surface recognized as an antimicrobial material by the US Environmental Protection Agency.

Currently, copper nanoparticles (CuNPs) are most commonly synthesised by chemical techniques such as chemical reduction (Shankar and Rhim 2014), micro-emulsion (Solanki et al. 2010), sonochemical reduction (Kumar et al. 2001), microwave assisted (Yallappa et al. 2013), and hydrothermal syntheses (Giannousi et al. 2014) which generate nanoparticles with specific characteristics. Physical methods also enable the production of CuNPs with different sizes and morphologies through laser ablation (Stelzig et al. 2011), metal vapor (Ponce and Klabunde 2005), pulsed wire discharge (Murai et al. 2007), and mechanical milling. Green and sustainable technologies also dabble in biogenic reduction (Abboud et al. 2014; Lee et al. 2013) for obtaining CuNPs. The copper nanoparticles obtained possess higher antimicrobial activity then its bulk precursor, which numerous research studies exploit in several copper based nanocomposites. Despite an incomplete comprehension of the intricate antibacterial mechanisms behind the copper based materials, it is believed that their antimicrobial effects are multifaceted with the release of soluble copper (Cu^{2+}) ions being the chief cytotoxic mechanism (Wu et al. 2009). The biocidal effect of these ions involves them interacting either directly with the bacterial cellular membrane or intracellular components to produce reactive oxygen species (ROS), lipid peroxidation, protein oxidation and DNA degradation (Chatterjee et al. 2014). Additional mechanisms that have been documented entails the aggregation and dissolution of CuNPs within the bacterial membrane, causing alterations in permeability. This process leads to the subsequent liberation of intracellular biomolecules and the disruption of the proton motive force across the plasma membrane (Amro et al. 2000;

Azam et al. 2012; Jiang et al. 2009). Studies have also demonstrated that the antibacterial properties of CuNPs associated with the release of Cu^{2+}, are directly related to size. Although, antibacterial activity of copper nanoparticles is not potent as AgNPs since, almost double MIC of CuNPs is required to have the same effect as nano-silver on gram-negative or gram-positive bacteria (Palza et al. 2015). However, copper based polymer nanocomposites still offer an interesting alternative to attenuate the persisting concern of bacterial resistance given their significant antibacterial properties, and relatively low production cost. Therefore, copper based PNCs are popular in applications such as medical devices, wound dressings, water purification filters, and food packaging (Tamayo et al. 2016).

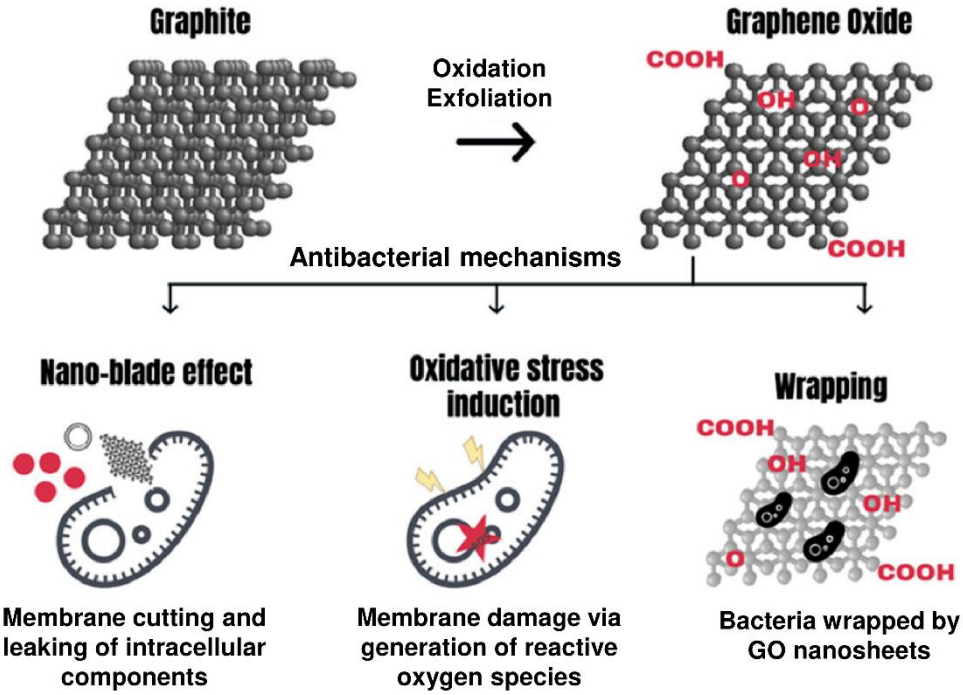

Figure 2.4 Schematic representation of graphene oxide (GO) structure with its three plausible antibacterial action mechanisms (Reprinted with permission from Cacaci et al. (2020). Copyright (2021) Springer Nature).

Graphene oxide (GO)

Graphene and its derivatives are at the forefront of nanomaterials research ever since its nobel-prize winning isolation from graphite in 2004, using the scotch-tape peeling technique (Geim and Novoselov 2007). These 2D carbon sheets have drawn significant attention because of its superior electrical, thermal, mechanical, optical and antimicrobial properties. Specifically, the oxidized form of graphene i.e. graphene oxide (GO) have been widely

studied in the scientific literature in comparison to their counterparts (Matharu et al. 2020). Graphene oxide, when dispersed and exfoliated in solvents is a single layer of graphite oxide and its structural arrangement consists of sp^3 and sp^2 hybridized carbon atoms arranged in a hexagonal lattice with carboxyl or carbonyl, hydroxyl and epoxy groups on its edges and basal planes (Compton and Nguyen 2010; Park and Ruoff 2009; Zhu et al. 2010) (Figure 2.4). GO is mostly obtained by chemical oxidation of graphite and its subsequent exfoliation by ultrasonication which leads to increased distance between carbon layers by breaking its sp^2 - sp^2 hybridized structure (Lee et al. 2016). Different routes have been applied such as Brodie, Staudenmaier, and Hummers method or with minor modifications. Brodie's and Staudenmaier's techniques were deemed to be explosion risks due to high reaction temperatures and corrosive chemicals (Brodie 1859; Poh et al. 2012; Staudenmaier 1898). However, the most popular procedure to have been developed for synthesizing GO is by Hummers Jr and Offeman (1958), which uses sodium nitrate ($NaNO_3$) and potassium permanganate ($KMnO_4$) with the combination of sulphuric acid (H_2SO_4). The popularity of this methodology is vindicated by its eco-friendliness and room for variation (Alkhouzaam et al. 2020).

These methods generate defects (oxygen containing functional groups) on carbon layer and their existence facilitates the interactions with biomolecules of microorganisms thus, inducing cell death without an intracellular process. This antibacterial effect of GO is attributed to various mechanisms such as nano-knife, membrane stress, oxidative stress, entrapment, and basal plane etc. The nanosheets of GO with their sharp edges have the potential to physically harm bacterial membranes via "nano-knife" behaviour, resulting in bacterial inactivation through the leakage of intracellular components such as proteins, enzymes, lipids and DNA (Akhavan and Ghaderi 2010; Liu et al. 2011). Further, the oxidative stress induced by the production of ROS by GO can trigger DNA damage and disrupt mitochondrial function, leading to the inhibition of bacterial growth (Pieper et al. 2016; Zhao et al. 2014). This oxidative stress could also be ROS or superoxide-anion independent as generated by oxidation of glutathione (GSH) which also disrupts the normal functional of bacterial cell. Another hypothesized biocidal mechanism of GO is called the "wrapping" or entrapment, in which bacteria initially gets wrapped around by thin layers of GO. These nanosheets then segregate bacteria from the surrounding environment and terminate its proliferation on account of blockage of gas/ion exchange (Jayanthi et al. 2016). These elaborate mechanisms have facilitated graphene oxide (GO) to possess the highest

antibacterial potency while assessing toxicity towards *E. coli* in comparison to graphite, graphite oxide, and reduced graphene oxide (rGO) (Liu et al. 2011). The functional groups on the basal planes makes GO hydrophilic, which improves its biocompatibility and water dispersibility, necessary for biological applications (Dreyer et al. 2010; Konios et al. 2014). Thus, in addition to being easily modifiable by chemical and thermal reactions, GO has attracted great attention for its use as nano-sized fillers in polymeric and/or inorganic composites (Compton and Nguyen 2010). GO reinforced polymer nanocomposites possess exceptionally high elastic modulus, superior electrical and thermal conductivity as well as excellent bioactivity (antibacterial and biocompatibility), which ensures their applicability in various industrial and biomedical fields such as energy storage, scaffold, packaging, biomaterial coatings, and biosensors etc. (Gungordu Er et al. 2023) (Table 2.3).

2.3 Synthesis of Polymer Nanocomposites (PNCs)

The main objective in formation of polymer nanocomposites is to ensure the uniform distribution of nanomaterials throughout the polymer matrix such that interfacial interactions between polymer and nanomaterials are enormous and the maximum degree of the nano-dimensional interphases are generated. However, due to the dimensional difference between nanomaterials and conventional microscale fillers, the uniform distribution of nanofillers is manifested in the following aspects. For instance, if the filling process follows the volume fraction, a significantly higher quantity of nanofillers is needed compared to microfillers to achieve the same volume fraction. Consequently, the nanoparticles within the matrix experience crowding with elevated van der Waals and electrostatic interactions among particles, hindering uniform distribution. Additionally, high aspect ratio of anisotropic nanofillers such as graphene, renders them more susceptible to agglomeration as they minimize their surface energy through π–π stacking. Therefore, to combat such distribution challenges, two different methods of infusing the nanomaterials into a host matrix have been explored, *in situ* and *ex situ* (Chen et al. 2011; Guo et al. 2014), exemplified in Figure 2.5. Each of these techniques have their own set of merits and drawbacks, with researchers generally opting for the one that aligns with their convenience or yields an improved composite matrix. Ultimately, the selection of the synthesis approach depends on various considerations, including the polymeric system, intended application, particle size distribution, and size prerequisites (Rao and Geckeler 2011).

2.3.1 *In situ* synthesis of PNCs

Diverse types of polymer nanocomposites (PNCs) have been produced through *in situ* methods, with distinct functionalities applicable to a variety of antimicrobial uses. The technique achieves a more consistent dispersion of nanoparticles within the polymer support material, creating interpenetrating networks that improves compatibility between the components and establish robust interfacial interactions (Kango et al. 2013). This approach is well-suited for crafting polymer nanocomposites characterized by a narrow particle size distribution and distinct morphology and revolves around three fundamental processes, namely:

- Incorporating pre-synthesized nanoparticles into monomers or precursors of polymeric materials
- Addition of nanoparticle precursors into pre-existing polymer matrices, and
- Concurrently synthesis of nanoparticles and the polymeric support.

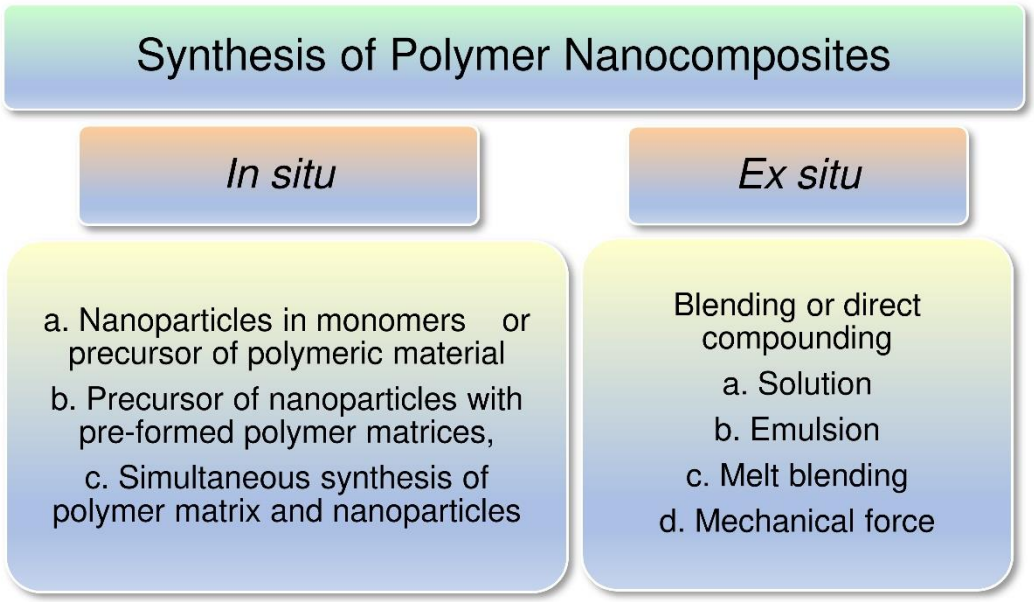

Figure 2.5 Summary of preparation routes for polymeric nanocomposites.

In the first process, the nanomaterial is independently prepared using a suitable and compatible method. Following the synthesis (functionalization or modification) of nanoparticles, they are introduced into monomers or precursors of chosen polymeric matrices to create diverse PNCs. This *in situ* synthesis pathway is particularly well-suited when there is a need for nanoparticle functionalization or modification (Lü et al. 2016). The *in situ* synthesis approach, entailing the amalgamation of pre-formed polymer matrices as the

reaction medium with nanoparticle precursors, is also a widely used technique for crafting PNCs. Typically, the initial polymerization phase is succeeded by polymer modification, after which the nanoparticles are introduced into the polymer matrices. It can be accomplished using various chemical procedures and during the agitation of the host matrices, these nanomaterials are generated, dispersed, and rendered stable. This method is primarily employed for polymer hydrogel nanocomposites, leveraging the presence of numerous functional groups within the macromolecules and a water-rich environment to enhance the stability and dispersion of metals.

The last method of simultaneous *in situ* synthesis of both nanoparticles and the polymer support matrix has been equally reported and involves two steps. The monomer absorbs metal ions and undergoes polymerization, followed by subsequent *in situ* reduction of the metal precursor within the polymer matrix through chemical reduction or decomposition (such as, photolysis, thermolysis, or radiolysis) (Carotenuto et al. 2005), resulting in the formation of polymer chains encapsulating the intercalated nanoparticles. This method provides the ability to regulate particle size distribution and morphology, effectively preventing nanoparticle agglomeration while ensuring a well-maintained spatial distribution within the polymer phase. The stability, preferred structure, and oxidation state of the nanoparticles are guided by the chemistry of the monomer-polymer chemistry, while the nanoparticles contribute to crosslinking reactions (in the case of resins). This method also reduces the reliance on solvents and lowers the external energy needed for mixing due to the low viscosity of the monomers. Among various methods, the sol-gel process stands out as a highly promising technique for *in situ* creation of metal-polymer nanocomposites. The sol-gel process encompasses two vital reactions: hydrolysis and condensation, which occur in multiple steps and follow each other in succession (Camargo et al. 2009).

2.3.2 *Ex situ* synthesis of PNCs

Ex situ technique is known as simple blending or direct compounding, where nanomaterials are first synthesized independently from the host matrix. Subsequently, these materials are suspended within a solvent compatible with the host material or presented straightforwardly as a powder. Following this, they are integrated as the nanofiller into the host matrix which acts as a dispersion medium. For direct incorporation of the nanoparticles into the polymer matrix, blending techniques such as solution, application of mechanical force, emulsion, and

melt-mixing are employed (Karak 2009). This approach is relished by metal-polymer nanocomposites synthesis and is based on the breakdown of the aggregated metal nanoparticles during the mixing process. The surfaces of metal nanoparticles are shielded by a monolayer of organic molecules such as quaternary ammonium, amines, and sulfonic acids. These metal nanoparticles are physically enclosed within the polymer matrix through secondary interactions, including hydrogen bonding. Ultimately, the metal-polymer nanocomposites are subjected to conventional manufacturing molding techniques such as injection, extrusion, compression, rotational, calendaring, and casting etc. The *ex situ* approach is documented as offering a facile and expeditious route for fabricating PNCs since, all of the necessary components are already generated. However, the inherent issue of nanoparticle agglomeration could lead to the uneven dispersion of nanoparticles within the polymer blend (Kango et al. 2013). Despite the mentioned challenge concerning blending methods, these techniques have been consistently employed in the synthesis of polymer nanocomposites.

2.4 Versatility (forms) of PNCs for Antibacterial Applications

One of the prominent advantages of polymer nanocomposites lies in their versatility, enabling the fabrication of intricate structures or forms tailored to meet specific requirements and target diverse antibacterial applications. From films and coatings that guard medical devices/implants (Liu et al. 2021) and food packaging against microbial colonization (Alghamdi et al. 2022), to nanocomposite fibers and textiles with inherent antimicrobial properties for wound dressings (Bharathi and Stalin 2019) and sportswear (Khude et al. 2023), the applications are diverse and impactful. Nanocomposite hydrogels and membranes offer clean water and air through efficient disinfection and filtration (Deng et al. 2017; Li et al. 2020), while scaffolds and injectable gels provide localized protection and support tissue regeneration (Dai et al. 2018; Hasan et al. 2018). Further, these materials can also be designed for responsive behaviour, releasing antimicrobial agents when triggered by specific environmental cues (Xue et al. 2016). The expanding horizons of polymer nanocomposites bear testament to their significant potential in addressing infection control, healthcare improvements, and ecological balance. Now, within the scope of antibacterial applications explored in this thesis, about water disinfection and biomedical implant coatings, the subsequent sections will delve into bulk nanocomposites, namely hydrogels, and thin-film nanocomposites, specifically coatings, respectively in depth.

2.4.1 Hydrogels and their Characteristics Employed in Water Treatment and Disinfection

The origins of hydrogels can be traced back to 1960, when Wichterle and Lim pioneered their development by creating poly (2-hydroxyethyl methacrylate) (PHEMA). This breakthrough led to its application in the contact lens industry, showcasing the hydrogel's distinctive ability to imbibe moisture while preserving its network structure. This event marked a significant step forward in the advancement of contemporary hydrogel technology (Dimatteo et al. 2018; Ghorpade et al. 2019). By definition, hydrogels are distinctive 3D crosslinked polymeric mesh structures, which possess the capacity to absorb significant volumes of water within their interstitial spaces, while retaining these bonds and upholding the network structure when in a swollen state (Gulrez et al. 2011). The ability of hydrogels to absorb water arises from the presence of polar hydrophilic functional groups, such as SO_3H, OH, NH_2, COOH, $CONH_2$, etc, distributed as branching elements throughout the polymer network. Hydrogels' resistance to dissolution even in swollen state stems from cross-links between network chains. Thus, tendency of hydrogels to absorb water attributed to their swelling behaviour, is influenced by factors such as the hydrophilicity of attached functional groups, the nature of the swelling medium, and the strength of crosslinked bonds (Ahmed 2015; Bhattarai et al. 2010).

Hydrogels can be categorized based on various criteria, including their origin (natural, synthetic, or hybrid), pore size (non-porous, microporous, or super porous), composition (homopolymer, copolymer, or multipolymer), cross-linking nature (chemical or physical), morphological structure (amorphous, crystalline, or semi-crystalline), degradability (biodegradable or non-biodegradable), physical appearance (matrix, film, or sphere), charge properties (neutral, ionic, amphoteric, or zwitterionic), network type (semi-interpenetrating or fully interpenetrating), and responsiveness (chemical – pH, oxidant components, or glucose presence; biochemical – antigen, enzyme, or ligand presence; physical – temperature, pressure, or light), among others (Ahmed 2015; de Oliveira Cruz et al. 2020; Devi and Gaba 2019; Ullah et al. 2015). It is important to highlight that categorizing individual hydrogels into specific classes is neither rigid nor unchangeable. This classification methodology permits researchers to assemble materials exhibiting similar attributes or to discern recurring trends. This approach facilitates the advancement and sharing of research efforts. Among these various criteria, the categorization based on degradability has garnered significant

interest, primarily driven by the increasing focus on environmental preservation. As mentioned earlier, within the myriad of materials employed for hydrogel design, the utilization of biopolymers such as alginate, chitosan, lignin, cellulose, gelatin, starch, carrageenan, and natural gums emerges as notable (Ahmed 2012; Barik et al. 2020; Pooresmaeil and Namazi 2020). Meanwhile, frequently utilized synthetic polymers include polylactic acid (PLA), polyglycolic acid (PGA), polyacrylic acid (PAA), polyvinyl alcohol (PVA), polyethylene glycol (PEG), and polyvinyl pyrrolidone (PVP). Biopolymers are regarded as great substitutes ecologically, with notable qualities such as cost-effectiveness, non-toxicity, and widespread availability. However, challenges persist in terms of insufficient mechanical robustness and limited stability, thereby necessitating further resolution (Pérez-Álvarez et al. 2019). Typically, synthetic hydrogels exhibit strong covalent bonds within their matrix, leading to greater mechanical strength, extended durability, and enhanced adsorption capacity (Gyles et al. 2017). Hydrogels formed through the combination of synthetic and natural polymers expand the application domains and combine overall characteristics of their individual components (Jing et al. 2013). Generally, these hybrid materials are effective in removing bacteria from aqueous solutions (Wang et al. 2019). In the preceding decade, there has been a discernible emergence of resourceful materials such as nanomaterials, bioinspired and biomimetic membranes, and polymeric hydrogel nanocomposites etc. meticulously engineered to cater to the demands of water treatment applications (Alvarez et al. 2018; Qu et al. 2013; Zhou et al. 2019). These hydrogels, have showcased their potential in establishing and maintaining sustained water security through multiple avenues such as setting new benchmarks in various water treatment domains by outperforming conventional materials. Additionally, these hydrogels have enabled the introduction of innovative approaches that present alternatives to conventional water treatment methods. Moreover, they have also expanded the range of viable/exploitable water sources beyond the traditional options.

Instances of such hydrogels with exceptional performance comprise of superabsorbent and hydrophilic hydrogels with high bactericidal efficiency, that can be innovatively used to rapidly absorb microbiologically contaminated water and then release the disinfected water within few minutes. Hydrogels possessing suitable pore sizes and exhibiting underwater super oleophobic characteristics that facilitate the swift separation of oil-water mixtures via accelerated gravity-driven filtration processes (Matsubayashi et al. 2017). Stimuli-responsive hydrogels characterized by high charge density that aid in desalination process, either as innovative agents for forward osmosis or as unique membrane structures capable of

selectively absorbing ion-depleted water (Höpfner et al. 2010; Li et al. 2011). Hydrogels with notable moisture-absorption capacity even in low relative-humidity environments that effectively convert vapor into collectible liquid water (Matsumoto et al. 2018; Yao et al. 2020; Zhao et al. 2019). The remarkable performance demonstrated by the aforementioned hydrogels mentioned can be attributed to certain distinctive characteristics, which include:

a) High water absorption and retention- Hydrogels can absorb and retain a substantial amount of water or aqueous solutions, often swelling to several times their dry weight. There are three distinct water states within their hydrated networks, 'primary bound water' latched to polar hydrophilic groups, 'secondary bound water' to hydrophobic groups, and 'free or bulk water' occupying inter-chain spaces and larger pores at swelling equilibrium.
b) Large surface area and porosity- The 3D porous network structure of hydrogels provides a large surface area for diffusion of small molecules, ions, and dissolved contaminants in water which maximizes their pollutant removal efficiency.
c) Swelling and Deswelling- Hydrogels display reversible swelling and deswelling capacity in response to environmental-stimuli conditions such as pH, temperature, and ionic strength. Their switchable wettability behaviour can be utilized to release or retrieve absorbed pollutants, enabling hydrogels' reusability.
d) Antibacterial Properties: Hydrogels incorporated with antibacterial agents or nanoparticles exhibit inherent or enhanced antibacterial activity, which is valuable for pathogen removal from contaminated natural water sources.
e) Slow Release of Active Agents- Hydrogels loaded with disinfectants, antimicrobial agents can release them slowly over time owing to their complex structures. This controlled release enhances the efficiency of disinfection processes and reduce the need for frequent chemical dosing.
f) Biocompatibility- Most natural polymer based hydrogels are biocompatible (non-cytotoxic) and don't harm aquatic life when used in water treatment of natural water bodies.

Other properties such as selective sorptivity (towards heavy metals, dyes, viruses, and bacteria), low fouling, biodegradability, mechanical strength, and conformational flexibility are also exploited in various water treatment and disinfection applications.

Synthesis of Polymer Nanocomposite Hydrogels

For hydrogel fabrication, the host or polymer matrix has been prepared through a process called ‘gelation’, which pertains to the interconnection of macromolecular chains, initially resulting in increasingly larger, branched polymers that remain soluble, based on the starting material's structure and conformation. The blend of these polydisperse, soluble branched polymers is termed as 'sol' and the ongoing progression of the linking process leads to the enlargement of the branched polymer's size, accompanied by a reduction in solubility. The 'infinite polymer' formed is referred to as the 'gel' or 'network,' interpenetrated by finite branched polymers. The shift from a state featuring finite branched polymers to one with an infinite molecule structure is termed the 'sol-gel transition' (or 'gelation'), and the essential point at which the gel structure emerges is termed the 'gel point' (Rubinstein and Colby 2003). The process of gelation can occur through either physical linking or chemical linking, respectively referred to as physical or chemical gelation. ‘Physical’ or ‘reversible gels’ are formed when the networks are connected through molecular entanglements or secondary forces such as ionic, electrostatic, van der Waals, hydrophobic interactions, or hydrogen bonding. These physical interactions prevent dissolution and are characterized by their finite durations, reversibility (undergoing continuous cycles of breaking and reforming), and susceptibility to disruption through alterations in physical conditions or the application of stress (Hennink and van Nostrum 2012). In contrast, when the networks are cross-linked through more robust and stable covalent bonds (substituting hydrogen bonds), they form 'permanent' or 'chemical' gels. These achieve equilibrium swelling state determined by the interaction parameter between the polymer and water, as well as the density of crosslinks (Rosiak and Yoshii 1999).

Unlike pristine polymeric hydrogels, the structural basis of nanocomposite hydrogels lies in the multiple interactions between nanoparticles and the polymer. For instance, the considerable elasticity found in nanocomposite hydrogels stems from the strong cross-linking facilitated by ionic bonds between polymer cations and nanoparticle anions. In addition, the capacity for dissipating detrimental energy arises from hydrogen bonds between the amino or carboxyl groups of polymers and the oxygen-containing functional groups of NPs. These bonds serve as reversible cross-linkages, breaking and reforming as needed (Le Ferrand et al. 2016; Liu et al. 2012; Pan et al. 2017; Zhang et al. 2017). Blending the polymer and NPs directly through physical mixing is a straightforward method for creating nanocomposite

hydrogels. However, this approach is unsuitable for producing hydrogels with remarkable mechanical properties, primarily due to the feeble interactions between polymers and NPs (Le Ferrand et al. 2016). A broad variety of nanoparticle-hydrogel composites have been formulated, incorporating different types of nanoparticles into a cohesive bulk hydrogel structure for obtaining stable and mechanically strong structures. Five main approaches with variations of chemical cross-linking methods such as *in situ* polymerization, *in situ* growth of NPs and so on have been explored to achieve uniform distribution (Figure 2.6). The chosen approach is partially influenced by the ultimate application of the nanoparticle-hydrogel composite.

a) Creating Hydrogels within a Nanoparticle Suspension

The most straightforward approach to create a nanocomposite hydrogel involves the gelation of monomers within a nanoparticle suspension. For instance, Liu et al. (2013) employed this approach to synthesize photo-modulable thermos-responsive hydrogel through the incorporation of unilamellar titania nanosheets (TiNSs) as photocatalytic cross-linking agents. In their innovative approach, it was observed that the nanoparticles served as photo-catalysts rather than traditional cross-linking agents. Notably, the utilization of a bisfunctional monomer, N,N'-methylenebisacrylamide (MBAAm), was essential for achieving the creation of hydrogels with robust mechanical properties.

b) Integrating Nanoparticles into Pre-formed Hydrogels

In this technique, nanoparticles are incorporated within a hydrogel that has already been formed, subsequently allowing the nanoparticles to permeate the hydrogel matrix. Pardo ‐ Yissar et al. (2001) integrated AuNPs into a polyacrylamide (PAAm) gel post electro-polymerization formation. For nanoparticle introduction, the "breathing in" procedure consisted of: a) immersing the gel in acetone, causing it to shrink and expel water (breathing out); b) then immersing the contracted gel in an aqueous solution of citrate-stabilized AuNPs for swelling (breathing in), thus incorporating the suspended nanoparticles. Thorough washing with water removed weakly surface-adsorbed nanoparticles. During the next "breathing out" phase, nanoparticles remained trapped within the gel, due to physical entanglement and hydrogen bonding between polymer chains and nanoparticle surfaces. Using a similar approach, Gogoi and Chowdhury (2014) immersed chitosan hydrogel in a suspension of silver nanoparticles (AgNPs), leading to the absorption of AgNPs within the hydrogel matrix.

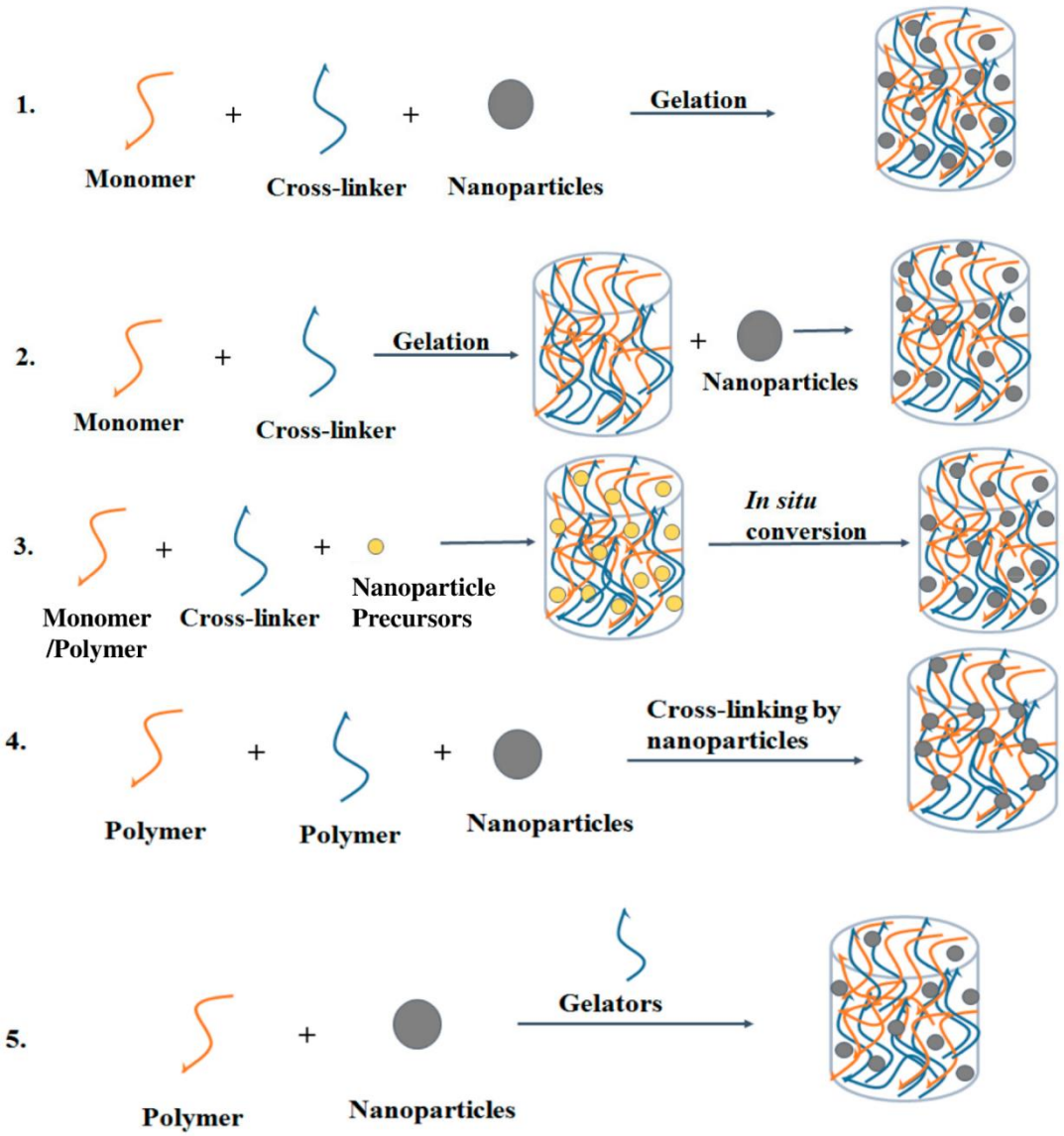

Figure 2.6 Five main approaches to get nanocomposite hydrogels with a uniform distribution of nanoparticles: (1) formation of the hydrogel in nanoparticle suspension; (2) incorporation of nanoparticles into pre-formed hydrogel; (3) formation of reactive nanoparticles within a pre-formed hydrogel; (4) cross-linking of hydrogel by nanoparticles and (5) hydrogel formation using nanoparticles, cross-linking agents and polymers. (Reprinted with permission from Wahid et al. (2017). Copyright (2017) MDPI).

c) Generating Reactive (*in situ*) Nanoparticles within a Pre-Existing Hydrogel

In this method, a pre-existing hydrogel serves as a 'nanoreactor', within which nanoparticles are generated from their precursors through a sequence of necessary treatments. The technique is becoming increasingly popular for its technological superiority over the *ex situ* process, as it allows for relatively easy manipulation of nanoparticle size and morphology

(Mohan et al. 2010). This process is best suited for production of metal/metal oxide nanoparticles-hydrogel network systems. Metal ions can be adsorbed onto the hydrogel's functional groups via electrostatic or dipole-ion interactions. Subsequently, these metal ions can undergo self-assembly (Wang et al. 2008), electrochemical deposition, co-precipitation (Xiong et al. 2011), and similar processes, leading to the generation of metal or metal oxide nanoparticles. The ion exchange transpires between the metal ions present within the solution and the functional groups inherent to the hydrogel in absorption process. Following absorption, metal ions can undergo reduction through the utilization of reducing agents such as $NaBH_4$ (Ozay et al. 2011), citrate (Thomas et al. 2007) etc. to form metal nanoparticles of varied sizes. Saravanan et al. (2007) demonstrated this approach via free-radical cross-linking polymerization of acrylamide monomer in an aqueous medium containing Ag^+ ions. Following functionalization with Ag^+ ions, the PAAm hydrogel matrix underwent hydrolysis to produce well-dispersed AgNPs of size 4-7 nm within it. The symmetrical configuration and consistent intensity of SPR bands revealed that AgNPs size remained unchanged with varying Ag^+ ion concentration, indicating absence of aggregation as corroborated by electron microscopy. In a recent investigation, Varaprasad and colleagues utilized a green reducing agent (mint leaves extract) to reduce Ag^+ ions within a gelation mixture of Carbopol 980 NF and acrylamide, resulting in the creation of composite hydrogels intended for antibacterial applications (Varaprasad et al. 2014).

d) Utilizing Nanoparticles for Cross-Linking in Hydrogel Formation

Nanoparticle cross-linkers such as such as titania, CNTs, silica, graphene oxide, and nanoclay, possess substantial surface activity and are capable of binding a significant number of polymer chains (more than 100) (Haraguchi 2011; Pasqui et al. 2011). When subjected to deformation, a section of the polymer chains may disengage from the nanoparticle, leading to a partial release of stored elastic energy. This increased energy dissipation contributes to the nanocomposite hydrogel's superior toughness and stretchability compared to conventional hydrogels with covalent cross-linking. Rose et al. (2014) extended the versatility of employing nanoparticles as cross-linking agents, focusing on their application in facilitating adhesion between two hydrogels. The researchers showcased the attainment of robust and swift adhesion between two hydrogels under ambient conditions, by introducing a droplet of nanoparticle solution onto the gel's surface and subsequently bringing the second gel into contact with it. SiNPs, for instance, enabled the successful bonding of two sections of

biological tissue (calf liver). Consequently, such material holds significant potential for artificial muscles and cartilage engineering applications.

e) Hydrogel Formation Using Nanoparticles, Polymers and Cross-Linking Agents

Using this approach, Wu et al. (2013) produced Si-based anodes via SiNPs incorporation into a conductive polymer hydrogel. Through *in situ* polymerization process, the hydrogel formed a cohesive 3D network structure, enveloping SiNPs within the conducting polymer. The hydrogel originated from the combination of aniline, phytic acid, and Si-NP in water, with subsequent introduction of ammonium persulfate as an oxidizing agent via a scalable solution-phase synthesis. The rapid oxidation and polymerization of aniline led to cross-linked polyaniline formation, resulting in a dark green viscous gel due to phytic acid (gelator). Subsequently, Subsequently, the gel was coated onto a copper foil current collector, dried to yield a uniform film suitable for a wide range of electrochemical applications.

Antibacterial Performance of PNC Hydrogels in Water Disinfection

Many researchers have been motivated to study the interactions between microbes and the hydrogel matrix which have facilitated the application of polymer nanocomposite hydrogels for water disinfection processes (Table 2.4). Few recent studies corroborated hydrogels immobilized with metallic nanoparticles acting in the inactivation or removal of microorganisms from water. For instance, Wang et al. (2021) developed polydopamine coated chitosan hydrogel beads by chemical cross-linking and immobilized *in situ* synthesized AgNPs (>50 nm) on its surface to eradicate chemical (dyes, heavy metals) and bacterial contaminants from water. The antibacterial assay revealed about 4-6 log reduction (depending upon beads dosage) from an initial concentration of 10^6 CFU mL^{-1} of *E. coli* and *S. aureus* within 24 h. The cationic and hydrophobic groups present in the chitosan hydrogel along with the release of Ag^+ ions collectively caused bacterial death due to membrane damage in this case. Similarly, Somayajula et al. (2019) through *in situ* chemical reduction method simultaneously synthesized and immobilized AgNPs on polyethylene glycol acrylate and poly acrylic acid based hydrogel membrane. The test samples containing AgNPs inhibited 98.4% of *E. coli* growth in culture media compared to the 25% deactivation rate of pristine membranes. The observations in this study indicated that AgNPs within hydrogel not only effectively resisted adhesion of bacteria cells, but also facilitated destruction of the bacteria cells attached to the surfaces.

Table 2.4 Polymer Nanocomposite Hydrogels Applied for Microorganisms Removal in Water.

Hydrogel (composition)	**NPs size**	**Synthesis**	**Test microorganisms**	**Inactivation performance**	**Death mechanism(s)**	**Reference**
Calcium alginate/ diatomite/AgNPs	<100 nm	Chemical crosslinking-*ex situ* formed NPs integration	*S. aureus*, *E. coli*	68.5-98.7% inhibition, 60 min.	Ag^+ leach-kill, membrane damage	Zhao et al. (2021)
Reduced graphene oxide/ZnO/ polyether sulfone	-	*ex situ* formed NCs-surface grafting	*E. coli*, *B. subtilis*, *P. aeruginosa*	>90% inhibition	Contact-kill, membrane damage	Zhang et al. (2022)
Polydopamine coated chitosan/AgNPs	>50 nm	Chemical crosslinking-*in situ* NPs formation	*S. aureus*, *E. coli*	4-6 log reduction (10^6 CFU mL^{-1}, 24h)	Ag^+ leach-kill, membrane damage	Wang et al. (2021)
Polyacrylamide/graphene oxide/AgNPs	-	*In situ* gamma radiation	*S. aureus*, *E. coli*	>90% inhibition	ROS generation, membrane damage, protein leakage	Sivaselvam et al. (2021)
Chitosan /AgCl/ZnO		Chemical crosslinking-*ex situ* formed NPs integration	*S. aureus*, *E. coli*	95-99% inhibition	ROS generation	Taghizadeh et al. (2020)
Guar gum/MIL-100(Fe)/AgNPs	2 µm	Self-crosslinking-*ex situ* formed NCs integration	*E. coli*	99.6% inhibition	Metal-ion leach-kill, membrane damage	Duan et al. (2020)
Polyvinylpyrrolidone / Quantum carbon dots	7 nm	Chemical crosslinking	*S. aureus*, *E. coli*	3.7 log reduction	Contact-kill, membrane damage	Nayak et al. (2020)

Gum tragacanth/graphene oxide/AgNPs	13 nm	Chemical crosslinking-*in situ* NPs formation	*S. aureus*	ZOI: 14 mm	AgNPs leach-kill, membrane damage	Sahraei and Ghaemy (2017)
Polyvinyl alcohol /biochar/AgNPs	-	Chemical crosslinking-*ex situ* formed NPs integration	*E. coli, S. aureus, P. aeruginosa*	>90% inhibition	AgNPs, Ag^+ leach-kill, membrane damage	Zhao et al. (2021)
Polyaniline/Poly acrylic acid-co-Acrylamide/AgNPs	-	Copolymerization-*in situ* NPs formation	*E. coli*	ZOI: 8 mm	AgNPs leach-kill, membrane damage	Hosseinzadeh and Barghi (2019)
Polyethylene glycol acrylate/Poly acrylic acid/AgNPs	-	Physical crosslinking-*in situ* NPs formation	*E. coli*	98.4% inhibition	Ag^+ leach-kill; membrane damage	Somayajula et al. (2019)
Co-doped ZnO NPs/Poly vinyl alcohol	11-22 nm	Chemical crosslinking-*ex situ* formed NPs integration-precipitation	*S. aureus, B. subtilis, E. coli, S. salivarius.*	ZOI: 15.7-21.7 mm	ROS generation	Abubshait et al. (2023)
Calcium alginate/Bovine serum albumin/Carboxymethyl chitosan-capped-AgNPs	5-60 nm	Chemical crosslinking-*ex situ* formed NPs integration-	*E. coli*	ZOI: 11-13 mm	AgNPs leach-kill, membrane damage	Xu et al. (2022)
Gelatin- Poly acrylic acid/AgNPs	30-50 nm	Chemical crosslinking-*ex situ* formed NPs integration	*E. coli, S. aureus*	ZOI: 7.3-12.2 mm	AgNPs leach-kill, membrane damage	Dil and Sadeghi (2018)

*ZOI: Zone of inhibition; NCs: Nanocomposites; ROS: Reactive oxygen species

Nanoparticles generated via *ex situ* chemical or green synthesis techniques have also been incorporated in various hydrogel systems to target bacterial removal from water sources. For example, Zhao et al. (2021) prepared polyvinyl alcohol gels including *ex situ* synthesized nano-silver conjugated with biochar to disinfect drinking water. The nanocomposite at 0.6 g L^{-1} dose, displayed the strongest bacteriostatic effect with >90% inhibition of *E. coli*, *S. aureus*, and *P. aeruginosa* (initially at 10^8 CFU mL^{-1}) within 7h and retained 80% of its bactericidal capacity after 10 reuses. Further, simulated polluted water tests conducted in adsorption column (bed height 18 cm, flow rate 2 mL s^{-1}) revealed over 90% *E. coli* inhibition until filtration of 600 column volumes. The bacterial eradication mechanism was attributed to permeation of cell membrane and internal structure damage by synergistics of AgNPs and Ag^+ ions. Another group of researchers incorporated nano-silver/diatomite into calcium alginate hydrogel beads to remove methylene blue dye and disinfect water (Zhao et al. 2021). The nanocomposite hydrogels demonstrated excellent antibacterial activity within 60 minutes against *S. aureus* and *E. coli* with 68% and 99% elimination rates, respectively. In yet another study by Taghizadeh et al. (2020), bimetallic AgCl/ZnO nanostructures in chitosan hydrogel demonstrated 95% and 99% inactivation of *S. aureus* and *E. coli*, respectively under visible light. The inactivation rate constants (k x 10^{-3} min^{-1}) of chitosan/AgCl/ZnO composite in photocatalytic disinfection experiments were 2.3 to 5 times higher than its pristine counterparts.

Carbon based materials, particularly graphene oxide, has successfully been applied synergistically with metal nanoparticles for enhanced antibacterial action in various applications of water treatment. For instance, Sahraei and Ghaemy (2017) produced highly bactericidal hydrogel nanocomposite of tragacanth gum containing graphene oxide (GO) and AgNPs, which displayed 14 mm zone of inhibition against *S. aureus* in disc diffusion assay. More recently, Sivaselvam et al. (2021) incorporated graphene oxide in polyacrylamide (PAM) and *in situ* synthesized AgNPs in polymer matrix via gamma irradiation to form a multifunctional nanocomposite hydrogel for removal of microbes and dyes. The antibacterial activity of PAM/GO/Ag hydrogels evaluated through colony count method yielded excellent results with over 90% inhibition of both *E. coli* and *S. aureus* achieved under 2 h. The antibacterial mechanism of these hydrogels was attributed to membrane damage and oxidative stress corroborated through independent protein leakage and ROS production detection assays.

2.4.2 Coatings and their Characteristics Employed in Biomedical Implants

The emergence of polymer nanocomposite coatings is a relatively recent advancement, gaining significant attention in 2000s while its applications in biomedical, food, and aerospace industries has continued to advance from mid-2000s to present day. Coatings involve the application or dispersion of a material onto a substrate, resulting in the creation of an extra layer on the surface. The terms 'thin-film nanocomposites' and 'polymer nanocomposite coatings' are often used interchangeably to describe their application process, as these modify or enhance the substrate's properties while forming a film-like layer with thin profile. PNC coatings consist of densely packed grains and interphase boundaries, where the spacing between these layers closely approaches inter-atomic distances. Consequently, corrosion and microbial entities are inhibited from penetrating the surface of protected substrate, thereby enhancing coating efficiency (Chen et al. 2020; Huang et al. 2020; Kaew-on et al. 2020).

Since, classification of PNC coatings can be dissected in many ways depending upon the materials and applications involved, only types pertaining to antimicrobial activity will be discussed. Antimicrobial PNC coatings can be divided into three primary groups namely, adhesion-resistant, releasing-type, and contact bactericidal coatings, in accordance with their approach to intervene in the infection and biofilm formation processes. Bacterial adhesion, colonization and subsequent biofilm formation is the root cause of implant related infections (IRIs) and anti-adhesion coatings aim to hinder these initial stages through non-cytotoxic mechanisms (Idumah et al. 2020). In such coatings, nanomaterials that can resist bacterial protein adsorption, such as SiNPs, (Polytetrafluoroethylene) PTFE NPs, graphene along with the combination of polyethylene glycol (PEG), hydrophobic polymers or brushes, and zwitterionic polymers are employed. Releasing-type coatings demonstrate their antibacterial effect by gradually releasing antibacterial agents (nanoparticles) from coated implant surface in a controlled mode, which enables the elimination of both adherent and adjacent planktonic bacteria. The release of incorporated antibacterial agents is achieved by diffusion into the aqueous medium, erosion/degradation, or hydrolysis of covalent bonds (Campoccia et al. 2013; Cloutier et al. 2015), thus delivering a high antibacterial agent concentration locally, without exceeding systemic toxicity or ecotoxicity limits. Despite this, due to the inherent limitations in the reservoir capacity of such coatings for antibacterial agents, their effectiveness remains transient in nature. The nanomaterials utilized for this technique

include metal/metal-oxides such as Ag, ZnO, Cu and polymer like PLGA, PCL, PLA etc. The contact-killing coatings have been designed to address the challenge of depleting reservoirs encountered in release-type materials (Tiller et al. 2001). In this approach, adhered bacteria are eradicated due to their cell membrane disruption (penetrating the microbial envelope) by the nanomaterials and polymers affixed to the implant surface (Lewis and Klibanov 2005). As the primary modes of operation revolve around membrane interactions, involving physical rupture or charge interference, the most potent agents for contact bactericidal coatings have predominantly been cationic polymers with inherent antibacterial activity such as chitosan, polyethyleneimine (PEI) and nanoparticles such graphene oxide nanosheets, CNTs, TiO_2 etc.

In recent times, researchers have sought to improve surface and bio-integration of biomedical implants/substrates through two approaches i.e. coatings and surface modification (chemical modification of substrate). However, coatings stand as a superior choice over surface modification for augmenting implant efficacy owing to their precise functionalities, reproducibility, and manufacturing & regulatory ease. Diverse coatings showcasing remarkable performance have been formulated to serve distinct objectives on biomedical implants. Examples of such coatings include conducting and non-toxic polymer-nanosheet coatings that can be deposited and patterned on any substrate and has a contact-killing effect on bacteria (planktonic and biofilms) even at low concentrations (Carpio et al. 2012). Coatings consisting of terpolymer with nanospheres demonstrating antifouling characteristics by supressing protein adsorption (Deng et al. 2021). Coatings fabricated with biopolymer-nanotubes characterized by hydrophobic-hydrophilic asymmetric wettability that assist in lowering corrosion rate of implant exposed to physiological fluids (Jian et al. 2023). Coatings with significant synergistic abilities such as antifouling and anticorrosion paired with antibacterial properties that also impart high mechanical strength to the implant underneath (Arukalam et al. 2016; Zhang et al. 2021). Coatings with such exceptional capabilities resonate with their unique and distinctive characteristics such as broad spectrum antibacterial activity, corrosion resistance, advanced clinical compatibility, and localized delivery of therapeutic agent. The uniformity intrinsic to PNC coatings ensures consistent performance across the entirety of the implant surface, while their versatile composition accommodates nanoparticles, polymers, and biomolecules, which enable multifaceted enhancements. Additionally, their conformity to accommodate intricate implant geometries and preserve mechanical properties of bulk substrate, reaffirm their pre-eminence in optimizing implant functions.

Fabrication Methodologies of Polymer Nanocomposite Coatings on Implants

Various techniques can be utilized to create PNC coatings, with the selection of a particular deposition method determined by factors including the intended coating application, desired properties, coating thickness, production cost, implant material, and substrate temperature limits. The techniques can be broadly divided into mechanical, physical, chemical and/or combination of these approaches. The most promising and efficient methods include dip coating, electrospinning, solution/drop casting, electrodeposition, chemical vapor deposition (CVD), spray coating, although other methods such as 3D printing, layer-by-layer assembly, physical vapor deposition (PVD), and magnetron sputtering, are also used.

Solution or drop casting, a facile and equipment-free coating technique, which minimizes material waste, entails depositing liquid droplets of nanocomposite suspensions onto a substrate with subsequent solvent evaporation (drying). Consequently, it results in a dense coating/thin-film over substrate, where its attributes are influenced by parameters such as dispersion concentration or volume, surrounding temperature, drying process parameters (such as residual solvent), and evaporation rate etc. (Kajal et al. 2018; Kumar et al. 2020). The customizability, cost-effectiveness, and ease of scale-up of this technique finds broad-range applications in biomedical field. For instance, Zarghami et al. (2021) developed a chitosan/bioactive glass nanoparticles coating with vancomycin by means of drop casting over Ti implant and reported its significant adhesive and anti-infective properties.

Dip coating, also known as immersion coating, is a similar technique widely used in laboratories and industries due to its simplicity, adaptability to various substrate shapes, adjustable coating thickness, and economic viability (Neacşu et al. 2016). It involves immersing the pre-treated metal substrate in the coating mixture and leaving the substrate in the mixture for a specified time. Then raising the substrate out of the mixture to form a wet film, drain excess liquid and finally drying the coating through solvent evaporation, forming a thin film (which can be further solidified by conventional or laser sintering) (Kakaei et al. 2019). Immersion time, withdrawal speed, immersion cycles, temperature, inertial force, solution viscosity, gravitational force, and surface tension are all factors influencing the dip coating process (Lončarević and Čupić 2019; Sahoo et al. 2018). An ideal bioactive bone material, nanohydroxyapatite, which is widely used for its osteoconductivity and bio-corrosion resistance (Abdal-hay et al. 2013), has been successfully incorporated into

polycaprolactone film-based coatings and applied to magnesium alloy implants using the dip coating technique.

Electrophoretic deposition (EPD) is a simple process which involves immersing electrodes in a PNC colloidal suspension and applying a potential between them. The process includes suspended particles moving toward the oppositely charged electrode (substrate), depositing onto it, and forming a uniform coating (Thandapani et al. 2018). EPD is valued for its simplicity, eco-friendliness, speed, and versatility in designing coatings of various shapes. Challenges include scalability and achieving adhesion and crack-free coatings without additional high-temperature sintering (Bree et al. 2019). Although the technique is mainly used for the production of ceramic coatings however, polymer nanocomposite coatings can be successfully obtained [155]. For instance, chitosan/gelatin loaded with silica nanoparticles and gentamicin were electrodeposited on AISI 316L implant that facilitated sustained release for a period of 21 days demonstrating excellent antibacterial activity and ST-2 stromal cell proliferation (Aydemir et al. 2020).

3D printing is a technique capable of constructing 3D objects by interpreting computer-aided designs (CAD) or scanners (Jakus 2019; Palmara et al. 2021) and has shown significant potential in pharmaceutical and biomedical applications due to its adaptability with diverse materials, intricate geometry creation, and time efficiency (Beg et al. 2020). The capability for on-site fabrication positions it as a promising avenue for personalized bioactive coatings on orthopaedic implants (Nikolova and Apostolova 2022). A variety of 3D printing technologies can be employed for controlled release coating systems, including selective laser sintering, drop-on-demand, semi-solid extrusion (SSE), and fused deposition modelling (FDM) (Cook et al. 2014; Yang et al. 2021). In an interesting study, bioactive and biocompatible composite coatings comprising of carboxymethyl cellulose (CMC), alginate with nanofibrillated cellulose (NFC) and clindamycin were applied to metal implants (316LVM and Ti90Al6V4) using 3D printing technology. This allowed controlled release of the drug for more than 2 months and NFC provided antibacterial activity to be used to prevent postoperative infections (Maver et al. 2021).

Table 2.5 Antimicrobial Activity of Polymer Nanocomposite Coatings Applied on Diverse Biomedical Implant Surfaces.

Coating (composition)	Substrate	Processing route	Test microorganism	Inactivation performance	Death mechanism(s)	Biocompatibility	Reference
Alginate-Chitosan/Mn-Zn substituted hydroxyapatite/graphene oxide	AZ91 Mg alloy	Electrophoretic deposition	*E. coli, S. aureus*	ZOI: 10-19 mm	-	MTT: No osteoblast cells cytotoxicity	Liu et al. (2021)
Polytetrafluorethylene/ AgNPs	316L stainless steel	Dip-coating	*E. coli*	75-90% inhibition over 3 days	Ag^{+} leach-kill	MTT: 75-56% L929 fibroblast cell viability	Zhang et al. (2021)
Hydroxyapatite/chitosan/graphene oxide	AZ91D Mg alloy	Electrophoretic deposition	*E. coli, S. aureus*	OD_{600}: 0.04-2.5 after 24h	Oxidative stress, membrane damage	-	Askarnia et al. (2021)
Chitosan/ZnO	Ti	Dip-coating	*E. coli*	OD_{600}: <0.04 after 24h	ROS generation	CCK-8: >98% MG-63 and human osteoblast cell viability	Lin et al. (2021)
Polyvinylpyrrolidone/ graphene oxide	316L stainless steel	Electrophoretic deposition	*Pseudomonas sp., Bacillus sp.*	Bacterial density (CFU cm^{-2}): 4 orders reduction Biofilm thickness (µm): 2 orders reduction	ROS generation, oxidative stress	-	Jena et al. (2021)
Chitosan/gelatin/silica-gentamicin NPs	316L stainless steel	Electrophoretic deposition	*E. coli, S. aureus*	ZOI: 3.9-4.1 cm MIC: 0.25-4 mg L^{-1}	-	WST-8: No stromal ST-2 cells cytotoxicity	Aydemir et al. (2020)

Poly-L-lactic acid/graphene oxide-AgNPs	Mg alloy	Electro-spinning	*E. coli, S. aureus*	ZOI: 3.0-5.3 mm 65-97% reduction	Contact-kill, membrane damage	MTT: 70-99% MG-63 osteoblast cell viability	Bakhsheshi-Rad et al. (2020)
Catechol-functionalized chitosan/AgNPs	Ti	Ester linkage	*E. coli, S. aureus*	35-72% reduction	-	MTT: >90% L929 fibroblast cell viability	Cheng et al. (2019)
Chitosan/CuNPs	316L stainless steel	Electrophoretic deposition	*E. coli, S. aureus*	3.5-6 log reduction	-	-	Tabesh et al. (2019)
Chitosan/ hydroxyapatite/iron oxide	Mg alloy	Electrophoretic deposition	*E. coli, S. aureus*	ZOI: 6-18 mm	ROS generation	Hemolysis: 3.6-4.1%	Singh et al. (2021)
Carboxymethyl chitosan-gallic acid/AgNPs	Ti	Dip-coating	*E. coli, S. aureus*	ZOI: 17-23 mm 2 log reduction	-	CCK-8: 98% mesenchymal stem cell viability	Ren et al. (2021)
Chitosan/graphene oxide	Ti	Spin-coating	*S. mutans*	OD_{600}: <0.5 Biofilm thickness (µm): 2 orders reduction	-	WST: 1.6 times MC3T3-E1 osteoblast cell proliferation	Park et al. (2020)
Chitosan/poly vinyl alcohol/AgNPs	Ti	Solution casting-evaporation	*E. coli, S. aureus*	OD_{600}: <0.9 after 24h	Ag^{+} leach-kill, contact-kill	No Saos-2 cell cytotoxicity	Mishra et al. (2017)
Poly (lactic acid)/ZnO	AZ31 Mg alloy	Dip-coating	*E. coli*	ZOI: 13-14 mm	-	CCK-8: 1.7 times MC3T3-E1 osteoblast cell proliferation	Mousa et al. (2018)

*ZOI: Zone of inhibition; ROS: Reactive oxygen species

Antibacterial Performance of PNC Coatings in Biomedical Implants

This section delves into a comprehensive review of research studies that have critically examined the efficacy of polymer nanocomposites as antibacterial implant coatings on various substrates. Inorganic nanoparticles based PNC coatings employing Ag, ZnO, and Cu as active biocidal agents have been employed to confer protection against implant related infections (IRIs). Zhang et al. (2021) synthesized AgNPs incorporated polytetrafluorethylene coating on 316L stainless steel substrate via dip-coating procedure which resulted in 75% to 90% *E. coli* eradication over the course of 3 days. The sustained release of silver ions also resulted in inhibition of ~50% bacterial biomass accumulation. Mishra and co-workers fabricated AgNPs cored polyvinyl alcohol nanocapsules embedded in chitosan matrix as a titanium (Ti) implant coating through solution casting-evaporation technique. The coatings effectively reduced *E. coli* and *S. aureus* growth while being completely biocompatible to Saos-2 cells (Mishra et al. 2017). Lin et al. (2021) used dip-coating method to produce a chitosan based coating containing ZnO NPs on Ti substrate with superior antimicrobial efficacy. The composite dropped OD_{600} of *E. coli* culture to <0.4 within 24 h via ROS generation and maintained >98% viability with MG-63 and human osteoblast cells. Mousa et al. (2018) by employing a similar technique deposited a poly (lactic acid)/ZnO coating on magnesium (Mg) alloy which successfully inhibited *E. coli* growth and aided in MC3T3-E1 osteoblast cell proliferation. Tabesh et al. (2019) coated 316L stainless steel (SS) with chitosan containing CuNPs composite by electrophoretic deposition (EPD). All coated specimens were reported to have significant antibacterial ability with 3.5-6 log reduction in *E. coli* and *S. aureus* cultures.

Graphene derivatives being potent against range of pathogens, have also been applied frequently in conjunction with polymers for implant coatings. Park et al. (2020) deposited graphene oxide substituted chitosan composite on Ti disks via spin-coating procedure to form antibacterial dental implants. The coated samples containing 1 wt.% of GO eliminated 50% of *Streptococcus mutans* cells in test culture and reduced the biofilm thickness from ~18 µm to ~9 µm. Higher concentration of GO (3 and 5 wt.%) in chitosan reduced the overall biocidal capacity of coatings however, did not affect the MC3T3-E1 osteoblast cell proliferation. More recently, Jena et al. (2021) utilized EPD to coat 316L SS with polyvinylpyrrolidone/ graphene oxide (GP) to obtain a protective layer against corrosion and bacteria. The coated specimens displayed a 4 orders magnitude reduction in bacterial density of *Pseudomonas sp.* and *Bacillus sp.* compared to the $>1.5 \times 10^4$ CFU cm^{-2} of bacterial density on uncoated

surfaces. Additionally, GP coated SS substrates demonstrated an average thickness of biofilm of *Pseudomonas sp.* and *Bacillus sp*. to be 13 µm and 16 µm in comparison to 35 µm and 41 µm on uncoated substrates, respectively. The biocidal mechanism of these coatings was attributed to ROS generation leading to oxidative stress which disrupts the bacterial cell morphology and cause leakage of vital intracellular molecules. The influence of GO content in polymer composites on the antibacterial activity seems to be concentration-specific (Liu et al. 2014; Mazaheri et al. 2014; Zhang et al. 2018). Askarnia et al. (2021) produced ternary hydroxyapatite/chitosan composite coatings with varying amount of graphene oxide (0.5, 1, 2 wt.%) on magnesium alloy by EPD. Turbidity assay against *E. coli* and *S. aureus* demonstrated complete eradication of bacterial cells in the case of coatings containing 2 wt.% GO and about 1.5-1.9 times turbidity reduction in coatings with ≤1 wt.% GO. Bakhsheshi-Rad et al. (2020) also co-incorporated different concentrations of graphene oxide- AgNPs (1, 2, 3 wt.%) into poly-L-lactic acid and deposited the resultant nanocomposite on Mg alloy substrate via electrospinning method. They reported a higher antibacterial effect with increasing GO-AgNPs concentrations as were evident with consistent increase in bacterial inhibition from 65% to 95% and 68 to 97% against *E. coli* and *S. aureus*, respectively. Contact-active antibacterial mechanism owing to sharp edges of GO was deemed to be predominant. The escalation of GO-AgNPs content also displayed a detrimental effect on cytocompatibility of the coatings as the MG-63 osteoblast cell viability decreased from 99% to 70% after 7 days in MTT assay. Table 2.5 summarizes the different antibacterial or infection resistant coatings discussed in this section and more.

2.5 Remaining Challenges and Prospective directions

Significant progress in the development of various types of antimicrobial polymer nanocomposites has provided promising and innovative strategies to overcome the prevalence of microbes and their associated infections. However, few remaining challenges unveiled through the course of this literature survey limiting the practical applications of PNCs are addressed here.

- Most relevant reports on PNC hydrogels for water disinfection have often prioritized the elimination of naturally occurring microbiological contaminants while sometimes disregarding a critical facet- presence of polymicrobial population in polluted waterways. Particularly, the persistence nature of microorganisms associated with healthcare and medical waste in water has presented a unique set of challenges. Therefore, hydrogels

must be targeted with multi-pronged approach, to eradicate microbial pollutants of broader spectrum as well.

- Various hydrogel-nanoparticle composites have shown promising disinfection outcomes primarily within the context of simulated water conditions. While these simulated environments provide controlled settings for initial testing and assessment, it is also easy to misrepresent the conditions and to account for possible interferences within polluted real-water systems. Consequently, transition to comprehensive studies employing real water can help us to completely understand the feasibility and reliability of nanocomposite hydrogels in the wider realm of water disinfection.

- The current landscape of chitosan hydrogel nanocomposite research in water disinfection predominantly revolves around studies conducted in batch process conditions. There is a need to conduct the disinfection process, by optimizing operational design to improve process continuity towards a quasi-continuous or, ideally, a continuous-flow mode of operation to better capture the dynamic nature of real-world water treatment processes.

- It has been noticed that drying process at some stage of solvent-based coatings formation on substrates becomes inevitable in certain approaches (such as solution casting-evaporation). Improper drying can influence variables such as residual solvent, which has been ascribed to cause certain coating defects (blisters, cracks) when present in vast quantities. Such conditions have been challenging the long-term adhesion and stability of nanocomposite coatings on various surfaces. Therefore, investigating the cardinal influence of drying process parameters while fabricating antibacterial coating composites can extend their translational attributes in practical biomedical applications.

- The complexity of multiple antimicrobial mechanisms exerted by nanoparticles individually or in combination with other agents presents another challenge. The antimicrobial mechanisms in present studies are proposed or hypothesized based on interactions between bacterial cells and single-component nanomaterials. However, these interactions are bound to be altered in the presence of additional compounds within the polymer-based nanocomposites. Thus, to explore the exact nature of the antimicrobial mechanisms, in different nanocomposites (hydrogels or coatings), research efforts combining varied experimental procedures in an inter-disciplinary fashion are required.

- It is also noted that most studies have overlooked the issue of biodegradability of the nanocomposite materials, both during their development and exhaustion after intended reuses. Moreover, employing natural polymers in the manufacturing of PNCs does not inherently come with a guaranteed sustainability certification. Therefore, addressing the evaluation of biodegradability is critical in ensuring the translational success of the materials developed in the lab into sustainable and practical technologies.

- The major concern associated with utilization of antibacterial nanocomposites in biomedical or environmental applications is their "biocompatibility factor". These materials in the event of uncertain leaching have been linked to severe toxicity issues in the surrounding environment which can cause adverse effects on healthy tissues and cells. The biological reliability of these nanocomposites through studies taking into consideration the possible risks to one's health need to be investigated in further detail, as limited data is available. Thus, chemical characterizations assessing potential levels of leachable agents paired with toxicologic characterizations evaluating mammalian cell toxicity, hemolysis, and physiological compatibility under simulated body fluids can help overcome existing challenges.

Therefore, current work presented in this thesis endeavors to address the aforementioned research gaps.

Chapter 3

Materials and Methods

3.1 Synthesis of Nano-silver loaded Chitosan-Poly(vinyl alcohol) (CS/PVA/Ag) Hydrogel

3.1.1 Preparation of Chitosan-PVA (CS/PVA) Hydrogel Composite

A previously reported method (Agnihotri et al. 2012) was adopted for the synthesis of hydrogels. A 2% w/v chitosan suspension was prepared in 2% v/v acetic acid solution while stirring overnight at 40 °C. A clear chitosan solution, devoid of any insoluble impurities was obtained through centrifugation and filtration. Similarly, a 4% w/v PVA solution was prepared in distilled water at 90 °C under vigorous stirring for 4 h. Chitosan and PVA solutions were added in equal ratios (1:1) in a beaker and stirred at 60 °C initially for 2 h and then at 25 °C over the next 12 h to obtain a homogeneous blend suspension. To this solution, 100 µL, 25% v/v glutaraldehyde was added drop wise for cross linking the two polymeric residues under constant stirring at 25 °C. The solution was then casted in test tubes and cured at 45 °C in a hot air oven for gelation. The formed hydrogels were removed from casting molds through precipitation with 12% w/v NaOH solution at room temperature for 8 h. The hydrogels were then washed repeatedly with distilled water to remove the residual NaOH. Hydrogels were subjected to five repeated freeze/thaw cycles, with each cycle comprising of a freezing step (16 h at -20 °C) followed by a thawing step (3 h at 25 °C) to develop porous network structures within the hydrogel system.

3.1.2 Fabrication of CS/PVA/Ag Hydrogel Nanocomposite

The prepared hydrogels were sliced into discs (10 mm × 6 mm) and introduced into a vial containing 20 mL, 10 mM silver nitrate ($AgNO_3$) aq. solution for 24 h. After required incubation, discs were washed thrice with DI water to remove any unbound silver ions. These silver loaded hydrogels were transferred into a beaker containing 60 mL of 10 mM sodium borohydride ($NaBH_4$) solution and allowed for 10 minutes for the reduction of silver ions to silver nanoparticles (AgNPs). The hydrogel discs were again rinsed with DI water, dried under vacuum, and sealed in plastic bags till further use. These discs with loaded silver nanoparticles were designated as CS/PVA/Ag hydrogels.

3.1.3 Characterization of Pristine and Ag-Loaded Hydrogel Composites

The optical spectra of hydrogel films were recorded on a UV-Vis spectrometer (Shimadzu 2600, Japan) with diffuse reflectance accessory in a wavelength range of 200–600 nm. All spectra were recorded in triplicate. The variations in the chemical composition and functional

moieties of pristine and Ag loaded CS/PVA hydrogels were carried out using Fourier-transform infra-red spectroscopy (FTIR, Nicklet 380 Thermo Fisher, USA). The hydrogels were initially dried for 48 h in a lyophilizer so as to remove all moisture/adsorbed water vapors and were mixed with dried KBr to form pellets using hydraulic press. The spectra were recorded from 4000 cm^{-1} to 500 cm^{-1} at 25 °C with 32 scans at a spectral resolution of 4 cm^{-1}. The thermal degradation studies were done using differential scanning calorimetry (DSC131 evo, SETARAM Instrumentation, France). For this, the lyophilized hydrogel samples were analyzed with a heating/cooling rate of 20K min^{-1} under N_2 atmosphere. The surface morphology of pristine and Ag loaded hydrogels was compared using scanning electron microscope (FE-SEM, Hitachi SU-8010, Japan). A fine thin slice of hydrogel samples were coated with gold sputtering and placed on to sample stubs using a double sided carbon tape. Elemental analysis and composition of the hydrogel samples were also investigated through Energy-dispersive X-ray spectroscopy (EDX) in conjunction with FE-SEM.

3.2 Swelling Capacity of Hydrogel Composites

An initial dry weight of lyophilized hydrogel discs (10 mm × 6 mm) was calculated and designated as W_1. The hydrogels were soaked in distilled water at 25 °C while, the swollen weight of corresponding hydrogel discs were determined (W_2) at regular time interval over a span of 2 h after surface wiping. The swelling ratio (S%) defined as the ratio of water content retained within the swollen hydrogel (W_2) to the dry weight (W_1), was calculated as per the Equation 3.1. In a similar procedure, the impact of temperature on swelling ratio of CS/PVA/Ag hydrogel was also evaluated over a broad range from 15-45 °C.

$$S\ (\%) = \left(\frac{W_2 - W_1}{W_1} \right) \times 100 \qquad \text{Eq. 3.1}$$

3.3 Strain-specific Disinfection Potential

The antibacterial activity of synthesized CS/PVA and CS/PVA/Ag were primarily tested in both solid and liquid medium through disc diffusion and viable cell count methods, respectively against four bacterial strains. To simulate microbiological contamination, *Escherichia coli* MTCC 739 (ATCC 10536) and *Enterobacter aerogenes* NCIM 5139 (ATCC 13048) were employed for the inoculation of influent water to represent faecal and

non-faecal contaminants (Kristanti et al. 2022). On the other hand, *S. aureus* NCIM 2127 (ATCC 9144) and *S. epidermidis* NCIM 2493 (ATCC 12228) were selected as representatives of healthcare-associated contaminants that might get introduced in natural waters due to unsafe disposal of biomedical waste via various channels such as domestic, hospital, and industrial (Kooshki et al. 2023). These *E. coli*, *E. aerogenes*, *S. aureus* strains were particularly selected from ATCC database based upon their application as test microorganisms in evaluation of bactericidal ability of water disinfectants in time-kill assays. In contrast to the other species examined here, *S. epidermidis* has been commonly associated with human skin, infected medical devices and cannot be exclusively classified as waterborne pathogen. However, investigation into the inactivation of *S. epidermidis* presented in this research was necessary to establish a reference point for infections caused by such opportunistic pathogens in water through human-related activities. Therefore, inclusion of these findings in this work serves the purpose of baseline comparison and comprehensiveness.

3.3.1 Disc Diffusion Assays

The qualitative aspects of antibacterial activity of CS/PVA and CS/PVA/Ag hydrogels were analysed through disc diffusion method. Briefly, nutrient agar (NA) plates were spread with 100 µL of chosen microbial solution in the range of ~10^6-10^7 CFU mL^{-1}. Once dried, composite sample discs (10 mm × 6 mm) were then placed on the surface of inoculated agar plates. 100 µL of 1X sterile phosphate buffer saline (PBS) was then poured onto sample discs and after drying, plates were kept at 37 °C in the BOD incubator (Caltan® NSW-152, NSW Ltd., New Delhi). The diameters of inhibition zones were measured after 24 h.

3.3.2 Colony Forming/count Assay

Quantitative assays for determining bacterial killing were done through the standard pour plate culture method against all four bacterial strains. Briefly, the sterilized flasks containing nutrient broth (NB) media were inoculated with 10 µL repeatedly sub-cultured microbial strain and kept in rotary shaker at 37 °C at 120 rpm for 14-16 h. During end of the log phase of microbial growth, grown cultures were isolated in pellets through centrifugation, washed thrice with 1X PBS and were finally resuspended in it. The disinfection studies were performed at a fixed initial bacterial concentrations (N_o= ~10^3-10^5 CFU mL^{-1}) of each strain by diluting their respective harvested suspension (~1×10^9 CFU mL^{-1}) through optical density

measurements using a spectrophotometer (Shimadzu 2600, Japan). For instance, flasks with ~10^3 CFU mL^{-1} microbial contamination (100 mL) were introduced with hydrogel discs (two of each i.e. CS/PVA and CS/PVA/Ag; 10 mm × 6 mm). The flasks were incubated at 37 °C, 120 rpm in rotary shaker (Excella® E25, New Brunswick™, USA) while the aliquots from it were withdrawn at different time intervals (0, 15, 30, 60, 90, 120, 240 minutes) for plating over agar plates. The number of viable bacterial colonies were counted in triplicates after incubating for a period of 18-24 h.

3.4 Reusability of Hydrogel Nanocomposites, Silver loading and Release Profile

Reusability

The hydrogel nanocomposites (CS/PVA/Ag) were assessed for it reuse capacity for ten repetitive cycles of water disinfection. For this study, hydrogels discs (10 mm × 6 mm) were incubated in different batch reactors (~10^3 CFU mL^{-1}, 100 mL) containing two bacterial suspensions, *E. coli* and *S. aureus* for a period of 4 h at 37 °C under continuous shaking at 120 rpm. After 4 h, nanocomposites were retrieved from the respective suspensions and aliquots were employed to check disinfection rates using colony count method. The CS/PVA/Ag hydrogels were washed twice with sterile distilled water and then reintroduced to fresh bacterial batch reactor under similar conditions. The procedure was repeated over ten cycles, with the antibacterial activity in the first cycle marked as 100%, while subsequent cycles were assessed for residual activities.

Silver Loading and Release Profile

The extent of mass loading of AgNPs inside CS/PVA/Ag hydrogels was determined using Inductively coupled plasma-Atomic emission spectrometer (ICP-AES, ARCOS-simultaneous ICP Spectrometer, Germany). For this purpose, a known amount of hydrogel (10 mm × 6 mm; weight-132.1 mg) was crushed thoroughly and dispersed in conc. HNO_3 acid solution (3 mL) overnight to ensure complete dissolution. The solution was diluted appropriately using distilled water (7 mL) and filtered to remove the remnants of hydrogels. The filtered solution was then subjected to ICP-AES analyses. The kinetics of silver ions release form hydrogel in aqueous phase was also determined after every hydrogel reuse. The hydrogels were placed in screw-cap flasks containing deionized water (100 mL) and incubated for 7 days at 37 °C. The required aliquots were taken after 24 h time interval and subjected to ICP-AES analyses.

3.5 Biofilm Assay

Pre-grown cultures of both *E. coli* and *S. aureus* were diluted 1:100 in freshly prepared Luria broth (LB) media and assayed separately. CS/PVA and CS/PVA/Ag hydrogel films (10 mm × 10 mm) were introduced in each well containing 100 µL of diluted bacterial suspension in a 96-well micro-titer plate and were incubated at 37 °C for a duration of 48 h. Wells containing only unsterilized media (i.e., devoid of both microbes and hydrogel) were taken as negative controls while, bacteria inoculated media without any hydrogel were taken as positive control. After required time period, the media was removed and cells were thoroughly washed with 1X PBS buffer under brisk shaking so as to remove the possible planktonic bacteria, if remains in each well of the microtiter plate. A 125 µL, 0.1% (w/v) crystal violet dye was then added in all wells and stained for 20 minutes at room temperature. The excess crystal violet was removed by washing with 1X PBS twice under vigorous shaking and was allowed to dry in air. For quantification of adherent cells, the cell bound crystal violet was dissolved in their respective solvents (200 µL, 30% acetic acid for *S. aureus*; 80% ethanol for *E. coli*) as specified in earlier studies (Merritt et al. 2011) by covering plates and incubated for 10-15 minutes at room temperature. The biofilm growth of both species was finally monitored at 570 nm using a micro plate reader (BioRad, USA). A two-tailed student's t-test was used to determine the differences in biofilm formation between the control and each group. The P value of < 0.005 was taken as significant.

3.6 Disinfection of Natural Water Resources

The efficacy of CS/PVA/Ag hydrogels in disinfecting environmentally relevant water resources i.e., Bhakra canal, ground water, and tap water within Patiala district, Punjab, India was determined. The chosen water samples were inspected for physicochemical parameters such as alkalinity, hardness, dissolved/suspended solids, and total microbial count. The disinfection experiments were conducted against natural water sources without any purification steps, either at their natural microbial contaminants level or spiked externally with desired bacterial strains as contaminants. Two CS/PVA/Ag hydrogel discs (10 mm × 6 mm) were introduced in each of the flasks containing 100 mL of canal and tap water and incubated at 37 °C in rotary shaker at 120 rpm. The aliquots withdrawn from flasks at different time intervals (0, 45, 90 minutes) were plated over agar plates to estimate the number of viable bacterial colonies after 24 h incubation period. Additionally, another set of experiments were conducted for these water sources spiked with external contaminant *S.*

aureus at a concentration of ~10^5 CFU mL^{-1}. The flasks containing externally spiked canal, ground water, and tap water were treated with CS/PVA/Ag hydrogel discs at 37 °C in an incubator shaker. Next, 100 µL aliquots collected from sample flasks at time intervals of 0, 60, 120, and 180 minutes were subjected to colony count assay.

3.7 Synthesis of Nano-Ag Loaded Chitosan-Graphene Oxide (CS/GO/Ag) Hydrogels

3.7.1 Synthesis of Graphene Oxide (GO)

Graphene oxide was prepared using natural graphite powder through a modified Hummers method as described by Zhang et al. (2010) with desired modifications. In a typical experiment, 2 g graphite and 1 g sodium nitrate were added in a 250 mL flask at 0 °C. Subsequently, with continuous stirring, 50 mL of concentrated H_2SO_4 was slowly added to the flask at 5 °C. The mixture stirred for 2 h, with $KMnO_4$ added incrementally to control the temperature (maintained at ~10 °C). The temperature was then raised to 35 °C, and stirring continued for 12 h. Following incubation, 90 mL water was cautiously introduced into the solution under vigorous stirring. A dark brown suspension was formed at the end of this step. To convert the remaining permanganate and MnO_2 into soluble $MnSO_4$, the suspension was further treated by adding a mixture of H_2O_2 (7 mL, 30%) and water (55 mL). The resulting bright yellow suspension indicated the completion of the reaction. Graphite oxide was separated from the reaction mixture through centrifugation. The yellow-brown graphite oxide sludge underwent three washes with 150 mL of 3% HCl (at approximately 40 °C) and was finally dried at 40 °C for 24 h under vacuum. Before each use, the graphite oxide powder was transformed into graphene oxide (GO) by ultrasonication at room temperature. The as-prepared aqueous GO suspension was then utilized in subsequent studies.

3.7.2 Formation and Optimization of Chitosan/Graphene Oxide (CS/GO) Hydrogels

A series of chitosan (CS) working solutions with different concentrations (1%, 2%, and 3% w/v) were first prepared by dissolving predetermined amount of chitosan in 50 mL of acetic acid solution of varied strength (1%, 2%, 3% v/v) respectively, while stirring overnight at 40 °C. Graphene oxide (GO) suspensions were prepared by adding various amounts of GO (10.4, 26, 52, 208, and 416 mg) in 2 mL of distilled water at 25 °C followed by ultrasonication in an ultrasonic bath (PCI analytics-9L, India), operated at 33±3 KHz for 4 h. Respective GO suspensions were added separately to chitosan solutions and mixed together via two-step stirring process (40 °C for 2 h, followed by 25 °C for 12 h) to obtain a

homogeneous blend with final GO concentrations of 0.02, 0.05, 0.1, 0.4, and 0.8% w/v. For cross-linking, 280 µL of 25% v/v glutaraldehyde was added drop wise to the chitosan-GO suspensions under constant stirring at 25 °C for 5 minutes. The solutions were then transferred to sterile syringe molds for curing at 50 °C for 6 h in a hot air oven for gelation. The detachment of cured hydrogels from molds was done via precipitation with 12% w/v NaOH solution at room temperature for 6 h. The hydrogels were washed thrice with distilled water to remove residual NaOH and subjected to seven freeze/thaw cycles, with each cycle comprising of a freezing stage (16 h at -20 °C) followed by a thawing stage (2 h at 25 °C) to develop semi-interpenetrating networks within the hydrogel. The resulting composites were qualitatively assessed for their consistency in order to tune optimal CS and GO content in hydrogel formation.

3.7.3 The Extent of Silver Nanoparticles Immobilization onto CS/GO Hydrogels

In the final fabrication phase, hydrogel discs (10 mm × 6 mm) were incubated in a vial containing 20 mL, 10 mM aqueous silver nitrate ($AgNO_3$) solution for 24 h, followed by repeated washing with distilled water to remove any unbound silver ions. These silver ion-loaded hydrogels were then transferred into a beaker containing 60 mL, 10 mM sodium borohydride ($NaBH_4$) solution and allowed to react for 30 minutes to reduce the silver ions to silver nanoparticles (AgNPs). The hydrogel discs received a final rinse with distilled water, were dried under vacuum, and sealed in plastic bags for future use. These discs loaded with silver nanoparticles were designated as CS/GO/Ag hydrogels.

3.7.4 Material Characterization

The optical spectra of graphene oxide (1 mg mL^{-1}, sonicated) formed was recorded on a UV-Vis spectrometer (Shimadzu 2600, Japan) in a wavelength range of 200–800 nm. All spectra were recorded in triplicate. Fourier-transform infra-red spectroscopy (FTIR, Nicklet 380 Thermo Fisher, USA) analyses of both pristine and Ag loaded CS/GO hydrogels were carried out in the 500–4000 cm^{-1} range. The samples were initially dried for 48 h in a lyophilizer so as to remove all moisture/adsorbed water vapors from the hydrogels and the obtained characteristics peaks were compared. The sample crystallinity was evaluated using XRD analysis (X-ray diffractometer, PANalytical X-pert Pro, The Netherlands) with Cu Kα radiation (λ = 1.5406 Å) over a scanning range (2θ) from 10° to 90° at slow scan rate (2.0° min^{-1}). Raman spectra of GO and hydrogel composites were produced using a LabRam

HR800 Raman spectroscope (Horiba Jobin-Yvon, France). The surface morphology of pristine and Ag loaded hydrogels was compared using scanning electron microscope (FE-SEM, Hitachi SU-8010, Japan). A fine thin slice of hydrogel samples were coated with gold sputtering and placed on to sample stubs using a double sided carbon tape. Elemental analysis and composition of the hydrogel samples were also investigated through Energy-dispersive X-ray spectroscopy (EDX). The shape and size of the silver nanoparticles were investigated by high resolution transmission electron microscopy (TEM, JEOL JEM-F200, Japan). Mechanical properties of the hydrogels were measured with Shimadzu Autograph AG100KNG universal testing machine (UTM) equipped with a 5 kN load cell with a constant rate of 1 mm min^{-1}. The specific surface area of samples was calculated by Brunauer-Emmett-Teller (BET) method via the low-temperature N_2 adsorption-desorption isotherms (NOVA touch 4L, Quantachrome Instruments, USA). The samples were outgassed for 1 h at 80 °C before the test. Moreover, the average pore size and pore volume of the samples were measured by the Barrett-Joyner-Halenda (BJH) sorption model. X-ray photoelectron spectroscopy (XPS, ESCALAB, Thermo Fischer Scientific, USA) was done to analyse the elemental surface composition and confirm the formation of silver nanoparticles in hydrogel nanocomposite. The thermal degradation studies were done using (DSC) differential scanning calorimetry (DSC131 EVO, Setaram Instrumentation, France) and (TGA) thermo gravimetric analysis (Setsys, Setaram Instrumentation, France). For DSC, the lyophilized hydrogel samples were analyzed with a heating/cooling rate of 20 K min^{-1} under N_2 atmosphere. For TGA, the samples were operated under 100 mL min^{-1} N_2 gas flow in temperature range of 25-300 °C.

3.8 Swelling Capacity of CS/GO and CS/GO/Ag Hydrogel Composites

To calculate the swelling ratios, circular hydrogel discs (10 mm × 6 mm) were lyophilized to remove all moisture, and their initial dry weights were determined and labelled as W_1. These hydrogel discs were then immersed in distilled water at 25 °C, and the swollen weights of the corresponding hydrogel discs were recorded (W_2) at regular intervals within a 1-hour period, after surface wiping. As discussed before, the swelling ratio (S%) was computed as the ratio of water content retained within the swollen hydrogel (W_2) to the dry weight (W_1), as shown in Equation 3.1. Similarly, separate experiments were conducted to assess the swelling ratios of CS/GO/Ag hydrogel over a wide temperature range from 25 to 55 °C.

3.9 Silver Loading and Release Profile

The determination of the amount of AgNPs loaded in the CS/GO/Ag hydrogel was conducted using Microwave Plasma-Atomic Emission spectrometer (MP-AES, Agilent 4100, USA). To accomplish this, a known weight of the hydrogel (10 mm × 6 mm; weight-136.0 mg) was thoroughly crushed and dispersed in a solution of conc. HNO_3 acid (3 mL) overnight to ensure complete dissolution. Subsequently, the solution was diluted with distilled water (7 mL) and filtered to remove any remaining traces of the hydrogel. The filtered solution was then subjected to analysis using MP-AES. Furthermore, the release kinetics of silver ions in the aqueous phase following each reuse of the hydrogel were also determined. Briefly, the hydrogels were placed in screw-cap flasks containing deionized water (100 mL) and incubated for 96 h at 37 °C. The aliquots were taken from the flasks at different time intervals and subjected to analysis using Inductively Coupled Plasma-Atomic Emission spectrometer (ICP-AES).

3.10 Biodegradation of Hydrogels

Natural soil obtained from TIET campus, Patiala (Punjab, India) was used as the biodegradation medium. The soil, after removal of coarse aggregates and stones, was supplemented with urea (6 g kg^{-1}) to encourage an active microbial flora. The samples to be tested for biodegradation were dried in the oven at 32 °C for 2 days and weighed (W_o). The hydrogel specimens (10 mm × 6 mm) were buried approximately 10 cm in depth from the surface of the soil in pots containing 20 cm of soil (Cui et al. 2019; Kumar et al. 2019). The samples were left in the soil for 60 days where weight loss measurements were taken after every 15 days. Meanwhile, the test medium with samples was maintained at a temperature (28–38 °C) with daily addition of water to replenish any loss due to evaporation. Consequently, after specific time intervals the degraded hydrogel fragments were removed, brushed, cleaned and oven-dried at 32 °C, until no changes in weight occurred. After that, all samples were placed in a desiccator for 1 h and allowed to cool and finally, dried hydrogels were weighed (W_d). The reduction in the mass percentage of the samples due to the degradation process was calculated using Equation 3.2. Additionally, another set of hydrogels were pre-treated using a weak tricarboxylic acid present in lemons before burying in soil to evaluate the effect of pre-treatment on biodegradation process.

$$\text{Weight loss (\%)} = \left(\frac{W_o - W_d}{W_o} \right) \times 100 \qquad \text{(Eq. 3.2)}$$

3.11 Disinfection Ability Evaluation and Reusability of Hydrogel Nanocomposites

Primarily, the antibacterial efficacy of synthesized CS/GO and CS/GO/Ag hydrogels were investigated in both solid and liquid medium through disc diffusion and viable colony count methods, respectively against four bacterial strains. In the standard tests, *Enterobacter aerogenes* NCIM 5139 (ATCC 13048) and *Escherichia coli* MTCC 739 (ATCC 10536) were selected as faecal or non-faecal contaminant models present in drinking water. While, *S. aureus* NCIM 2127 (ATCC 9144) and *S. epidermidis* NCIM 2493 (ATCC 12228) were taken as biomedical contagion representatives that could enter natural waters through improper healthcare-waste disposal.

3.11.1 Disc Diffusion Study

For disc diffusion method, 100 µL of chosen microbial solutions in the range of ~10^6-10^7 CFU mL^{-1} were spread on nutrient agar (NA) plates. CS/GO and CS/GO/Ag composite discs (10 mm × 6 mm) were placed on the surface of inoculated agar plates and 1X sterile phosphate buffer saline (PBS, 100 µL) was then poured onto sample discs. After incubation at 37 °C in the incubator chamber and the diameters of inhibition zones were measured after 24 h.

3.11.2 Colony Forming/count Assay

Bacterial inactivation rates were then determined quantitively through standard colony forming assay against all four bacterial strains. Briefly, the sterilized nutrient broth media containing flasks were inoculated with 10 µL, repeatedly sub-cultured microbial strain and kept in rotary shaker at 37 °C at 120 rpm for 14-16 h. During the end of exponential log phase, microbial cultures were isolated in pellets through centrifugation, washed thrice with 1X PBS and were finally resuspended in it. The disinfection studies were performed at a fixed initial bacterial concentrations (N_0= ~10^3-10^6 CFU mL^{-1}) of each strain by diluting their respective harvested suspension (~1×10^9 CFU mL^{-1}) through optical density measurements using a spectrophotometer. The hydrogel discs (two of each i.e. CS/GO and CS/GO/Ag; 10 mm × 6 mm) were introduced in flasks with ~10^3 CFU mL^{-1} microbial load and incubated at 37 °C in rotary shaker (120 rpm). 100 µL aliquots from flasks were withdrawn at different

time intervals (0, 15, 30, 60, 90, 120, 240, 360 minutes) for plating over agar plates. The number of viable bacterial colonies were counted in triplicates after incubating for a period of 24 h.

3.11.3 Reuse Potential of Nano-Silver Loaded CS/GO Composites

The reuse index of CS/GO/Ag hydrogel nanocomposites for multiple cycles of water disinfection was evaluated. Briefly, small hydrogel discs (10 mm × 6 mm) were placed in separate batch reactors (~10^3 CFU mL^{-1}, 100 mL) containing various suspensions of *E. aerogenes*, *E. coli*, *S. aureus*, and *S. epidermidis*. The solutions were then incubated for 2 h at 37 °C with continuous shaking at 120 rpm. After the incubation period, the nanocomposites were removed from the bacterial suspensions, and samples of the suspensions were taken to determine the disinfection rates using the colony count method. The retrieved hydrogels were washed twice with sterile distilled water and then introduced into a new with fresh bacteria under the same conditions as the first cycle. This process was repeated for a total of ten cycles, and the antibacterial activity observed in the first cycle was considered as 100%. The antibacterial activities during the subsequent cycles were determined as residual activities.

3.12 Antibacterial Mechanism Investigation

3.12.1 Bacterial Morphology through FE-SEM

Bacterial strains (*E.coli* and *S. aureus* each, ~10^6 CFU mL^{-1}) were exposed to CS/GO/Ag hydrogels for 6 h at 37 °C to investigate any ultra-structural changes, that are likely to occur in bacterial cells after direct contact. The untreated bacterial cells were used as a negative control. After the required treatment, bacterial pellet was harvested by centrifugation at 5000 rpm for 10 minutes and washed twice with PBS solution. The cells were fixed in PBS suspension containing 2.5% glutaraldehyde (500 µL) for 3 h. After primary fixation, cells were centrifuged at 5000 rpm and rinsed twice with PBS solution. Cells were completely dehydrated with a graded ethanol series (30%, 50%, 70%, 90%, and 100%) for 15 minutes in each treatment (Xing et al. 2022). A 10 µL aliquot was drop casted on a stainless steel surface (5 mm × 5 mm), dried under Infra-red lamp and immediately analysed using field emission gun scanning electron microscopy (FEG-SEM, ZEISS Sigma 500, Germany).

3.12.2 Intracellular Reactive Oxygen Species (ROS) Measurement

The ROS generation levels in bacterial cells were determined by employing nitro blue tetrazolium (NBT) reduction assay (Marathe et al. 2013). Initially, bacterial suspensions (~10^6 CFU mL^{-1}) were incubated at 37 °C for 6 h in the presence of CS/GO/Ag hydrogels and untreated bacterial cells were taken as negative control. Afterwards, 375 µL, NBT solution (1 mg mL^{-1}) was added to cell suspensions and incubated again at 37 °C for 30 minutes. Then 75 µL, 0.1M HCl was added to terminate the reaction followed by centrifugation at 5000 rpm for 10 minutes to recover bacterial pellets. Dimethyl sulfoxide (DMSO, 300 µL) was used to extract the reduced NBT from obtained bacterial pellets. Finally, the extracted solutions were diluted with 300 µL PBS and the optical density of bluish violet formazan was recorded at 575 nm.

3.12.3 GSH Oxidation

To investigate the ROS independent oxidative stress, *in vitro* GSH (glutathione) oxidation was assessed by Ellman's assay (Xing et al. 2022). Bicarbonate buffer (50 mM, pH = 8.6) was used as reaction solution and all samples were prepared in triplicates. CS/GO and CS/GO/Ag composites (4 mg each) were added separately into 1 mL of GSH solution (0.8 mM) to initiate oxidation. Then all the mixtures were placed in a shaker with a speed of 150 rpm for 2 h in dark. After incubation, 3.5 mL of 0.05 M Tris-HCl and 70 µL of 100 mM 5, 5′-dithiobis- (2-nitrobenzoic acid) (Ellman's reagent) were added into the mixtures to yield yellow product. The mixtures were filtrated through 0.22 µm syringe filters with membrane (Himedia, India). Measurements of the thiol content with all samples were carried out at 412 nm using ELISA reader (Thermo Scientific Multiskan® spectrum, USA). Pure GSH solution was used as negative control and GSH solution with H_2O_2 (1 mM) as positive control. The loss of GSH was calculated by the formula mentioned in Equation 3.3.

$$\text{Loss of GSH (\%)} = \left(\frac{\text{Mean OD}_{\text{Negative control}} - \text{Mean OD}_{\text{Test sample}}}{\text{Mean OD}_{\text{Negative control}}} \right) \times 100 \qquad \text{(Eq. 3.3)}$$

3.12.4 Protein Leakage Assay

Bradford's assay was employed to quantitatively estimate intracellular protein leakage from bacterial cells (Xing et al. 2022). The hydrogel nanocomposites were incubated with bacterial cells (~10^6 CFU mL^{-1}) at 37 °C for 6 h in an incubator shaker. Treated bacterial culture

aliquots (1 mL) from each test vial were then withdrawn and centrifuged for 30 minutes at 1600 rpm and 4 °C temperature. Finally, Bradford's reagent (5 mL) was added to collected supernatants and the corresponding absorbance at 595 nm was measured. Concentration of protein released from compromised bacterial cells was determined using a standard curve of bovine serum albumin (BSA).

3.12.5 Lactate Dehydrogenase (LDH) Release Assay

LDH test determined the cell membrane integrity on a premise that cytosolic enzyme lactate dehydrogenases are released into culture medium upon cell death due to plasma membrane damage. The LDH release intensity was verified by measuring the formation of NADH (from NAD^+) in the stoichiometric conversion of iodonitrotetrazolium chloride to iodonitrotetrazolium formazan at 490 nm spectrophotometrically (Kroll et al. 2012). For this experiment, bacterial cultures ($\sim 10^6$ CFU mL^{-1}) were incubated with hydrogel samples in an incubator shaker for 6 h at 37 °C. The samples were then transferred to microcentrifuge tubes after required duration and centrifuged for 5 minutes at 1200 rpm. In a 96-well plate, 180 µL, LDH reagent was added to each well containing 60 µL of supernatant and incubated for 30 minutes at room temperature in dark. After incubation, the optical density of each well was recorded at 490 nm on an ELISA reader. 0.1% Triton X-100 and 0.85% saline suspensions were designated as positive and negative controls, respectively. LDH release percentage was calculated using OD_{490} values in Equation 3.4. The LDH activity of positive control was considered 100% and activity of all other test samples was calculated relatively.

$$\text{LDH Release \%} = \left(\frac{\text{Mean OD}_{\text{Test sample}} - \text{Mean OD}_{\text{Negative control}}}{\text{Mean OD}_{\text{Positive control}} - \text{Mean OD}_{\text{Negative control}}} \right) \times 100 \qquad \text{(Eq. 3.4)}$$

3.13 Continuous-flow Water Disinfection using CS/GO/Ag Hydrogel Composites

In order to expand the application potential of CS/GO/Ag hydrogel nanocomposites, we investigated their disinfection efficacy as a filter column in fixed-bed reactor by using antibacterial rate as an index. Initial experiments were conducted employing a hydrogel column (11 mm diameter, 20 cm bed height, bed porosity 0.38) through which simulated water infested with *S. aureus*, was circulated through a peristaltic pump. Hydrogel column, on both sides was packed with glass wool to ensure consistent retention of the hydrogel throughout the column experiments. The column reactor framework was arranged in a

chamber equipped with UV light for sterilization and a thermostat to maintain working temperature of 37 °C. The column was first ran with sterile saline solution devoid of any microbial contaminants for 10 minutes under UV light and then with test solution under visible light. After the filter column ran steadily for a while, the filtrate was collected and the antibacterial rate at different time intervals of a disinfection cycle was calculated by plate counting method using untreated water as a control.

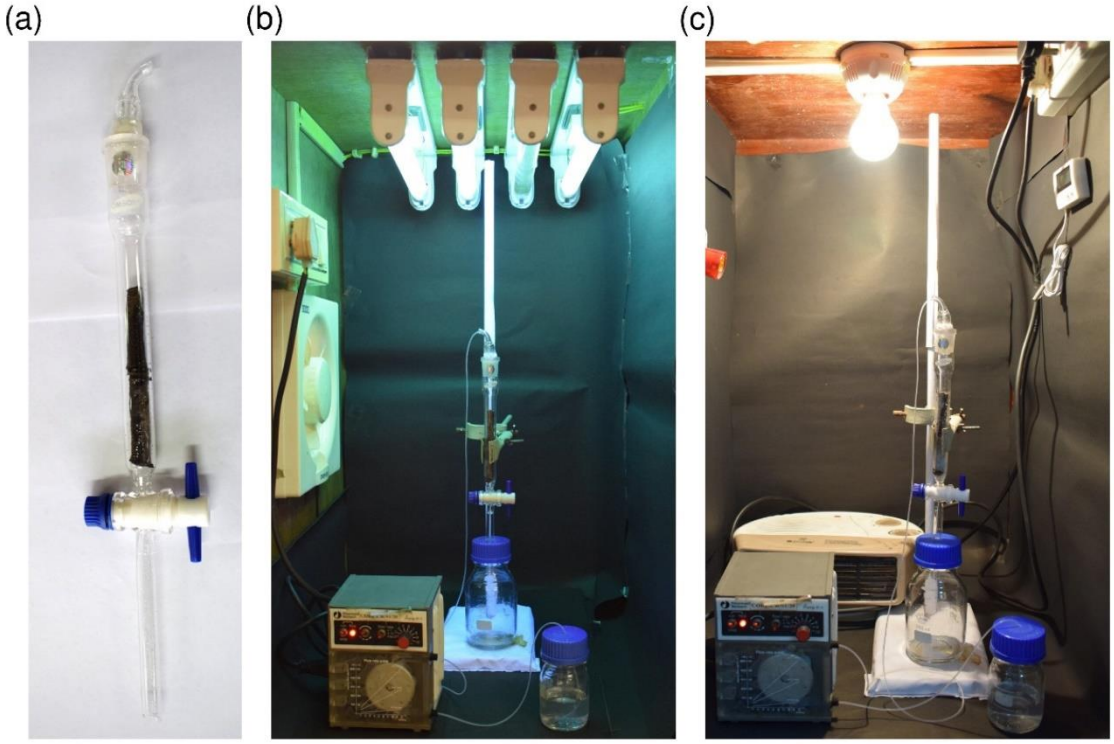

Figure 3.1 Photographic image of (a) column reactor packed with nano-silver immobilized CS/GO hydrogels. Real-time setup for (b) column sterilization under UV light, and (c) microbial disinfection under visible light.

The single variable method was adopted to successively inspect the effect on antibacterial rate of CS/GO/Ag hydrogel filter from four influencing factors such as, flow-rate (1.3-5.1 mL min^{-1}), bed height (2-16 cm), high bacterial load (10^4-10^6 CFU mL^{-1}), and reuse times (5 cycles). The effective range of individual process parameters resulting in the highest disinfection rate (%) was assessed by varying one factor while keeping the other factors constant. Subsequently, this column reactor was then employed to disinfect water from natural sources at optimized flow-rate and bed height to ensure maximum efficiency. For this purpose, the water samples were systematically collected from various sources i.e., river

water (Bhakra canal) and rain water within Patiala district, Punjab, India and analysed for water quality parameters.

3.14 Modelling Disinfection Kinetics and Statistical Analysis

The non-linear disinfection data in continuous-flow reactor were fitted to two relevant kinetic models viz. 'log-linear +shoulder' and 'Weibull' using GInaFiT, v1.6 (Excel add-in) (Buzrul 2022; Ghodsi et al. 2021; Thakur et al. 2021). The log-linear +shoulder model assumes presence of more resistant microbial subpopulation which leads to initial lag period "shoulder" on kinetic data followed by inactivation phase and microorganisms concentration after time (t), N is given by:

$$\log N = \log N_o + k.(s - t).\log(e) - \log[1 + (e^{k.S} - 1).e^{-k.t}] \quad \text{(Eq. 3.5)}$$

Where, N_0 is initial bacterial concentration, k is maximum reduction rate constant (min^{-1}), and S is shoulder length. Alternatively, Weibull model presumes microbial subpopulations as heterogeneous with varying sensitivity levels such that each cell death in the face of external stress depends upon exposure times. Here, corresponding number of surviving bacteria after treatment is described by:

$$\log N = \log N_o - (t / \delta)^{\rho} \quad \text{(Eq. 3.6)}$$

Where, δ is the first decimal reduction time (min.) and ρ is dimensionless shape parameter. The corresponding inactivation parameters were determined and comparison between goodness of fit of each model was done by assessing multiple correlation coefficients (R^2) and root mean square errors (RMSE) values. The output fitted curves were presented graphically alongside experimental data.

3.15 *In vitro* Biocompatibility Analysis

The evaluation of cytotoxicity of hydrogel composites was determined by colorimetric MTT assay according to ISO 10993–5:2009 standards (ISO 2009). Prior to this analysis, hydrogel extracts were prepared in accordance with ISO 10993–12:2021 standards (Cui et al. 2019; ISO 2021). For the purpose, CS/GO and CS/GO/Ag hydrogel fragments were added to sterilized distilled water at a concentration of ~0.3 g mL^{-1} and incubated at 37 °C for 24 h. After this period, fragments were discarded, extracts (100% and 50%) were sterilized by 0.22 µm syringe filters.

3.15.1 Cytocompatibility in Human Peripheral Blood Mononuclear Cells (PBMCs)

PBMCs were isolated from healthy human blood through density gradient centrifugation aided by HiSep™ LSM 1077. Firstly, EDTA stabilized blood diluted in 1:1 ratio with sterile PBS, was overlaid carefully on HiSep™ solution and centrifuged at 400×g for 30 minutes at 20 °C. The mononuclear cells obtained in intermediate buffy layer were harvested and washed twice with sterile PBS before their final suspension in RPMI-1640. The trypan blue dye exclusion technique determined the number of viable cells on an automated cell counter (Curiosis Facscope™ B, Korea). In a flat bottomed 96-well plate, $\sim 1\times10^6$ cells/well of PBMCs were seeded with 100% extract and 50% diluted extract, respectively in triplicates at 37 °C with 5% CO_2 for 24 h in a CO_2 incubator (Thermo Fisher Forma™, USA). Any changes in morphology were viewed and recorded under an inverted microscope at this point. Subsequently, MTT reagent (5 mg mL^{-1} in PBS solution) was added to each well plate after supernatant decantation and kept further at 37 °C for 4 h. Dimethyl sulphoxide (DMSO) was then used as a solubilizing agent to dissolve the precipitated purple formazan crystals for 15 minutes and the final product in 96-well plate was read at 570 nm using ELISA microplate reader. Untreated PBMCs were taken as experimental control and the percentage of cell viability was calculated using Equation 3.7.

$$\text{Cell Viability \%} = \left(\frac{\text{Mean OD}_{\text{Test sample}}}{\text{Mean OD}_{\text{Negative control}}} \right) \times 100 \qquad \text{(Eq. 3.7)}$$

3.15.2 Cytocompatibility in Human Hepatocellular Carcinoma (HepG2) And African Green Monkey Kidney (Vero) cells

The cell lines, HepG2 and Vero were procured from National Centre for Cell Science (NCCS), Pune (India). The cells (HepG2 and Vero) were cultured in a seeding flask at 37 °C in 5% CO_2 in Dulbecco's Modified Eagle's Medium (DMEM) supplemented with 10% (v/v) fetal bovine serum (FBS) and 1% (v/v) penicillin-streptomycin. Cells were observed after every 2-3 days and subcultured accordingly. After reaching 70-80% confluency, HepG2 and Vero cells were harvested and prepared for MTT assay. The viable cells were counted and plated at a density of 1×10^4 cells/well (HepG2); $\sim 1\times10^6$ cells/well (Vero) in 96 well culture plates. Cell viability and cytotoxicity were assessed similarly by the method described for PBMCs.

3.16 Synthesis of Chitosan/Poly(vinyl alcohol)/Graphene Oxide (CS/PVA/GO) Coatings

3.16.1 Preparation of Casting Solutions

Chitosan/poly(vinyl alcohol)/graphene oxide (CS/PVA/GO) casting solutions were prepared as follows: Graphene oxide (GO) was prepared using natural graphite flakes through a modified Hummers method as explained earlier (Zhang et al. 2010). For polymeric mixture, chitosan powder was dissolved in dilute 2.5% acetic acid solution to make 3% w/v chitosan suspension and 4% w/v PVA solution was prepared separately in distilled water. Next, a 1: 1 ratio homogenous blend of CS and PVA was prepared by stirring at 60 °C initially for 2 h at 500 rpm and then at 25 °C over the next 12 h at 250 rpm. The precalculated amounts of GO (3, 4.5, 6, and 9 mg) were added to CS/PVA polymeric mixtures so as to achieve final GO concentrations of 0.05, 0.075, 0.1, 0.15% w/v, respectively. Detailed composition of coatings is presented in Table 3.1. Chitosan/PVA without GO was employed as the experimental control for casting solution. All sample solutions were then ultrasonicated for 2 h followed by homogenization under mechanical shaking (12 h, 150 rpm).

Table 3.1: Composition of various coatings

Coatings	Composition of Coatings
CS/PVA	CS: 1.39%, PVA: 1.85%, water + acetic acid: 96.76%
CS/PVA/$GO_{0.05}$	CS: 1.39%, PVA: 1.85%, GO: 0.05%, water + acetic acid: 96.71%
CS/PVA/ $GO_{0.075}$	CS: 1.39%, PVA: 1.85%, GO: 0.075%, water + acetic acid: 96.68%
CS/PVA/ $GO_{0.1}$	CS: 1.39%, PVA: 1.85%, GO: 0.1%, water + acetic acid: 96.65%
CS/PVA/ $GO_{0.15}$	CS: 1.39%, PVA: 1.85%, GO: 0.15%, water + acetic acid: 96.61%

3.16.2 Coating Fabrication and Gravimetric Analysis

Coating Fabrication

Chitosan/poly(vinyl alcohol)/graphene oxide (CS/PVA/GO) coatings were prepared using solution casting followed by evaporation technique. In brief, film-forming solutions were cast in the circular sample holder and left for drying at 25 °C. All the experiments were carried out in an air conditioned room without any air flow and temperature of the room was

maintained at 25 ± 1 °C. Drying behaviour of the coatings was determined using gravimetrical methodology during coating preparation. Two sets of coatings with initial thicknesses of ~700 μm and ~1400 μm were prepared using sample holder with depth: 1000 μm and 3000 μm, respectively. The obtained thin-films were designated according to the final GO concentrations (% w/v) in coating solutions as CS/PVA, CS/PVA/$GO_{0.05}$, CS/PVA/$GO_{0.075}$, CS/PVA/$GO_{0.1}$, and CS/PVA/$GO_{0.15}$ and stored under ambient conditions; protected from the direct sunlight before further analysis.

Gravimetric Drying

For gravimetric analysis, weight of the empty sample holder was recorded first and then weight of the casting solution with holder was recorded as a function of time using analytical weighing balance (Precisa ES225SM-DR, Switzerland; accuracy ±0.0001g). The continuous weighing was done until drying process halted which was indicated by consecutive constant readings. Various parameters such as residual solvent percentage, thickness, average solid and solvent concentrations were calculated using equations, given at an instance where, coating solution contains final concentrations of chitosan=1.39%, PVA= 1.85%, GO= 0.05% and solvent (water + acetic acid)= 95.71% in Table 3.2. The initial mass is let "m_o" and instantaneous mass as "m" in these coating formulations.

Table 3.2: Various Parameters Calculated in Gravimetric Analysis

Parameter	Calculation Formula
Mass of chitosan	$M_c = m_o \times \frac{1.39}{100}$
Mass of PVA	$M_{PVA} = m_o \times \frac{1.85}{100}$
Mass of GO	$M_{GO} = m_o \times \frac{0.05}{100}$
Mass of solvent	$M_s = m - M_c - M_{PVA} - M_{GO}$
Volume of coating	$V_{coating}$ = chitosan vol. + PVA vol. + GO vol. + solvent vol.
Instantaneous concentration of chitosan	$I_c = \frac{M_c}{V_{coating}}$
Instantaneous concentration of PVA	$I_{PVA} = \frac{M_{PVA}}{V_{coating}}$
Instantaneous concentration of GO	$I_{GO} = \frac{M_{GO}}{V_{coating}}$
Thickness of coating	$T = \frac{V_{coating}}{\text{Cross-sectional area of sample holder}}$
Residual solvent %	$RS = \left(\frac{\text{Mass of solvent}}{\text{Initial mass of solvent}}\right) \times 100$

3.16.3 Coating Stainless Steel Substrates with CS/PVA/GO Nanocomposites

Initially, 316L stainless steel (SS) substrates (15 mm × 15 mm × 2 mm) were cleaned using a series of ultrasonic treatments. First, they were kept in 70% acetone for 15 minutes, followed by 70% ethanol and deionized water for an equal duration. Afterwards, the substrates were dried in an ambient environment and stored in a sealed container to prevent surface contamination until further use. A simple spread casting method followed by solvent evaporation was used to coat the substrates. To achieve this, 100 µL of composite coating solutions were uniformly spread onto SS substrates and dried at room temperature for 24 h. The samples were labeled according to their final GO concentration (% w/v) in the coating suspensions as follows: CS/PVA, CS/PVA/$GO_{0.05}$, CS/PVA/$GO_{0.075}$, CS/PVA/$GO_{0.1}$, and

CS/PVA/$GO_{0.15}$. All coated substrates were kept under ambient conditions, shielded from direct sunlight, until subsequent analysis. Five sets of independent experiments were also performed to evaluate the reproducibility of coating fabrication process.

3.16.4 Material Characterization

The rheological properties of the test samples were carried out with a rotational rheometer (Anton Paar RheolabQC, Austria). The measurements were carried out at temperature of 25˚C with shear rate increasing from 0^{-1} to 100 s^{-1}. The microstructures, morphology and cross-sectional surface topography of thin-film coatings were observed through scanning electron microscopy (SEM, Hitachi S-3400N, Japan). Prior to examination, each sample was sputtered with gold for making samples conductive. Fourier transform infrared spectra (FTIR, Perkin Elmer-Spectrum RX-IFTIR) was measured over the range 4000-500 cm^{-1} while Raman spectra of pristine GO were produced using a LabRam HR800 Raman spectroscope (Horiba Jobin-Yvon, France). The crystal structure and phase characterization were analyzed using wide-angle X-ray diffraction (XRD, Panalytical X'Pert Pro, The Netherlands) over a 2θ region of 5–70° with a scan rate of 2° min^{-1}. The UV transmission spectra were recorded using a UV spectrophotometer (Shimadzu UV 2600, Japan). Thermal degradation of the samples was performed via Differential Scanning Colorimetry (DSC, 131 EVO analyzer, SETARAM Instrumentation, France) with a heating/cooling rate of 20 K min^{-1} under nitrogen atmosphere. Mechanical properties of coating films (50 mm x 30 mm) were measured with Shimadzu Autograph AG100KNG universal testing machine (UTM) equipped with a 5 kN load cell with a constant rate of 1 mm min^{-1}.

3.17 Evaluation of Antimicrobial Activity of Coatings

Staphylococcus aureus and *Staphylococcus epidermidis* are one of the most commonly reported (about four cases in five) microbial species to cause biomaterial associated infections (Oliveira et al. 2018). Hence, the antimicrobial efficacy of CS/PVA/GO coatings on SS surfaces were examined against clinically relevant strains of *Staphylococcus aureus* NCIM 2127 (ATCC 9144) and *Staphylococcus epidermidis* NCIM 2493 (ATCC 12228) at various test conditions. The selection of aforementioned *S. aureus* and *S. epidermidis* strains from culture collection database was based on their established utility as *in vitro* models for quality control purposes in pharmaceutical, biomedical, and personal care applications.

3.17.1 Antibacterial Contact Assay

The surface decontamination of coated 316L surgical SS substrates was performed through UV exposure for 30 minutes in a sterilized laminar airflow chamber (Biosafety Cabinet, Thermadyne, India). In a separate experiment, a 100 µL bacterial suspension (*S. aureus* or *S. epidermidis*, $\sim 10^6$ CFU mL^{-1}) was spread onto petri plates containing nutrient agar. The coated SS substrates were carefully placed onto the surface of petri plates and incubated at 37 °C. The coated substrates were periodically removed from plates after a contact time interval of 1 h, 2 h, 4 h, and 6 h, respectively. After 24 h, the plates were monitored and again kept in incubator at 37 °C for 30 days.

3.17.2 Antibacterial Drop Test

The antibacterial efficacy of coated SS substrates was further examined using an antibacterial drop test. In brief, bacteria were inoculated into the nutrient broth media and cultured at 37 °C for 18-20 h in an incubator shaker at 150 rpm. Cultured bacteria were harvested and diluted with 1X PBS to attain $\sim 10^6$ CFU mL^{-1} as initial count for studies. A 100 µL bacterial suspension was evenly spread over the surface of coated SS substrates placed on solid agar media (coated side up). Once dried, petri plates supporting coated substrates were incubated at 37 °C for 1 h. After required incubation, bacteria attached on SS substrates were washed with 1 mL PBS, a 100 µL of which was re-spread on a fresh nutrient agar plate and incubated at 37 °C for 24 h and thereafter, used for counting bacterial colonies. The remaining washed-out bacterial suspension was immediately used for live/dead bacterial staining assay. In another independent experiment, similar steps were repeated as above to test the antimicrobial efficacy of coatings at incubation of 6 h.

3.17.3 LIVE/DEAD Bacterial Staining Assay

The bacterial cell viability was verified by a two-colour fluorescent staining test. Fluorescein diacetate (FDA) and propidium iodide (PI) fluorescence reagents were used as viable and non-viable stain probes respectively, through which survived and dead cells would fairly be distinguished. Bacterial suspension (500 µL) from the antibacterial drop test was incubated with FDA/PI stains for 15 minutes under dark. A fluorescence microscope (Nikon Eclipse50i, Japan) was used to capture images of live/dead bacteria where, viable cells were viewed under FITC mode at λ_{ex} 465-495 nm) and non-viable cells under TRITC mode at λ_{ex} 532-554 nm.

3.18 Mechanism(s) of Antibacterial Action of Coatings

3.18.1 Assessment of Morphological Damage

Bacterial strains (*S. aureus* and *S. epidermidis* each, 10^6 CFU mL^{-1}) were exposed to CS/PVA/GO coated SS substrate (15 × 15 mm^2) for 6 h at 37 °C to investigate any ultra-structural changes in bacterial cells, after direct contact with antibacterial coatings. Bacteria exposed to pristine SS substrate were used as positive control. After the required treatment, bacterial pellet was harvested by centrifugation at 5000 rpm for 10 minutes and washed twice with 1X PBS solution. The cells were fixed in PBS suspension containing 2.5% glutaraldehyde (500 µL) for 3 h. After primary fixation, cells were centrifuged at 5000 rpm and rinsed twice with PBS. Cells were completely dehydrated with a graded ethanol series (30%, 50%, 70%, 90%, and 100%) for 15 minutes each (Huang et al. 2017). A 10 µL aliquot was drop casted on a SS surface (5 mm × 5 mm), dried under laminar air-flow and immediately analysed using field emission gun scanning electron microscopy (FEG-SEM).

3.18.2 Determination of Reactive Oxygen Species (ROS)

The level of ROS generation in bacterial cells was determined using nitro-blue tetrazolium (NBT) reduction assay with slight modifications (Marathe et al. 2013). *S. aureus* and *S. epidermidis* suspensions (10^6 CFU mL^{-1}) were initially cultured at 37 °C for 6 h in the presence of CS/PVA/GO coatings. Bacterial cells incubated in the absence of any material was taken as negative control. Thereafter, 375 µL of NBT solution (1 mg mL^{-1}) was added to the cell suspensions and incubated at 37 °C for 30 minutes. The reaction was terminated by adding 75 µL of 0.1M HCl and bacterial suspensions were recovered by centrifugation at 5000 rpm for 10 minutes. The obtained bacterial pellets were treated with 300 µL dimethyl sulfoxide (DMSO) to extract the reduced NBT. Finally, the extracted solutions were diluted with 300 µL PBS and the optical density of bluish-violet formazan was recorded at 575 nm.

3.18.3 Protein Leakage Assay

The quantitative estimation of intracellular protein leakage from bacterial cells was carried out using Bradford's assay (Fang et al. 2019). The coating substrates were incubated with bacterial cells (10^6 CFU mL^{-1}) at 37 °C for 6 h in an incubator shaker. From each test vial, 1 mL of treated culture aliquot was withdrawn and centrifuged at 6000 rpm, 4˚C for 30 minutes. The supernatant was treated with Bradford's reagent (5 mL) for 5 minutes and the

corresponding absorbance was measured at 595 nm. The protein concentration was determined using a standard curve of bovine serum albumin.

3.18.4 Lactate Dehydrogenase (LDH) Release Assay

The intensity of LDH release was determined by the stoichiometric conversion of iodonitrotetrazolium chloride to iodonitrotetrazolium formazan at 490 nm spectrophotometrically, due to the formation of NADH (Kroll et al. 2012). For microplate assay, bacterial cells ($\sim 10^6$ CFU mL^{-1}) were exposed to coating samples for 6 h at 37 °C. After this duration, samples were transferred to microcentrifuge tubes and centrifuged at 1200 rpm for 5 minutes. A 60 µL supernatant was transferred to a 96-well plate onto which 180 µL LDH reagent was added to each well and incubated for 30 minutes at 25 °C. After incubation, the optical density of each well was recorded at 490 nm on an ELISA reader. A 0.85% saline suspension and 0.1% Triton X-100 were taken as negative and positive controls, respectively. The % LDH release was calculated using OD_{490} values in Equation 3.8. The LDH activity of positive control was considered 100% and activity of all other test samples was calculated relatively.

$$\text{LDH Release \%} = \left(\frac{\text{Mean OD}_{\text{Test sample}} - \text{Mean OD}_{\text{Negative control}}}{\text{Mean OD}_{\text{Positive control}} - \text{Mean OD}_{\text{Negative control}}} \right) \times 100 \qquad \text{(Eq. 3.8)}$$

3.19 Biocompatibility Analyses

3.19.1 Hemocompatibility

To assess the biocompatibility of the coatings with blood, a hemolytic assay was performed using human red blood cells (RBCs), following a previously reported method with minor modifications (Eivazzadeh-Keihan et al. 2021; Shamszadeh et al. 2022). In brief, RBCs were isolated from fresh human blood by centrifugation (4000 rpm, 5 minutes), washed three times with PBS buffer, and diluted to a final concentration of 5% (v/v) in 1X PBS. A 500 µL RBC suspension was added to each vial containing coating samples (10×10 mm^2; 6.83 mg). Positive and negative controls were prepared using 0.1% Triton X-100 and sterile PBS solutions, respectively. All samples were incubated in a shaking incubator (100 rpm) at 37 °C for 1 h. After incubation, the coatings were physically removed and the remaining contents in the vials were centrifuged (2000 rpm, 10 minutes). The extent of hemolysis in the samples was calculated by measuring the absorbance (540 nm) of the supernatant using Equation 3.9.

The degree of hemolysis (%) in the coatings was determined by using the biomaterial hemolytic index values (H) established in the guidelines of the American Society of Testing and Materials (ASTM) F756-00.

$$\text{Hemolysis \%} = \left(\frac{\text{Mean OD}_{\text{Test sample}} - \text{Mean OD}_{\text{Negative control}}}{\text{Mean OD}_{\text{Postive control}} - \text{Mean OD}_{\text{Negative control}}} \right) \times 100 \qquad \text{(Eq. 3.9)}$$

3.19.2 Cytocompatibility in Human Peripheral Blood Mononuclear Cells

The MTT assay was used to determine the cytotoxicity of CS/PVA/GO coatings against human peripheral blood mononuclear cells (PBMCs). PBMCs were isolated from a healthy human blood through density gradient centrifugation with HiSep™ LSM 1077 (Valliammai et al. 2021). First, EDTA-stabilized blood was diluted in 1:1 ratio with sterile PBS (pH 7.2), then overlaid carefully on HiSep™ solution and was centrifuged (400×g, 20 °C) for 30 minutes. After centrifugation, the intermediate buffy layer containing PBMCs was harvested and washed twice with sterile PBS before suspending cells in RPMI-1640. The number of viable cells were determined by trypan blue dye exclusion technique on an automated cell counter.

For MTT assay, suspensions soaked with each of the coating films at varied concentrations of 2, 4, 6 mg mL^{-1} were prepared first. Then ~1×10^6 cells/well were seeded along with the coating suspensions and incubated at 37 °C with 5% CO_2 for 24 h in a CO_2 incubator. At this point, any changes in morphology were viewed and recorded under an inverted microscope. After required treatments, the supernatants were discarded and MTT reagent (5 mg mL^{-1} in PBS solution) was added to each well and again kept further at 37 °C for 4 h. The MTT solution was then removed, and DMSO was added to each well to dissolve the formazan crystals. The absorbance of the solubilized formazan was measured at 570 nm using a microplate reader. Cell viability was expressed as a percentage of viable cells in comparison to the untreated control cells (Equation 3.10).

$$\text{Cell Viability \%} = \left(\frac{\text{Mean OD}_{\text{Test sample}}}{\text{Mean OD}_{\text{Negative control}}} \right) \times 100 \qquad \text{(Eq. 3.10)}$$

3.19.3 Cytocompatibility in Human Hepatocellular Carcinoma Cells (HepG2)

The HepG2 cells were cultured in a seeding flask at 37 °C in 5% CO_2 in Dulbecco's Modified Eagle's Medium supplemented with 10% (v/v) fetal bovine serum and 1% (v/v) penicillin-streptomycin. The cell culture was monitored after every 2-3 days and adherent cells were detached by trypsinization in between sub-cultures. After attaining 60-80% confluency, HepG2 cells were harvested and prepared for MTT assay. The viable cells were counted and plated at a density of 1×10^4 cells/well in a 96-well plate. Cell viability and cytotoxicity were assessed similarly, as described for PBMCs.

3.20 Degradation of Coatings in Simulated Biological Fluid

The coated substrates were subjected to hydrolytic degradation analysis in a simulated biological fluid (SBF) in compliance with ASTM F1635-16 standards. The SBF was prepared using an established procedure mentioned in (Kokubo and Takadama (2006)). The coated samples were immersed in 15 mL of SBF and incubated at 37 °C for the desired time periods (1, 3, 7, 10, and 14 days). Prior to immersion, the initial dry weight of each sample (W_o) was determined while weight after immersion was designated as 'W'. The dry weight of uncoated SS substrate was recorded as 'W_b'. SBF was replaced every 24 h and its pH value was measured every day. The degradation rate was then calculated as the percentage weight loss after specific period using Equation 3.11. Finally, the dried coatings were analysed through FE-SEM to evaluate the extent of degradation and its effects on their morphology.

$$\text{Weight Loss \%} = \left(\frac{W_o - W}{W_o - W_b}\right)\times 100 \qquad \text{(Eq. 3.11)}$$

3.21 Statistical Analyses

All experiments were performed in triplicates and results were expressed as mean ±standard deviation values. Data were evaluated for statistical significance by analysis of variance (ANOVA), followed by Tukey's Multiple Comparison Test, $p < 0.05$ using GraphPad Prism 8.0.1 software.

Chapter 4

Results and Discussion

4.1 Nano-silver loaded Chitosan-Poly(vinyl alcohol)-Silver (CS/PVA/Ag) Hydrogel

The schematic representation of synthesizing silver nanoparticles onto chitosan-PVA hydrogel is shown in Figure 4.1. An *in situ* approach was employed for loading nano-silver where most of the Ag^+ ions were exchanged from the solution into hydrogel networks by anchoring through functional groups of polymers while remaining silver ions were occupied within the semi-interpenetrating networks of the CS/PVA hydrogel.

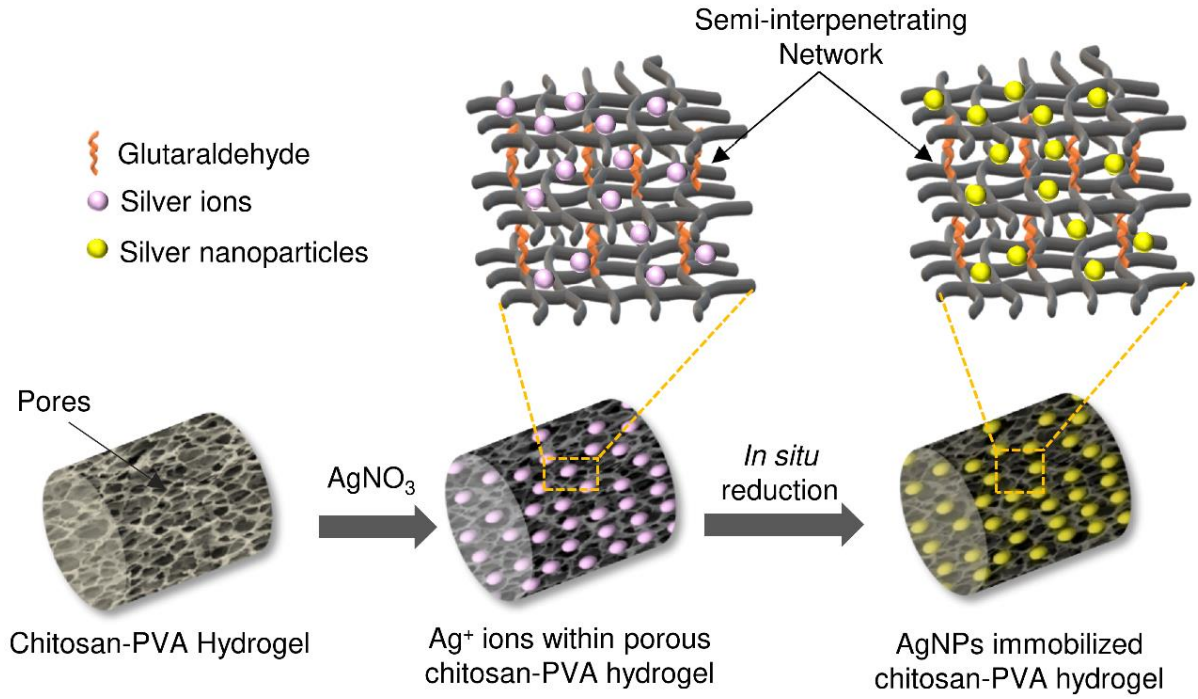

Figure 4.1 Schematic representation of chitosan-PVA hydrogel acting as nano reactor for synthesizing silver nanoparticles and their subsequent immobilization within the semi interpenetrating network of hydrogel.

In fact, amine and hydroxyl functional moieties naturally present within the CS/PVA hydrogel acted as nucleation sites, allowing stable anchoring of silver ions which were progressively reduced into AgNPs through a suitable reducing agent (Agnihotri et al. 2012). The precipitated CS/PVA hydrogel initially changed from golden yellow to opaque yellow in colour with development of porous network structures after freeze-thaw treatment (Figure 4.2a-b). The light yellow coloured hydrogel subsequently turned brownish black after reduction which could be ascribed to *in situ* formed AgNPs and their eventual immobilization within the porous networks (Figure 4.2c). The polymeric network of CS/PVA thus served the

dual role, both as a reactor for synthesizing AgNPs in concurrent with providing a template for their subsequent immobilization.

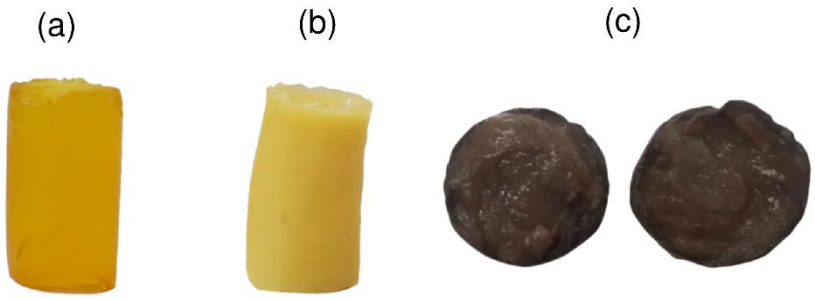

Figure 4.2 The photographic image of pristine chitosan-PVA hydrogel (a) before (b) after freeze-thaw treatments for generating porous morphology and (b) AgNPs loaded chitosan-PVA hydrogel (cross-section).

4.1.1 Characterization of Chitosan/PVA/AgNPs Hydrogel

In situ immobilization of AgNPs onto CS/PVA hydrogel was evaluated through diffuse reflectance spectroscopy (Figure 4.3a). It is evident while AgNPs-immobilized hydrogel displayed a distinct Surface Plasmon Resonance at 421 nm, which confirmed the successful loading of nano-silver, no such extinction peak was observed in pristine CS/PVA hydrogel. A full width at half maximum (FWHM) value of 122 indicated that silver would have uniformly distributed throughout the surface of CS/PVA hydrogel in its nanoparticulate form. Further, the stability of CS/PVA/Ag hydrogel was evaluated over a period of 5 five months where no significant variation in its original SPR or FWHM value was observed.

The FTIR spectra of chitosan-PVA hydrogel before and after immobilizing AgNPs were also compared (Figure 4.3b). An absorption peak at 3280 cm^{-1} corresponds to the characteristics OH and/or NH stretching vibrations, appeared in both variants of CS/PVA hydrogel due to intermolecular hydrogen bonding between two polymeric residues. Besides, a new vibrational band at 3450 cm^{-1} appeared in CS/PVA/AgNPs hydrogel which confirms that AgNPs were firmly bonded to hierarchical networks of chitosan/PVA hydrogel during their synthesis and growth stages. Similarly, a few other characteristic peaks at 2925 cm^{-1}, 1453 cm^{-1} and 1323 cm^{-1} appeared in both hydrogel forms, which could be ascribed to CH stretching, CH bending and CN stretching in polymeric template respectively, and remain unaltered even after loading AgNPs. Interestingly, the peak at 1674 cm^{-1} in pristine chitosan-PVA, which is

attributed to carbonyl (-C=O) bond stretching (Yang et al. 2004) not only appeared with reduced intensity in CS/PVA/Ag hydrogel, but it also shifted to a lower frequency, i.e., 1638 cm^{-1}. This clearly indicates though stronger intermolecular interactions occurred between hydroxyl groups of PVA and hydroxyl/amine groups of chitosan while forming hydrogel, many free -OH and $-NH_2$ moieties would still be available as nucleation sites to Ag^+ ions for their *in situ* synthesis in concurrent with their immobilization. It is worth noting that the absorption band at ~1100 cm^{-1} refers to the crystallization sensitive peak of PVA, which appeared in both pristine and Ag loaded hydrogel with same intensity. This validates that incorporating AgNPs did not alter the overall crystallinity of PVA in the blend polymer.

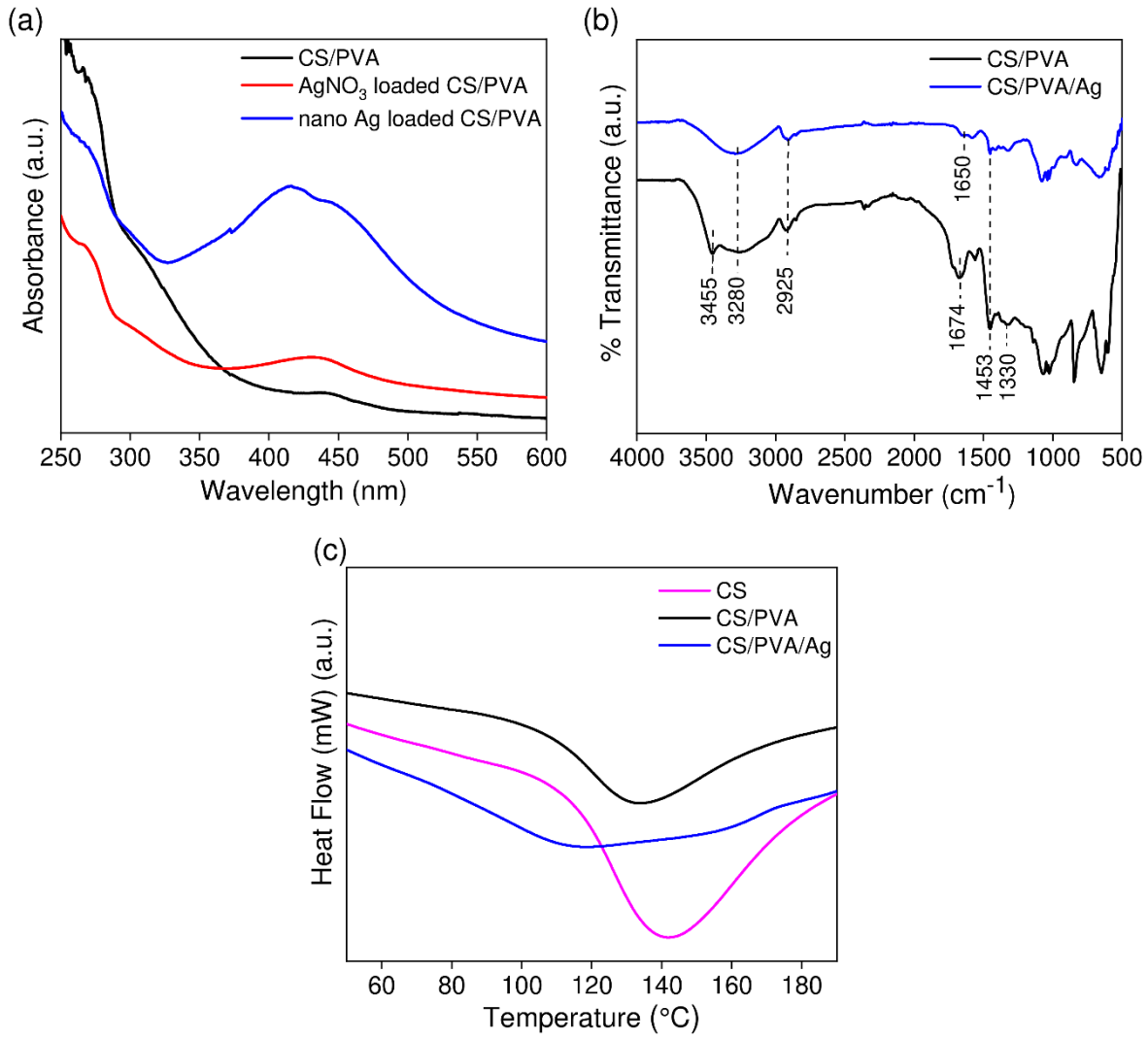

Figure 4.3 Characterization of pristine, ionic silver and nano-Ag loaded CS/PVA hydrogels through (a) Diffuse reflectance spectroscopy, (b) FTIR, and (c) Differential scanning calorimetry (DSC).

Dried hydrogels were investigated using differential scanning calorimetry (DSC) to determine its miscibility and water retention characteristics (Figure 4.3c). The thermogram profile of pure chitosan exhibited its typical dissociation peak at 150 °C, which noticeably reduced to 144 °C after blending with PVA. This is a clear indication of strong hydrogen-bonding between chitosan and PVA polymeric residues (Chuang et al. 1999). In contrast, immobilizing AgNPs on to CS/PVA hydrogel resulted to a significant loss in thermal characteristics (dissociation peak 80 °C), which occurred due be the fact that incorporated AgNPs would have minimized the interactions between water moieties and hydrogel structure. Nevertheless, a good miscibility between AgNPs and CS/PVA blend composites are in good accord with our previous study where incorporation of nanoparticles reduced the overall hydrophilicity of the nanocomposite hydrogel (Agnihotri et al. 2012).

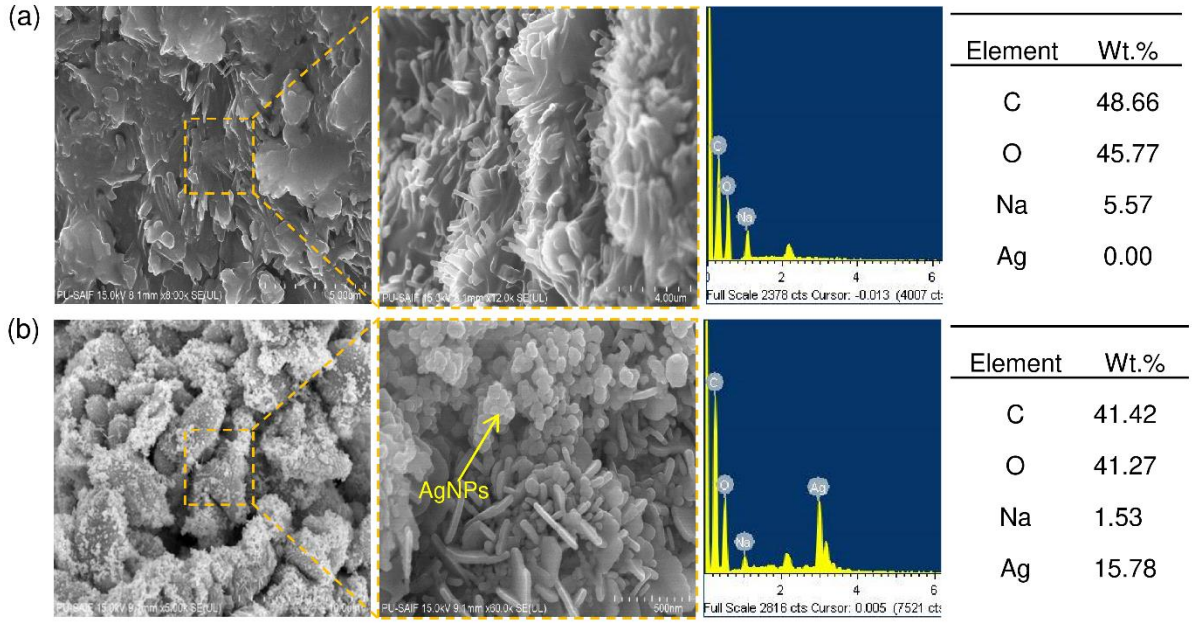

Figure 4.4 FE-SEM micrographs of two forms of hydrogel composites *i.e.* (a) pristine and (b) *in situ* synthesized AgNPs showing surface morphology distinctions as a result of localized, dense immobilization of nano-silver.

The optical characteristics corroborated with electron microscopy (FE-SEM) analyses, where hydrogel nanocomposites depicted a distinct variation in surface topography after immobilizing AgNPs (Figure 4.4a-b). The *in situ* immobilized AgNPs existed in aggregated form, uniformly distributed over the entire surface of CS/PVA with high density (15.8 % by weight) as depicted through EDX analyses. The characteristics peaks of carbon (C), sodium

(Na) and oxygen (O) elements appeared due to the chitosan/PVA polymeric blend, a peak at ~2.93 KV further validated the existence of silver as AgNPs. It is clear that such a uniform dispersion of AgNPs did not affect the overall structural integrity of CS/PVA hydrogel and yielded a stable intercalation of AgNPs within their semi-interpenetrating networks. Rather, an enhancement in tensile strength would be anticipated after incorporating AgNPs in CS/PVA hydrogel (Xu et al. 2019).

4.2 Swelling Capacity of Hydrogel Composites

The results for time-dependent and temperature-dependent swelling kinetics are demonstrated in Figure 4.5. Both pristine and AgNPs-loaded hydrogel swelled rapidly and attained maximum swelling i.e., equilibrium within 60 minutes under the tested conditions (at 25 °C, pH 7). The swelling behavior of both hydrogel forms indicated that it could carry a large volume of water while maintaining its structural integrity and strength. Interestingly, CS/PVA/Ag hydrogel demonstrated reduced swelling capacities (67.2 ± 5.9%) than their pristine form (52.5 ± 3.6%). This is ascribed to the reduction in surface functional-moieties of CS/PVA polymer after incorporating AgNPs, which became less available for water molecules to form stable hydrogen bonding such that the diffusion of water inside the hydrogel was critically hindered.

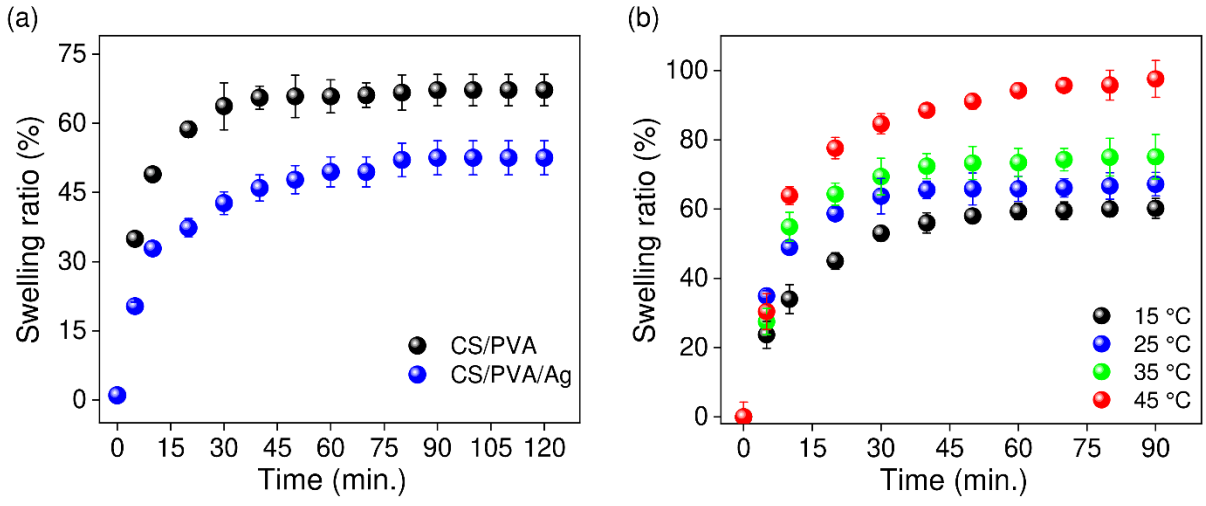

Figure 4.5 (a) Dynamic swelling behaviour of two hydrogel variants under ambient conditions (20% relative humidity, pH 7, 25 °C) and (b) Temperature dependent swelling kinetics of Ag-loaded chitosan-PVA hydrogel at wide temperature range typically manifested in Indian subcontinent.

The temperature-dependent swelling kinetics of CS/PVA/Ag hydrogel was also evaluated at pH 7 under a broad temperature range (15-45 °C), typically manifested within Indian subcontinent in a year (Figure 3b). Results indicated that the swelling ratio of hydrogel increased with increasing temperature of the gel. The Ag loaded CS/PVA hydrogels exhibited a temperature-responsive swelling behaviour due to reversible association/dissociation of hydrogen bonding within the semi-interpenetrating networks (Kim et al. 2005).

4.3 Disinfection Studies of Nano-Silver Loaded Chitosan-PVA Hydrogel

4.3.1 Disc Diffusion Assay

The biocidal effects of CS/PVA/Ag hydrogels were primarily tested against four bacterial strains with diverse pathogenicity in solid agar medium. As earlier reported (Agnihotri et al. 2012; Agnihotri et al. 2014), the antibacterial activity of CS/PVA/Ag hydrogel was compared with its pristine form using disc diffusion methods (Figure 4.6) and the data is summarized in Table 4.1.

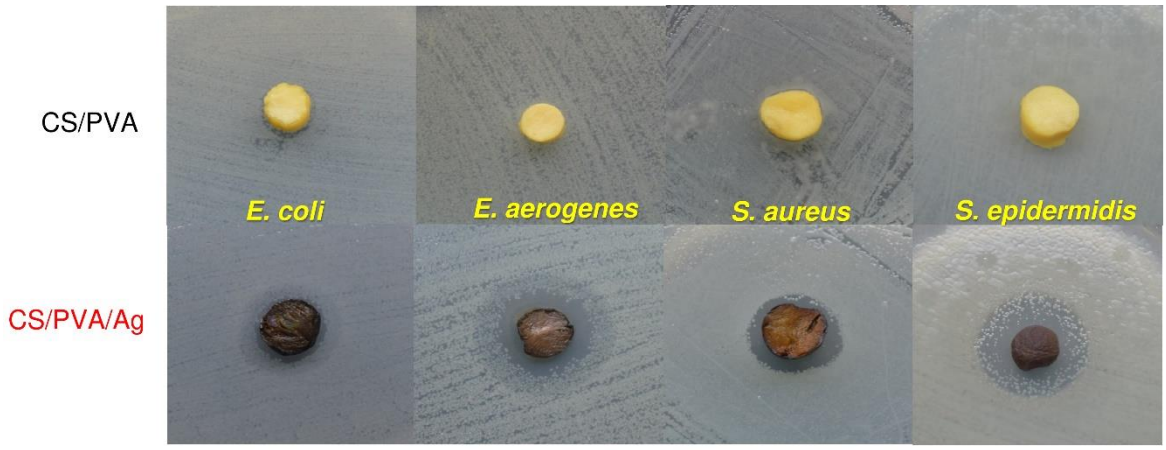

Figure 4.6 Disc diffusion tests for comparing the antibacterial activity of hydrogel before and after immobilizing silver nanoparticles (CS/PVA/Ag) in solid media.

It is evident that pure CS/PVA hydrogel did not elicit any visible zone of inhibition (ZoI) and even the presence of chitosan having inherent antimicrobial characteristics could not contribute towards biocidal activity. On contrary, the CS/PVA/Ag hydrogel showed a distinct antibacterial activity against all four tested microorganisms having ZoI ranging from 13 to 21 mm. A clear ZoI in solid agar media is indicative of the mobility of Ag^{+}/AgNPs from hydrogel in an amount sufficient to inhibit the growth of microbes present in the surrounding

regions. Out of the selected strains, *E. coli* and *S. epidermidis* appeared to be the least and most sensitive bacterial species respectively, against the Ag-reinforced hydrogel.

Table 4.1 The comparative values of zone of inhibition (ZoI) appeared in disc diffusion tests of pristine and Ag-loaded chitosan-PVA hydrogel against four representative bacterial strains.

Sample	**Zone of Inhibition (ZoI, mm)**			
	E. coli	*E. aerogenes*	*S. aureus*	*S. epidermidis*
CS/PVA	Nil	Nil	Nil	Nil
CS/PVA/Ag	13.29 ± 0.27^{d}	17.55 ± 0.67^{b}	16.08 ± 0.53^{c}	21.14 ± 0.19^{a}

Mean values displaying different letters within the treatment are significantly different at $P < 0.05$

4.3.2 Colony Forming/count Assay

The disinfection performance of hydrogels was further evaluated in liquid medium at a fixed initial bacterial concentrations of 10^3 CFU mL^{-1} in a 100 mL batch reactor (Figure 4.7a-d). We found that the CS/PVA hydrogel devoid of immobilized AgNPs could not elicit 100% killing against all four strains even after 4 h under similar environment (Figure 4.8). In contrast, CS/PVA/Ag hydrogel were bactericidal against all four strains, where complete disinfection could be achieved within 2-3 h for all the tested conditions (Figure 4.9). Comparing all bacterial strains, although CS/PVA/Ag hydrogel appeared to be more effective against natural water contaminants i.e., *E. coli* and *E. aerogenes*, it was equally biocidal towards the bacterial species associated with biomedical infections, *i.e.*, *S. aureus* and *S. epidermidis* with a marginal delay in time by only 60 minutes.

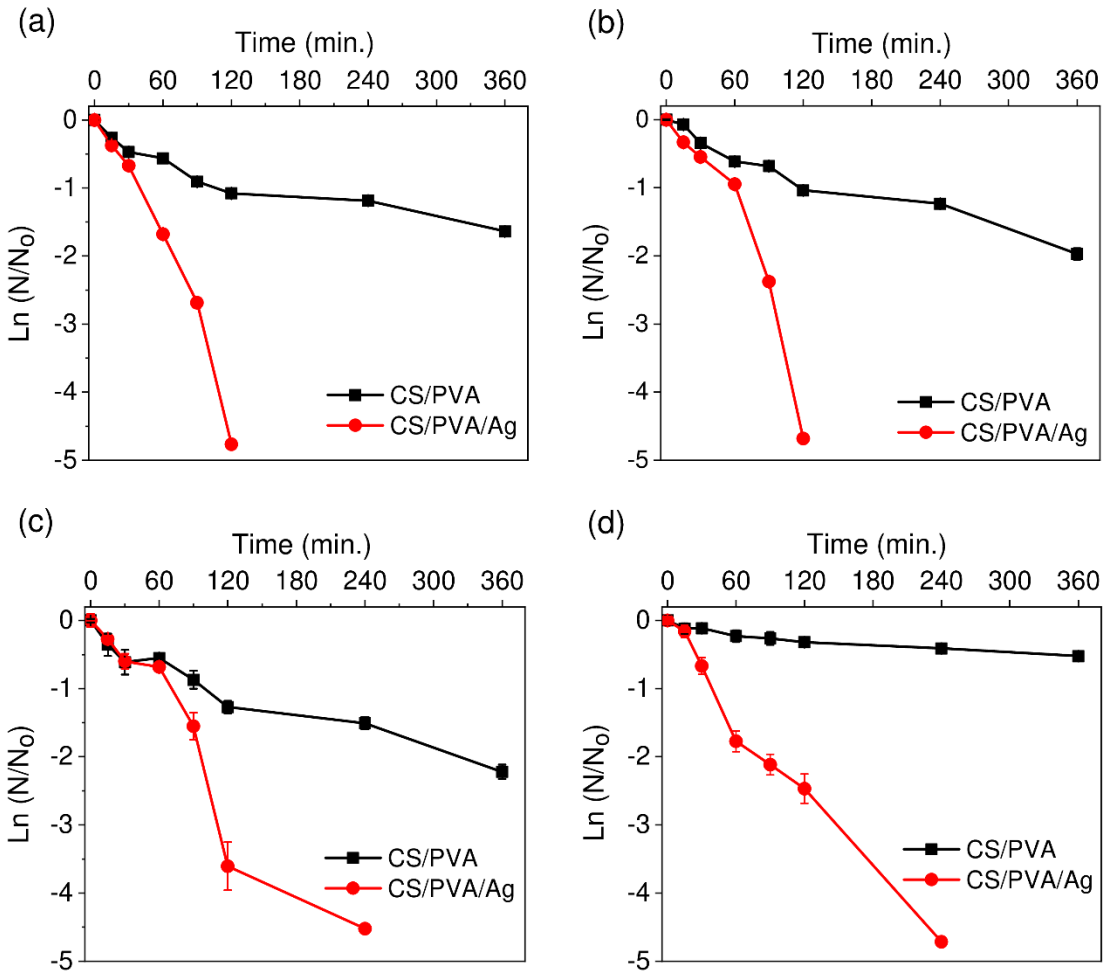

Figure 4.7 The strain-specific disinfection potential of hydrogels was evaluated in liquid suspension against four strains (a) *E. coli* MTCC 739 (b) *E. aerogenes* NCIM 5139 (c) *S. aureus* NCIM 2127 and (d) *S. epidermidis* NCIM 2493 as representatives for water and biomedical contamination. (N_o = Initial bacterial concentration, N = bacterial concentration after treatment, CFU mL^{-1}).

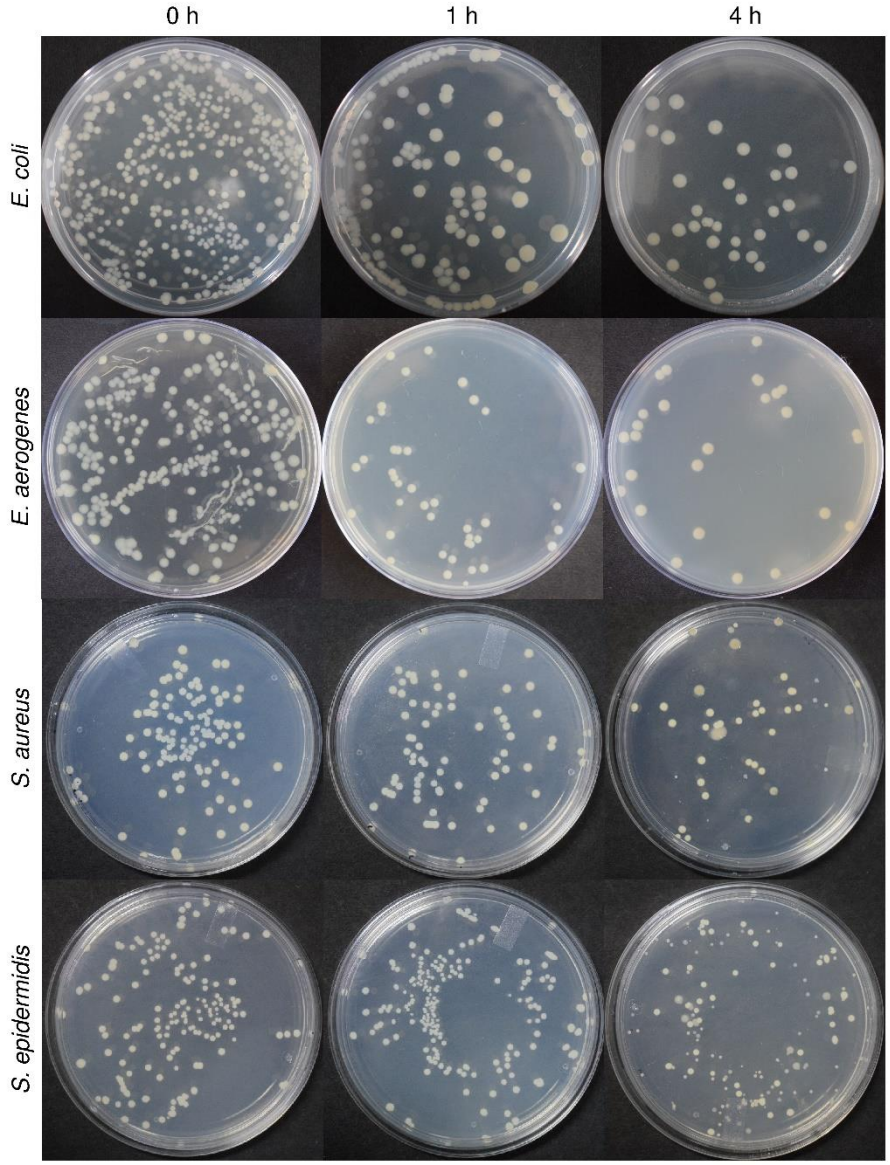

Figure 4.8 The comparative rate of reduction in bacterial viability was evaluated after treating with pure chitosan-PVA hydrogel disc (10 mm diameter) in a simulated potable water suspension (100 mL) having an initial bacterial concentration of 10^3 CFU mL^{-1}. The disinfection studies were performed against *E. coli*, *E. aerogenes*, *S. aureus*, and *S. epidermidis* plated on nutrient agar at time intervals of 0, 1, and 4 h under similar conditions.

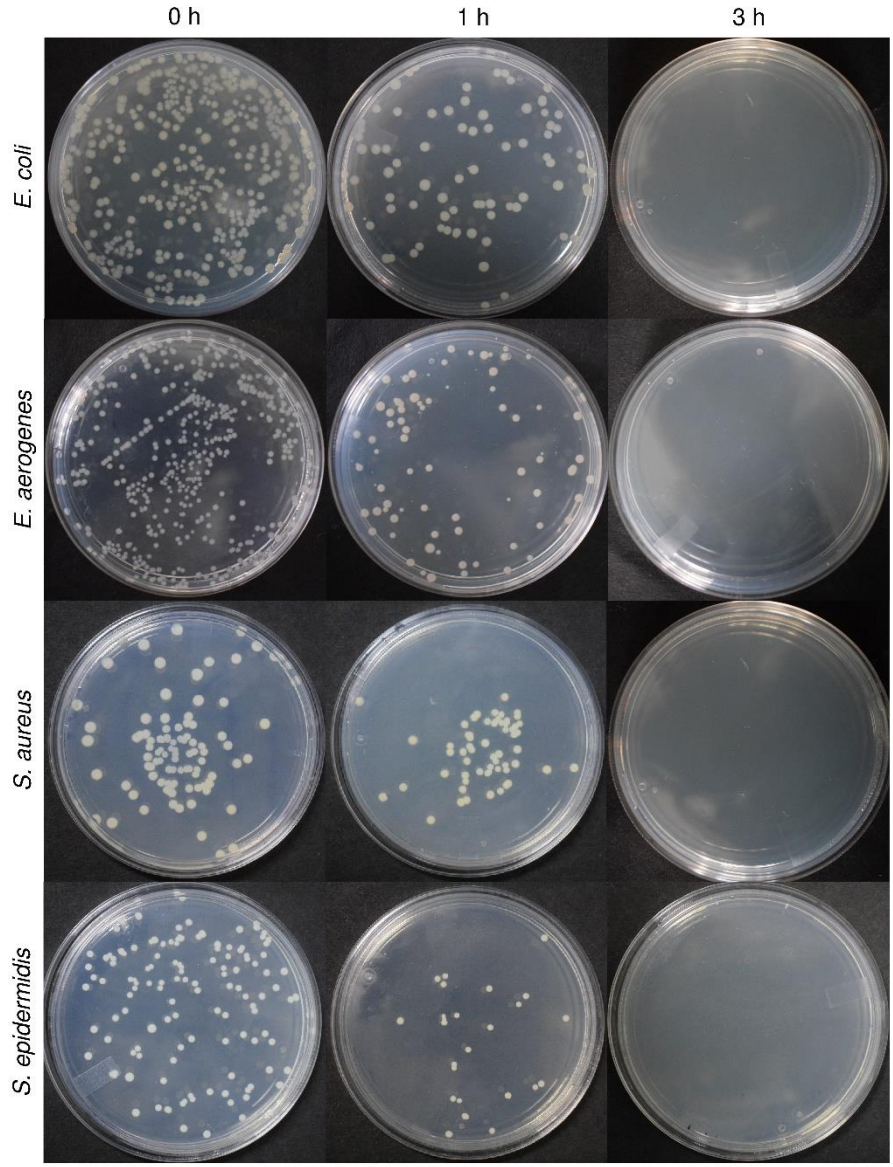

Figure 4.9 The comparative rate of reduction in bacterial viability was evaluated after treating with chitosan-PVA/Ag hydrogel disc (10 mm diameter) in a simulated potable water suspension (100 mL) having an initial bacterial concentration of 10^3 CFU mL^{-1}. The disinfection studies were performed against *E. coli*, *E. aerogenes*, *S. aureus*, and *S. epidermidis* plated on nutrient agar at time intervals of 0, 1, and 3 h under similar conditions.

We also evidenced a distinct strain-specific disinfection potential of CS/PVA/Ag hydrogel where the sensitivity of various bacterial species followed an order: *E. coli*~ *E. aerogenes* > *S. aureus* >*S. epidermidis* (Figure 4.10a). Even at higher bacterial concentrations (10^4-10^6 CFU mL^{-1}), > 90% microbial killing could be achieved against *E. coli* using CS/PVA/Ag hydrogel and inhibited ~80% *S. aureus* cells at similar initial bacterial counts (Figure 4.10b).

Although similar extent of disinfection could be achieved within 120 minutes against *E. coli* and *E. aerogenes* whereas, it was prolonged to 4 h for both *S. aureus* and *S. epidermidis* microbial strains. These results, therefore suggest an excellent disinfection performance of CS/PVA/Ag hydrogel for a wide range of bacterial population.

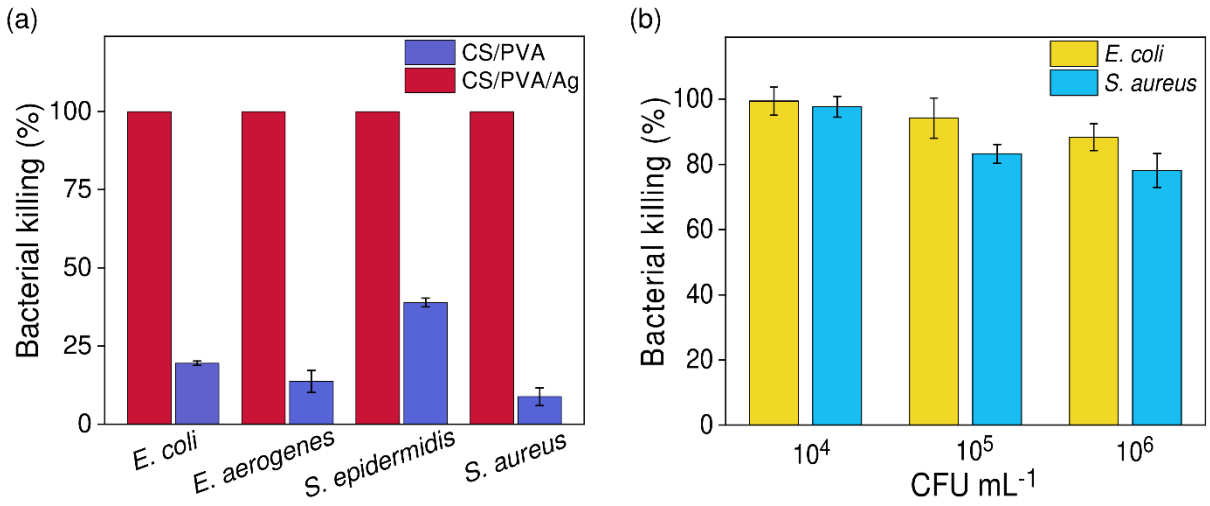

Figure 4.10 (a) A comparative disinfection ability of hydrogels tested under ambient physico-chemical conditions and (b) Disinfection performance of Ag-loaded hydrogel at higher initial bacterial concentration (10^4-10^6) against two bacteria, *E. coli* and *S. aureus*.

4.4 Reusability of Hydrogel Nanocomposites, Silver Release Profile and Mechanism of Action of Disinfection

4.4.1 Reuse Potential of CS/PVA/Ag Hydrogel Nanocomposite

The capacity to reuse hydrogel is an important feature to claim its sustainable affordability for water disinfection purposes. As shown in Figure 4.11a, CS/PVA/Ag hydrogel could retain ≥99.5% biocidal activity against *E. coli* for 8 repeated use and was marginally reduced to ~92% over the next two cycles. The Ag-loaded hydrogel appeared to be less effective against *S. aureus* where the residual activity of hydrogel was progressively reduced after every use. The disinfection performance of hydrogel at 6th usage attained its threshold value, after which biocidal activity was sharply declined to ~32%. At first instance, a higher retention of antibacterial activity of hydrogels against Gram-negative bacteria, *E. coli* than Gram-positive bacteria (*S. aureus*) appeared to be the result of their strain-selective biocidal performance. However, a thorough analysis justifying the variation in disinfection performance against

different strains may provide some useful insights about the mechanism of bactericidal action of hydrogel during disinfection.

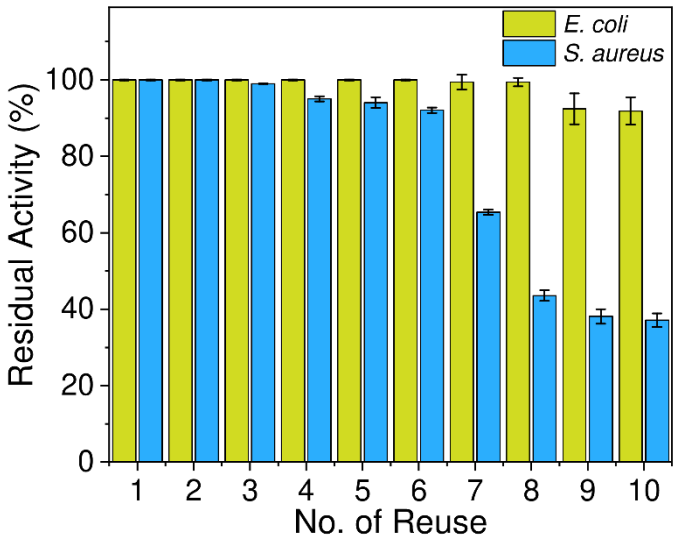

Figure 4.11 The disinfection potential of Ag-loaded chitosan PVA hydrogel on multiple reuses determined over 10 cycles against *E. coli* and *S. aureus* as representatives of water and biomedical contaminants, respectively.

It is well known that the presence of peptidoglycan layer on the cell wall of *S. aureus* makes them more resistant to withstand harsh environment, toxins, chemicals and even antibacterial agents, as compared to *E. coli* cells (Kubo et al. 2018). Moreover, *S. aureus* belong to sessile, adherent microbial communities which rapidly form multilayer biofilm virtually over all surfaces making them resistant towards the contact-active antibacterial action (Archer et al. 2011). We also speculated that after 6 repeated uses, the formation of similar stagnant biofilm of *S. aureus* over hydrogel could be the responsible cause for reduction in its biocidal activity. Possibly, the establishment of *S. aureus* biofilm could adversely affected the outer, exposed surface of porous hydrogel such that water along with microbial contaminants could not get diffused in interiors of the hydrogel causing a lower direct-contact between bacterial cells and the immobilized AgNPs. Such results are in agreement with a recent study by Agnihotri et al. (2019), where immobilized AgNPs over silica surfaces have shown a significant reduction in disinfection performance.

4.4.2 Silver Release and Mechanism of Action of Disinfection

The practical viability of silver nanocomposites for potable water applications is greatly linked to the extent of release of silver into the aqueous systems. Due to its adverse eco-toxicological effects, we analysed the silver content of treated water in two different conditions, first when incubated in aqueous environment over a longer period of time and second, after every reuse. The total amount of silver content in CS/PVA/Ag hydrogel was measured as 9.47 mg g^{-1} hydrogel through ICP-AES. As predicted, the release characteristics of hydrogel exposed for long-duration (up to 7 days) in deionized water indicated a strong anchoring of *in situ* synthesized AgNPs within hydrogel networks where, the amount of silver released was determined as 0.08 ± 0.005% and 0.41 ± 0.007% of total loaded Ag after 2nd and 7th day of incubation, respectively (Figure 4.12a). Further, we evaluated the corresponding silver release from the hydrogel after each reuse (Figure 4.12b). The maximum amount of silver in effluent was measured as 74.3± 4.2 ppb after 10th use, which falls below the permissible limit of Ag in drinking water (100 ppb) as per USEPA and WHO guidelines (WHO 2011). Although the amount of Ag released in suspension was increased after every use, the rate of silver release profile was progressively reduced after repeated usage and eventually saturated after 8th reuse.

We hypothesize that silver release kinetics is mediated via a two-step process of oxidative dissolution of immobilized AgNPs under ambient conditions. First, a rapid diffusion of water inside porous hydrogel inevitably facilitates reaction between the surface exposed silver atoms (Ag^0 as AgNPs) with dissolved oxygen. This results in the formation of silver (I) oxide, Ag_2O layer as surface passivation over AgNPs at sub-nanoscale. The silver oxide layer acts as a reservoir of silver ions, which get released into the system till the oxidative dissolution of Ag_2O continues as shown below:

$$4Ag^0_{(s)} + O_{2(aq)} \xrightarrow{\text{Oxidation}} 2Ag_2O_{(s)} \qquad \text{(Eq. 4.1)}$$

$$2Ag_2O_{(s)} + 4H_3O^+_{(aq)} \xrightarrow{\text{Dissolution}} 4Ag^+_{(aq)} + 6H_2O_{(aq)} \qquad \text{(Eq. 4.2)}$$

Therefore, an overall high rate of release of silver during early stages of hydrogel use can be explained through diffusion-limited process in which, AgNPs lying at the surface of hydrogel were preferentially solvated due to short-diffusion pathways. It is imperative that water diffusion within interiors of the hydrogel networks would be adversely affected upon

repeated usage. This might resulted in an increasingly tortuous pathway for water molecules to reach the rest of deeply buried AgNPs and carrying their oxidative dissolution. As a result, water molecules would be slowly-diffused inside the more compact, denser regions of the polymeric hydrogel and elicited a reduced rate of silver release in subsequent uses, as evidenced in this study.

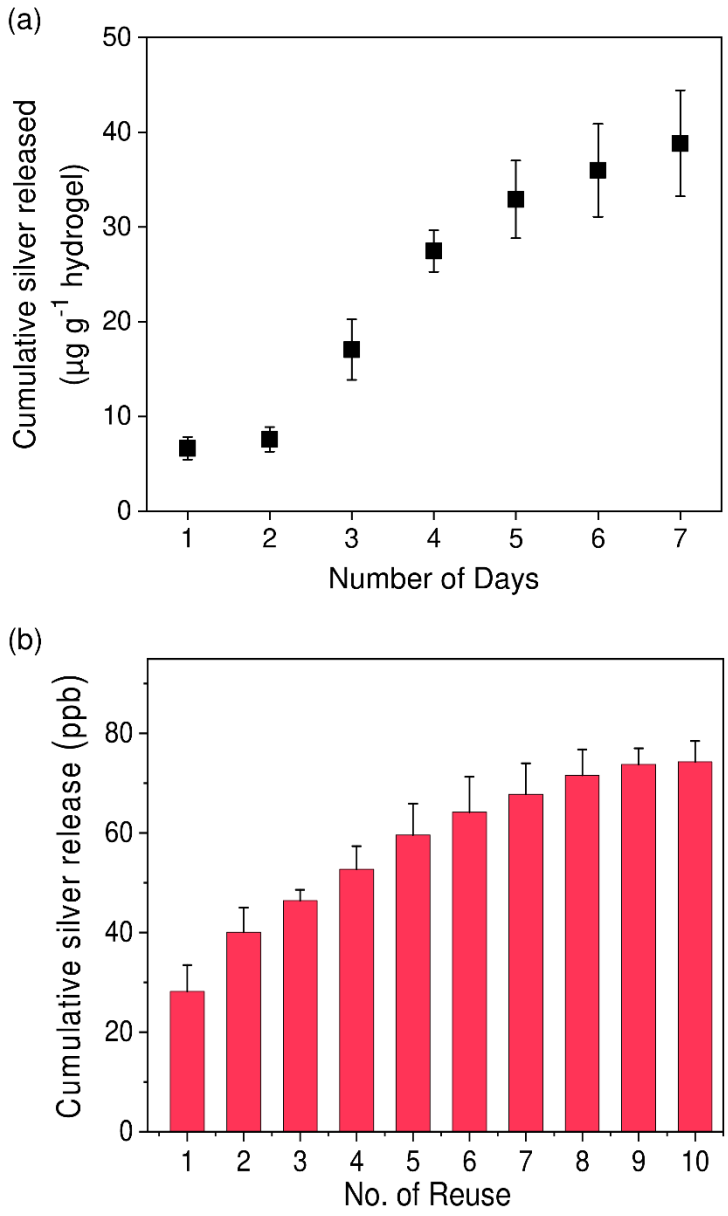

Figure 4.12 (a) The amount of silver released from CS/PVA/Ag hydrogel after immersing in deionized water over a period of seven days and (b) Corresponding silver release profile investigated under identical conditions in deionized water, devoid of any contaminants.

The above silver-release results are an indicative of the strong AgNPs retention capacity of CS/PVA hydrogel, where silver leaching (either ions/nanoparticles, or both) cannot solely dictate its disinfection potential. These results are in accordance with earlier reports (Agnihotri et al. 2015; Agnihotri et al. 2013; Agnihotri et al. 2019) where it has been demonstrated that surface immobilized AgNPs could perform more effectively for water disinfection due to their predominant contact-active role of "capture and kill" and the contribution of Ag release, even if occurs to an amount just sufficient to elicit the biocidal effect. We evidenced similar phenomenon while correlating disinfection profile and silver release kinetics upon repeated usage, where it was observed that the extent of disinfection remained unaffected by varying silver release into the system. All these finding provide compelling evidences to elucidate the mechanism of disinfection of CS/PVA/Ag hydrogel, which is predominantly contact-killing driven (Hoop et al. 2016; Vilela et al. 2017).

4.5 Anti-Biofilm Activities of Hydrogel

It is evident that the inherent characteristics of drinking water system (DWS) in urban communities may sometime make the conditions favorable for a few opportunistic microbes to grow, attach and eventually form a biofilm (Maes et al. 2019). This situation can become even worse if DWS gets contaminated with healthcare-associated microbes due to the unsafe disposal of biomedical waste. These contaminants may enter in drinking water either through broken water pipelines at nearby waste dumping site or leaching of microbes in the surrounding environment. Several researchers have proven that under such water quality conditions, faecal contaminants persist longer in DWS and become more resistant towards used disinfectants using the attached biofilm as a shelter/reservoir for their survival and regrowth (Abberton et al. 2016).

Henceforth, we investigated the ability of CS/PVA hydrogel inhibiting the biofilm formation of two bacterial strains, *E. coli* and *S. aureus,* before and after incorporating silver nanoparticles. In case with *E. coli,* CS/PVA/Ag hydrogel depicted 75% reduction in bacterial biofilm as compared to positive control after 24 h and worked effectively with similar extent of anti-biofilm inhibition after 48 h as well (Figure 4.13a). Even, the presence of chitosan polymer with inherent antimicrobial characteristics could not contribute towards any reduction in the bacterial biofilm for pristine CS/PVA hydrogel. With *S. aureus*, CS/PVA/Ag hydrogel demonstrated ~78% reduction in bacterial biofilm after 24 h as compared to positive

control and achieved even greater anti-biofilm features (87%) after 48 h (Figure 4.13b). On the contrary, pristine CS/PVA showed an increase in biofilm formation after 48 h. We conclude that a variation in biofilm formation among two different microbial strains did not affect the anti-biofilm characteristics of CS/PVA/Ag hydrogel. In fact, immobilized AgNPs on to the CS/PVA hydrogel impeded biofilm formation of both *E. coli* and *S. aureus* till 48 h and hence, we could predict the disinfection behavior of this hydrogel for natural ecosystems under controlled conditions.

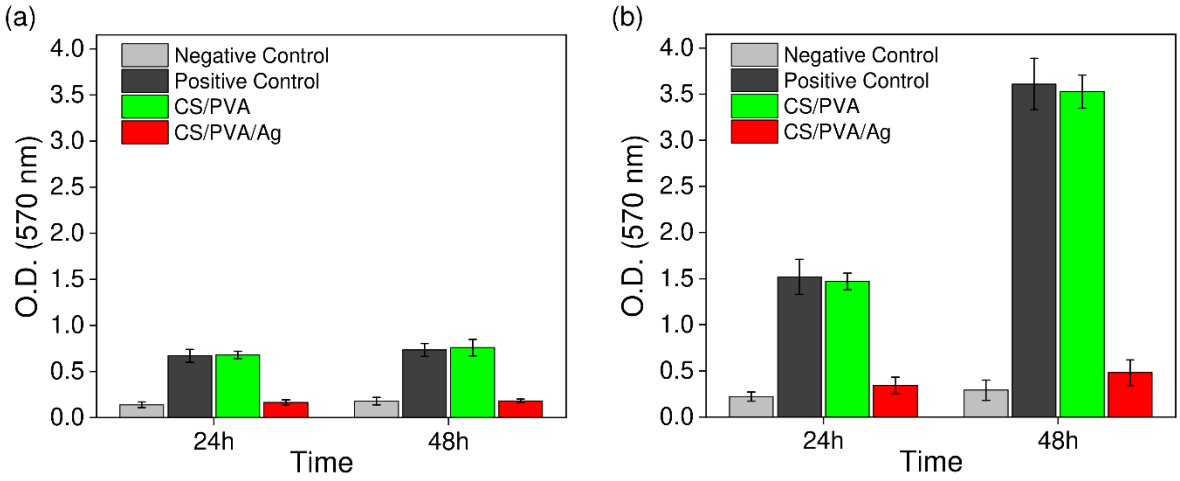

Figure 4.13 Anti-biofilm characteristics of pristine and Ag loaded CS-PVA hydrogel against (a) *E. coli* and (b) *S. aureus* over a period of 48 h.

4.6 Disinfection of Natural Water Resources

Very recently, it has been reported about the impact of water quality parameters (alkalinity, hardness and natural organic matter) on disinfection performance of immobilized AgNPs for simulated lake water (Agnihotri et al. 2019). In present study, we extended our efforts to demonstrate the disinfection efficacy of CS/PVA/Ag hydrogel in environmental samples systematically collected from three water sources i.e., Bhakra canal, ground water and tap water within Patiala district, Punjab, India and their physicochemical parameters are summarized in Table 4.2. The chosen water samples include vast and complex habitats for diverse microbial communities, where groundwater and canal water samples were found having the least and highest microbial counts, respectively. However, no fecal indicator bacteria and endotoxins were detected in the environmental samples of tap water. The disinfection studies, where environmental samples with intrinsic micro biota depicted complete killing of contaminants within 60 and 90 minutes in tap water and canal water,

respectively (Figure 4.14a). It is imperative that tap water, supplied through municipal supply would primarily have been treated with disinfectants and could possibly get contaminated during water distribution system. The disinfection studies were not conducted for ground water samples due to insignificant microbial counts.

Later, a few experiments were conducted for similar water sources with externally spiked *S. aureus* (initial bacterial counts ~10^5 CFU mL^{-1}), simulating conditions for the leakage of biomedical contaminants into potable water from nearby dumping sites (Figure 4.14b). It was observed that the CS/PVA/Ag hydrogel was able to disinfect all natural water samples with 100% efficacy even with higher bacterial counts, where the time to achieve disinfection was observed to be 180 minutes for canal and tap water and 120 minutes for ground water. It seems the inherent water chemistry conditions of all three water samples were responsible for such variations in disinfection performance of the Ag-loaded hydrogels. Based on a previous study, the difference in disinfection time of disinfection supports the likelihood of impact of immobilized AgNPs in the aquatic environment is highly dependent on pH and temperature (Agnihotri et al. 2019).

Table 4.2 Physicochemical characteristics of three water sources in Patiala district, Pb, India.

Characteristics	**Water Samples**		
Water Sources	Bhakra Canal	Tube Well	Urban Supply
Water Type	River water	Ground water	Tap water
Locations	30.299° N 76.326° E	30.289° N 76.416° E	30.356° N 76.367° E
Odour	Odourless	Odourless	Odourless
pH	7.98 ± 0.11	7.18 ± 0.04	7.45 ± 0.18
Alkalinity (mg L^{-1} as $CaCO_3$)	98	327	292
TDS (mg L^{-1})	138	448	500
TSS (mg L^{-1})	10	12	16
BOD (mg L^{-1})	<5	<5	<5
COD (mg L^{-1})	<5	<5	<5
Total Hardness (mg L^{-1} as $CaCO_3$)	56.4	332	427
Microbial colony counts (CFU mL^{-1})	240 ± 11	55 ± 7	255 ± 31

It is observed that contaminated water supplies from municipal reservoirs, groundwater, canals/lakes, and rivers exhibit various levels of contamination which may pose serious health risks. However, little is understood about the consequences pertaining to leakage of biomedical contaminants from waste disposal sites in nearby areas of water reservoirs. These biomedical contaminants are likely to be translocated through sewage and surface runoff and subsequently percolated to aquifers, which are the major sources of washing, and irrigation, other than drinking in India. Since, developing countries cannot afford expensive technologies for eradicating or managing the biomedical waste, we presented the employability of CS/PVA/Ag hydrogel as one of the feasible solutions for mitigating biomedical contaminants in natural water systems and improving the potable water quality.

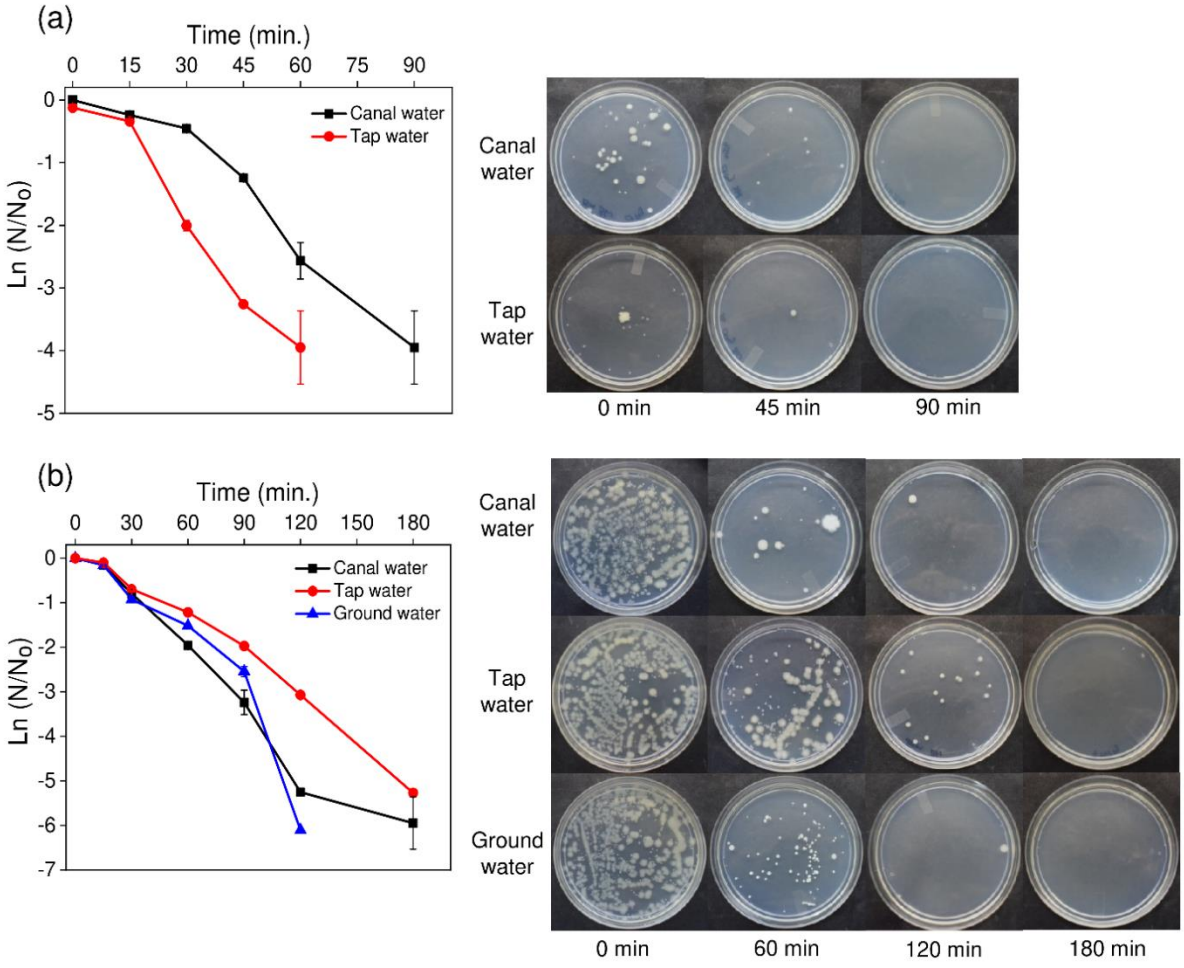

Figure 4.14 Disinfection performance of nano-silver loaded chitosan-PVA hydrogel against natural samples *i.e.*, canal water, groundwater and tap water with (a) inherent micro biota and (b) externally spiked contaminants, *S. aureus* was tested at 10^3-10^4 CFU mL^{-1}. Corresponding images depict a distinct reduction in bacterial population with duration of treatment.

4.7 Development of Nano-Ag Loaded Chitosan-Graphene Oxide (CS/GO/Ag) Hydrogels

4.7.1 Synthesis and Optimization of Chitosan/Graphene Oxide (CS/GO) Hydrogels

The formation behaviours of CS/GO hydrogels as a function of CS and GO concentration are depicted in Figure 4.15 and Table 4.3. An initial qualitative assessment confirmed that concentration of chitosan greatly influenced the formation of hydrogel, i.e., hydrogel formed only at CS concentrations of ≥2% w/v. The composites prepared in 1% w/v CS solution remained in sol state even after 7 h of curing and hydrogels formed with employment of 2% w/v CS solution were feeble in nature complete with cracks and fractures. At even higher concentration of CS (3% w/v), hydrogel composites were obtained ranging from mechanically robust to very weak gels.

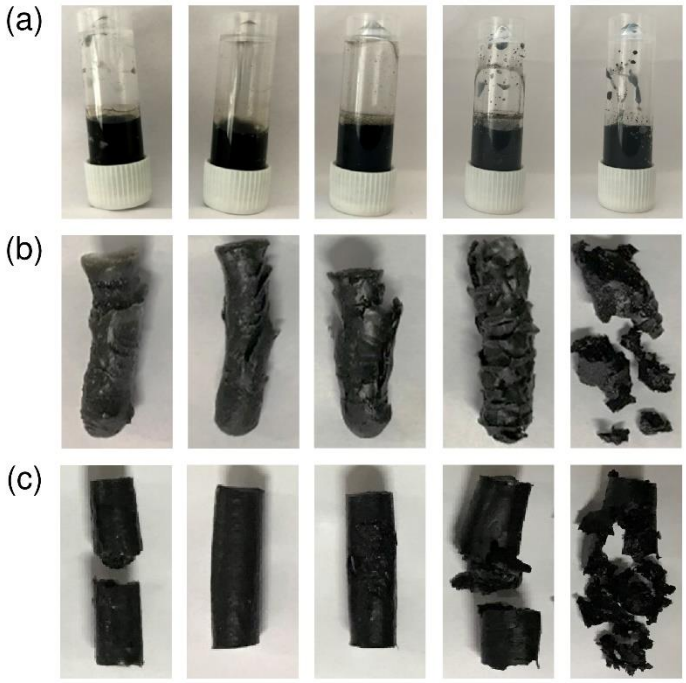

Figure 4.15 Morphology of hydrogels containing (a) 1% w/v CS, (b) 2% w/v CS, and (c) 3% w/v CS with varied GO concentration of 0.02%, 0.05%, 0.1%, 0.4%, and 0.8% in each (left to right).

The observed phenomenon could be attributed to strength ratio of repulsion and bonding forces between GO sheets, which determines the stability of the hydrogel (Qi et al. 2018). Graphene oxide disperses completely into single layers due to the strong repulsion between its negatively charged sheets while chitosan carries a positive charge due to its protonated amino groups (An and Dultz 2007; Chabot et al. 2014). Apart from electrostatic interactions,

hydroxyl groups of CS can form multiple hydrogen bonds with adjacent GO sheets. Consequently, at sufficiently higher concentrations (≥2% w/v), CS is capable of bonding negatively charged GO sheets together, resulting in the rapid gelation of mixture into a standalone hydrogel. Further, adding excessive amounts of GO (≥0.1% w/v) results in its precipitation as the GO sheets align in a parallel and compact manner with increased contact area, which ultimately impedes stable gel formation. Eventually, the hydrogels corresponding to CS and GO content of 3% w/v and 0.05% w/v, respectively with strong structural integrity were selected and employed for further loading of silver nanoparticles.

Table 4.3 Qualitative assessment of the consistency of cross-linked CS/GO hydrogel composites upon variation of the concentrations of chitosan and graphene oxide.

Chitosan (CS) Conc. (w/v%)	**Graphene Oxide (GO) conc. (w/v%)**	**Hydrogel formation (Qualitative description)**
1.0	0.02	Sol
1.0	0.05	Sol
1.0	0.1	Sol
1.0	0.4	Sol
1.0	0.8	Sol
2.0	0.02	Very weak gel with cracks
2.0	0.05	Very weak gel with cracks
2.0	0.1	Extremely cracked gel
2.0	0.4	Extremely cracked gel
2.0	0.8	No stable gel
3.0	0.02	Weak gel
3.0	**0.05**	**Robust gel***
3.0	0.1	Gel with slight cracks
3.0	0.4	Very weak gel
3.0	0.8	No stable gel

*After optimization, cross-linked CS/GO hybrids consisting of 3.0% chitosan and 0.05% graphene oxide were selected for further analyses and usage in the entire study.

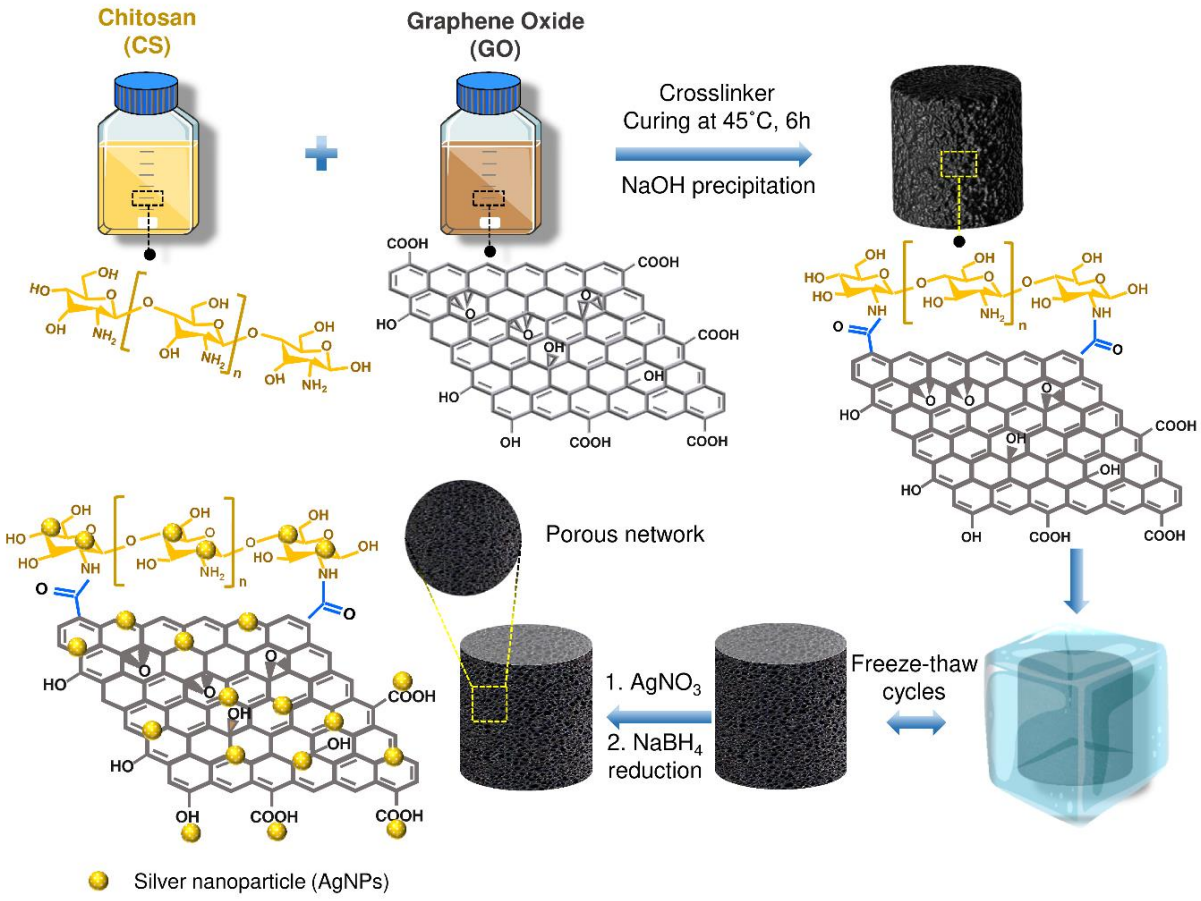

Figure 4.16 Schematic illustration of chitosan/GO hydrogel as a 'nano reactor' for *in situ* synthesis and instant immobilization of silver nanoparticles within its porous network.

Figure 4.16 illustrates the formation of in-situ crosslinked silver nanoparticles (AgNPs) within the chitosan-graphene oxide (CS/GO) hydrogel. The porous network of CS/GO hydrogel, developed through repeated freeze-thaw treatments, serve as nano reactor for synthesizing AgNPs and their subsequent immobilization. We witnessed that the 3D structure of hydrogels, characterized by interconnected pores, high-density functional groups, and a large surface area facilitates the diffusion of silver ions and their entrapment within the gel matrix (Agnihotri et al. 2012; Kaur et al. 2021). As a result, when the precursor hydrogel is introduced into an aqueous $AgNO_3$ solution, a significant portion of Ag^+ ions becomes anchored to functional moieties on the CS/GO hydrogel via ion-exchange mechanism(s). The remaining Ag^+ ions occupy interstitial space within the crosslinked gel network. In case of chitosan-derived hydrogels, these interactions appears too strong that it creates 'nucleation sites' within the space, where Ag^+ ions undergo reduction with a suitable reducing agent, transforming into AgNPs. Hence, an immediate change in the colour (dark green to brownish

black) of hydrogel was observed due to surface plasmon excitation of *in situ* synthesized AgNPs. The newly-synthesized AgNPs instantaneously get immobilized within the porous networks even in the absence of any external stabilizing agent (Figure 4.17). The use of sodium borohydride, a strong reducing agent also facilitated the generation of ultra-small AgNPs (average size 4 nm), which is known to exhibit a greater antibacterial activity than their larger counterparts (Agnihotri et al. 2014).

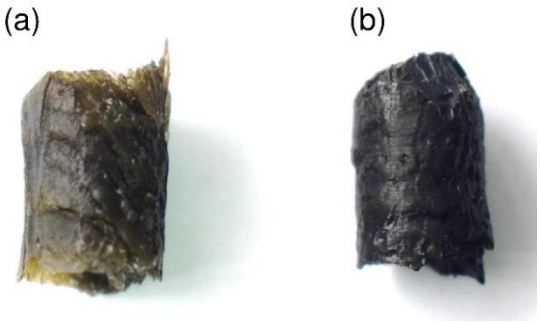

Figure 4.17 Photographic image showing hydrogels (a) before and (b) after silver nanoparticles immobilization.

4.7.2 Characterization of Pristine (CS/GO) and Nano-Silver Immobilized Chitosan-GO (CS/GO/Ag) Hydrogels

The UV-visible spectrum and FTIR analyses (Figure 4.18) of as-synthesized GO confirm the presence of abundant hydroxyl groups and oxygen moieties on the surface of GO (Yu et al. 2016).

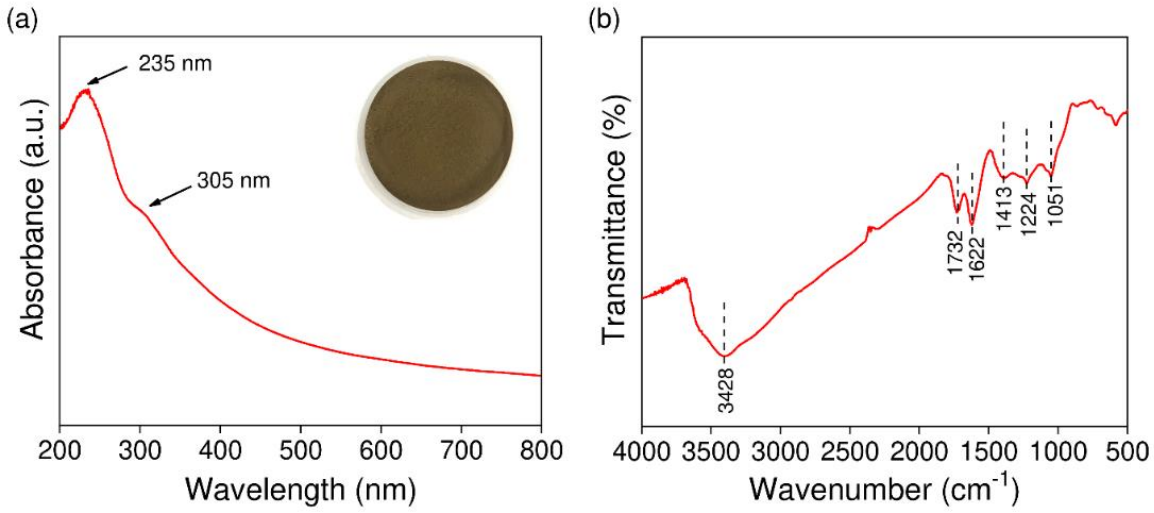

Figure 4.18 Material characterization displaying (a) UV-Vis spectra (inset shows synthesized graphene oxide of brown chroma) and (b) FTIR spectra of graphene oxide (GO).

The FTIR spectra of chitosan-GO hydrogel before and after immobilizing AgNPs was compared (Figure 4.19a). A broad peak at 3430 cm^{-1} associated with OH and/or NH stretching vibrations, appeared in both variants of CS-GO hydrogel due to the synergistic association of hydrogen bonding and electrostatic interactions between chitosan and negatively-charged GO. Similarly, several other characteristic peaks at 2877 cm^{-1}, 1577 cm^{-1} and 1018 cm^{-1} attributed to C–H stretching, C=C stretching, and stretching vibrations of C–O- groups on polysaccharide skeleton respectively, appeared in both hydrogel forms and remained unchanged even after loading AgNPs. Notably, the peak at 1632 cm^{-1} in pristine chitosan-GO, due to carbonyl (C=O) stretching not only exhibited reduced intensity but also shifted to a lower frequency of 1618 cm^{-1} in CS/GO/Ag hydrogel (Khawaja et al. 2018). These observations suggest that although stronger intermolecular interactions occurred between CS and GO during hydrogel formation, numerous free -OH moieties still remained available as 'nucleation sites' for Ag^{+} ions during *in situ* synthesis and their instant immobilization. We therefore envisaged a localized anchoring of AgNPs to the hierarchical networks of chitosan/GO hydrogel during nucleation and growth stages.

The X-ray diffraction pattern (Figure 4.19b) of pure GO showed a typical sharp peak at 2θ = 10.5° (001) with a d spacing of 0.816 nm (Yu et al. 2016). In contrast, the CS/GO composite displayed a broad peak at 2θ =16.1°, indicating the presence of strong interactions between GO and chitosan components, which hindered the regular stacking of GO sheets (Jiao et al. 2015). Additionally, a small peak appeared at 2θ = 38.7° (inset) in the CS/GO/Ag hydrogel, attributed to the presence of face-centered cubic planes (FCC, 111) of crystalline AgNPs (Pounraj et al. 2018).

The Raman spectra of the hydrogel nanocomposites exhibited three distinct peaks at 1362 cm^{-1} (C-C), 1607 cm^{-1} (C=C), and 2760 cm^{-1} corresponding to the D, G, and 2D bands of graphene oxide, respectively (Figure 4.19c). The D band is attributed to edges and disordered carbon, including other defects resulting from dangling bonds in the lattice. In contrast the G band is associated with the graphitic hexagon-pinch mode (Yadav et al. 2014). A Raman shift, observed in the D and G bands at 1351 cm^{-1} and 1604 cm^{-1}, respectively, confirms the presence of hydrogen-bonded components in the CS/GO hydrogel, as previously witnessed. The I_D/I_G intensity ratio of GO was determined to be 1.013, indicating disorder in the GO layers due to the oxidation of graphite. The position and shape of D band in Raman spectra also dictates multi-layered GO sheets (García-Cruz et al. 2016; Kumar et al. 2021). Notable,

the CS/GO/Ag composite exhibited a higher I_D/I_G ratio (1.164) compared to GO and CS/GO (1.161), suggesting the structural defects due to the annealing temperature (Liao et al. 2018; Nath et al. 2018).

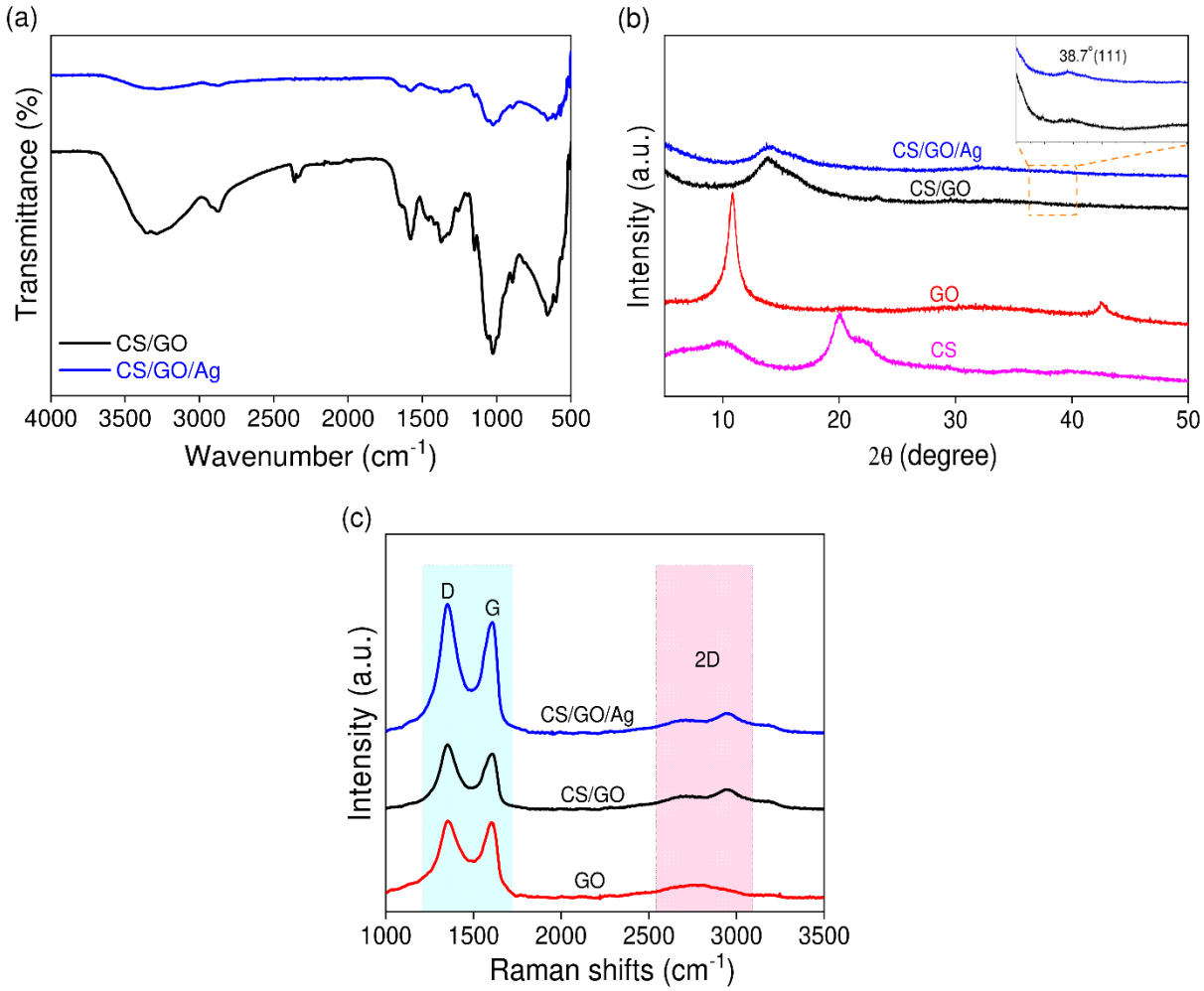

Figure 4.19 Analytical characterization of pristine and nano-Ag loaded CS-GO hydrogels through (a) FTIR spectroscopy, (b) XRD analyses and (c) Raman spectroscopy.

The topography analysis of the hydrogel nanocomposites before and after AgNPs immobilization, conducted using electron microscopy (Figure 4.20a-d), yielded similar observations. The cyclic freeze-thaw treatments induced both liquid-solid and liquid-liquid phase separations, promoting the strong adherence of GO sheets to CS polymers through hydrogen bonding (Figure 4.20a-b). Consequently, the resulting CS/GO hydrogel matrix exhibited dense intercalation of GO sheets, a high porosity and random microstructures. This porous matrix, particularly ease in facile synthesis and immobilization of AgNPs without compromising the structural integrity (Figure 4.20c-d).

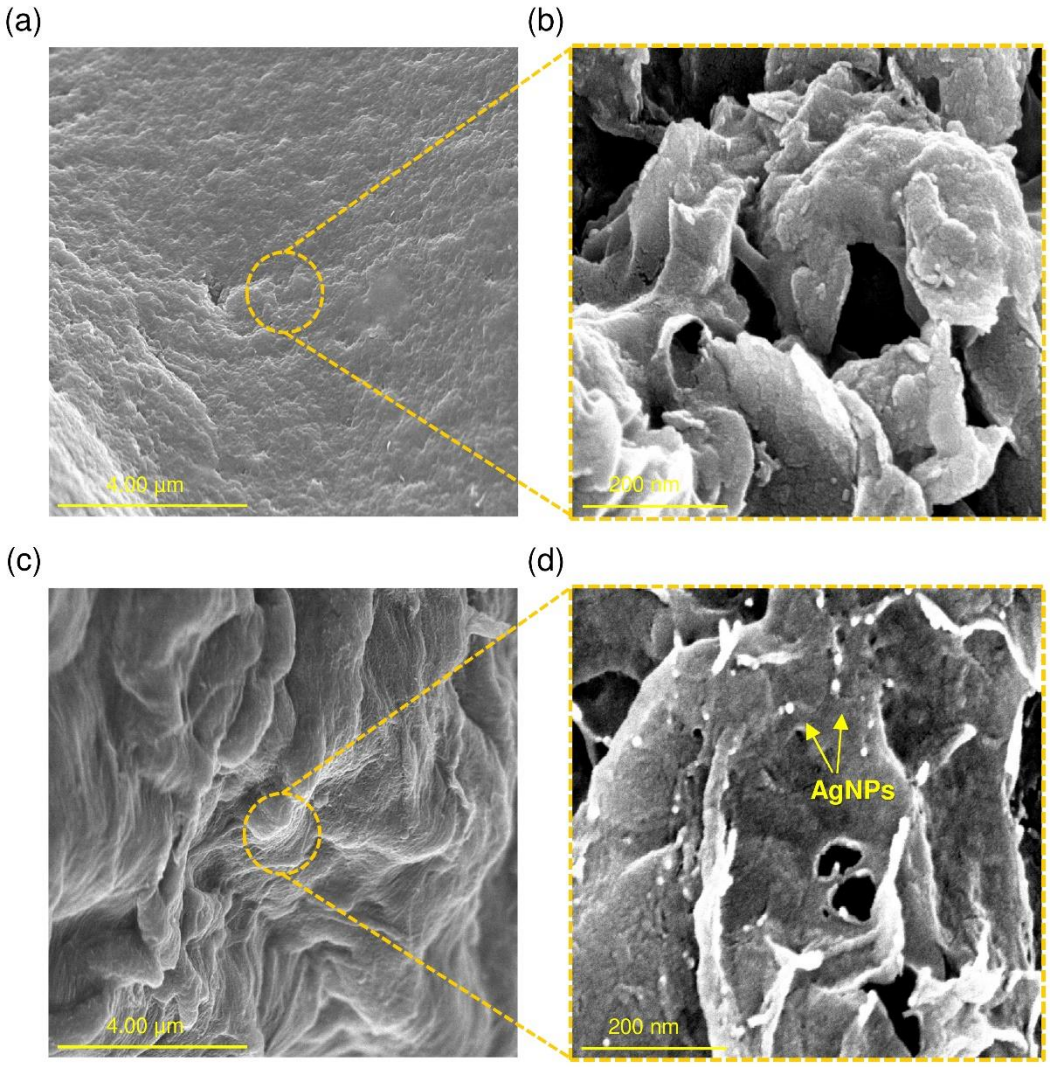

Figure 4.20 High-resolution SEM micrographs of (a, b) CS/GO and (c, d) CS/GO/Ag hydrogels confirming the presence of silver nanoparticles (Ag).

The energy-dispersive X-ray spectroscopy (EDS) analysis revealed a prominent peak at ~2.93 KeV, confirming the presence of silver at high proportion (13.95 % by weight), alongside the characteristic elements in CS/GO blend (Figure 4.21a and 4.21c). The corresponding elemental mapping confirmed a uniform distribution of nano-silver throughout the surface of the CS/GO/Ag hydrogel matrix (Figure 4.21b and 4.21d).

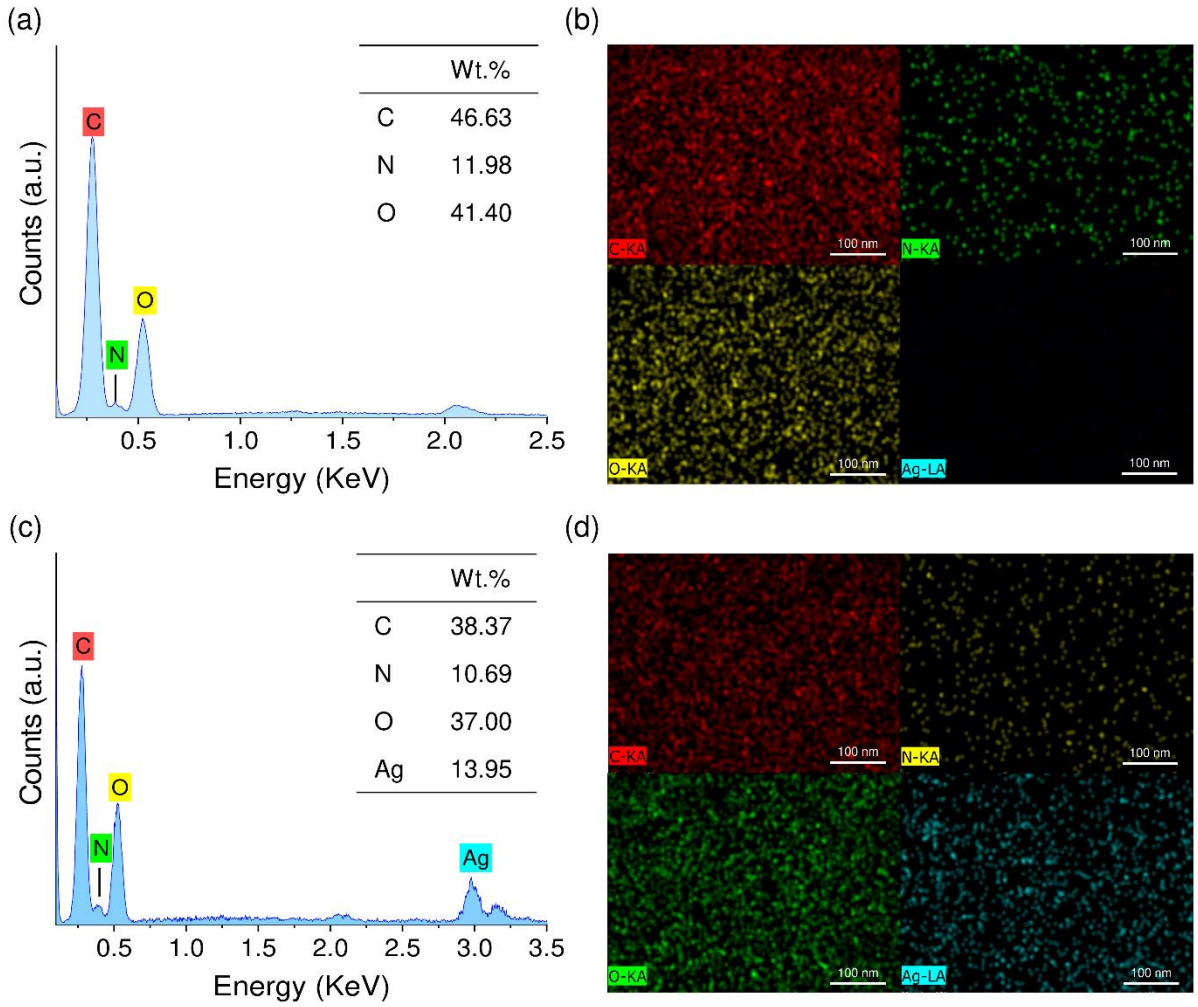

Figure 4.21 EDS spectra of (a) CS/GO and (c) CS/GO/Ag hydrogels and the uniform distribution of elements Carbon (C), Nitrogen (N), Oxygen (O) corroborated by corresponding (b, d) elemental mapping.

To evaluate the 'state of existence' of silver nanoparticles within hydrogel network, the CS/GO/Ag hydrogel was finely ground using ball-mill, then dispersed in distilled water for 12 h and sonicated thereafter. This process facilitated the retrieval of immobilized AgNPs from the gel network (Tyliszczak et al. 2017). The UV-Spectroscopy analysis of the suspension showed a characteristic extinction peak of AgNPs at ~400 nm (Figure 4.22a). Further, transmission electron microscopy (TEM) examination (Figure 4.22b) demonstrated that *in situ* synthesized AgNPs exhibited a spherical shape, with an average diameter of ~4.2 nm (Figure 4.22c) and were fully segregated. The SAED diffraction (inset) supported the XRD findings, confirming the existence of AgNPs in (111) FCC planes.

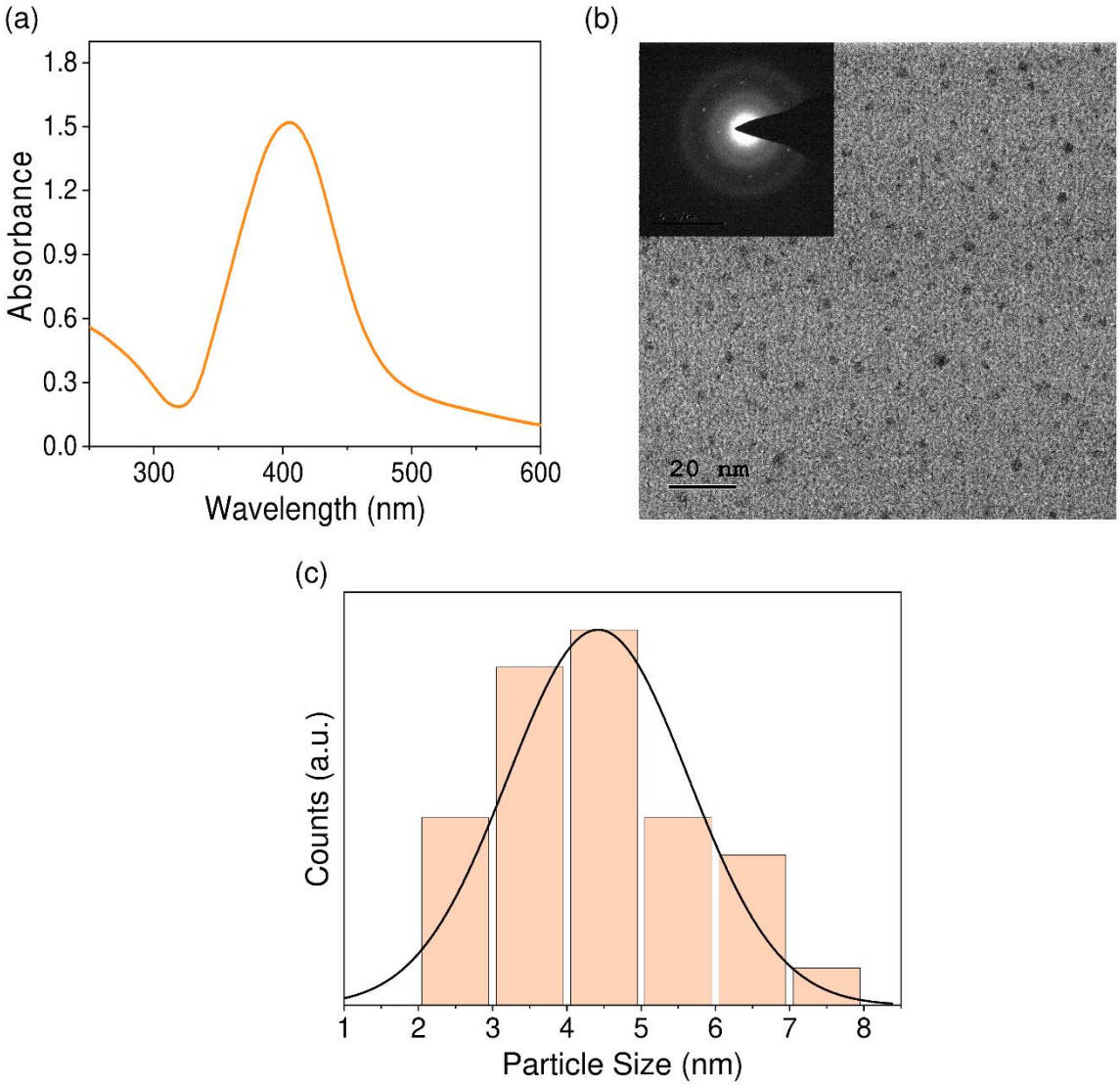

Figure 4.22 (a) UV-Vis spectroscopy and (b) TEM micrograph of *in situ* synthesized AgNPs within CS/GO hydrogel (inset shows the corresponding SAED pattern) and (b) the size distribution histogram of AgNPs observed under TEM.

The textural properties of both pristine CS/GO and CS/GO/Ag hydrogels were studied through N_2 adsorption–desorption isotherms and the corresponding pore size distribution curves provided in Figure 4.23a and Figure 4.23b, respectively. The data suggest that both forms of the hydrogel displayed a type III isotherm with a hysteresis loop, indicating their macro porous nature. The BET surface area of CS/GO/Ag was found to be 2.0 $m^2\ g^{-1}$, three-fold higher than the corresponding value for CS/GO (0.63 $m^2\ g^{-1}$). Such increase in surface area can be attributed to the immobilization of AgNPs on the hierarchical networks of hydrogel.

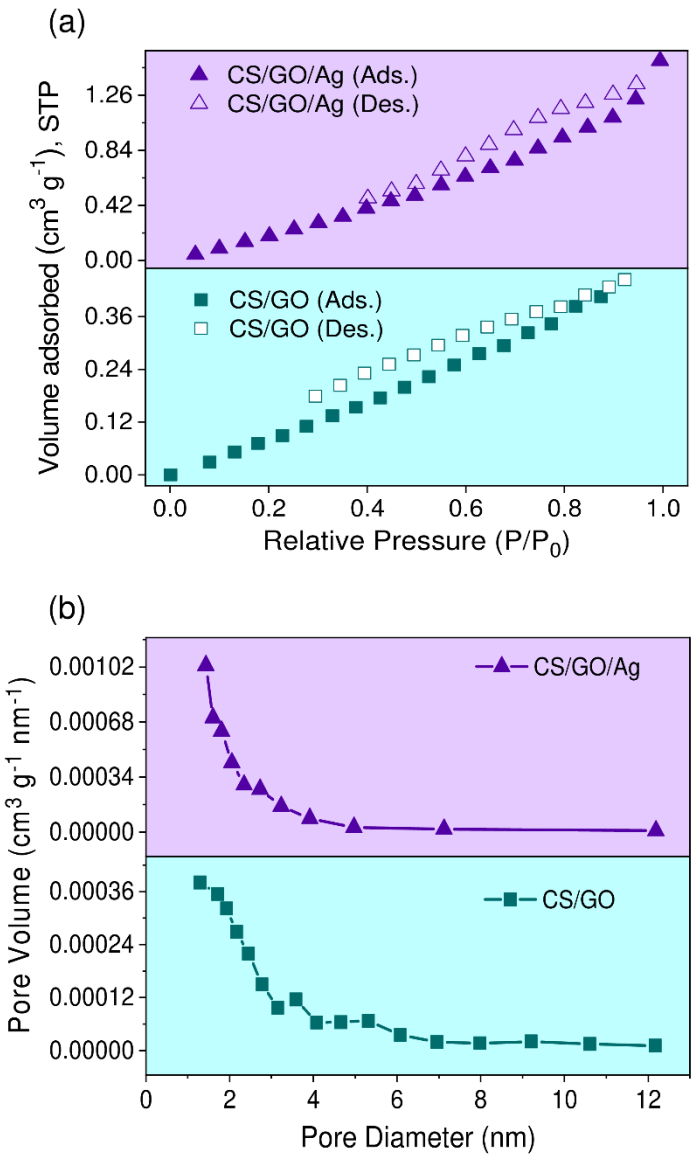

Figure 4.23 (a) N_2 adsorption–desorption isotherms and (b) Pore size distribution in CS/GO and CS/GO/Ag nanocomposites acquired through BET analyses.

Notably, the total pore volume and average pore diameter of pristine CS/GO were observed to be 9.26×10^{-4} cm^3 g^{-1} and 4.37 nm, respectively, whereas CS/GO/Ag exhibited values of 2.82×10^{-3} cm^3 g^{-1} and 3.42 nm, respectively. These results confirm the successful anchoring of AgNPs within the porous morphologies of the hydrogel, resulting in an increase in pore volume a reduction in average pore diameter (Kumar et al. 2021). Collectively, CS/GO/Ag nanocomposite possesses favourable porosity and a larger surface area, facilitating rapid water permeation within the hydrogel. Furthermore, since the contact-driven bacterial killing primarily occurs at the bacteria-water interface, an increased surface area offered by the hydrogel is expected to improve its efficacy in water disinfection.

To assess the mechanical properties of hydrogel nanocomposites, both compressive and tensile tests were conducted on cylindrical-shaped samples. The CS/GO hydrogel exhibited a compressive of 0.24 ± 0.04 MPa (at 39.49 ± 5.45% break strain) and a tensile strength of 3.13 ± 0.26 MPa (at 13.04 ± 2.09% break strain) under a load of 2.4 Kgf (Figure 4.24). After AgNPs immobilization, the compressive and tensile strengths of CS/GO/Ag hydrogel increased to 0.40 ± 0.12 MPa (at 64.10 ± 0.21% break strain) and 4.21 ± 1.13 MPa (at 47.11 ± 5.12% break strain), respectively, under a load of 43 Kgf. This enhancement in mechanical strength occurred due to strong hydrogen bonding and electrostatic interactions between functional groups (amino, hydroxyl) present in hydrogel matrix and the well-dispersed nanomaterial phase, facilitated by the addition of AgNPs (Pounraj et al. 2018). These interactions, influenced by the presence of AgNPs, exhibit knot-tying functions (Yadollahi et al. 2015) which restrict the expansion of polymer chains and result in the formation of a compact structure, leading to improved load transfer. A strong mechanical strength is crucial for designing a hydrogel-based water disinfection system to ensure its durability and stability under continuous fluid flow and pressure. The system's ability to withstand mechanical stress and maintain its structural integrity is essential for long-term, efficient operation without the risk of structure failure or performance deterioration.

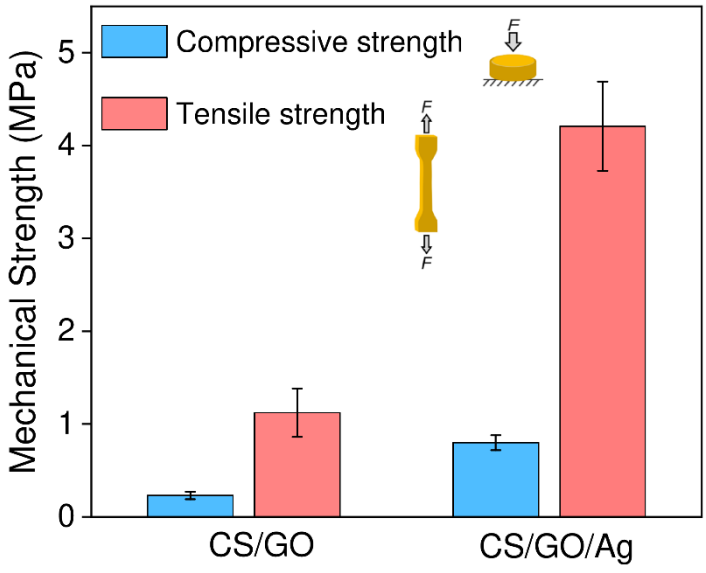

Figure 4.24 Compressive and tensile mechanical strength of hydrogels before and after loading of silver nanoparticles.

Surface chemistry and interactions in the nanocomposite were analyzed using X-ray photoelectron spectroscopy (XPS). The survey spectra of both hydrogel variants exhibited

characteristic peaks of C(1s), N(1s), and O(1s), while the Ag(3d) peak was only present in the CS/GO/Ag composite (Figure 4.25a). Deconvolution of XPS peaks in the CS/GO/Ag composite was performed in detail. For instance, the deconvolution of C(1s) (Figure 4.25b) revealed a peak at 284.7 eV attributed to C-C, C-H, and C=C bonds. Additional peaks at 286.4, 287.7, 288.3, and 289.5 eV were assigned to various oxygen-containing C-OH, C-O-C, C=O, and O=C-OH bonds. The N(1s) peaks (Figure 4.25c) indicated the presence of amine groups and N^+ segments at 399.4 and 401.4 eV, respectively, demonstrating covalent bonding and weak interactions between CS molecules and GO sheets.

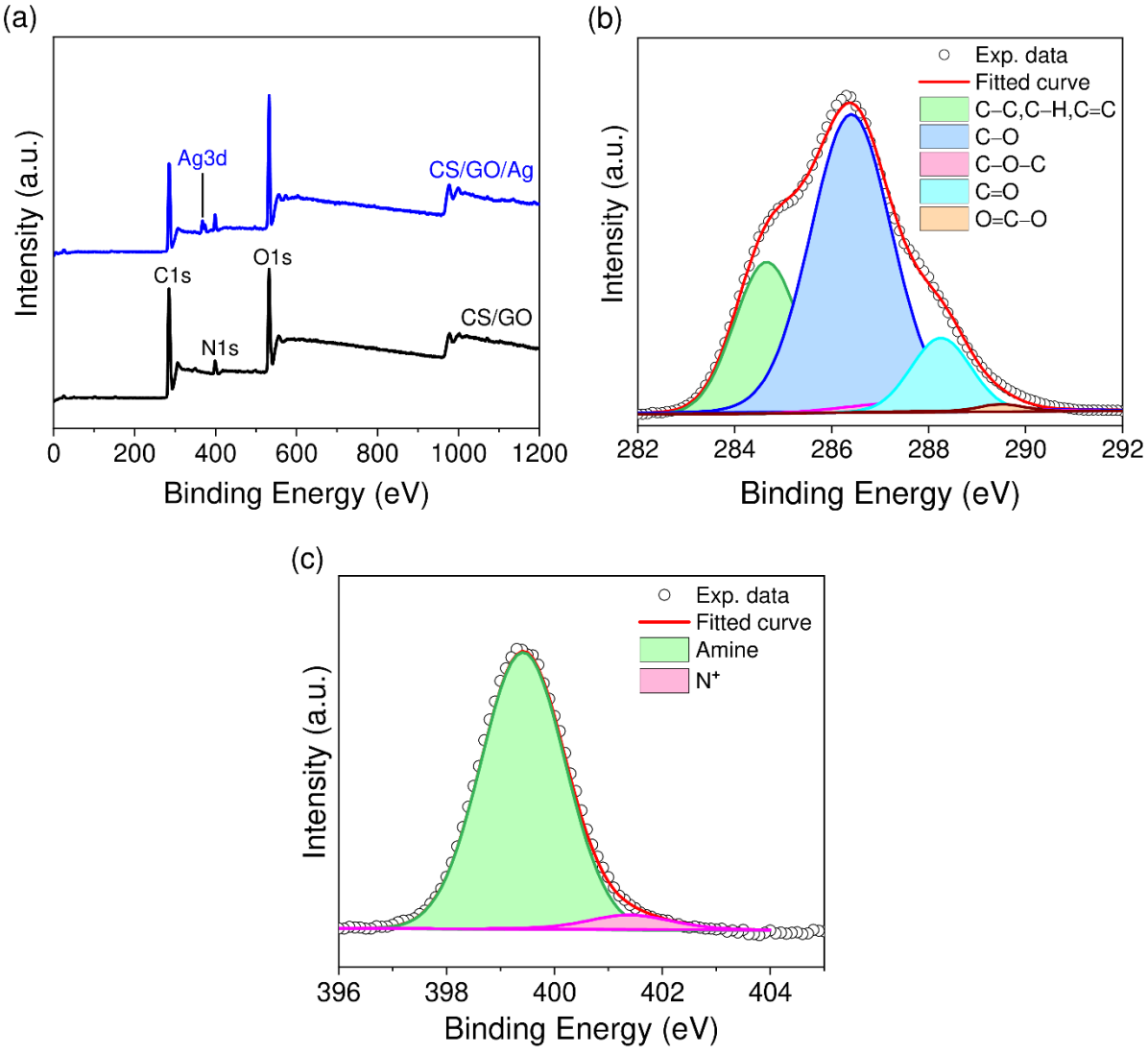

Figure 4.25 (a) Survey XPS spectra of pristine and CS/GO/Ag hydrogels, deconvolution of XPS peaks (b) C1s and c) N(1s) of CS/GO/Ag nanocomposite.

Further, the O(1s) peak (Figure 4.26a) was deconvoluted into two components, one at 532.0 eV due to surface hydroxyl groups and another at 533.0 eV assigned to oxygen in water molecules adsorbed in hydrogel nanocomposite. The Ag(3d) exhibited peaks at 368.4 and 374.4 eV corresponding to Ag(3d5/2) and Ag(3d3/2) binding energies, respectively (Figure 4.26b). Such peak splitting of 3d doublet by 6.0 eV confirms the existence of metallic silver in CS/GO/Ag hydrogels (Akhavan 2009). Furthermore, deconvolution of Ag(3d5/2) revealed peaks at 368.4 and 367.6 eV, corresponding to Ag and Ag_2O, indicating that 65.4% and 34.6% of the silver existed in Ag^0 and Ag^+ chemical states, respectively (Jiao et al. 2015).

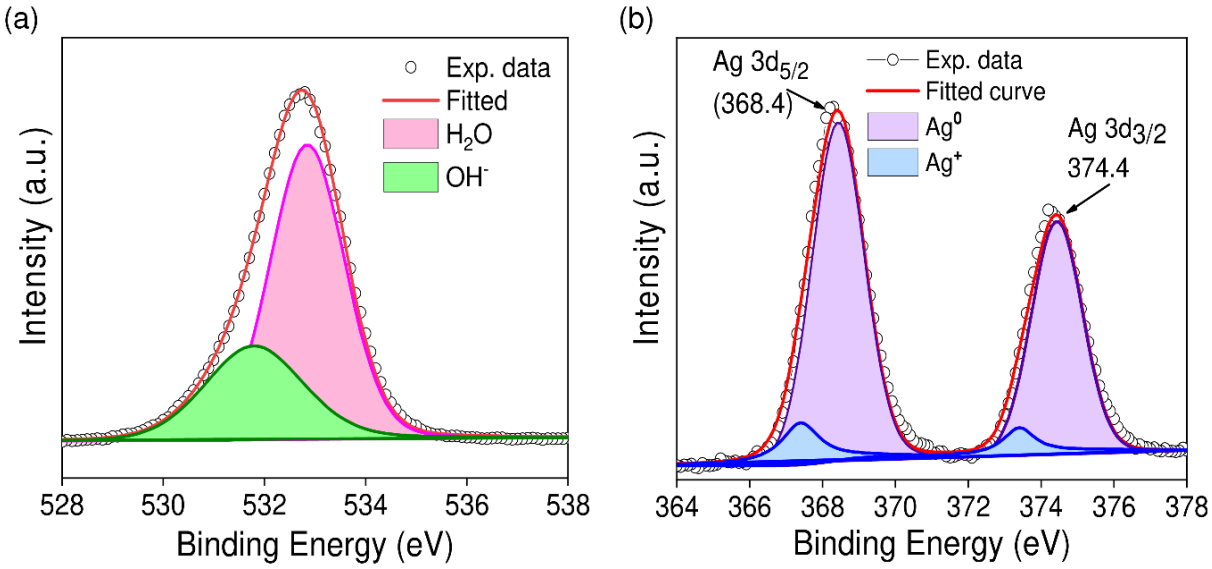

Figure 4.26 XPS spectral analysis of CS/GO/Ag hydrogel nanocomposite, high resolution spectra and deconvolution of (a) O(1s) and (b) Ag(3d) peaks.

Thermogravimetric analysis (TGA) was used to assess the thermostability of CS/GO-based composites. The CS/GO experienced a weight loss of ~13% between 30 and 190˚C, primarily due to moisture evaporation (Figure 4.27a). A maximum weight loss of ~38% occurred at 290˚C jointly due to the decomposition of functional moieties present in the chitosan along with GO, which is thermally unstable and undergoes pyrolysis, releasing CO, CO_2 and water (Stankovich et al. 2007). The third stage involved further decomposition (~16.2% weight loss) of the remaining backbone residues of chitosan polymer. Since thermal decomposition of pure chitosan residues majorly occurs near 300˚C (Yadav et al. 2014), a lower thermal stability of CS/GO hydrogel appeared due to the existence of ionically-bonded NH_3^+ and COO^- groups. The presence of graphene oxide further reduced nanocomposites' crystallinity and weakened the rigidity of CS chains. As compared to pristine GO, which undergoes

weight loss at ~230˚C (Nath et al. 2018), the CS/GO hydrogel demonstrated an improved thermal stability. Also, with a total weight loss of 66.6%, the CS/GO/Ag hydrogel exhibited a marginally better thermal resistance than CS/GO composite (weight loss, 67.5%) solely due to silver nanoparticles.

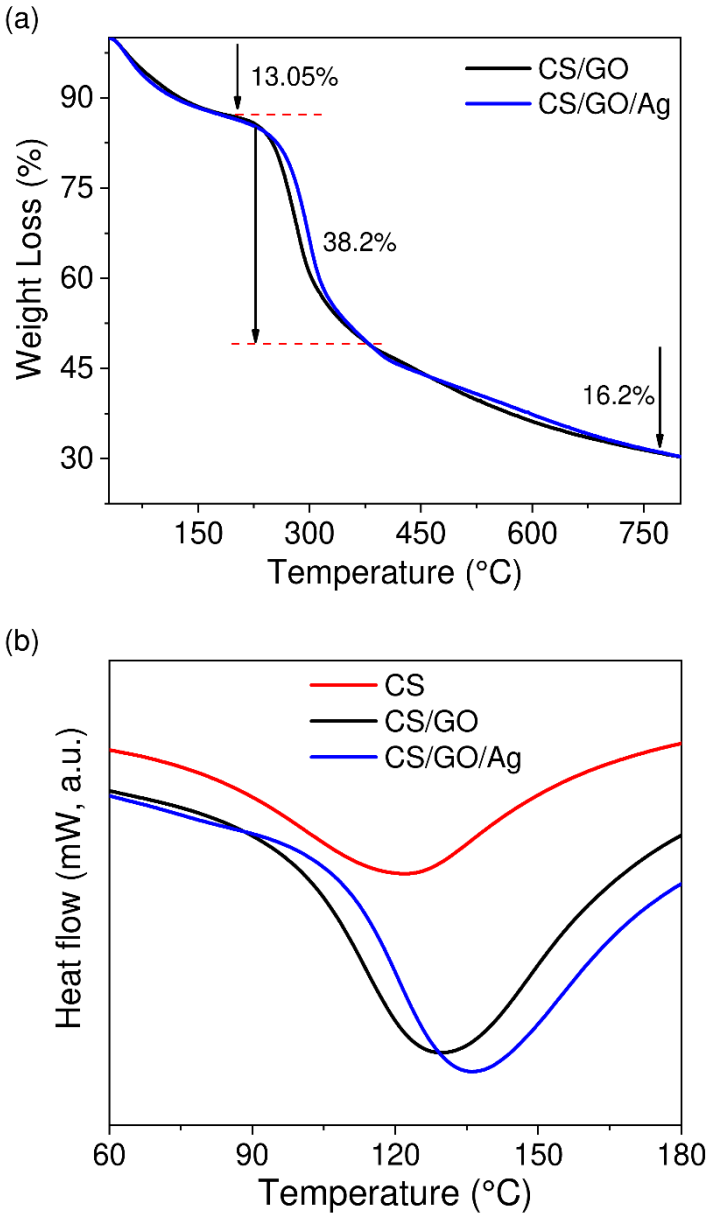

Figure 4.27 Thermal characteristics of hydrogel nanocomposites as depicted by (a) thermogravimetric (TGA) curves, and (b) Differential scanning colorimetry (DSC) thermograms.

Differential scanning calorimetry (DSC) measurements were conducted to analyse phase transitions within the composites (Figure 4.27b). The thermogram of pristine chitosan

exhibited a glass transition temperature, T_g at 120 °C, which was shifted to 130 °C and 136 °C for CS/GO and CS/GO/Ag composites, respectively. This shift to higher temperatures suggests an improvement in the thermal properties of the composites due to the addition of graphene oxide (GO) and silver nanoparticles (AgNPs). Thus, a uniform dispersion of GO and AgNPs within hydrogel may effectively restrict the motion of chitosan chains via electrostatic interactions attraction and hydrogen bonding, exhibiting improved thermal characteristics (Ma et al. 2012).

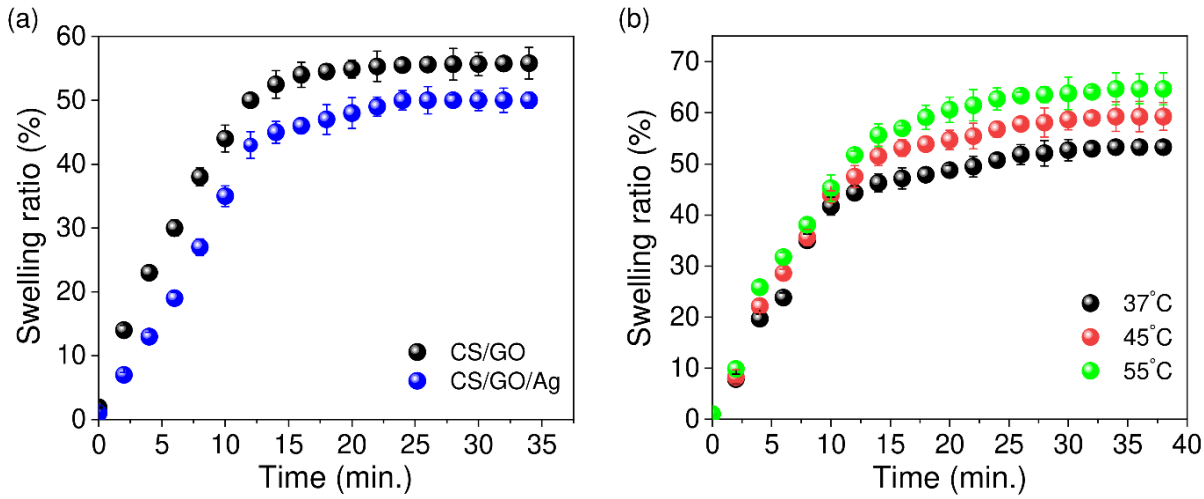

Figure 4. 28 (a) Dynamic swelling behaviour of hydrogel variants under ambient conditions (pH 7, 25 °C) and (b) Temperature dependent swelling kinetics of AgNPs-loaded chitosan-GO hydrogel at wide temperature range.

4.8 Dynamic Swelling Behaviour

The time and temperature-dependent swelling kinetics are shown in Figure 4.28a and 4.28b, respectively. Under ambient conditions (25 °C, pH 7), both pristine and silver-loaded CS/GO hydrogels exhibited fast swelling, reaching its equilibrium within 24 minutes. This behaviour confirms a rapid water permeation capacity of the hydrogel while maintaining its structural integrity. Notably, the CS/GO/Ag hydrogel displayed reduced swelling ratios (50.2 ± 1.3%) compared to its pristine form (55.8 ± 2.5%). As evidenced earlier (Kaur et al. 2021), the presence of *in situ* immobilized AgNPs circumvents the availability of free hydrophilic functional moieties within the CS/GO matrix, thus impeding the formations of stable hydrogen bonds with water molecules. Consequently, this leads to an induced lowering in the hydrophilicity of the hydrogel, hindering water diffusion within its structure. We further assessed the temperature-dependent swelling kinetics of CS/GO/Ag hydrogel within a broad

temperature range of 37-55 °C at pH 7 (Figure 4.28b). Remarkably, as the temperature of the surrounding solution increased from 37 to 55 °C, the swelling capacity increased from 53.3 ± 1.1% to 64.7 ± 3.2%, which is attributed to reversible association and dissociation of hydrogen bonding within semi-interpenetrating networks of the hydrogel (Kim et al. 2005).

4.9 Silver Release Kinetics and Oxidative Dissolution

Nano-silver based disinfection devices is often evaluated based on the extent of 'silver release' into aqueous systems, as it may pose serious eco-toxicological consequences. Hence, we compared the net silver loading i.e., 0.122 ± 0.005 mg g^{-1} hydrogel with the amount released in treated water under long-term, practically relevant conditions. Figure 4.29a illustrates the release profile of silver from CS/GO/Ag hydrogel in deionized water over an extended period of up to 3 days. Within the first hour, the amount of silver released was 40.2 ± 2.0 ppb, which rapidly increased to 70.8 ± 1.8 ppb over the next 6 hours. Notably, the rate of silver release was progressively reduced and eventually reached a plateau after 36 hours. After 96 hours of incubation, a maximum silver release of 87.4 ± 2.3 ppb was detected in suspension, which lies within the permissible limit of silver in drinking water (WHO 2021). The total amount of silver released after 10 days of incubation was found to be only 0.12 ± 0.03% of the total silver loaded. Such a low rate of silver release can be explained by the following hypothesis;

As evidenced before (Agnihotri et al. 2018), AgNPs, composed of silver atoms (Ag^0), invariably react with dissolved oxygen, creating a sub-nanoscale layer of silver (I) oxide, Ag_2O, on their surface. This layer serves as a reservoir of silver ions (Ag^+), responsible for their gradual release in aqueous suspension through oxidative dissolution (Figure 4.29b). The oxidative dissolution of Ag_2O thus occurs even at a neutral pH of the releasing medium. However, the silver oxide layer undergoes protonation in acidic pH, liberating a much higher concentration of Ag^+ ions and causing an accelerated oxidative dissolution of AgNPs. This pronounced dissolution is undesirable as it severely restricts colloidal stability and, in turn, the efficacy of AgNPs. On the contrary, the Ag_2O layer under alkaline conditions initially gets converted into an unstable compound $[Ag(OH)_2]^-$, which undergoes reversible conversion into Ag_2O. In this way, Ag_2O preserves its stability over AgNPs' surface via 'stern layer' formation and mediates a restricted release of Ag^+ ions under alkaline conditions, preserving the colloidal stability of AgNPs too. The silver release profile further

provides compelling evidence of an intriguing 'shielding' phenomenon that offers a reduced surface oxidation of immobilized AgNPs, surpassing the influence of their strong anchoring within the hydrogel networks.

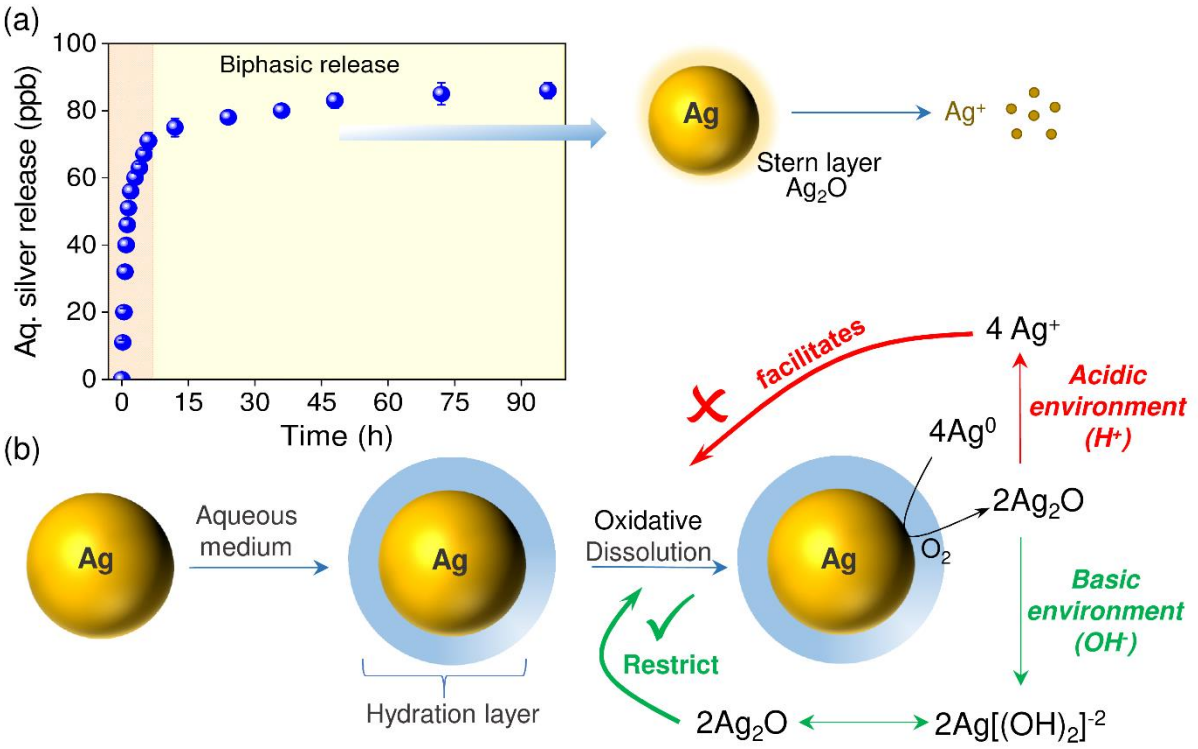

Figure 4.29 (a) Silver release profile of CS/GO/Ag hydrogel in aqueous medium over the course of three days and (b) Schematic illustration of restricted oxidative-dissolution of silver nanoparticles in immobilized state within hydrogel network.

4.10 Biodegradation Study

A soil burial test was conducted to assess environmental sustainability of the hydrogel, as improper disposal of solid waste into soil or landfills may pose adverse effects (He et al. 2019). This test indirectly measures the 'extent' of hydrogel biodegradation with weight loss (%) over a stipulated period of burial in soil (Figure 4.30a). Over a 60-day burial period, the pristine CS/GO hydrogel exhibited faster degradation, resulting in a more weight loss (13.3%) than CS/GO/Ag with a total weight loss of ~5%. A lower degradation of AgNPs-laden CS/GO/Ag hydrogel can be explained in many ways. Firstly, the potent antimicrobial properties of silver nanoparticles could suppress local soil microbiota at burial site, hampering the pace of biodegradation. The presence of noble element, silver within hydrogel might also impede its degradation rate in its metallic state (Ag^0). Furthermore, when buried

under deeper soil layers, limited oxygen availability could render silver nanoparticles less susceptible to oxidation, leading to reduced degradation of hydrogel.

To enhance biodegradation, hydrogels were pre-treated with concentrated lemon juice for approximately 15 minutes, followed by drying before burial. This pre-treatment led to accelerated weight loss in hydrogels, reaching a maximum of 38% (CS/GO) and 31% within a 2-month period. We envisaged a dual-benefit of this pre-treatment for degradation purposes. The presence of citric acid, in lemon juice induces the surface oxidation of AgNPs and transforming them into ionic state (Ag^{+}), causing more leaching (Sankar et al. 2013). Secondly, citric acid facilitates quicker degradation of hydrogel by structure exfoliation, weakening intermolecular bonds and loosening hydrogel networks (Basuki et al. 2015). Optical images of hydrogels buried in soil after 60 days (Figure 4.30b) evidenced the accelerated biodegradation after pre-treatment displaying disintegrated fragments as the internal structure of hydrogels started to degrade meanwhile, only minute surface irregularities with deepening of grooves could be observed for non-treated samples. These pre-treatment also likely to facilitate weight loss, creating a larger surface area for soil bacteria to engage with.

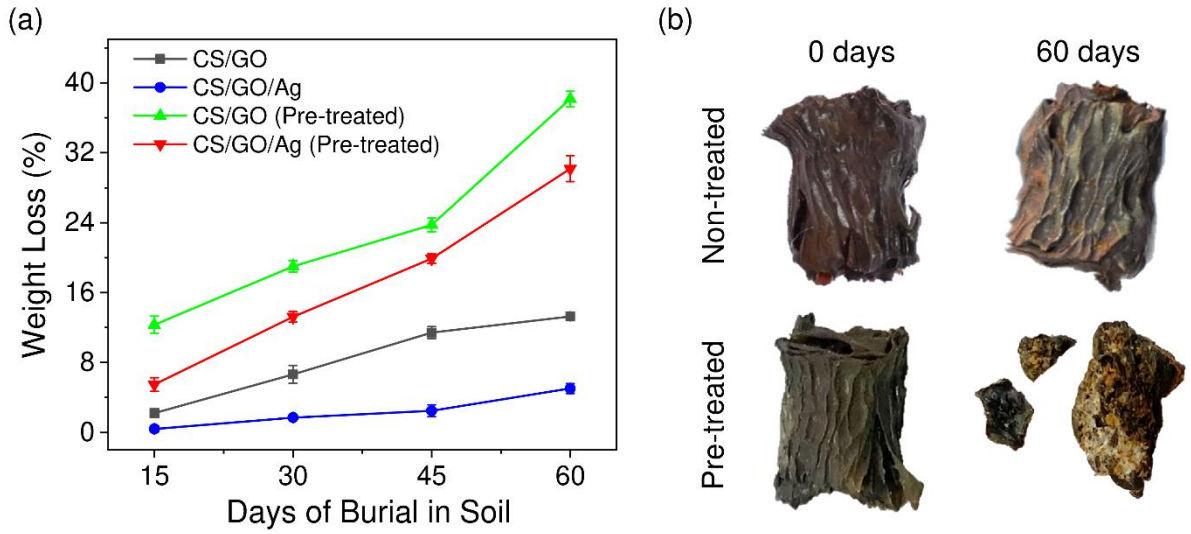

Figure 4.30 (a) Soil biodegradability of hydrogel variants before and after pre-treatment, analysed through weight loss % w.r.t burial time over a period of 60 days and (b) Photographic images displaying direct visual evidence for the effect of pre-treatment on intensity of soil biodegradation of CS/GO/Ag hydrogels over the course of 60 days.

4.11 Species-Specific Disinfection and Reusability of CS/GO and CS/GO/Ag Hydrogels

4.11.1 Disc Diffusion Assay

The biocidal effects of CS/GO/Ag hydrogels were primarily tested against four bacterial strains with diverse pathogenicity in solid agar medium. The antibacterial activity of CS/GO/Ag hydrogel was compared with its pristine form using disc diffusion methods (Figure 4.31) and the data is summarized in Table 4.4.

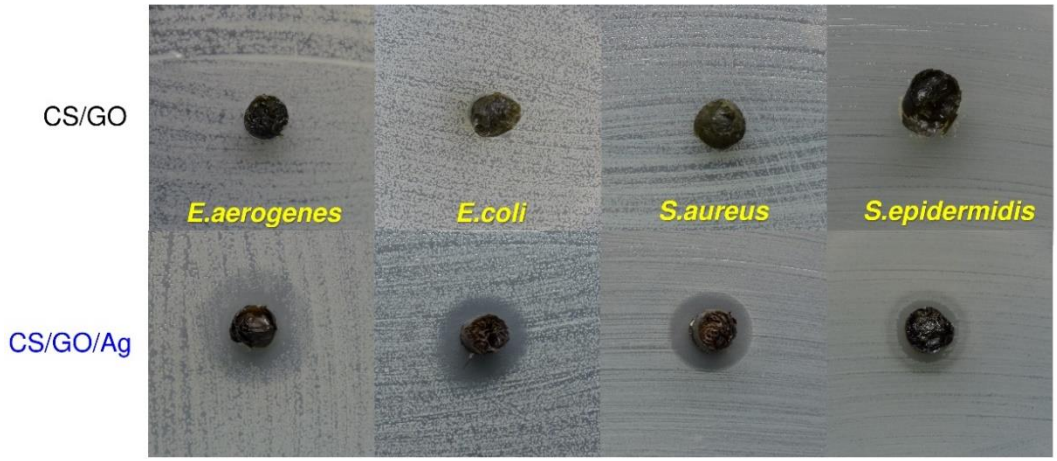

Figure 4.31 Solid disc diffusion studies to elucidate the bacteriostatic activity of CS/GO and CS/GO/Ag hydrogels on nutrient agar medium.

Pure CS/GO hydrogel did not exhibit any visible zone of inhibition (ZoI), suggesting that the presence of chitosan, having innate antimicrobial character alone could not contribute to biocidal activity. In contrast, the CS/GO/Ag hydrogel demonstrated significant antibacterial activity against all four tested microorganisms, resulting in ZoI values ranging from 13.1 to 16.8 mm. Among the selected strains, *E. aerogenes* and *S. epidermidis* exhibited the highest and lowest sensitivity, respectively, to the hydrogel.

Table 4.4 The comparative values of zone of inhibition (ZoI) appeared in disc diffusion tests of pristine and Ag-loaded chitosan-GO hydrogel against four representative bacterial strains.

Sample	**Zone of Inhibition (ZoI, mm)**			
	E. aerogenes	*E. coli*	*S. aureus*	*S. epidermidis*
CS/GO	Nil	Nil	Nil	Nil
CS/GO/Ag	16.84 ± 0.22^{a}	16.38 ± 0.20^{a}	14.9 ± 0.16^{b}	13.09 ± 0.10^{c}

Mean values sharing a common letter within the treatment are not significant at $P < 0.05$

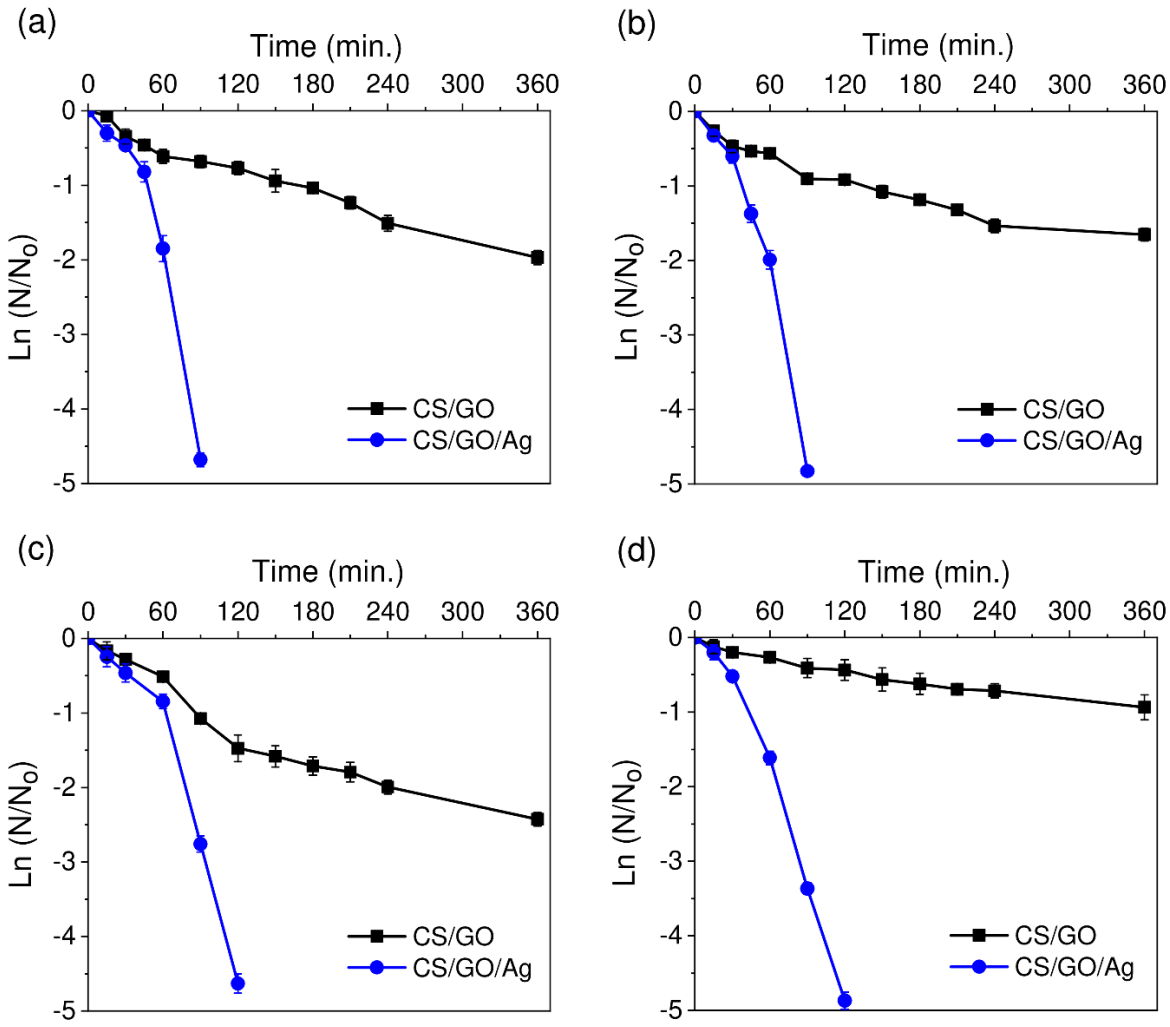

Figure 4.32 The species-specific disinfection kinetics of hydrogels evaluated in 100 mL batch reactors against four strains (a) *E. aerogenes*, (b) *E. coli*, (c) *S. aureus*, and (d) *S. epidermidis* at initial concentration of 10^3 CFU mL^{-1}. (N_o = Initial bacterial concentration, N = bacterial concentration after treatment, CFU mL^{-1}).

4.11.2 Colony Forming Assay

The disinfection performance was further assessed in liquid medium using a 100 ml batch reactor with a fixed initial bacterial concentration of 10^3 CFU mL^{-1} (Figure 4.32a-d). Pristine CS/GO hydrogel failed to achieve complete bacterial eradication against all four strains even after 6 hours under the tested conditions (Figure 4.33). Whereas, CS/GO/Ag hydrogel displayed potent bactericidal activity against all four strains, achieving complete disinfection within 60-120 minutes (Figure 4.34). We observed a distinct species-specific disinfection capabilities of CS/GO/Ag hydrogel, with sensitivity order of *E. aerogenes* > *E. coli* > *S. aureus* > *S. epidermidis*. Interestingly, the hydrogel was found equally efficacious in

complete killing of natural water contaminants as well as biomedical pathogens with a marginal delay of only 30 minutes.

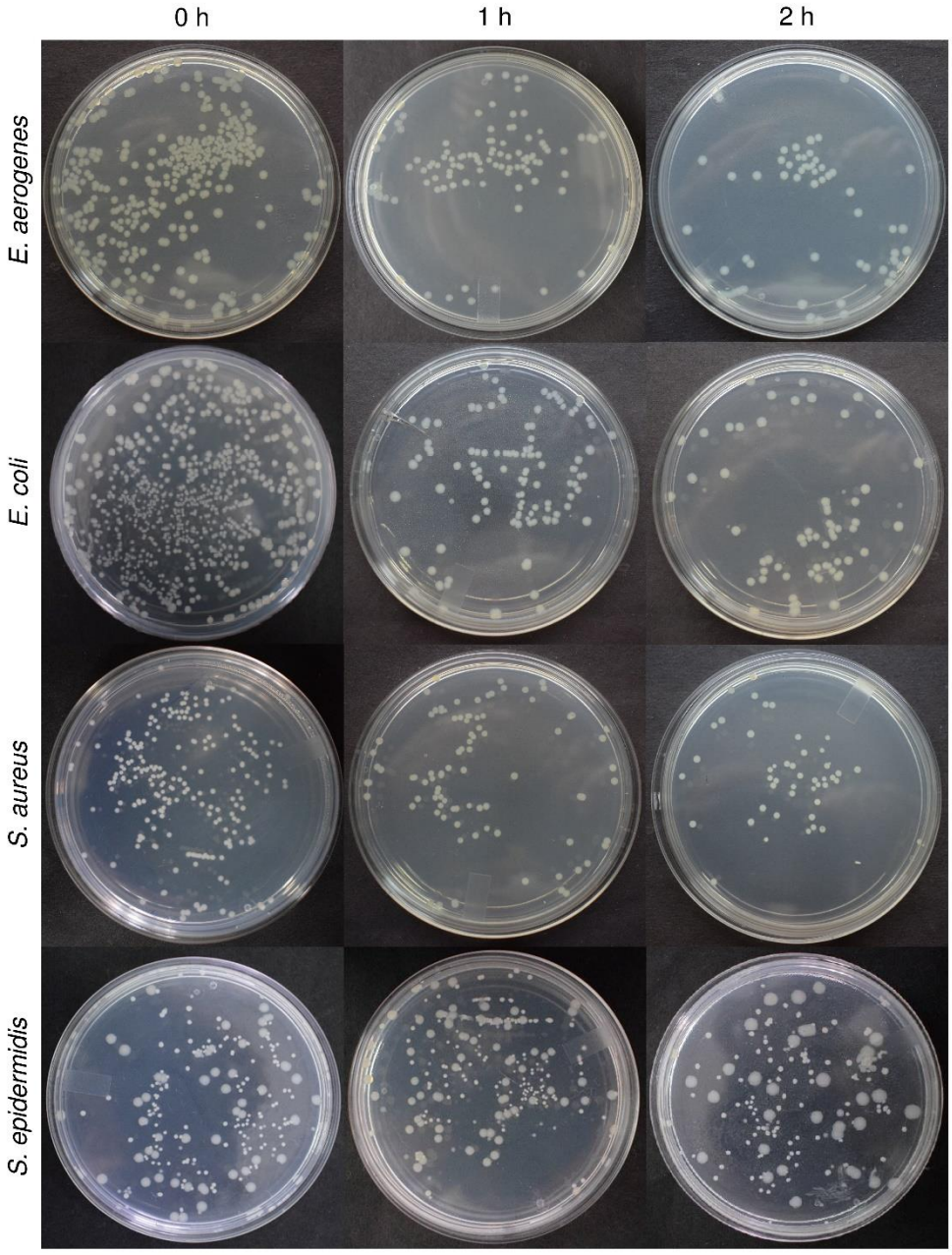

Figure 4.33 Photographic images of bacterial colonies describing the reduction rate in bacterial viability after treatment with pristine chitosan-GO hydrogel disc (diameter 10 mm) in artificially bacteria infested water medium with initial concentration of 10^3 CFU mL^{-1}. The treated aliquots were plated on nutrient agar at time intervals of 0, 1, and 2 h for *E. aerogenes*, *E. coli*, *S. aureus*, and *S. epidermidis* under similar conditions.

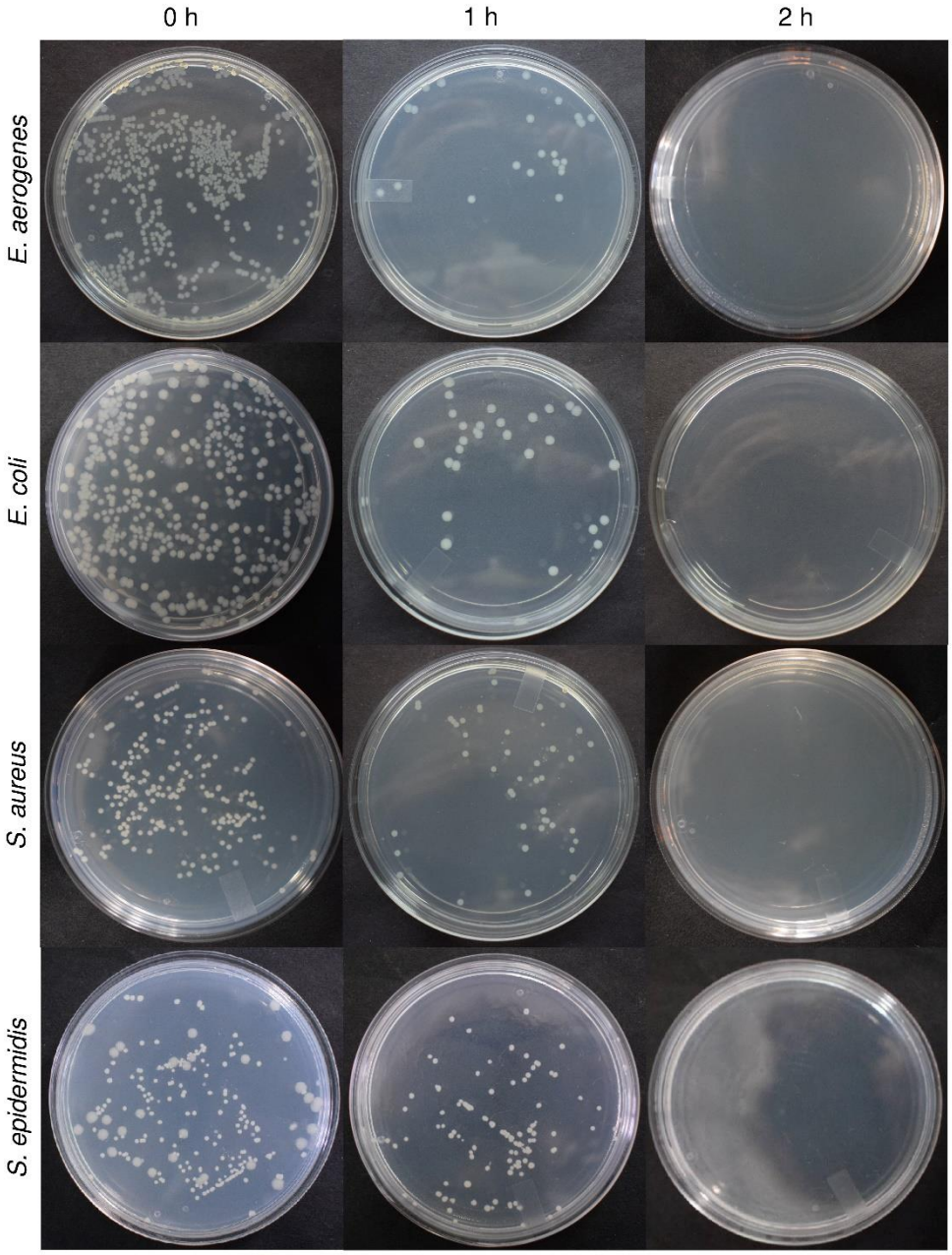

Figure 4.34 Photographic images of bacterial colonies describing the reduction rate in bacterial viability after treatment with chitosan-GO/Ag hydrogel disc (diameter 10 mm) in artificially bacteria infested water medium with initial concentration of 10^3 CFU mL^{-1}. The treated aliquots were plated on nutrient agar at time intervals of 0, 1, and 2 h for *E. aerogenes*, *E. coli*, *S. aureus*, and *S. epidermidis* under similar conditions.

We also evaluated the growth inhibition kinetics at higher bacterial loads, i.e., ~10^4-10^6 CFU mL^{-1}. The CS/GO/Ag hydrogel exhibited ≥90% killing against *E. aerogenes* and *E. coli* within 120 minutes, and ≥87.8% inhibition of *S. aureus* and *S. epidermidis*, at similar initial bacterial counts (Figure 4.35a). These findings highlight the exceptional disinfection performance of CS/GO/Ag hydrogel against a broad-spectrum bacterial species, suitable for practical applications

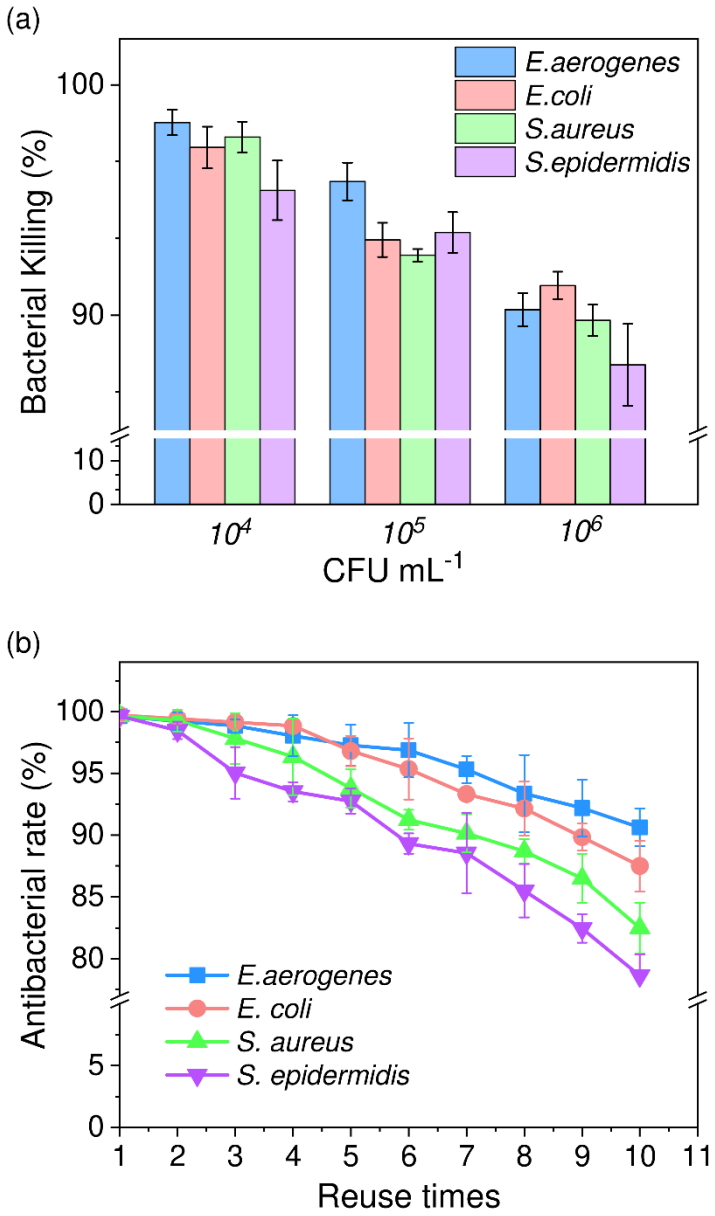

Figure 4.35 Disinfection performance of Ag-loaded hydrogel as a function of (a) higher initial bacterial concentrations (10^4-10^6) and, (b) reuse times against all four strains.

4.11.3 Reusability

The ability to reuse hydrogels is a crucial aspect when considering their sustainable affordability for water disinfection purposes. As depicted in Figure 4.35b, the CS/GO/Ag hydrogel maintained 98% biocidal activity against *E. aerogenes* & *E. coli* for 4 repeated usage, and then slightly reduced to 90.6% over the next six cycles. The hydrogel however displayed a relatively lower effectiveness against biomedical pathogens, *S. aureus* & *S. epidermidis* with 93.5% residual activity after 4 consecutive uses and progressively diminished to 82.5% after 10 cycles. This species-specific biocidal performance observed in disinfection studies can be attributed to differences in the structural morphology and organization of the bacterial cell wall. A thicker peptidoglycan layer on the cell wall of gram-positive species like *S. aureus* & *S. epidermidis* imparts greater protection against antibacterial agents than gram-negative bacteria, *E. aerogenes* and *E. coli* (Khawaja et al. 2018). Moreover, *S. aureus* & *S. epidermidis* belong to adherent and sessile microbial communities which promptly form multilayered biofilms virtually over all surfaces making them resistant towards antibacterial action (Götz 2002; Siciliano et al. 2023). Such results are in agreement with recent studies (Liu et al. 2022; Yang et al. 2023) on chitosan-PVA matrix functionalized with AgNPs, which reported higher inactivation rates for gram-negative bacteria than gram-positive cells.

4.12 Molecular Mechanisms underlying Antibacterial Action of Hydrogel

4.12.1 Assessment of Morphological Damage

Untreated (control) *E. coli* and *S. aureus* cells exhibited a normal morphology with a smooth surface and intact structure through FE-SEM micrographs (Figure 4.36). Whereas, CS/GO/Ag hydrogel-treated *E. coli* cells displayed a significant structural alterations characterized by perforated membranes with ‘pits’ and ‘holes’, indicating substantial damage to cellular integrity, as corroborated through disinfection studies. Treated *S. aureus* cells also displayed altered morphologies with small indents. However, the extent of damage was less pronounced compared to *E. coli*, in consistent with the observed differences in disinfection sensitivities. These findings strongly indicate that the antibacterial mechanism of CS/GO/Ag nanocomposites involves the disruption of cell membranes either due to the direct accumulation of AgNPs/Ag^{+} on the cell wall or inducing the oxidative stress, which arises from the synergistic effect of GO and AgNPs (Li et al. 2019). As a consequence, an irreversible damage occurs to the cell wall/membrane, leading to an increased cell

permeability that allows for the leakage of intracellular components and cause cell death (Huang et al. 2017; Panáček et al. 2021).

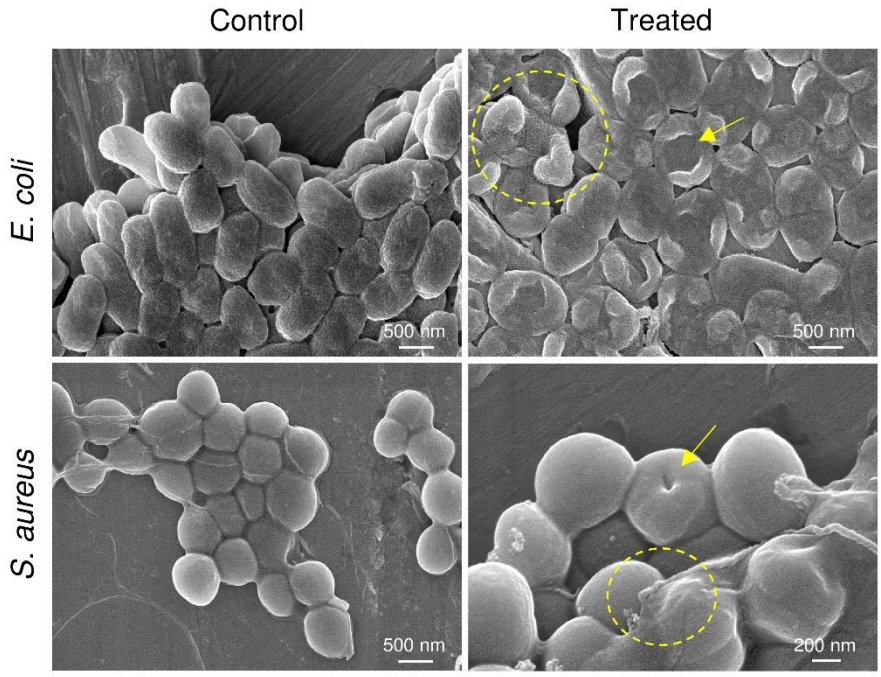

Figure 4.36 Antibacterial mechanism investigation in aspect of membrane integrity destruction, FE-SEM micrographs of untreated and CS/GO/Ag hydrogel treated *E. coli* and *S. aureus* cells.

4.12.2 ROS-mediated Oxidative Stress

We systematically investigated the extent of reactive oxygen species (ROS) generation in hydrogel-treated bacterial suspension (Figure 4.37a). While pure CS/GO hydrogel exhibited a relatively constant ROS levels, the presence of CS/GO/Ag hydrogels led to 2.7-3.9 fold increase in ROS production in *E. aerogenes*, *E. coli*, *S. aureus*, and *S. epidermidis*, respectively (Raw data has been added in appendix-D as Table A1). The enhanced ROS generation is linked to the ability of CS/GO/Ag hydrogels as electron donors on bacterial surface. A rapid electron transfer between AgNPs and GO in hydrogel composite, facilitated the absorption of surface oxygen, resulting in formation of various ROS viz. singlet oxygen, superoxide ions, and hydroxyl radicals (Panda et al. 2018; Zheng and Xie 2021). An abrupt rise in ROS levels at bacterial surfaces disrupts their defence mechanisms, leading to ROS accumulation and triggering the antibacterial response. The excessive ROS levels further initiate a series of oxidative stress reactions within bacteria. These reactions include

destabilization of membrane potential, depletion of ATP, formation of lipid peroxides, reduction in enzyme activity, and damage to cellular proteins and nucleic acids, eventually leading to bacterial cell death (Panda et al. 2018).

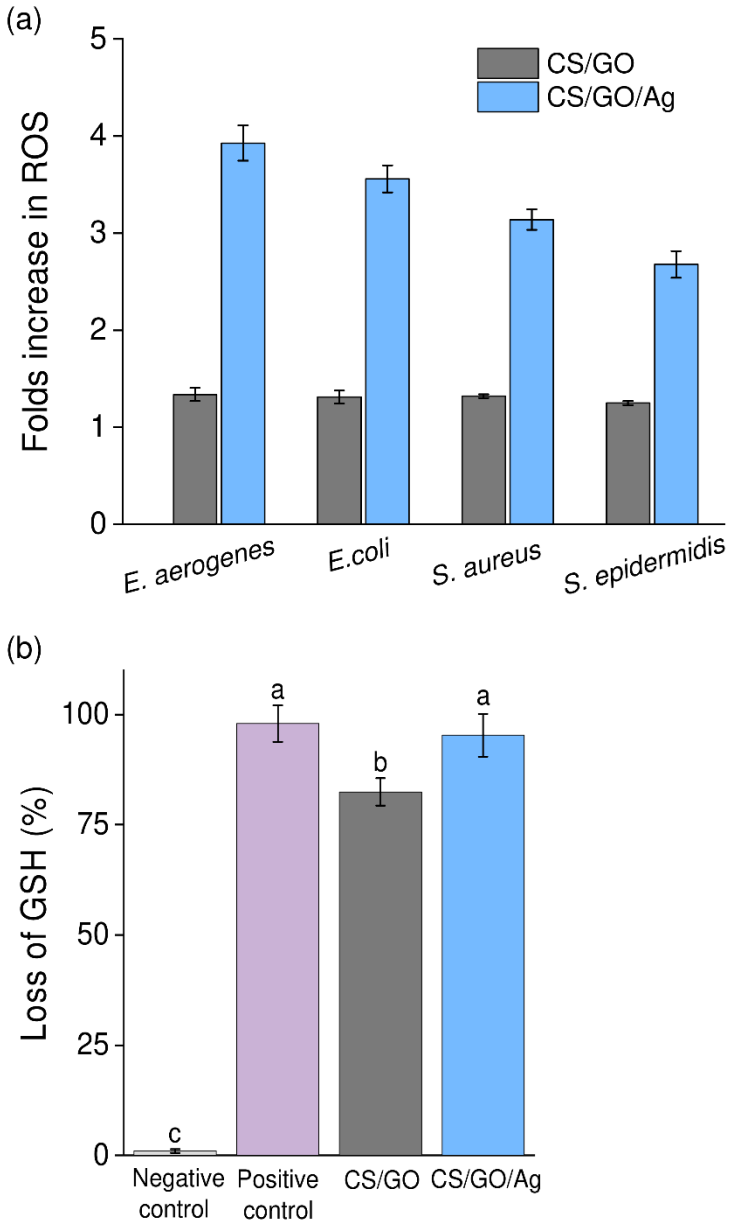

Figure 4.37 Antibacterial mechanism investigation in aspect of oxidative stress, (a) ROS level generation relative to control in *E. aerogenes*, *E. coli*, *S. aureus*, and *S. epidermidis* after exposure to pristine and Ag-loaded hydrogels and, (b) GSH oxidation at 412 nm induced by CS/GO/Ag composites comparative to pristine hydrogel and experimental controls. Mean values sharing a common letter within the columns are not significant at $P < 0.05$.

4.12.3 ROS-independent Oxidative stress

The oxidation of glutathione (GSH), an important bacterial cell constituent is also used as an oxidative stress indicator (Sajjad et al. 2017; Xing et al. 2022). We found that the negative control exhibited minimal GSH oxidation (Figure 4.37b). Pure CS/GO hydrogel displayed 82.42% oxidation of GSH, as the GO has been reported to mediate ROS-independent oxidative stress (Liu et al. 2011). Interestingly, exposure to the CS/GO/Ag hydrogel resulted in a marked increase in GSH oxidation, reaching 95.3%, which was comparable to the positive control group treated with 1 mM H_2O_2 (97.9%). This suggests that CS/GO/Ag hydrogel may release AgNPs/Ag^+ into the interiors of bacterial cell either through damaged cell membrane or by directly penetrating the bacterial cells under the account of direct contact. Consequently, a high oxidative stress induced by CS/GO/Ag could also play a significant role in the apoptosis of bacterial cells.

4.12.4 Cytoplasmic Proteins Leakage

The amount of intracellular proteins released due to membrane leakage was determined through Bradford assay (Figure 4.38a). Pure CS/GO hydrogels exhibited protein leakage ranging from 3.74-4.92 µg mL^{-1} due to the presence of antibacterial ingredients, chitosan and GO. Additionally, protein discharge through cell exocytosis and autolysis might have also contributed to this phenomenon (Li et al. 2019). However, the amount of released protein drastically enhanced against bacteria exposed with CS/GO/Ag hydrogel. The range of released protein was varied between 11.6-18.9 µg mL^{-1}, against all four bacterial strains. A significant protein leakage further confirms the induction of oxidative stress due to the presence of AgNPs to an extent that membrane permeability of the pathogenic bacteria get severely compromised. Consequently, increased membrane permeability would lead to the release of all intracellular components, including proteins.

4.12.5 Inhibition of Cellular Respiration

The amount of lactate dehydrogenase (LDH) release from cell-free culture medium is an indicator of membrane damage and inhibited respiration activity (Figure 4.38b). The LDH release (%) in pristine CS/GO hydrogel were found in range 40-59% against all four tested strains. In contrast, CS/GO/Ag hydrogel caused more LDH release, as dictated by values 61.7-77.2% for similar strains. An abrupt increase in LDH release in culture supernatants is a clear indication of more lysed bacterial cells (Jaworski et al. 2018). These results supports

that following the release of LDH, CS/GO/Ag hydrogels can suppress cellular respiration and reproduction by inhibiting respiratory chain activity.

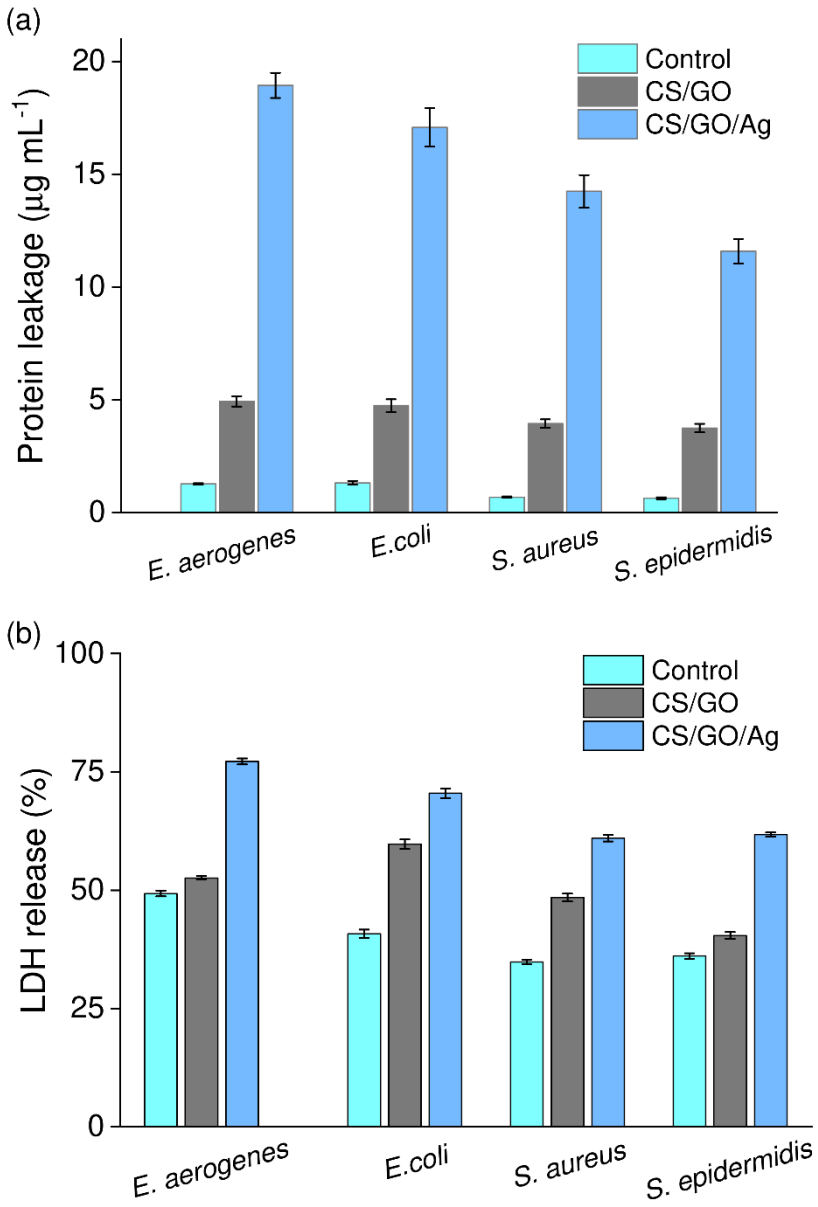

Figure 4.38 Antibacterial mechanism investigation in aspect of leakage of intracellular contents, (a) cytoplasmic proteins and, (b) respiratory chain dehydrogenases (LDH) from all four bacterial species after hydrogel treatment.

Considering all underlying mechanisms, we envisage a bimodal route of the antibacterial mechanism of CS/GO/Ag hydrogel (Figure 4.39) As a primary mechanism, when AgNPs/Ag^{+} ions come into direct contact with bacterial cell wall, they cause destabilization or change in membrane permeability resulting in the leakage of intracellular components (Makvandi et al. 2020). Concurrently, AgNPs significantly perturb the intracellular defence

mechanism of bacteria by inducing elevated ROS production and depleting GSH levels, leading to severe oxidative damage (Wang et al. 2023). Subsequently, they interfere with cellular functions by inhibiting enzymatic pathways and damaging DNA, ultimately leading to bacterial cell death. It is important to note that while AgNPs in the CS/GO/Ag hydrogel efficiently elicit a biocidal effect, GO also has the potential to display antibacterial character due to its large surface area, enabling effective interaction between microbial cells and AgNPs. The inclusion of GO would only augments the damage induced by silver, as it can raise ROS-independent oxidative stress (Liu et al. 2011) further highlighting its role in the hydrogel for synergistic antibacterial response.

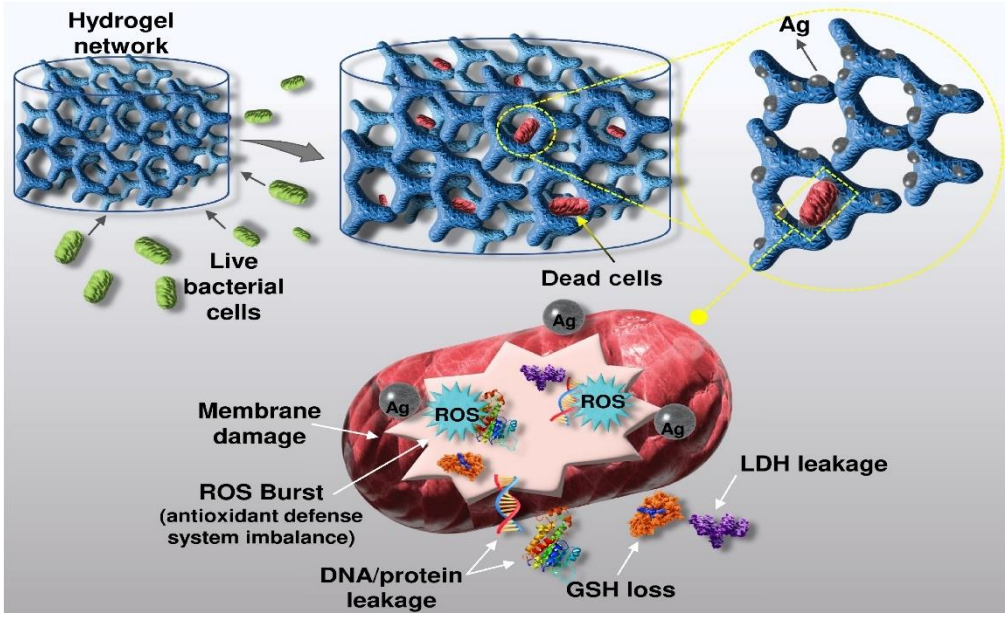

Figure 4.39 Schematic illustration of the proposed bimodal mechanism of CS/GO/Ag hydrogel.

4.13 Continuous-flow Water Disinfection

The core concept of water disinfection using a continuous flow hydrogel reactor is illustrated in Figure 4.40a. As a preliminary feature, we investigated the potential of utilizing CS/GO/Ag hydrogel as a column-bed for disinfection without requiring regeneration. The ultrapure water along with other natural water sources, i.e., rain water and river water were selected to carry out experiments (Figure 4.40b). The median disinfection capacity of hydrogel was observed to be highest in ultrapure water (3800 runs), followed by river water (3500 runs), and rainwater (3400 runs) before reaching complete exhaustion. We found hydrogel to be equally efficacious in executing disinfection across all water samples

envisaging practical adaptability of this system. Though, a slight variance in its maximum disinfection potential was observed in these samples, the overall biocidal effectiveness of the hydrogel remained consistent. This highlights a strong permeation capacity of hydrogel network, adequately preserving immobilized AgNPs from surface oxidation, even under environmentally relevant conditions containing traces of ionic species viz. chlorides, sulphates and carbonates (Figure 4.40c). Concomitantly, this shielding mechanism ensures a more profound bacteria-AgNPs interactions as water traverses the porous bed, optimizing the contact area and facilitating a rapid contact-driven disinfection response.

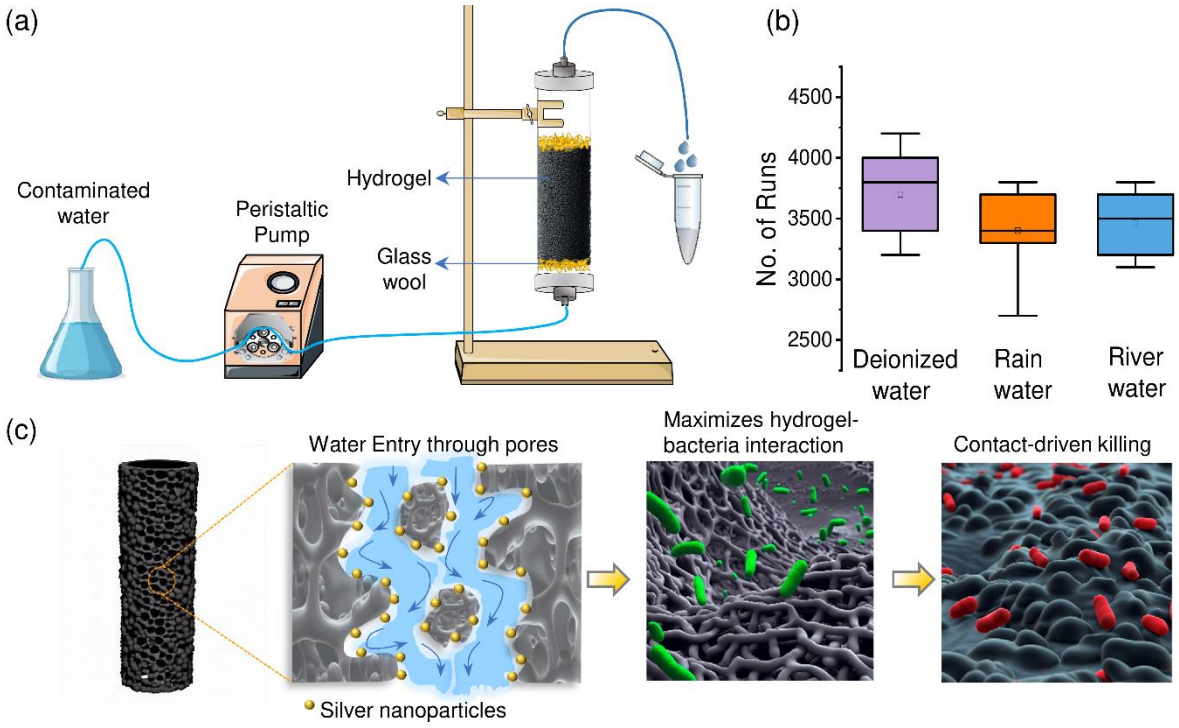

Figure 4.40 (a) Schematic representation of CS/GO/Ag hydrogels as a column filter in a continuous-flow disinfection reactor, (b) Hydrogel's capacity to disinfect water until complete exhaustion across multiple runs in distinct water samples: deionized water, rainwater, and river water, and (c) A mechanistic overview of continuous-flow water disinfection.

As a next step, three process parameters of fixed-bed reactor i.e., inlet flow rate, bed height and initial bacterial count were optimized to achieve maximum disinfection over long runs (Figure 4.41a-c). While analysing the impact of flow rate (1.3-5.1 mL min^{-1}), the initial bacterial load and hydrogel bed height were set to ~10^3 CFU mL^{-1} and 8 cm, respectively. Expectedly, the antibacterial rate was gradually decreased with increasing water flow as higher flow-rates critically reduce the hydraulic residence time (HRT) (Li et al. 2014),

rendering lesser possibilities of direct contact between hydrogel and contaminated water. Although >99% antibacterial activity could be achieved at both, 1.3 and 2.6 mL min^{-1} flow-rates, we opted 2.6 mL min^{-1} having ~3 minutes HRT for our studies as it leads to lesser operation time and eventually, lower power consumption in addition to higher reactor efficiency (Li et al. 2019). Similarly, a bed height of 8 cm and 10^3 CFU mL^{-1} as initial bacterial count was found as optimized values for achieving desired level of disinfection.

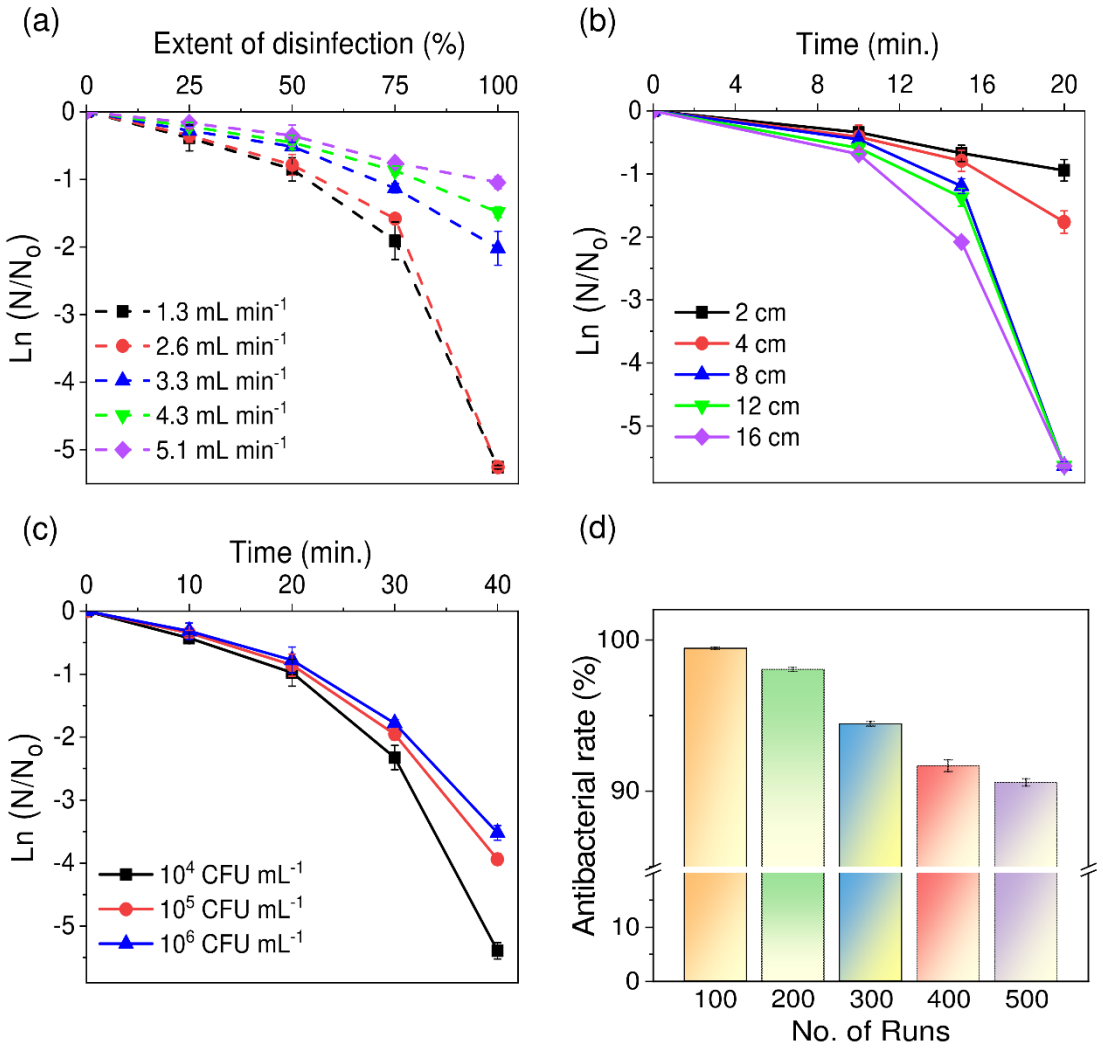

Figure 4.41 Effect of process parameters (a) water flow rate (b) filter bed height (c) initial bacterial load in inlet on the disinfection performance, and (d) Reuse potential of hydrogel-column filter to the number of runs till exhibiting ≥ 90% antibacterial rate. (N_o = Initial bacterial concentration, N = bacterial concentration after treatment, CFU mL^{-1}).

Employing optimized parameters, the hydrogel-based reactor yielded excellent results in disinfecting river water with each regeneration cycle (Figure 4.41d). Regeneration stands as a

critical process to replenish disinfection efficacy of inactive hydrogel, thereby enhancing its practical affordability and minimizing material loss. From a commercial standpoint, regeneration estimates the lifespan of the hydrogel-bed and its sustainable functionality. A freshly-installed hydrogel could disinfect ~10L of water without regeneration. Though, our observation highlighted a gradual decline in disinfection potential of the hydrogel-based reactor during continuous operation after its first use. As witnessed before, the inherent water chemistry such as, alkalinity, hardness and the presence of natural organic matter (NOM) inevitably affect surface passivation of AgNPs, even in their immobilized form and slow down the rate of silver release. The simultaneous existence of hardness (Ca^{2+} and Mg^{2+} based) and the NOM also induce charge neutralization of AgNPs, causing the formation of larger silver aggregates. The hydrogel bed displayed reusability for a maximum of five regeneration cycles before its antibacterial activity dropped below the 90% threshold, indicating it was no longer suitable for further disinfection purposes. The resilience of the hydrogel nanocomposite against natural resources is exemplified through its capability to disinfect large volumes of rain water (up to 30L) with a microbial load of 10^5 CFU mL^{-1} without regeneration (Figure 4.42a).

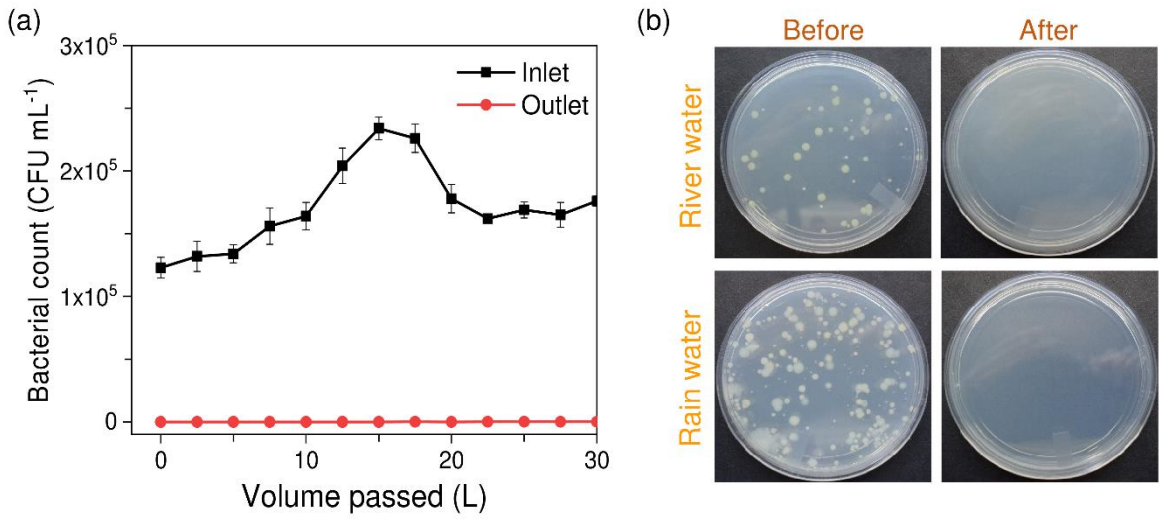

Figure 4.42 (a) Column data for the disinfection of *E. coli* contaminated water. (b) Culture plates displaying indigenous micro-flora in natural water samples and their subsequent removal using hydrogel-based reactor operated under optimized conditions (flow rate 2.6 mL min^{-1}, 8 cm bed height, 3 minutes).

The chosen samples i.e., river water and rain water include vast and complex habitats for diverse microbial communities and physicochemical parameters (Table 4.5). The CS/GO/Ag

hydrogel filter depicted complete killing of all natural contaminants within 20 minutes (Figure 4.42b).

Table 4.5 Physicochemical characteristics of natural water sources within Patiala district, Punjab, India

Characteristics	**Water Samples**	
Water Sources	Bhakra Canal	Direct rainfall
Water Type	River water	Rain water
Locations	30.303˚ N 76.328˚ E	30.354˚ N 76.371˚ E
Odour	Odourless	Odourless
pH	7.95 ± 0.15	7.20 ± 0.07
Total alkalinity	96	43
TDS (mg L^{-1})	131	25
TSS (mg L^{-1})	10	8
BOD (mg L^{-1})	<5	<5
COD (mg L^{-1})	<5	<5
Total Hardness (mg L^{-1} as $CaCO_3$)	58.5	41
Microbial colony counts (CFU mL^{-1})	48 ± 9	138 ± 14

4.14 Modelling of Disinfection Kinetics

The comparison of various models offers a valuable framework for enhancing our understandings and predictive ability for disinfection kinetics, and gaining deeper insights into the underlying mechanisms and variables that influence the disinfection process. The estimation of two different models, their kinetic parameters and regression coefficients are summarized in Table 4.6. The fitted curves to log-linear + shoulder model are shown in Figure 4.43a-c. The parameter 'k', which represents the maximum inactivation rate coefficient (min^{-1}) of disinfection process, declined either with increase in flow-rate (1.3- 5.1 mL min^{-1}) or the microbial load (10^4-10^6 CFU mL^{-1}). Whereas, an increase in bed height (2-16 cm) reflected a concomitant enhancement in antibacterial rate since the value of k increased from 0.16 ± 0.02 to 2.07 ± 0.22 min^{-1}. Applying log-linear + shoulder model also enabled in determining the protective mechanism of the bacteria, which is associated with the presence of more resistant sub-population. We observed that the shoulder length 'S' decreased with increase in flow-rate and microbial load which could be linked to lesser aggregation of the dead cells. Meanwhile, shoulder length increased with higher output of cell destruction as inactivation rate increased with bed height (Mustapha et al. 2020).

Table 4.6 Kinetic and statistical parameters of log-linear + shoulder and Weibull models obtained from the GInaFIT tool.

V	Log-linear +shoulder				Weibull			
FR	**k**	**S**	**R^2**	**RMSE**	**δ**	**ρ**	**R^2**	**RMSE**
1.3	0.34 ±0.06	67.04 ±5.32	0.9830	0.4230	63.44 ±4.61	4.30 ±0.54	0.9933	0.2456
2.6	0.31 ±0.05	63.80 ±4.18	0.9802	0.3931	68.84 ±5.01	3.54 ±0.80	0.9910	0.2860
3.3	0.08 ±0.01	42.70 ±7.12	0.9909	0.1084	71.90 ±3.98	2.02 ±0.27	0.9941	0.0875
4.3	0.05 ±0.01	39.87 ±6.28	0.9949	0.0595	81.38 ±3.03	1.75 ±0.19	0.9959	0.0533
5.1	0.04 ±0.00	34.48 ±8.84	0.9943	0.0460	95.89 ±3.97	1.42 ±0.19	0.9937	0.0482
BH								
2	0.16 ±0.02	6.92 ±1.91	0.9968	0.0403	20.61 ±0.86	1.38 ±0.18	0.9967	0.0406
4	0.40 ±0.09	10.42 ±2.29	0.9833	0.1685	16.14 ±1.01	2.51 ±0.53	0.9921	0.1159
8	1.63 ±0.32	12.54 ±1.20	0.9878	0.4804	14.77 ±0.85	3.41 ±0.28	0.9970	0.2476
12	1.98 ±0.29	13.98 ±0.57	0.9911	0.3202	14.26 ±1.12	5.01 ±1.08	0.9949	0.3168
16	2.07 ±0.22	13.79 ±0.77	0.9949	0.4180	12.09 ±0.53	5.61 ±1.00	0.9990	0.1365
BL								
10^4	0.56 ±0.12	20.17 ±3.87	0.9729	0.5060	22.50 ±1.71	2.33 ±0.21	0.9951	0.2146
10^5	0.38 ±0.05	17.73 ±2.89	0.9854	0.2714	22.83 ±1.28	2.39 ±0.22	0.9973	0.1172
10^6	0.34 ±0.05	17.66 ±2.75	0.9876	0.2239	23.63 ±1.20	2.86 ±0.36	0.9975	0.1005
NS								
RI	0.57 ±0.02	3.57 ±0.58	0.9988	0.0820	7.14 ±0.43	1.38 ±0.07	0.9990	0.0762
RA	0.77 ±0.11	4.41 ±2.19	0.9820	0.4203	7.16 ±1.03	1.65 ±0.22	0.9941	0.2396

V: Variables, FR: Flow-rate (in mL min^{-1}), BH: Bed height (in cm), BL: Bacterial load concentration (in CFU mL^{-1}), NS: Natural samples, RI: River water, RA: Rain water, RMSE: Root mean square error. Kinetic parameters are reported as mean ±SE at $p < 0.05$.

The simplicity and robustness of the Weibull model has been widely exploited for non-thermal microbial inactivation analysis too (Ghodsi et al. 2021; Thakur et al. 2021). The Weibull model resulted in distinctive curves (Figure 4.43d-f) with 'δ' and 'ρ' as kinetic parameters (Table 4.6). The scale parameter δ (min.), represent the time required for first decimal reduction of bacterial colonies and it is reciprocal of microbial inactivation rate. Thus, higher δ values depict slower disinfection process of microorganisms (Mustapha et al. 2020) and in this study, δ values were seen to be higher for flow-rate and microbial load kinetic variables than bed height.

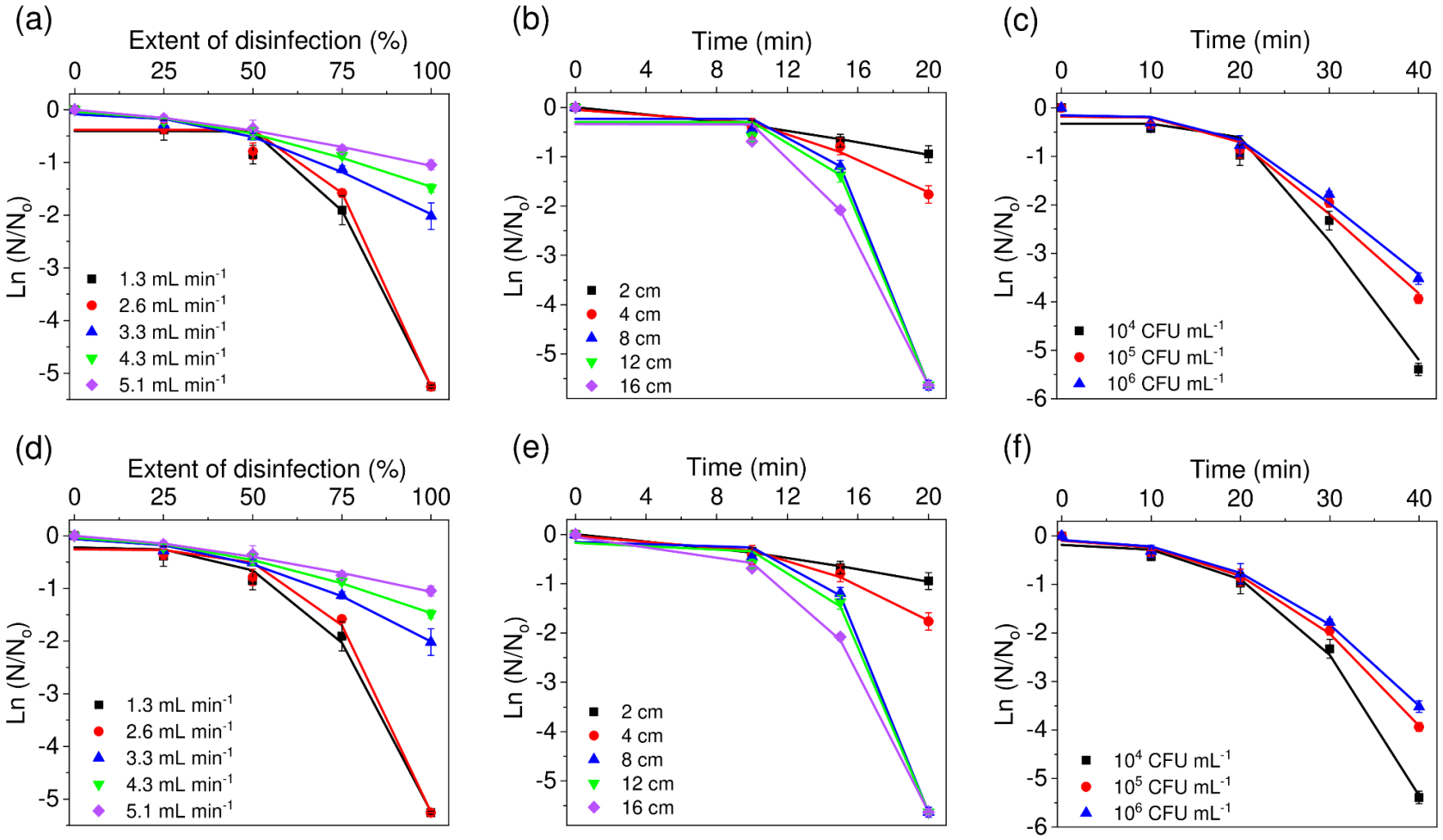

Figure 4.43 Effect of process parameters (a, d) water flow rate (b, e) filter bed height, and (c, f) initial bacterial load on the disinfection performance corroborated using log-linear +shoulder model (a-c) and Weibull model (d-f). The symbols represent experimental data while the solid lines show fitted data. (N_o = Initial bacterial concentration, N = bacterial concentration after treatment, CFU mL^{-1}).

With change of flow-rate from 1.3 to 2.6 mL min^{-1}, δ increased with first decimal reduction occurring after 63.44 ±4.61 and 68.84 ±5.01% progression of disinfection cycle, respectively has been completed. At highest flow-rate of 5.1 mL min^{-1}, decimal reduction time increased even further (95.89 ±3.97 %) thus, depicting lower antibacterial activity with increment in flow-rate. Similarly, increase in δ values from 22.50 ±1.71 to 23.63 ±1.20 minutes resonated well with slow bacterial killing rate when microbial concentration augmented from 10^4 to 10^6 CFU mL^{-1}. In contrast, decrease in decimal reduction time from 20.61 ± 0.86 to 14.77 ± 0.85 minutes with increase in bed height from 2 to 8 cm displayed the effectiveness of hydrogel in reduction of pathogens. Although, δ declined further by a margin of 2 minutes at 16 cm bed height however, the antibacterial rate (99%) remained unaffected. Furthermore, shape parameter 'ρ' defines the concave and convex curvature of fit at ρ <1 and >1 with "tailing/increasing resistance" and "shouldering/decreasing resistance" portion, respectively, attributing to variations in the resistance of bacteria to disinfection treatment (Buzrul 2022). In our study, with ρ >1 for all the kinetic variables depicted convex shaped inactivation trends implying that remaining cells have high probability of dying and over the time the bacterial cells have weakened and damage has increased.

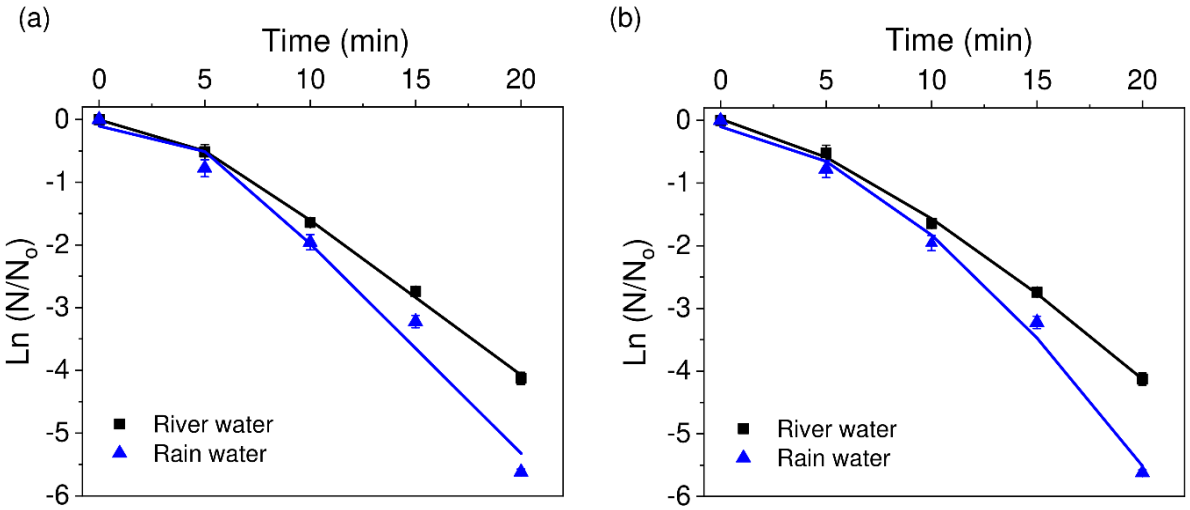

Figure 4.44 The disinfection kinetics of natural environmental samples (river and rain water) treated in continuous-flow hydrogel column reactor at optimized flow rate of 2.6 ± 0.18 mL min^{-1} and 8 cm bed height for 20 mins using (a) log-linear +shoulder model, and (b) Weibull model. Symbols represent experimental data while the solid lines show predicted data using mathematical models.

The studied models presented comparable fittings to the inactivation data as indicated by the determination coefficients and standard error values, which were within the typical range for microbial decontamination studies (Agnihotri et al. 2019; Esua et al. 2022). Generally, R^2 values close to 1 and smaller RMSE values denote the better fitting ability of a particular model (Buzrul 2022; Mustapha et al. 2020). The data for log-linear +shoulder model presented a fairly good fit for bacterial inactivation patterns with R^2 and RMSE values ranging 0.9802-0.9969; 0.0403-0.5060, respectively. However, the Weibull model satisfactorily explained and adequately described the disinfection data as it accounted for response variability in the range of 0.9910-0.9990 and 0.0406-0.3168 for R^2 and RMSE, respectively. Additionally, Weibull model also performed well for bacterial reduction patterns of natural water samples with δ, R^2 and RMSE values 7.14 ±0.43 min., 0.9990, and 0.0762 for river water; 7.16 ± 1.03 min., 0.9941, and 0.2396 for rain water (Figure 4.44a-b, Table 4.6).

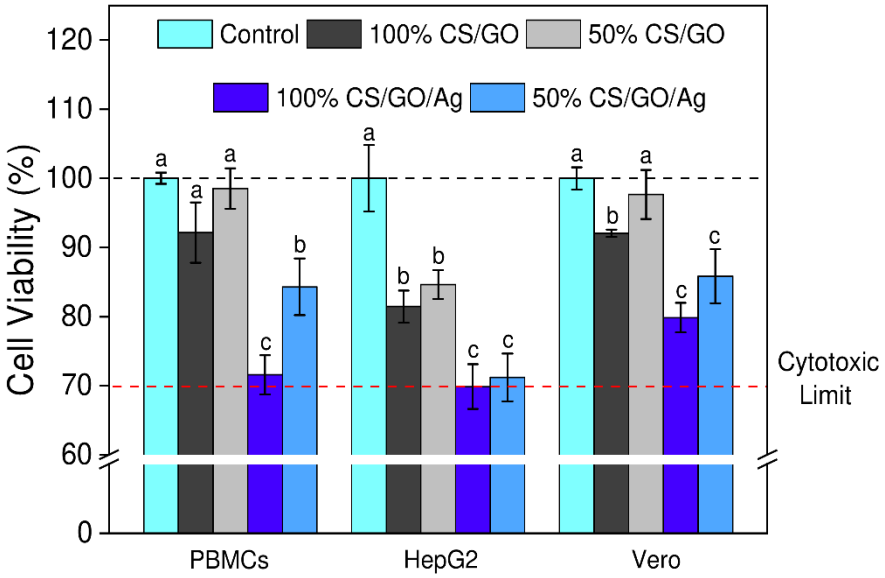

Figure 4.45 *In vitro* biocompatibility of 100% and 50% hydrogel extracts after 24 h incubation with PBMCs, HepG2 and Vero cell lines as determined by MTT assay and reported in terms of % cell viability. Mean values displaying different letters within the columns are significantly different at $P < 0.05$.

4.15 Mammalian Cell Cytotoxicity of CS/GO/Ag Hydrogel

The cytotoxicity of Ag-laden CS/GO hydrogel extracts (50%, 100%) was tested against human peripheral blood mononuclear cells (PBMCs), HepG2, and Vero cells (Figure 4.45).

PBMCs represent the primary defence line of immune system during nanomaterials' uptake in human body, while HepG2 and Vero cells served as *in vitro* models, aligning with ISO 10993-5 standards for biocompatibility assessments (ISO 2009). The standard reflects a cell viability of ≥70% as threshold level for cytotoxicity safety (red dashed line, Figure 4.45). Results indicated that neither CS/GO nor CS/GO/Ag hydrogel extracts induced any potential cytotoxicity in PBMCs, as both led to viabilities surpassing 70%. Specifically, pristine CS/GO extracts exhibited 92.1% and 98.5% cell viabilities against 100% and 50% extracts, respectively, whereas these values declined to 71.5% and 84.3% for 100% and 50% CS/GO/Ag hydrogel composite extracts. Similarly, in Vero cells, viabilities dropped from 85.8% to 79.8% with increasing CS/GO/Ag extract concentration (50% to 100%) while remaining above the red line.

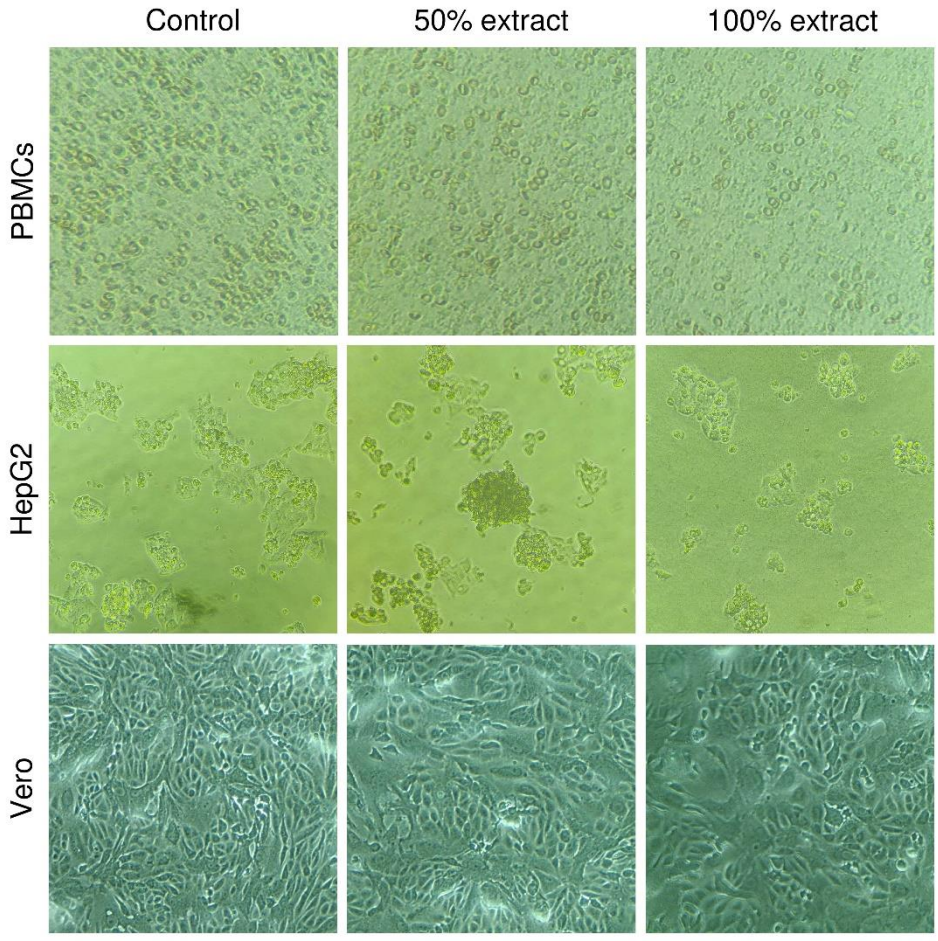

Figure 4.46 Bright-field microscopic images displaying morphology of PBMCs, HepG2, and Vero cell lines after treatment with 100% and 50% extracts of CS/GO/Ag nanocomposites in comparison to control cells.

In HepG2 cells, exposure to 100% Ag-loaded hydrogel extract led to a minor viability decrease of 69.8%, contrasting with a 71.2% viability for the 50% extract. The diminished viabilities observed with CS/GO/Ag hydrogels, compared to their pristine counterparts, stem from the cytotoxic potential of AgNPs, inducing apoptosis and necrosis via ROS-mediated oxidative stress (Paino and Zucolotto 2015; Panáček et al. 2021). We found HepG2 cells to be more sensitive to cytotoxicity of AgNPs than PBMCs and Vero cell lines. Optical micrographs also a displayed well defined and extended morphologies of cell lines with virtually no sign of cellular lysis and debris (Figure 4.46). Moreover, no significant change in shape of cells occurred and morphologies of treated cells were comparable to that of negative control. All these evidences establish the CS/GO/Ag hydrogel as non-cytotoxic against most of the mammalian cells.

4.16 Synthesis of Chitosan/Poly(vinyl alcohol)/Graphene Oxide (CS/PVA/GO) Coatings

The schematic representation of coating fabrication is shown in Figure 4.47. With spread casting and evaporation strategy, polymeric nanocomposite coatings from preformulated solutions were prepared. The casting solutions constituted of chitosan, PVA, and GO where, positively charged chitosan electrostatically interacted with negatively charged GO sheets. Additionally, strong hydrogen bonding between amino groups of chitosan and oxygen functionalities of GO were also prevalent. Meanwhile, hydroxyl groups on PVA chains formed stable intermolecular hydrogen bonds with oxygen groups of GO (Wang et al. 2015).

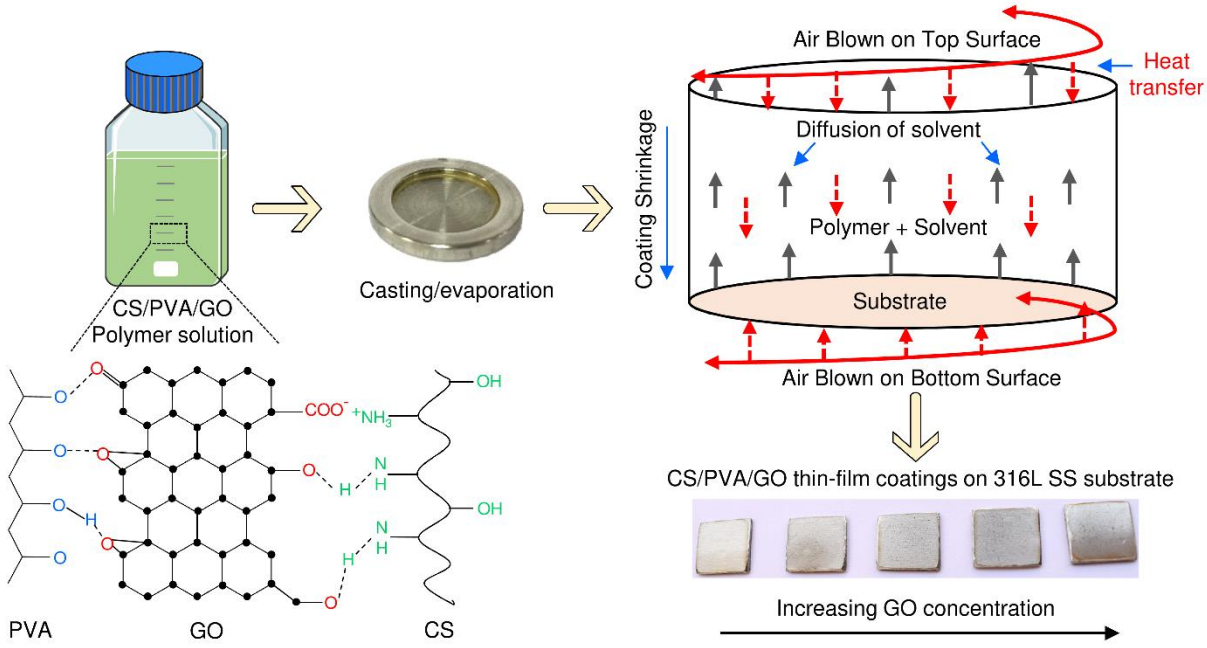

Figure 4.47 Schematic representation of plausible network interactions among chitosan, PVA, and GO for coatings formation along with driving forces behind their subsequent drying process.

The polymer solution dispersed onto the entire area of the sample holder started to evaporate instantly into the surrounding air, which resulted in instantaneous weight loss of coating solution. Since, the sample holder was made of impermeable 316L stainless steel, mass transfer could only take place from the top of casting solution to the air. However, heat transfer could take place from the both sides, top and bottom. The thickness of the coating contracted in the longitudinal direction towards the substrate. Initially, drying was externally controlled due to high solvent amount on the top surface. During the course of drying, the solvent level at top of the coating decreased and drying became internally controlled due to

the diffusion process within the coating. Therefore, combination of such driving forces in drying process resulted in formation of water based polymer thin-film coatings.

4.16.1 Gravimetric Drying Studies

The effect of graphene oxide (GO) content on the drying behaviour of chitosan-poly (vinyl alcohol) polymeric coatings was evaluated via different drying parameters. The initial thicknesses (~700 µm and ~1400 µm) in each case changed because some amount of solution remained in the micropipette tip while pouring. For better comparison of the results, each thickness has been normalized with respect to its initial thickness and plotted as required.

Residual Solvent

The amount of solvent that is left behind which then diffuses into the dried coating at the later stage is called residual solvent. It has been associated with the defects incurred during the drying process hence, residual solvent percentage of all coatings were determined. As shown in Figure 4.48a and Figure 4.49a, decrease in residual solvent percentage with increasing time period was witnessed in both cases. Initially, solvent evaporated at a faster rate due to the presence of high amount of solvent at the top surface. However, this rate decreased with progression of time as the process became diffusion controlled due to poor diffusion of solvent. For control coatings (CS/PVA), residual solvent (%) were recorded at the lowest in both cases (~700 µm-1.03%; ~1400 µm-1.67%), depicting that solvent was evaporated easily as compared to GO incorporated coatings.

With increment in GO concentration, increase in residual solvent percentage was observed i.e. 2.01%, 5.31%, 7.83%, and 9.97% for 0.05, 0.075, 0.1, and 0.15 wt.% GO, respectively in coatings of ~700 µm. On the other hand, in coatings of ~1400 µm initial thickness, solvent evaporation was 94.89%, 93.2%, 91.02%, and 89.79% when GO concentration increased from 0.05-0.15 wt.%. This phenomenon can be justified by the fact that graphene oxide has hydrophilic ability and polar molecular adsorption characteristics (Smith et al. 2019). Therefore, with high graphene oxide content, more amount of solvent remains attached to its polar functional groups such as (-COOH) carboxyl moieties. In control sample however, in the absence of GO as a counter effect more solvent was able to escape giving rise to the lowest amount of residual solvent. The increase in residual solvent (%) in ~1400 µm coatings as compared to ~700 µm coatings could be ascribed to the increase in initial volume of

coating solution which results in overall increases in the amount of graphene oxide. Hence, additional GO traps more solvent thereby giving rise in percentage of residual solvent.

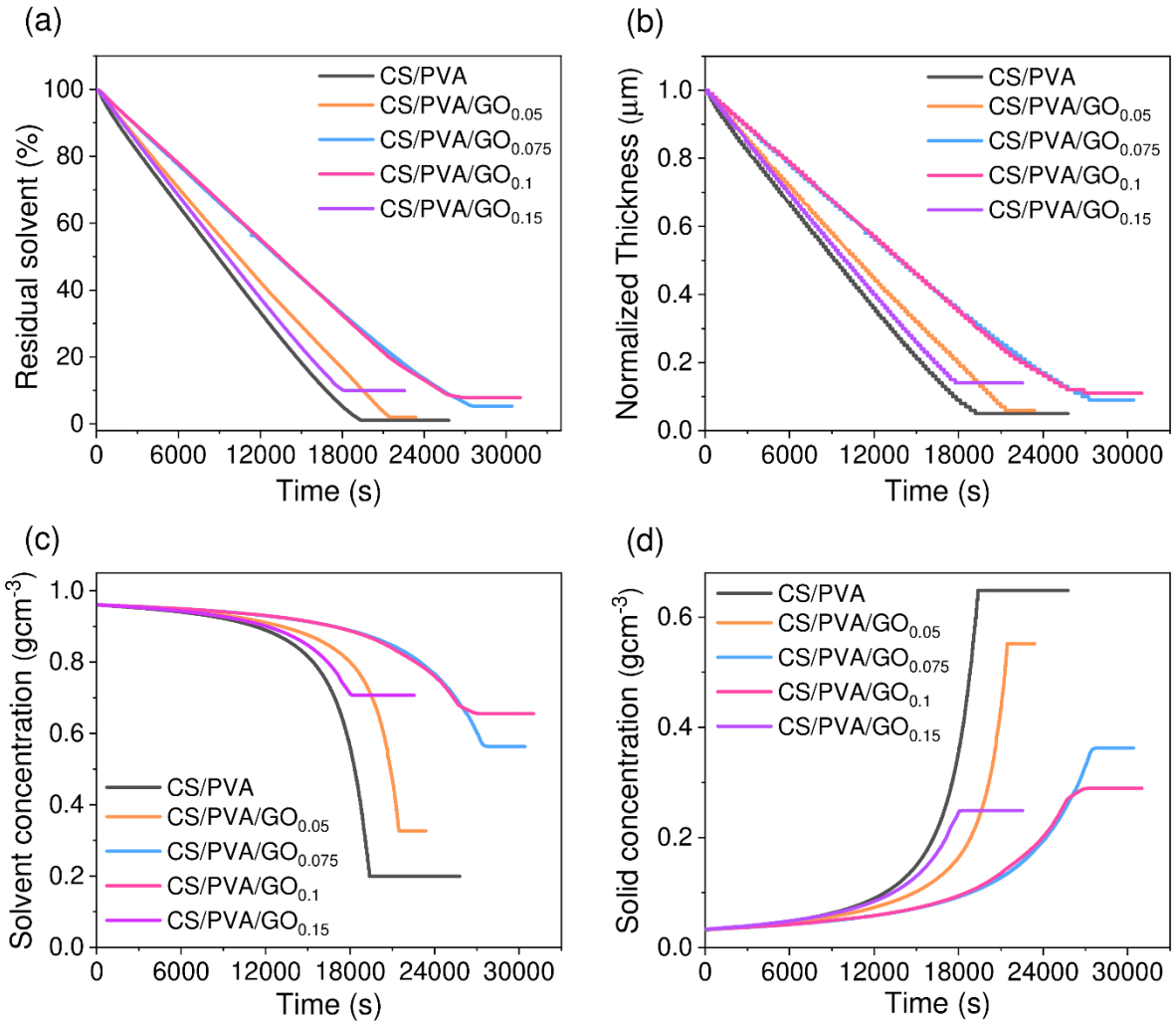

Figure 4.48 (a) Residual Solvent, (b) Normalized thickness, (c) Solvent concentration, and (d) solid concentration of coatings at ~700 µm plotted as a function of time.

Coating Thickness

Thickness of polymeric coatings observed, suggested a common linear descend with respect to time up to a certain point and then plateaued out (Figure 4.48b and Figure 4.49b). Coatings with initial thickness of ~700 µm at GO concentration of 0.05, 0.075, 0.1, and 0.15 wt.% reduced to final thickness of 44 µm, 71 µm, 88 µm, and 95 µm, respectively. While coatings with ~1400 µm initial thickness contracted to final values of 128 µm, 154 µm, 187 µm, and 203 µm with rise in GO concentration (Table 4.7). It is established that the coating left with high amount of residual solvent (%) at the end of drying period will be significantly thicker

(Sharma et al. 2017). Therefore, these observations aligned well with residual solvent (%) study. The introduction of graphene oxide as a filler resulted in increase of final coating thickness because higher amount of GO eventually entrapped more solvent in its structure. Amongst the coatings with graphene oxide, CS/PVA/$GO_{0.05}$ (~700 µm) had the lowest amount of residual solvent, leaving it the thinnest when completely dried.

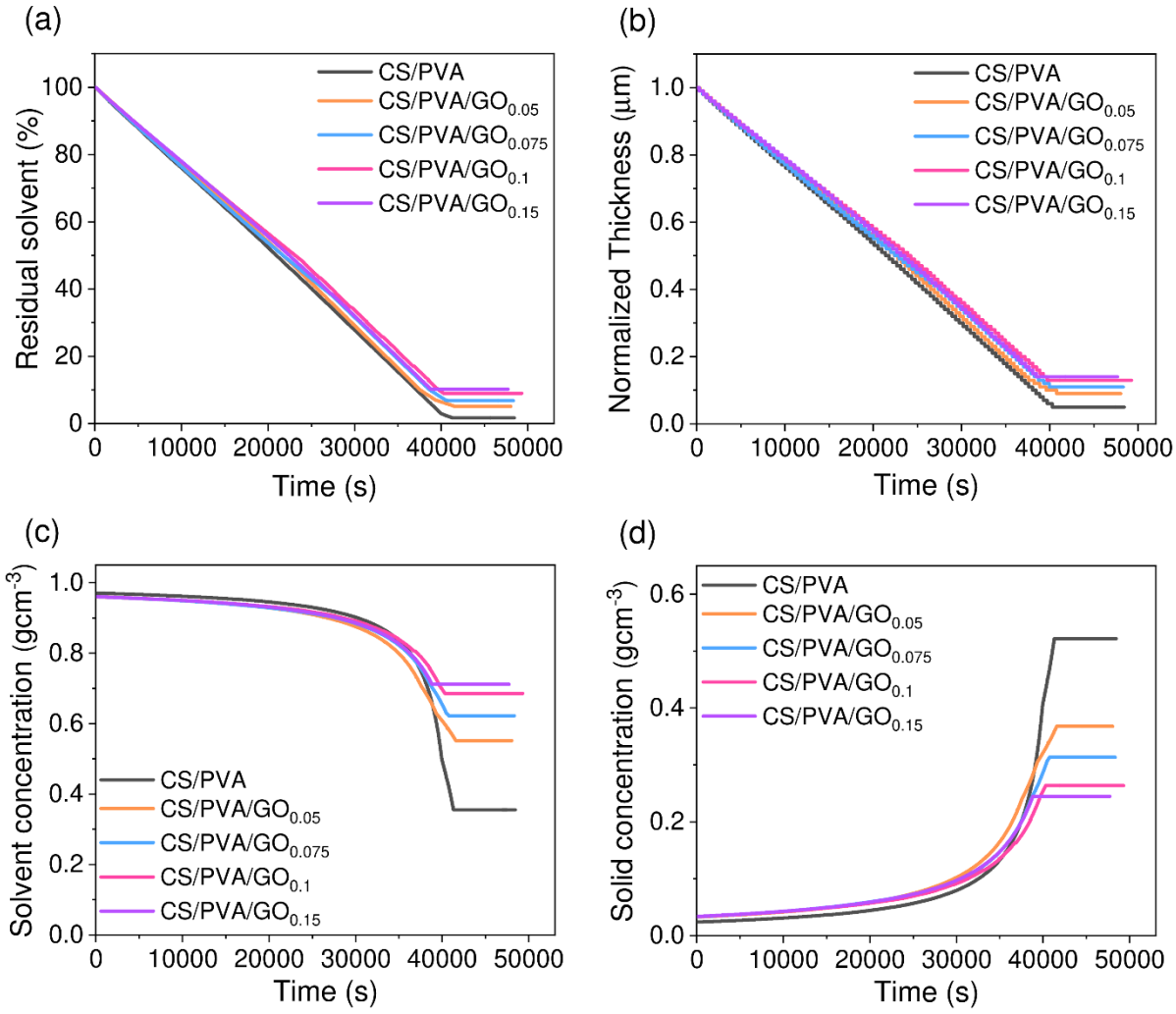

Figure 4.49 (a) Residual solvent, (b) Normalized thickness, (c) Solvent concentration, and (d) solid concentration of coatings at ~1400 µm plotted as a function of time.

Average Solvent Concentration

The average solvent concentration specifies the solvent evaporated from coating solutions which provides an insight on their drying period and residual solvent (%). An exponential decrease in solvent concentration with time was recorded as it started to evaporate under convection which levelled off after a while. In control coatings, the solvent concentration

reached to final values of 0.199 g cm^{-3} (~700 µm) and 0.356 g cm^{-3} (~1400 µm) before becoming constant. Final solvent concentrations for lower initial thickness coatings were 0.326 g cm^{-3}, 0.563 g cm^{-3}, 0.655 g cm^{-3}, and 0.707 g cm^{-3} with increasing GO concentrations (0.05-0.15 wt.%) at the end of their respective drying times (Figure 4.48c). In case of ~1400 µm thickness coatings, solvent concentration values increased to 0.552 g cm^{-3}, 0.622 g cm^{-3} , 0.685 g cm^{-3} , and 0.712 g cm^{-3} compared to their ~700 µm initial thickness counterpart (Figure 4.49c). It can be inferred from the recorded data that CS/PVA/$GO_{0.05}$ coatings had the least amount of solvent concentration which rendered them with least amount of residual solvent (%) possible.

The drying times for ~1400 µm initial thickness coatings were higher as compared to ~700 µm coatings, because of the greater initial volume, more amount of solvent needed to be evaporated. One interesting phenomenon observed in both cases was that coatings with highest GO concentration (0.15 wt.%) had almost comparable drying time to that of control. This could be due to the high adsorptive capacity and agglomeration of GO which makes it engulf significant amount of solvent (Smith et al. 2019). Therefore, a larger amount of residual solvent is entrapped while remaining free solvent evaporates very quickly resulting in shorter drying period. Experimental findings suggest that even if CS/PVA/$GO_{0.05}$ is taking more time but the end result is far better than other casting solutions.

Average Solid Concentration

The average solid concentration w.r.t time is shown in Figure 4.48d and Figure 4.49d for coatings with initial thickness ~700 µm and ~1400 µm, respectively. It was observed that the solid concentration increased exponentially with increase in time due to more solvent removal from the coating solutions. In coatings with ~700 µm thickness, the concentration of solids accumulated in CS/PVA/$GO_{0.05}$, CS/PVA/$GO_{0.075}$, CS/PVA/$GO_{0.1}$, and CS/PVA/$GO_{0.15}$ were 0.552 g cm^{-3}, 0.362 g cm^{-3}, 0.289 g cm^{-3} and 0.248 g cm^{-3}, respectively. While in ~1400 µm thickness coatings, final solid concentration of 0.368 g cm^{-3}, 0.313 g cm^{-3}, 0.264 g cm^{-3} and 0.245 g cm^{-3}, respectively was observed for GO concentration from 0.05-0.15 wt.%. The similar results were obtained previously where after evaporation of solvent, the coating with the highest solid concentration had the lowest percentage of residual solvent (Sharma et al. 2017). Amongst the coatings with GO, CS/PVA/$GO_{0.05}$ had the

highest final solid concentration and lowest residual solvent (%) owing to its high diffusion coefficient which led to more solvent removal.

Table 4.7 Summary of various physical parameters in designated coatings.

Coatings	Initial thickness (µm)	Ultimate thickness (µm)	Residual Solvent (%)	Solvent Conc. (g cm^{-3})	Solid Conc. (g cm^{-3})
CS/PVA	612	30	1.03	0.199	0.648
CS/PVA/$GO_{0.05}$	751	44	2.01	0.326	0.551
CS/PVA/ $GO_{0.075}$	786	71	5.31	0.563	0.362
CS/PVA/ $GO_{0.1}$	768	88	7.83	0.655	0.289
CS/PVA/ $GO_{0.15}$	701	95	9.97	0.707	0.248
CS/PVA	1446	73	2.17	0.417	0.471
CS/PVA/$GO_{0.05}$	1443	128	5.11	0.552	0.367
CS/PVA/ $GO_{0.075}$	1466	154	6.80	0.622	0.313
CS/PVA/ $GO_{0.1}$	1483	187	8.98	0.685	0.263
CS/PVA/ $GO_{0.15}$	1476	203	10.21	0.711	0.244

Considering the fact that only change in the experiment setup was the alteration in initial thickness (~700 µm and ~1400 µm), notably different drying behaviours were observed. The plausible reason behind this could be that a physical change i.e., thickness is affecting the drying behaviour to a larger extent. It implies that thicker coating (~1400 µm) may be more viscous on the top and solvent diffusion slows down to a significant degree. Drying times obtained here were longer than observed in conventional system due to utilization of water as solvent for coatings, which because of low volatility dried at a much slower pace. Therefore, coatings with slow drying rates (longer drying times) might create higher energy demands. However, the end result is much more environmental friendly than traditional coatings where, highly volatile organic solvents although dry faster but leave a toxic trail behind. From application point of view, coatings with comparatively less amount of residual solvent are usually preferred and their drying periods should not be abnormally longer. It is because of the fact that high residual solvent amounts may frequently give rise to coating defects like cratering, cissing, flaking and/or blistering etc (Arya et al. 2021). Furthermore, diffusion rates have partial restraint over thinner coatings, which leads to more rapid heating. Thus, in

thinner coatings likelihood of blistering decreases as the residual solvent drops more swiftly. Whereas, thicker coatings dry slowly due to higher solvent retention near their base, and are more vulnerable to blistering (Bhargava and Arya 2015). Considering these observations and based on earlier findings, thinner coatings of ~700 µm initial thickness were found particularly promising for further analysis, as shown in further studies.

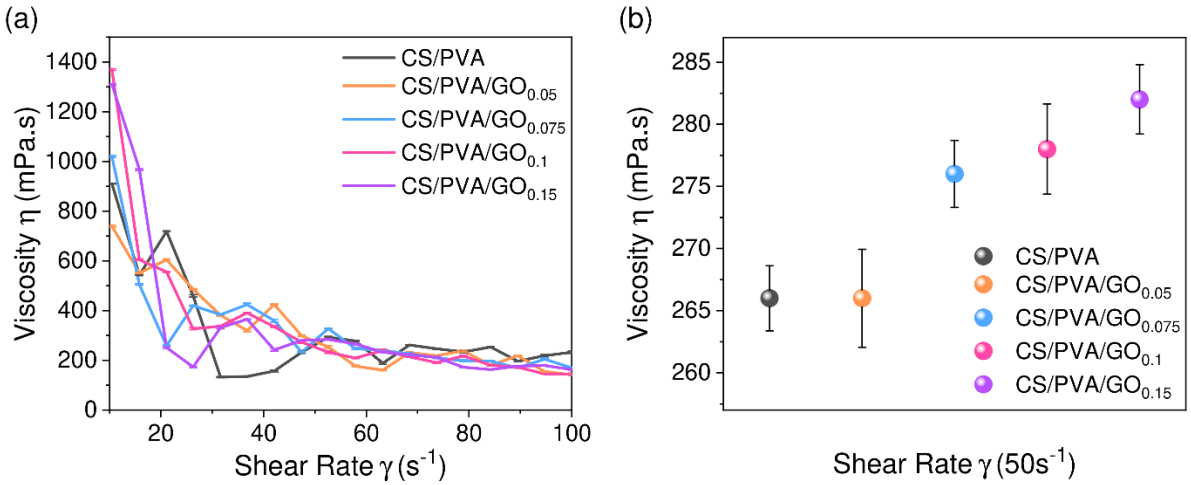

Figure 4.50 Rheological properties of various CS/PVA/GO coatings.

4.16.2 Material Characterization

Rheological analysis was performed to obtain information on interactions among polymers and graphene oxide. Chitosan, PVA, and graphene oxide can be well mixed and forms homogeneously aqueous and stable polymer solution at room temperature. It is well-known that dynamic rheology is a powerful tool for evaluating the structure of melts or solution. As shown in Figure 4.50a, the viscosity of these aqueous coating suspensions decreased with increase in shear rates (γ) from 10 to 100 s^{-1}. Thus, the CS/PVA/GO solutions exhibited a distinctive sheer thinning behaviour. For instance, the viscosity of CS/PVA/$GO_{0.05}$ decreased from about 0.75 Pa.s at $10s^{-1}$ to 0.14 Pa.s at 100 s^{-1}. The rheological pattern observed here is the most common type of non-Newtonian behaviour and is quite typical of suspensions, emulsions, and polymer solutions etc. (Barnes et al. 1989). It is the result of micro-structural rearrangements such as polymer chains disentanglement and stretching occurring in the plane of applied shear (Osswald and Rudolph 2015). Furthermore, the viscosity of the coating mixtures apparently increased with the addition of graphene oxide from 0.05-0.15 wt.%. The Figure 4.50b shows the viscosity of CS/PVA, CS/PVA/$GO_{0.05}$, CS/PVA/$GO_{0.075}$, CS/PVA/$GO_{0.1}$, and CS/PVA/$GO_{0.15}$ at a shear rate (γ) of 50 s^{-1} with values 0.266 ± 2.62,

0.266 ± 3.94, 0.276 ± 2.70, 0.287 ± 3.63 and 0.282 ± 2.79 Pa.s respectively. This result can be attributed to different amounts of GO present in these coatings. Even at small increments of GO concentrations, minute increase in viscosity values can be observed, which indicated altered interactions among the polymer molecules in the solution by GO.

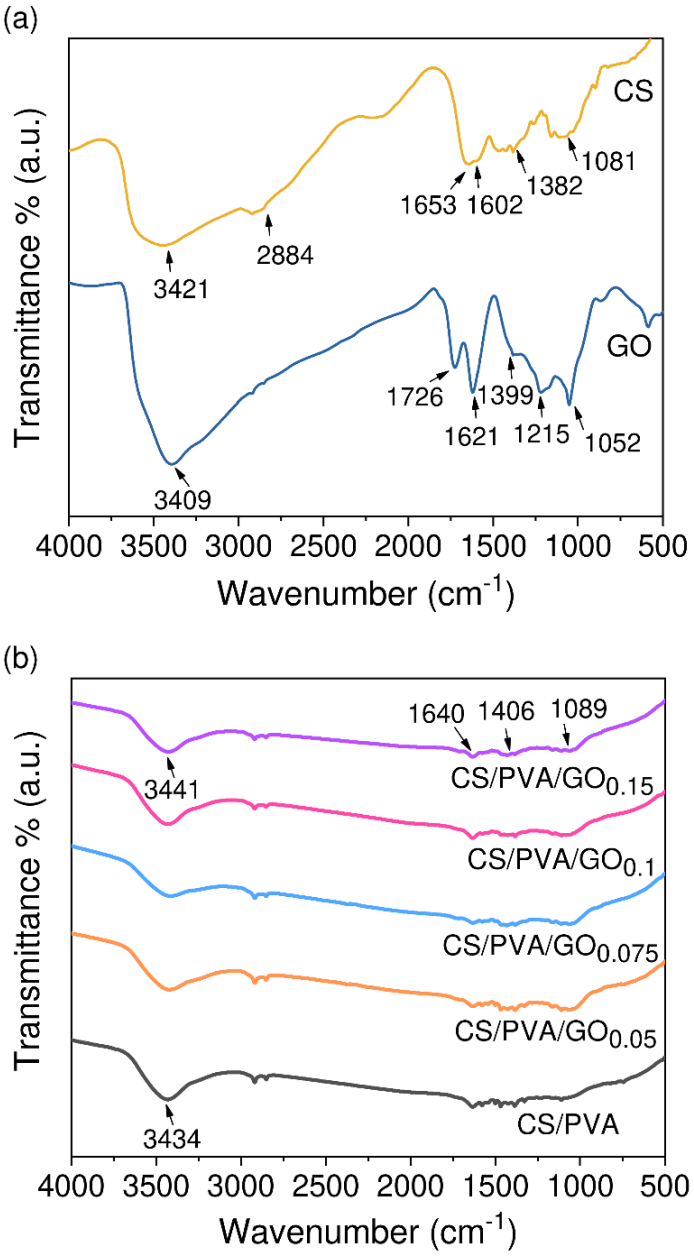

Figure 4.51 Material characterization displaying FTIR spectra of (a) chitosan, graphene oxide; (b) pristine and graphene-oxide loaded chitosan-PVA thin-film composites.

The variation in functional moieties of CS/PVA polymer matrix after graphene oxide introduction were determined through FTIR spectroscopy. FTIR spectrum of pure GO exhibited a strong peak at 3411 cm^{-1} due to stretching vibrations of hydroxyl (-OH) groups (Figure 4.51a). Other characteristics bands at 1726 cm^{-1} (stretching vibrations of C=O from carboxylic groups), 1401 cm^{-1} (O-H deformation vibrations), 1215 cm^{-1} (epoxy rings), 1052 cm^{-1} (C-OH bending) were also manifested. A peak at 1629 cm^{-1} due to C=C stretching modes validate its sp^2 configuration (Han et al. 2011). All these analyses confirmed the successful synthesis of graphene oxide. In chitosan, the vibrational peak at 1653 cm^{-1} was assigned to carbonyl (C=O) stretching of acetylated amino (-NHCO-) group (Figure 4.51a). A few other peaks at 3421 cm^{-1}, 2884 cm^{-1}, 1602 cm^{-1}, and 1382 cm^{-1} can be ascribed to -OH stretching, C-H stretching vibrations and N-H bending of amino groups, respectively present in chitosan polymer (Wang et al. 2015).

The FTIR spectra of CS/PVA/GO coatings (Figure 4.51b) displayed a relatively broader absorption band at 3441 cm^{-1} due to combined stretching effects of amine and hydroxyl groups contributed from chitosan and graphene oxide, respectively. As compared to pristine chitosan and GO, corresponding peaks at 1602 cm^{-1} ($-NH_2$ vibrations) and 1726 cm^{-1} (C=O stretching vibration of carboxylic groups) disappeared. Besides, the appearance of a new peak at 1640 cm^{-1} clearly indicates a stable association between CS/PVA polymeric blend and the oxygenated groups of GO via hydrogen bonding and electrostatic interactions (Ruiz et al. 2019). A slight decrease in the intensities of the OH-bands in CS/PVA/GO coatings than pristine CS/PVA (without GO) is consistent with the formation of intermolecular hydrogen bonds between GO and PVA, as witnessed before (Liu et al. 2014; Pandele et al. 2014; Ying et al. 2020). Further, no significant difference in the -OH band intensities was observed among the CS/PVA/GO coatings with varying GO content. This suggests that adding such a low proportionate of GO to CS/PVA matrix did not alter the hydrogen bonding already existed between the CS and PVA components.

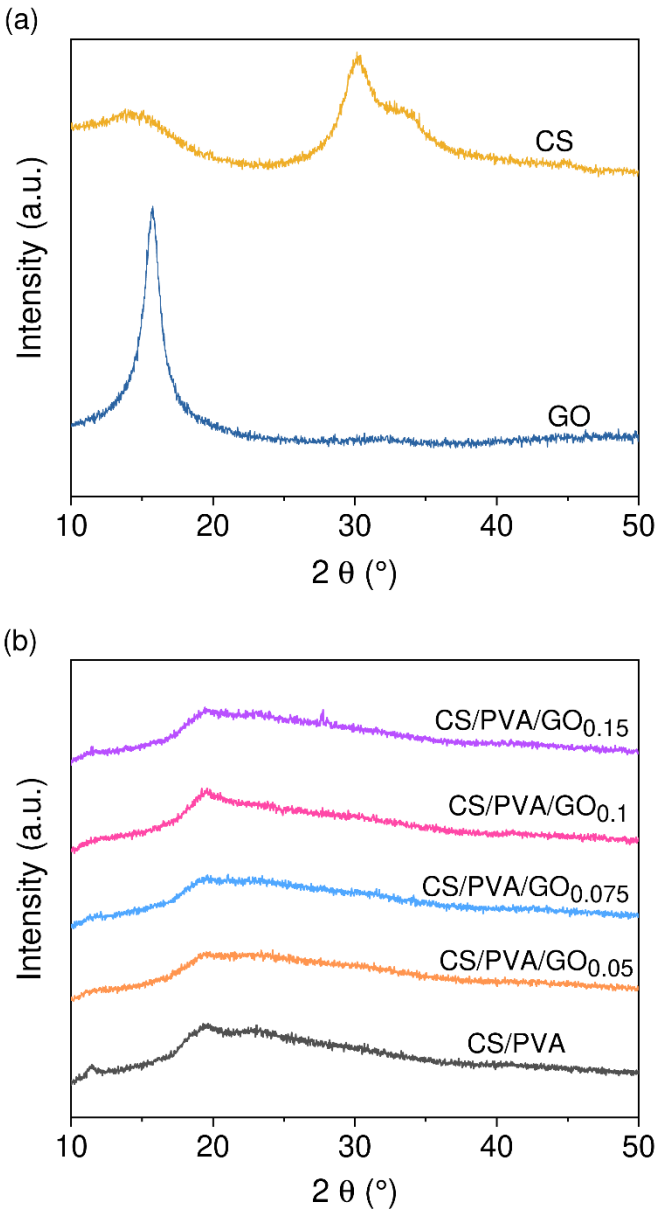

Figure 4.52 Material characterization displaying XRD spectra of (a) chitosan, graphene oxide; (b) pristine and graphene-oxide loaded chitosan-PVA thin-film composites.

XRD analyses were done to evaluate the structural integrity of polymer matrix before and after loading of graphene oxide. The XRD pattern of GO (Figure 4.52a) showed a characteristic 2θ peak at 10.9° (d-spacing, 0.816 nm) indicating the existence of oxygen containing moieties (Liao et al. 2011). The XRD pattern of chitosan at 2θ=10° reflected the hydrated crystalline structure and a broad peak 2θ=20° indicated the existence of amorphous structure (Han et al. 2011). The addition of GO to CS/PVA coatings led to an increase in the intensity of PVA lattice peak at 19.8° contributing towards an enhanced crystallinity of the PVA component (Figure 4.52b). On the other hand, the absence of a distinct GO peak at

10.9° may be attributed to the complete exfoliation of GO sheets and their integration within the hierarchical matrices of CS/PVA polymers (Wang et al. 2015). Furthermore, given the low proportion of GO (0.05-0.15 wt.%) in the CS/PVA/GO nanocomposites, it is possible that the characteristic diffraction peak of GO was too weak and overshadowed by the chitosan peak. These findings corroborate to similar studies done with CS/PVA/GO nanocomposites (Pandele et al. 2014; Pandele et al. 2017). Though the GO concentrations used in those studies were much higher (~10-47 folds) than the current work. XRD results also indicate a significant enhancement in polymer crystallinity after incorporating GO, which is likely to enhance mechanical strength of the coatings.

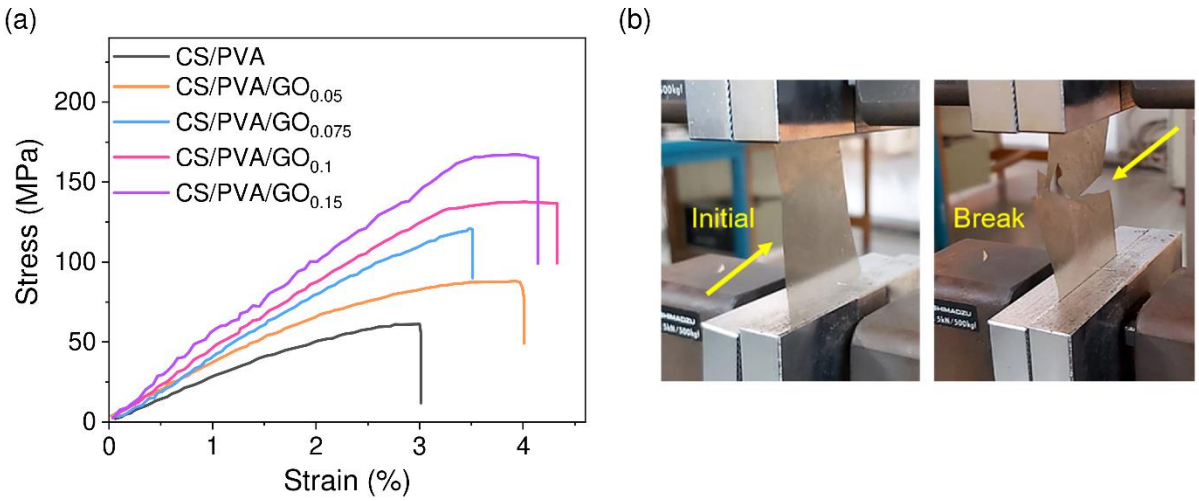

Figure 4.53 (a) Stress-strain curve of various CS/PVA composites after reinforcing GO with varying content (0.05-0.15 wt.%) and (b) Digital images of coating film at initial moment (left) and at breakpoint (right).

The mechanical properties of thin-film coatings on stainless steel surface were studied (Figure 4.53a). Stress–strain curve in all samples depicts a typical modulus and tensile strength at fracture behaviour of coatings. The curves exhibited a linear regime depicting maximum hydrogen-bond content during elastic stress until hydrogen-bonding network was severely ruptured. We analysed that incorporation of minute amount of GO (0.05 wt.%) intensified tensile strength and Young's modulus of CS/PVA coatings by 43% and 20% respectively. The tensile strength at break of CS/PVA/GO composite films was enhanced from 87.88 to 167.13 MPa while increasing the GO content from 0.05 to 0.15 wt.% (Table 4.8). The strong dependency of tensile strength on GO content is ascribed to great dispersion of GO into hierarchical networks of CS/PVA, which augments a strong hydrogen bonding

and electrostatic interactions at molecular level. As a result, under mechanical stress, energy released while forming hydrogen bond between CS/PVA matrix and GO always remains higher than energy loss during matrix deformation. Thus, better interactions among GO and CS/PVA provide better load transfer which ultimately leads to mechanical strength enhancement (Han et al. 2011; Rathod et al. 2016). Figure 4.53b demonstrates the breaking of composite thin-films at break point during tensile tests.

Table 4.8 Tensile strength and Young's Modulus of composite coatings.

Sample	**Tensile strength (σ) (MPa)**	**Young's Modulus (E) (MPa)**
CS/PVA	61.22 ± 2.67^{e}	24.40 ± 3.08^{d}
$CS/PVA/GO_{0.05}$	87.88 ± 2.23^{d}	29.15 ± 1.33^{c}
$CS/PVA/GO_{0.075}$	120.92 ± 5.36^{c}	30.84 ± 2.64^{c}
$CS/PVA/GO_{0.1}$	137.56 ± 4.97^{b}	34.24 ± 1.57^{b}
$CS/PVA/GO_{0.15}$	167.13 ± 6.22^{a}	42.28 ± 1.92^{a}

Mean values sharing a common letter within the treatment are not significant at $P < 0.05$ (Values are Mean ± SD, n=3)

Differential scanning colorimetry (DSC) was used to examine thermal stability of CS/PVA blended composites while varying GO loading. Since, both chitosan and PVA polymers are semi crystalline in nature their physico-microstructural properties depend rather strongly on crystallinity degree. In order to examine the influence of mobility of the chains with temperature, the glass transition region was analysed. The thermograms of all coating samples showed broad endothermic peaks in the temperature range of 100-140 °C, which is due to the evaporation of adsorbed water. Sharp peaks at higher temperatures were observed, which were attributed to crystalline melting transition (Figure 4.54a). Pure PVA sample showed endothermic peaks at 108 °C and 227 °C, which were assigned to the evaporation of adsorbed moisture and melting transition, respectively (Kumar et al. 2019). The thermogram analysis revealed that the CS/PVA coating exhibited peak broadening and a shift towards a lower temperature i.e., from 227 °C to 205 °C, indicating stable interactions between the polymer moieties. After the incorporation of GO in the coatings, DSC curves showed red shifts in the peaks in the range of 211-214 °C. This red shift resulted from the crosslinking of CS/PVA and GO through hydrogen bonds, which restricted the motion of molecular chains and increased the melting temperature of the coatings (Ma et al. 2012). It indicates that both

CS/PVA and GO were compatible while coating fabrication, which improved the overall thermal characteristics of nanocomposites.

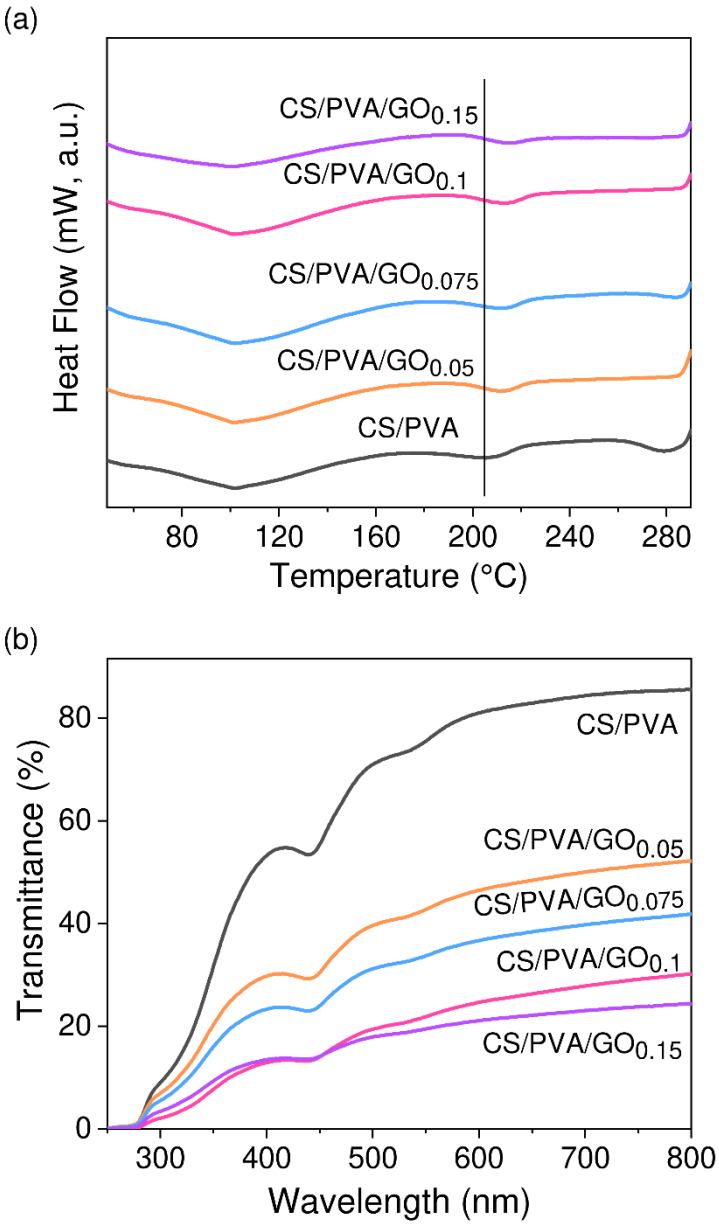

Figure 4.54 (a) DSC thermograms and, (b) Optical transmittance spectra of pristine and graphene-oxide loaded chitosan-PVA coatings.

The development of UV-protective materials is crucial while designing bioactive coatings, as they must remain protected against radiation-induced damage while maintaining their appearance and avoiding cracks for extended periods (Ahmed et al. 2019; Refaee et al. 2022). We analysed the UV-light shielding behaviour of CS/PVA films varying GO content through light transmittance (Figure 4.54b). Pristine CS/PVA films exhibited poor UV-absorption

capability having 53.2% transmittance and high transparency in UV region (200-400 nm). A proportionate rise in GO content however, significantly enhanced the UV-shielding effect of CS/PVA films. This was manifested through a drastic reduction in transmittance in CS/PVA/$GO_{0.05}$ (29.7%), CS/PVA/$GO_{0.075}$ (23.3%), CS/PVA/$GO_{0.1}$ (13.4%), and CS/PVA/$GO_{0.15}$ (12.9%) films. An increased GO content appeared responsible for such UV-blocking ability of organic coatings where planar structure and high C/O ratio of GO nanosheets imparted an effective barrier to UV light (Xie et al. 2015). Besides, GO sheets are well known UV-absorbers which potentially transform the adsorbed energy to less damaging thermal energy via photo-physical process. The incorporation of GO sheets onto CS/PVA based composite coatings prevent unsolicited UV-induced protein degradation at implants site (Xie et al. 2015) and thus improve tissue regeneration.

SEM micrographs unveiled the surface structure and interfacial interactions of coatings (Figure 4.55). The unusual tangentially curved morphologies in pristine CS/PVA surface were indicative of chitosan susceptibility to self-aggregation (Han et al. 2011). This was further verified after incorporating graphene oxide into chitosan/PVA matrix which resulted in better surface smoothness due to great dispersion, miscibility and strong interactions of GO with CS/PVA. The surface morphology of CS/PVA/$GO_{0.05}$ and CS/PVA/$GO_{0.075}$ coatings did not deviate much from their pristine form. Whereas, incorporating a higher GO content imparted slightly rough features on CS/PVA/$GO_{0.1}$ and CS/PVA/$GO_{0.15}$ film surfaces accompanied by larger artefacts. The cross-sectional images of coating films showed fractured surface along with grooves and rough edges (Figure 4.55). The polymeric blends appeared denser after incorporating GO sheets ascribable to synergistic charge carriers, complementary microstructures and superior chain entanglement among chitosan, PVA and GO. SEM micrographs did not show any individual exfoliated multi-layered GO sheets which envisaged a great adhesion as if they were well wrapped between layers of CS/PVA blends. Further, Energy dispersive X-Ray (EDX) analysis (Table 4.9) confirmed the presence of characteristic elements such as carbon (C), oxygen (O) and nitrogen (N). The revelation of proportional increase in oxygen content validated the increasing GO content in the coatings.

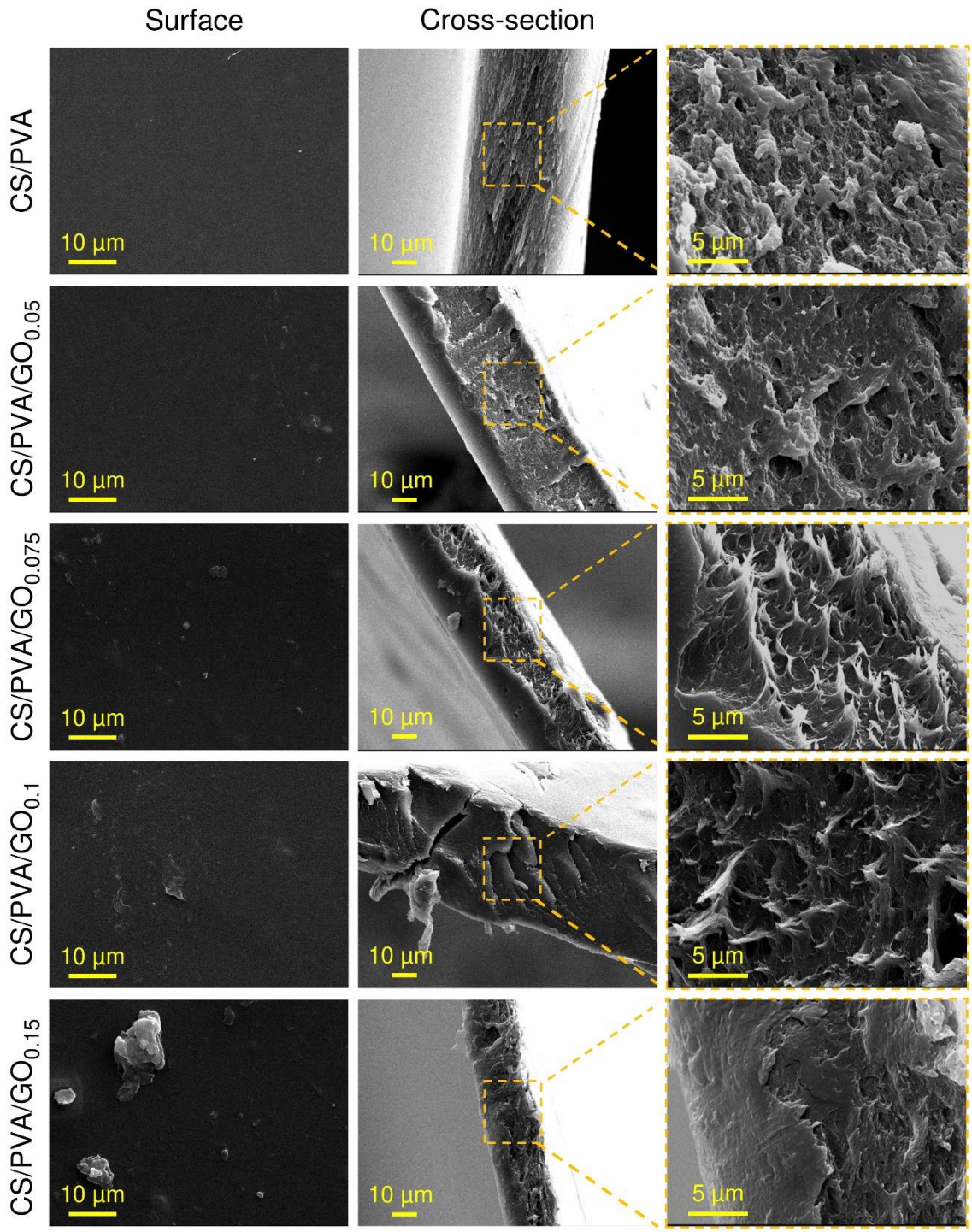

Figure 4.55 SEM micrographs showing surface topography and cross-sectional microstructures of pure chitosan-PVA (CS/PVA) and graphene oxide loaded chitosan-PVA (CS/PVA/GO) composites.

Table 4.9 Elemental composition (mass norm. %) of CS/PVA and CS/PVA/GO coatings.

	CS/PVA	**CS/PVA/GO$_{0.05}$**	**CS/PVA/GO$_{0.075}$**	**CS/PVA/GO$_{0.1}$**	**CS/PVA/GO$_{0.15}$**
C	50.60	50.47	49.48	49.37	48.53
O	36.54	39.47	40.26	40.56	40.70
N	3.42	2.88	2.52	2.77	3.21

4.17 Antibacterial Efficacy of Coatings

4.17.1 Antibacterial Contact Assay

The uncoated SS substrates did not show any inhibitory effect on bacterial growth, regardless of the bacterial species and incubation time (Figure 4.56). In contrast, CS/PVA/GO-coated substrates exhibited a significant inhibition of bacterial growth, forming a clear zone of inhibition (ZoI). Although increasing the GO content in CS/PVA coatings did not produce any noticeable changes in bacterial growth, the duration of the initial contact time certainly had a profound impact. Coatings that were in contact with bacteria for 1-4 h displayed only a bacteriostatic response since a permanent ZoI could not be established in the exposed area and was eventually replaced by bacterial growth from neighbouring areas over 10 days of aging (Figure 4.56). However, a 6 h contact duration was sufficient to impart a permanent antibacterial (bactericidal) response onto the coated surface, where no signs of bacterial growth were observed on the formed ZoI even after aging the plates for a month. This suggests that the biomedical coatings exhibit a contact-active behaviour, which sometimes provides a higher antibacterial response than materials that prefer release-mediated antibacterial action, as reported earlier (Agnihotri et al. 2015; Agnihotri et al. 2013).

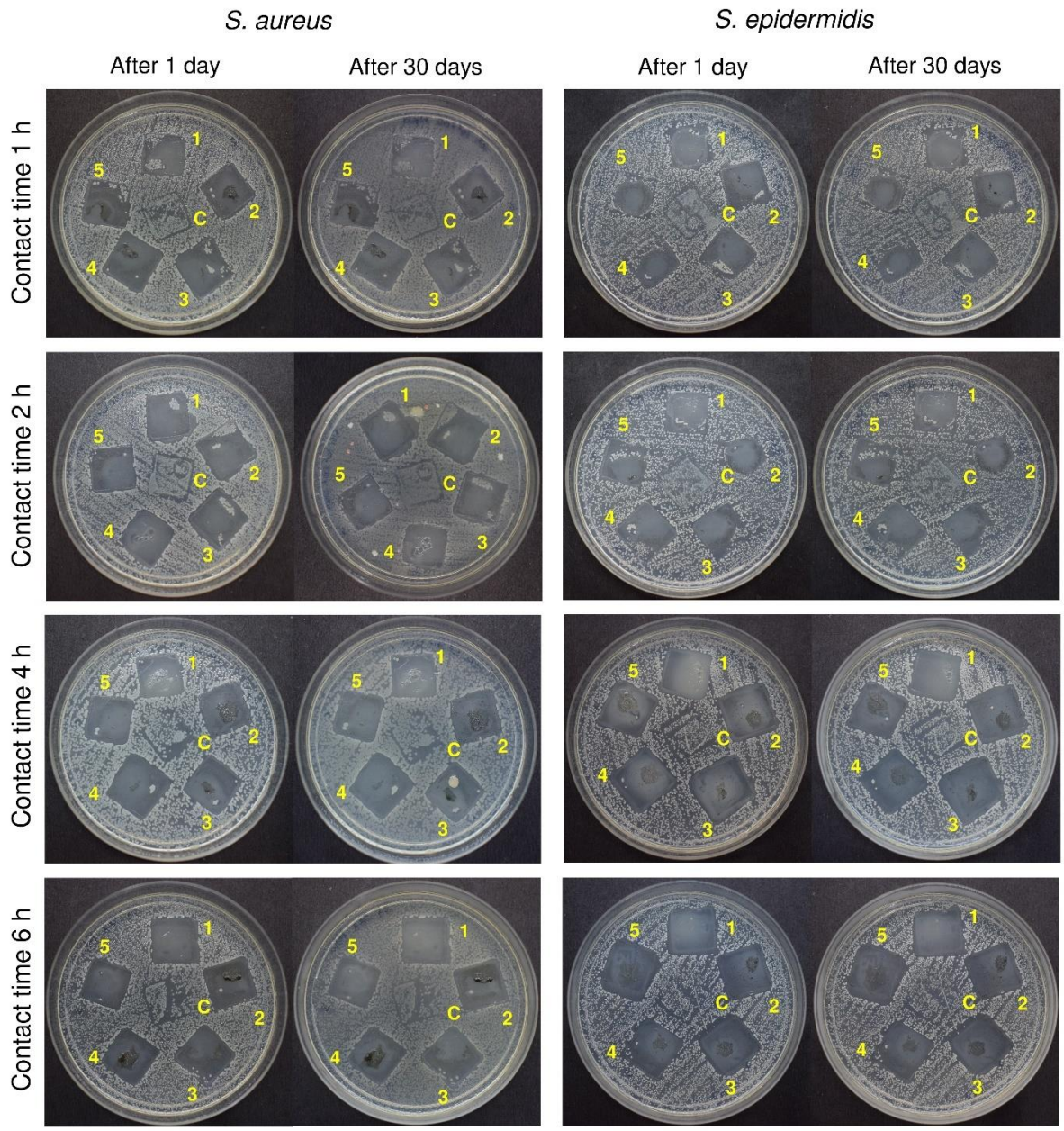

Figure 4.56 Contact bacterial growth inhibition of *S.aureus* and *S epidermidis* by coatings C=control; 1=CS/PVA; 2=CS/PVA/$GO_{0.05}$; 3=CS/PVA/$GO_{0.075}$; 4=CS/PVA/$GO_{0.1}$; 5=CS/PVA/$GO_{0.15}$ at 1 h, 2 h, 4 h & 6 h contact time after 1 day and its progression after 30 days.

4.17.2 Antibacterial Drop Test

The drop test results indicated that both *S. epidermidis* and *S. aureus* grew well on uncoated SS surface forming bacterial biofilm in 10 days. However, fewer bacterial colonies were propagated in CS/PVA/GO coatings revealing a significant antibacterial activity against both strains (Figure 4.57a). The cell viability (%) data of pristine CS/PVA coating also indicated

bacterial growth viz. 43.6% and 46.7% for *S. epidermidis* and *S. aureus*, respectively (Figure 4.57b). With increasing GO concentration (0.05-0.15 wt.%) in coatings, the cell viability reduced from 33.9 to 17.7% (*S. epidermidis)* and 22.8 to 10.9% (*S. aureus)* in just 1 h of incubation exhibiting an intense biocidal nature of the coatings.

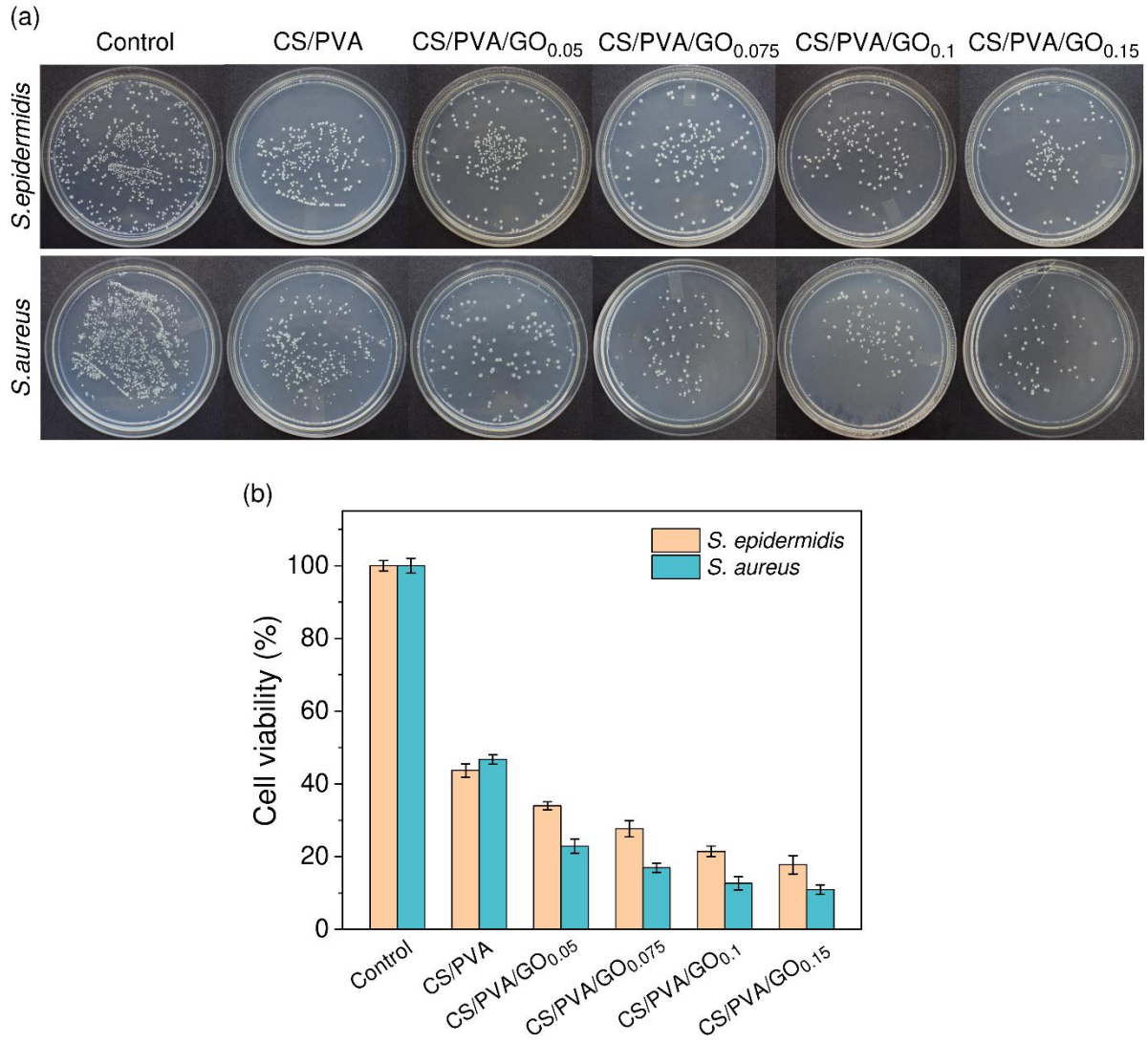

Figure 4.57 (a) Digital images of colony-forming unit of *S. epidermidis* and *S. aureus* incubated for 1 h on the control (pristine SS) and CS/PVA/GO coated SS surfaces. (b) Drop test for the quantitative analysis of bacterial cell viability (%) against CS/PVA/GO coatings for *S. aureus* and *S. epidermidis.*

Furthermore, increasing the incubation time to 6 h resulted in decrease of *S. epidermidis* cell viability from 14.6 to 7.8% and 8.9 to 2.9% in *S. aureus* cells when treated with coatings of GO content ≤0.075 wt.%. Complete eradication of *Staphylococcus sp.* cells was eventually

also observed at 6 h incubation with coatings containing higher GO concentrations of ≥0.1 wt.% (Figure 4.58a-b). The results obtained in this study demonstrate a superior antibacterial efficacy compared to previously reported literature (Khan et al. 2021; Ruiz et al. 2019; Tamayo Marín et al. 2019), where comparatively higher GO concentrations were required to induce effective bactericidal activity.

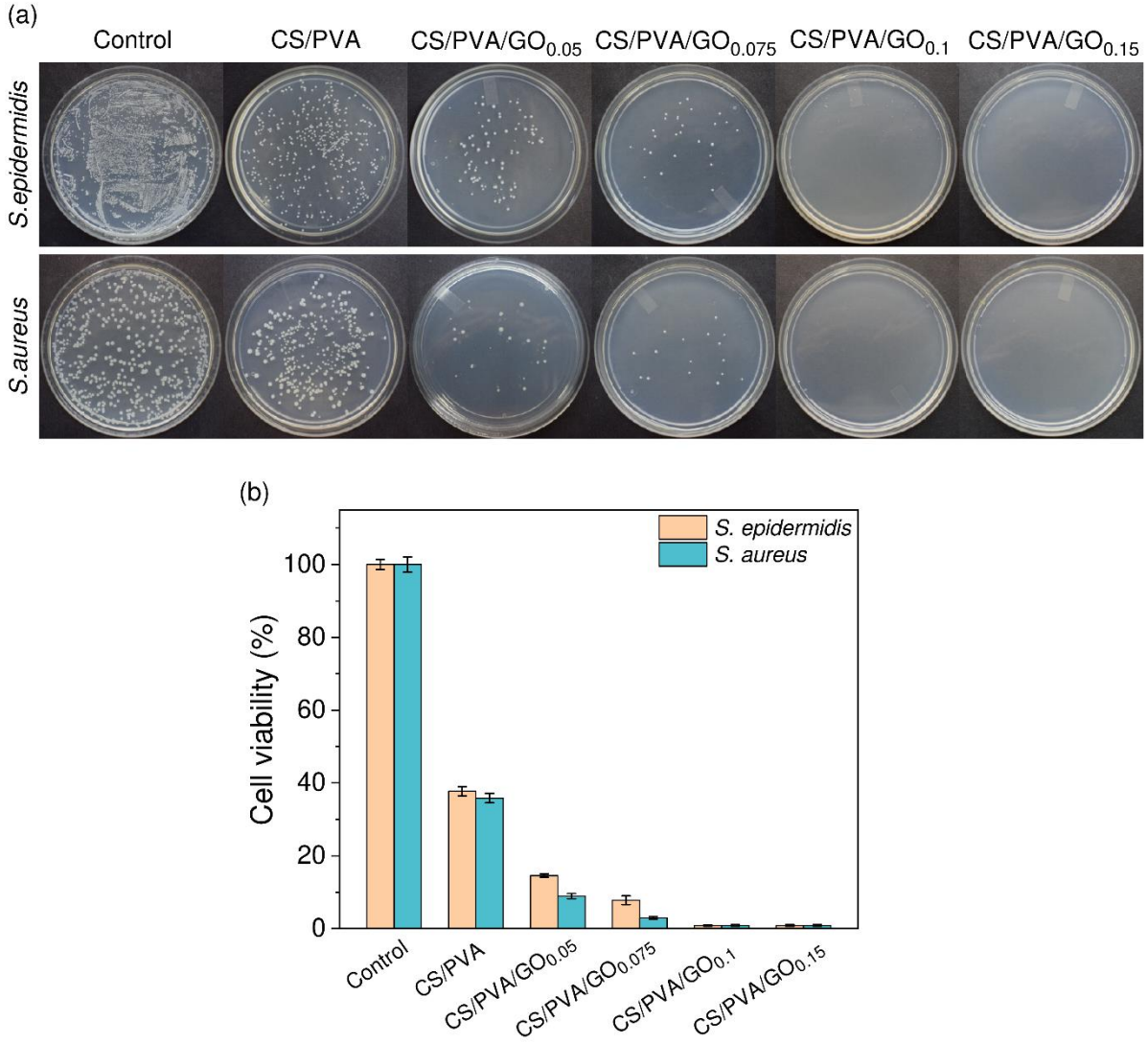

Figure 4.58 (a) Digital images of colony-forming unit of *S. epidermidis* and *S. aureus* incubated for 6 h on the control (pristine SS) and CS/PVA/GO coated SS surfaces. (b) Drop test for the quantitative analysis of bacterial cell viability (%) against CS/PVA/GO coatings for *S. aureus* and *S. epidermidis*.

The reproducibility of coatings' fabrication was also evaluated using a drop test, which revealed excellent replicability in terms of bioactivity, thus validating the efficacy of our procedure (Table 4.10).

Table 4.10 Bacterial cell viability (%) of *S. aureus* and *S. epidermidis* evaluated against CS/PVA/GO coatings in a drop test at time interval of 6 h.

	Cell viability %	
	S. aureus	***S. epidermidis***
Control	99.34 ± 0.95^{a}	99.69 ± 0.56^{a}
CS/PVA	36.92 ± 1.76^{b}	39.23 ± 0.86^{b}
$CS/PVA/GO_{0.05}$	10.04 ± 0.48^{c}	14.97 ± 0.31^{c}
$CS/PVA/GO_{0.075}$	3.14 ± 0.17^{d}	7.89 ± 0.20^{d}
$CS/PVA/GO_{0.1}$	0.066 ± 0.001^{e}	0.065 ± 0.002^{e}
$CS/PVA/GO_{0.15}$	0.063 ± 0.003^{e}	0.064 ± 0.002^{e}

Mean values sharing a common letter within the treatment are not significant at $P < 0.05$

4.17.3 LIVE/DEAD Assay

A live/dead bacterial staining assay was conducted to assess the membrane permeability of bacteria following exposure to the coatings. Fluorescein diacetate (FDA) accumulated by live bacteria displayed viable cells as green and propidium iodide (PI), a nucleotide-binding probe that can only enter cells with damaged membranes, presented the non-viable cells as red. The results, presented in Figure 4.59, show dominant green and negligible red fluorescence signals for the control groups, indicating that the untreated cells maintained a normal membrane. Compared to the negative control, the CS/PVA coating displayed some bacterial inhibition, likely due to the inherent bactericidal properties of chitosan moieties. The cationic moieties present in this polysaccharide are known to compromise the cellular framework of bacteria, leading to their death (Khan et al. 2021). In contrast, the GO-based coatings showed varied degrees of red fluorescence. As the GO content in coatings was increased from 0.05-0.15 wt.%, there was a significant enhancement in red fluorescence as the number of non-viable bacterial cells increased and only a few sporadic live bacteria cells survived. These results were attributed to the synergistic effect of GO and CS, which could more efficiently disrupt the bacterial cell membrane in contact with CS/PVA/GO coatings, leading to bacterial inactivation as a consequence of the leakage of intracellular metabolites through permeable membranes. Further, the fluorescent images showed a higher number of non-viable cells in

case of *S. aureus* than *S. epidermidis*, which were in good agreement with the antibacterial drop test results.

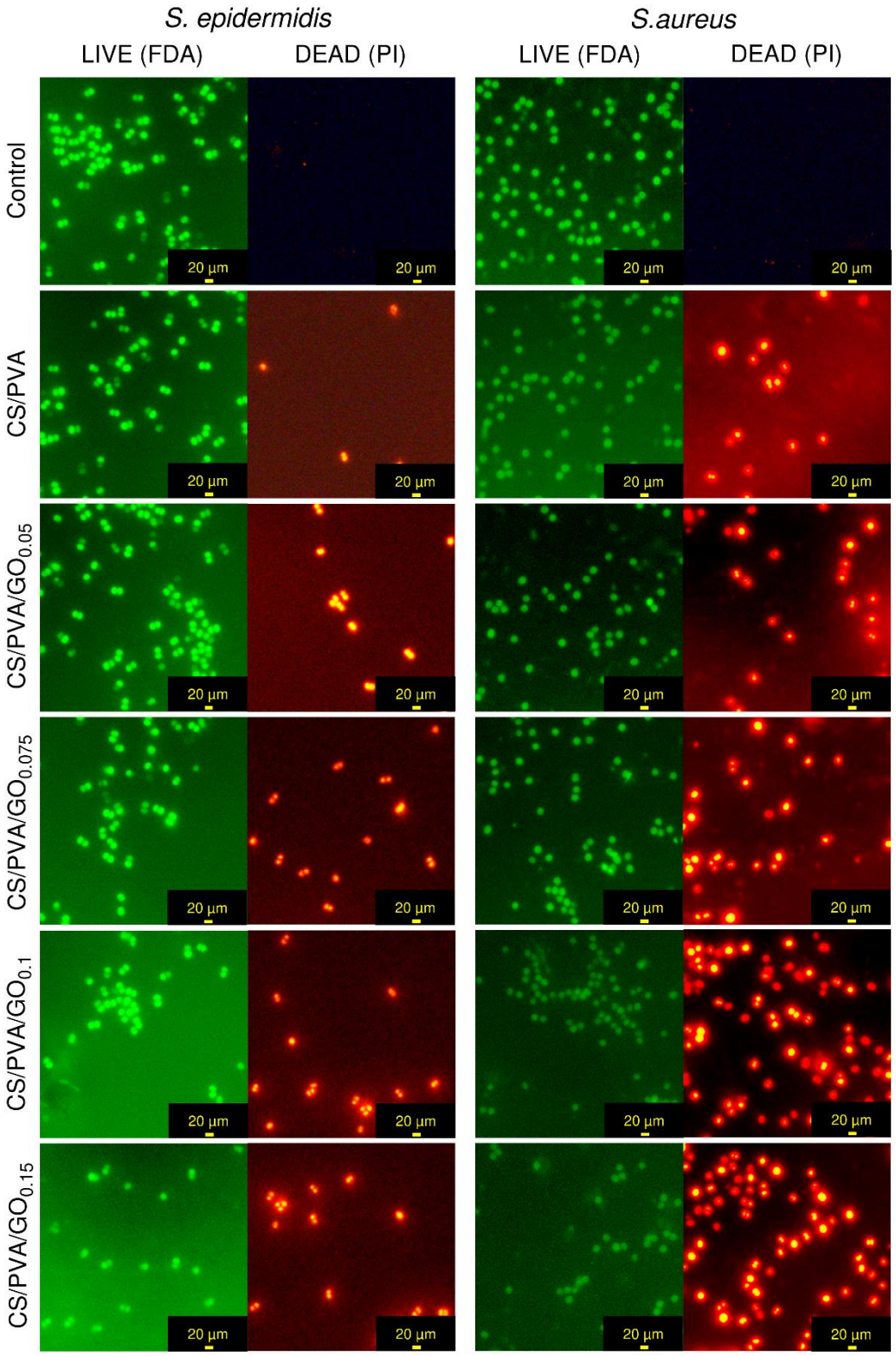

Figure 4.59 Fluorescent images showing the comparative distribution of live and dead cell of *S. epidermidis* and *S. aureus* bacteria when come in direct contact to CS/PVA/GO coatings.

4.18 Antibacterial Mechanism of Bioactive Coatings

Other than analysing the quantitative data for antibacterial analyses, it is equally important to understand the mechanistic insights into the functioning of antibacterial coatings while designing anti-biofouling surfaces for biomedical purposes. This can be understood well by elucidating the underlying mechanism of antibacterial action of these coatings.

4.18.1 Bacterial Morphology through SEM

The SEM images of untreated (control) cells revealed a typical glossy, circular, and grape-shaped morphology of *S. epidermidis* colonies with intact and smooth cell membranes (Figure 4.60). However, when treated with CS/PVA/GO coatings, significant morphological abnormalities were observed in *S. epidermidis*. The majority of bacterial cells appeared wrinkled with shrunken cell membranes, and perforated with pronounced breakages, indicating severe damage to cellular integrity. Similar findings were observed in *S. aureus* cells, which exhibited lysed cells and distorted shapes after exposure to CS/PVA/GO coatings. The exterior surface morphology analysis revealed irreversible damage to the cell membrane due to direct contact with immobilized GO sheets within CS/PVA matrices, as confirmed through material characterization. As previously reported, graphene oxide, when dispersed in a polymeric matrix, exhibits a much more lethal antibacterial action than its colloidal form (Ma et al. 2012). GO triggers ROS generation, causing severe membrane damage, forming pits/holes and enhancing membrane permeability (Agnihotri et al. 2015; Agnihotri et al. 2013; Liu et al. 2011).

4.18.2 Membrane Damage through ROS-triggered Oxidative Stress

The mechanism of antibacterial action via oxidative stress generation is evident in GO-based coatings (Figure 4.61a). Our observations reveal a 2-3 fold increase in ROS production in *S. epidermidis* and *S. aureus* cells when treated with CS/PVA/GO coatings (Raw data has been added in appendix-D as Table A2). The ROS production was consistent with an increase in GO content in the antibacterial coatings. This highlights the role of CS/PVA/GO coating as an electron donor on the bacterial surface, which reacts with oxygen molecules to generate superoxide radicals ($O_2^{\bullet-}$). Such an abrupt rise in ROS at bacterial surface could not be handled by their defence mechanism and get accumulated, resulting in an antibacterial response. Excessive levels of ROS may propel adverse events to bacteria furthermore viz.

enhanced membrane permeability, diminished enzymes activity and destruction of cellular proteins/nucleic acids, leading to bacterial death (Panda et al. 2018).

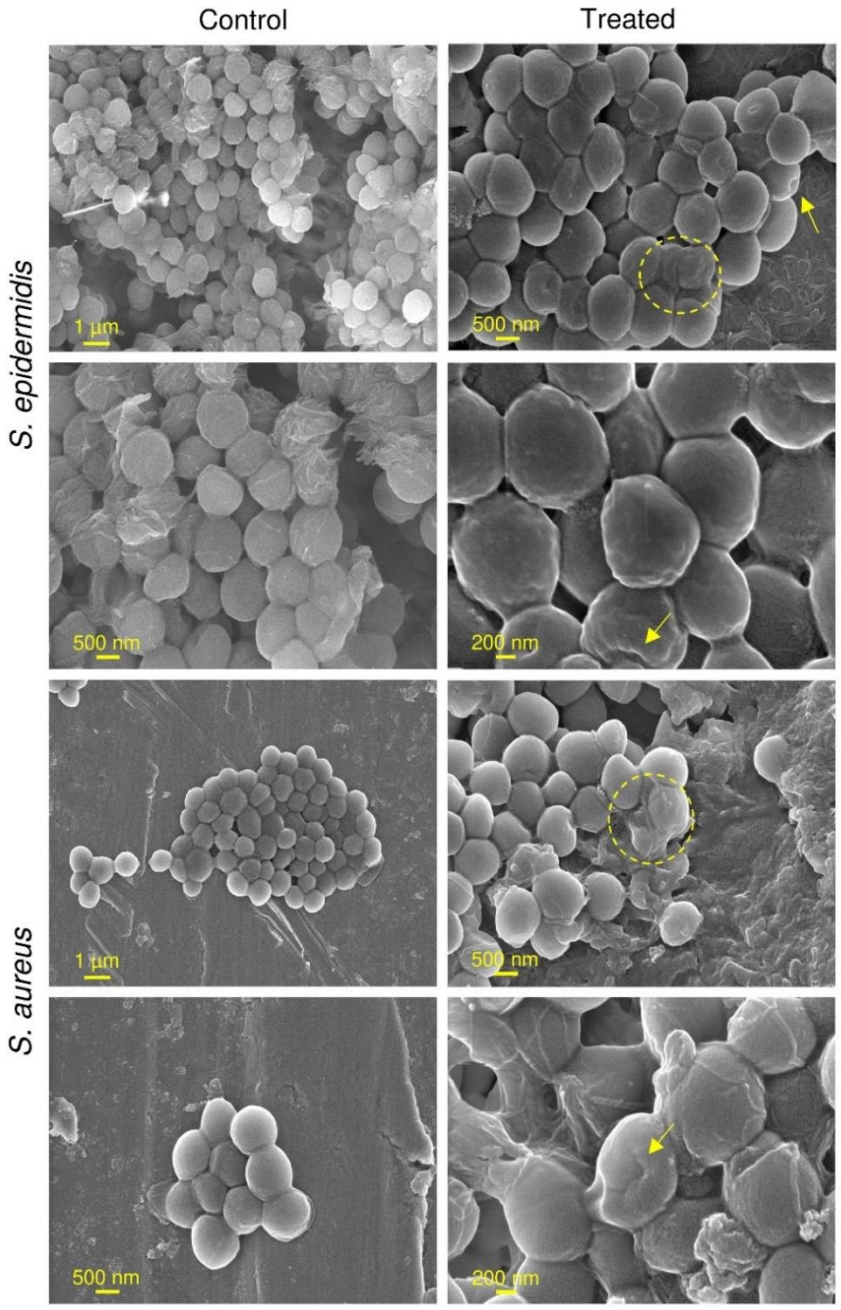

Figure 4.60 FE-SEM micrographs of *S. epidermidis* and *S. aureus* cells untreated (control) and treated with CS/PVA/GO coatings.

4.18.3 Leakage of Cytoplasmic Proteins

The release of intracellular proteins was evaluated to determine membrane leakage in treated bacterial cells (Figure 4.61b). No significant release of proteins was observed from untreated

S. epidermidis (1.87 µg mL^{-1}) and *S. aureus* (2.08 µg mL^{-1}) cells. However, upon introducing CS/PVA/GO coated SS substrates to both bacterial suspensions, the amount of released protein drastically enhanced by 8.5-9 folds. The increase in protein leakage 5.96-15.72 µg mL^{-1} in treated *S. epidermidis* and 8.07-18.43 µg mL^{-1} in treated *S. aureus* was also dependent on GO-content (0.05-0.15 wt.%) in the final nanocomposite coatings. This confirms our hypothesis that a GO-induced rise in ROS levels would have severely compromised membrane permeability of pathogenic bacteria resulting in the release of all intracellular components including proteins.

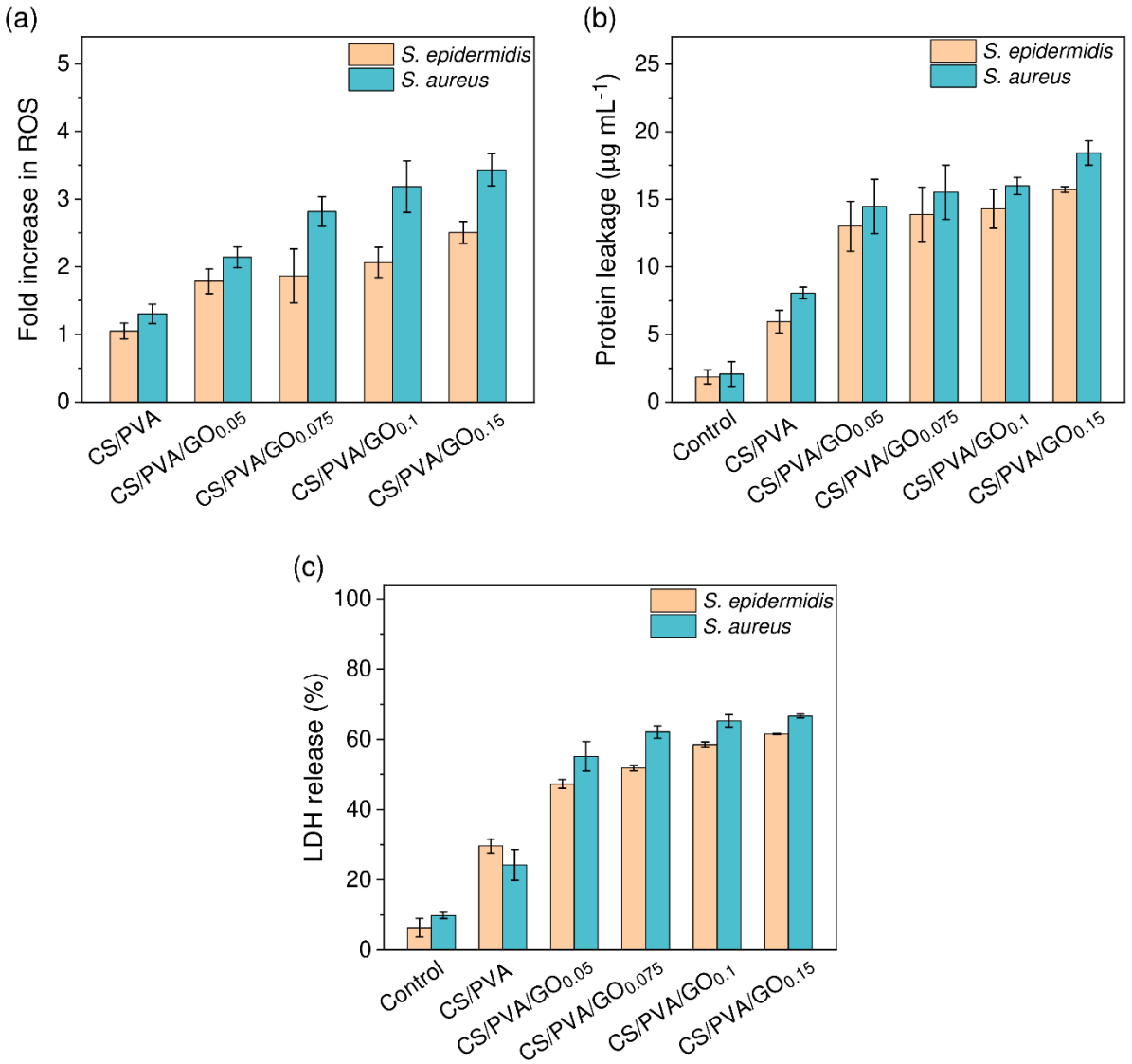

Figure 4.61 (a) Fold increase in intracellular ROS of *S. epidermidis* & *S. aureus* cells exposed to CS/PVA/GO composites, leakage of (b) cytoplasmic proteins and (c) respiratory chain lactate dehydrogenases from *S. epidermidis* & *S. aureus* cells exposed to various CS/PVA/GO coatings.

4.18.4 Suppression of Respiratory Chain Activity

LDH release assay was further employed to test bacterial cell membrane integrity (Figure 4.61c). SS substrates coated with CS/PVA/GO disrupted cellular respiration with significant difference among controls, CS/PVA and CS/PVA/GO coatings. The LDH release (%) in control and pristine CS/PVA were 6.4% and 29.6% (*S. epidermidis*) and 9.8%, 24.2% (*S. aureus*), respectively. As discussed earlier, introducing GO in bioactive coatings caused more release of LDH. For instance, CS/PVA/$GO_{0.05}$, CS/PVA/$GO_{0.075}$, CS/PVA/$GO_{0.1}$, and CS/PVA/$GO_{0.15}$ showed LDH release of 47.3%, 51.8%, 58.6%, and 61.5% for *S. epidermidis* while 55.2%, 62.1%, 65.2%, 66.6% for *S. aureus* respectively. An increase in LDH release in culture supernatants clearly indicates more lysed bacterial cells (Jaworski et al. 2018). Therefore, CS/PVA coatings having 0.15% GO disrupted the bacterial membrane most severely. These results indicated that following LDH release, an important enzyme in cellular respiration, CS/PVA/GO coatings are capable to suppress cellular respiration and reproduction by inhibiting respiratory chain activity.

Analysing results, a coupled mechanism of bacterial inhibition with CS/PVA/GO coatings was envisaged. We observed that both structural and chemical characteristics of GO, which often work synergistically, dictate its lethal action towards pathogens. A few studies claimed that direct contact of GO sheets with bacterial surface through their sharp edges can likely cause deep penetration and puncture membranes, often leading to cellular deformation (Ruiz et al. 2019; Yadav et al. 2017). However, such penetration of GO sheets onto bacterial suspension was difficult to predict as GO exists in immobilized state within CS/PVA matrix. Even during coating process, slow water evaporation forms a self-assembled surface where majority of GO sheets would lie flat in basal plane of the substrate surface. This observation aligned well to SEM micrographs where no signs of sharp edges of GO sheets were found. Therefore, in contrast to earlier reports, we eliminated the "nano-knife" behaviour of immobilized GO as its primary antibacterial action mechanism. As reported earlier (Hajji et al. 2016; Liu et al. 2018), while a contact-active CS/PVA hydrogel had shown remarkable biocidal effects, the inclusion of GO would only augment its action, which cannot be ignored. Besides, cell rupturing, protein leakage and respiratory dehydrogenases disruption via CS/PVA/GO coatings could have also been triggered by lipid peroxidation due to the oxidative nature of GO (Fan et al. 2017). Therefore, being passive in nature (non-releasing antimicrobial), the predominant mechanism of GO-based coatings was mediated through

oxidative stress (ROS generation) (Perreault et al. 2015). Damaged cell membrane further weakened the cellular integrity inhibiting its respiratory chain activity and promoting cytoplasmic leakage as the two main secondary mechanisms, leading to antibacterial response.

4.19 Evaluation of Biocompatibility

4.19.1 Hemolysis

In vitro hemolytic assays were performed to evaluate the compatibility of blood-contacting coatings. Percentage hemolysis of pristine CS/PVA, CS/PVA/$GO_{0.05}$, CS/PVA/$GO_{0.075}$, CS/PVA/$GO_{0.1}$, and CS/PVA/$GO_{0.15}$ coatings were recorded as 1.15%, 1.84%, 1.87%, 3.21% and 3.43%, respectively (Figure 4.62a). While a consistent increase in hemolysis was observed with increasing GO content, the extent of RBC rupture also became prominent. This could be attributed to toxicological response of GO against RBCs based upon its size, morphology, oxygen content, exfoliation extent, and surface charge. However, the hemolytic activity of GO is predominantly surface-linked, as the RBC disruption occurs due to strong electrostatic interactions between negatively-charged GO surface and positively-charged phosphatidylcholine lipids on RBC's outer membrane (Liao et al. 2011).

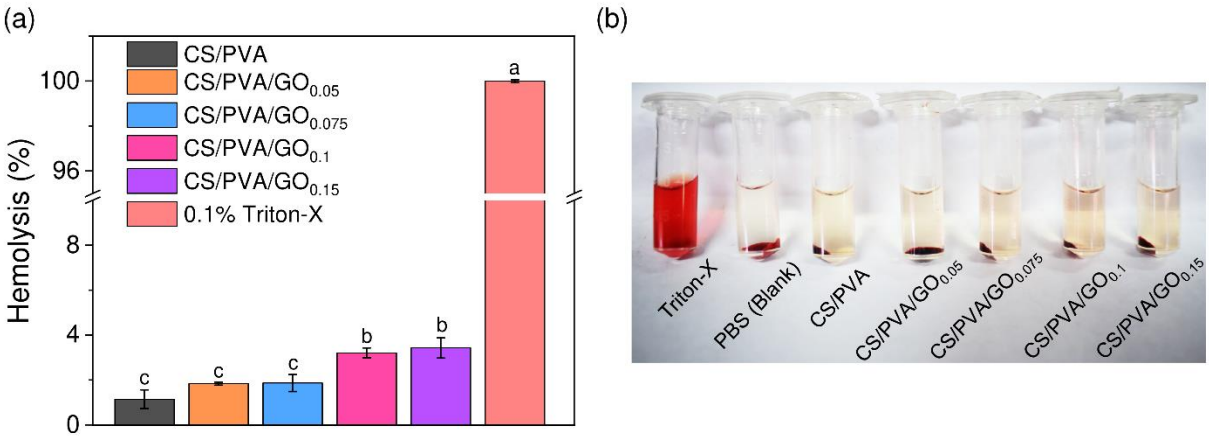

Figure 4.62 (a) Hemolysis of human erythrocytes by CS/PVA/GO composite coatings and, (b) Photographs from hemolytic activity test where PBS and Triton X-100 stand as negative and positive controls respectively. Mean values sharing a common letter within the treatment are not significant at $P < 0.05$.

Coatings having GO concentration <0.1% were classified as non-hemolytic (H<2%) as per the hemolysis grade defined by ASTM F756-00 standard (H= 0-2%, non-hemolytic; H= 2-5%, slightly hemolytic; H=>5%, hemolytic). Figure 4.62b represents an apparent difference in colour between the test samples, positive and negative control. Positive control causing 100% RBC lysis demonstrated bright red colour while the negative control was pale yellow. The test samples were observed having an incremental change in pink colour.

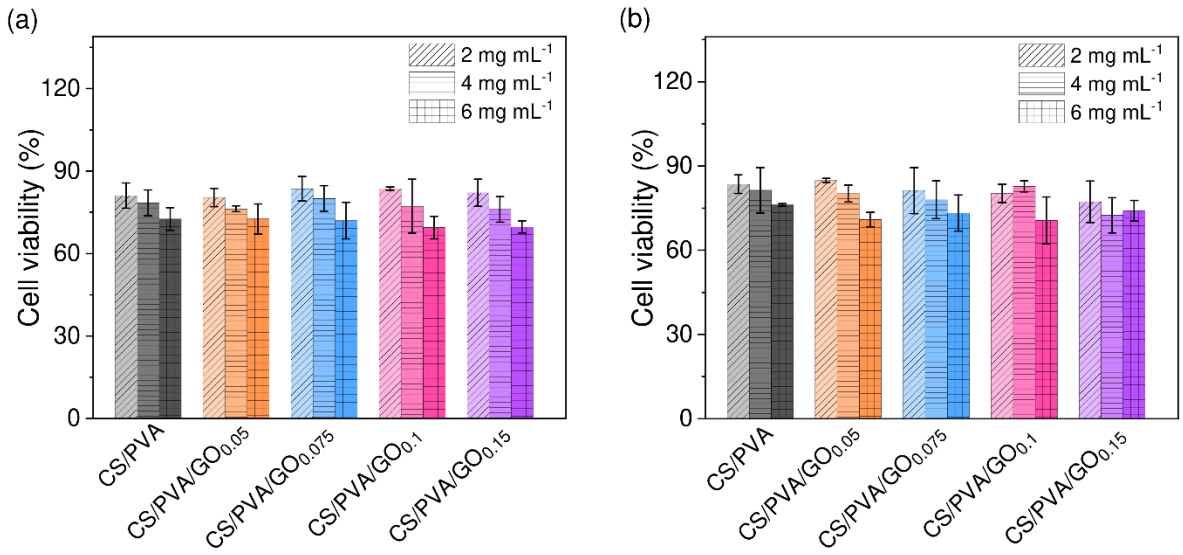

Figure 4.63 Cytotoxicity analysis of soak solutions obtained from CS/PVA/GO coatings at concentration range of 2-6 mg mL^{-1} on (a) PBMCs, and (b) HepG2 cells as determined by MTT assay. Results reported in terms of % cell viability and in controls cells (unexposed) 100% cell viability (0% cytotoxicity) was taken.

4.19.2 Cytotoxicity towards PBMCs and HepG2 Cells

Human peripheral blood mononuclear cells (PBMCs) represent one of the major population of cells that gather at the first line of immune defence during biomaterial implantation in human body (Greulich et al. 2011). Therefore, the cytotoxic impact of pristine and graphene oxide loaded coatings on PBMCs was investigated first (Figure 4.63a). We demonstrated that none of the coatings induced any cytotoxicity effects, where all test samples (CS/PVA/GO coatings) resulted in an average cell viability of 77.1% under the test concentration range of 2-6 mg mL^{-1}. HepG2 cells were employed as *in vitro* model for determining materials' cytotoxicity (Agnihotri et al. 2015; Mersch-Sundermann et al. 2004). As shown in Figure 4.63b, all bioactive coatings including the highest GO concentration (0.15 wt.%) demonstrated >70% cell viability under similar test conditions.

Additionally, when GO concentration in coating films was increased from 2 to 4 mg mL^{-1}, cell viability concomitantly decreased from 82.4% to 77.4% (PBMCs) and 80.9% to 78.3% (HepG2 cells). At 6 mg mL^{-1} GO concentration, mammalian cell viability further reduced to 72.22% (HepG2) and 70.92% (PBMCs).

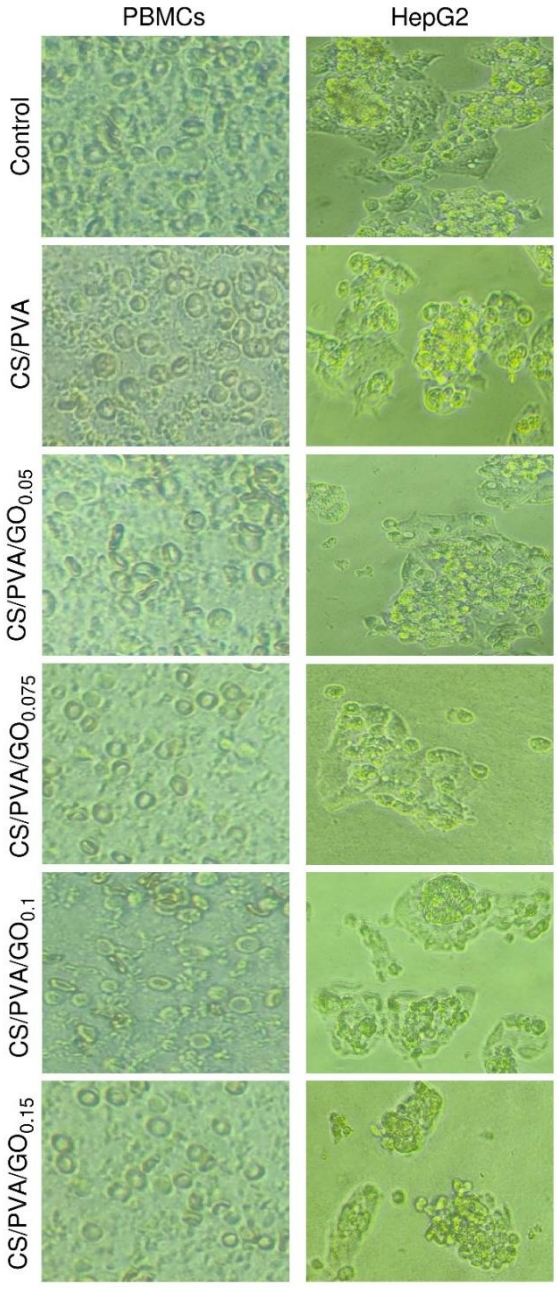

Figure 4.64 Bright-field microscopic images displaying morphology of PBMCs and HepG2 after treatment with 6 mg mL^{-1} soak solution of CS/PVA/GO coatings.

Microscopic analysis demonstrated virtually no significant change in shape of cells upon exposure to CS/PVA/GO coatings. Both, treated PBMCs and HepG2 cells exhibited well

defined and extended morphologies, similar to untreated ones (Figure 4.64). All coatings with GO displayed statistically significant decrease in survival of PBMCs and HepG2 cells compared to control. However, the difference between cell viability of coatings on account of increase in GO concentration was non-significant in both cell groups. As per the biocompatibility guidance, ISO 10993-5, 2009, 'Biological evaluation of medical devices', ≥70% cell viability obtained in test method is regarded as the cytotoxicity safety limit (Urzedo et al. 2020). Thus, we concluded that CS/PVA/GO coatings when coated on SS implants appear as non-cytotoxic against the targeted mammalian cells.

4.20 Degradation behaviour of CS/PVA/GO coatings

The purpose of evaluating extent of degradation in simulated body fluid over 14 days period was to determine coating's durability and estimate its longevity *in vivo* (Figure 4.65a). This would enable us to design a more reliable and long-lasting biomedical coatings. Following the 14-day testing period, pure CS/PVA coatings exhibited a final degradation of 87%, while CS/PVA/GO coatings displayed declining deterioration from 78% to 69% as the GO content increased from 0.05 to 0.15 wt.%. It is well-established that degradation of polymers in a body fluid occurs due to a complex series of events, including water absorption, molecule hydration, hydrogen bond rupture, and eventual hydrolysis of unstable bonds (Depan et al. 2011; Tamayo Marín et al. 2019). Our results indicate that increasing the GO content in Chitosan/PVA blends restrained the entry of SBF into the polymeric matrices, resulting in lower weight loss and consequently lower degradation (Ruiz et al. 2019). This finding underscores the strong adhesion and improved stability of CS/PVA/GO-based coatings (Tamayo Marín et al. 2019). We hypothesize that the extensive hydrogen bonding network between the polymer matrix and GO provides the CS/PVA/GO composite with high-energy links and immense chemical stability.

In addition, a gradual decline in solution pH was observed during the degradation processes of coatings (Figure 4.65b). This observation is an indicative of coating hydrolysis-led dissolution of a more susceptible and acidic moieties available in amorphous phases of the polymer matrix. As a result, the release of residual acetic acid and other harmless degradation by-products, typically present in chitosan polymer may have contributed to the lowering of the pH of SBF (Depan et al. 2013). As determined by ASTM F1635 standard, the admissible pH scales that promote and maintain vital functions in human body lie between 6 and 8. This

indicates that the values obtained in 6.7-7.5 range during coating degradation in this study lie within the reference domain of biological processes.

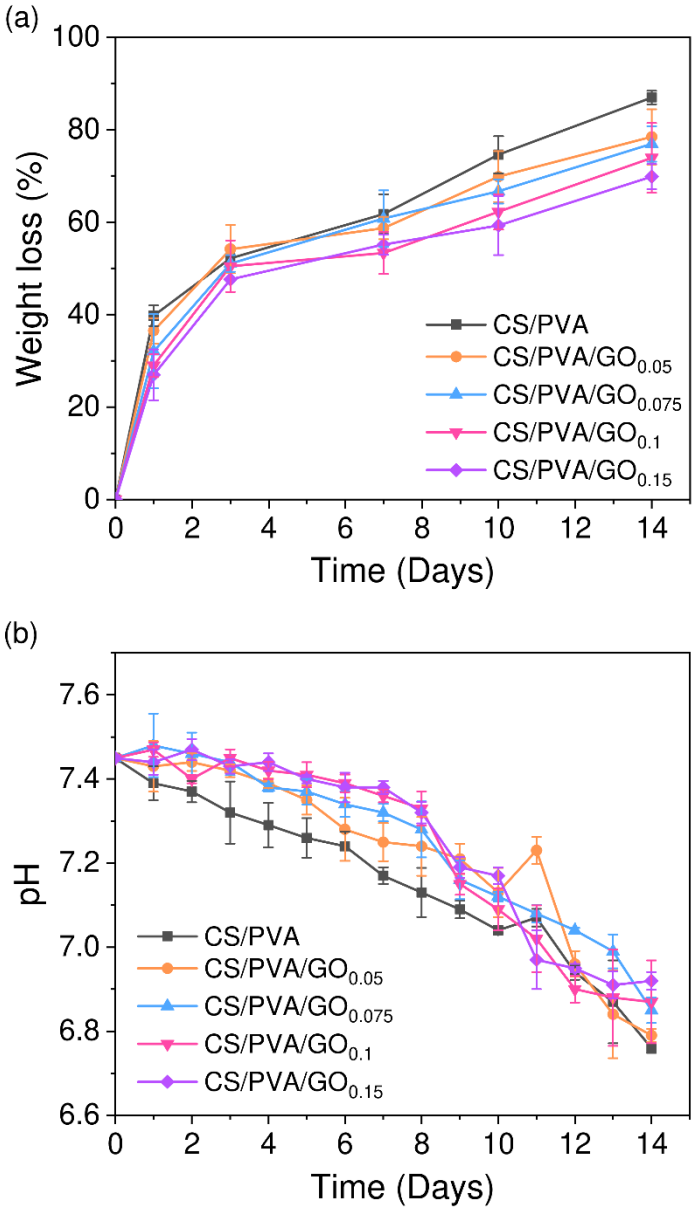

Figure 4.65 (a) Weight loss of CS/PVA/GO nanocomposite coatings and (b) Changes in pH of simulated body fluid, SBF at different time intervals over the span of 14 days.

The topographical changes in CS/PVA/GO coatings that might occur during the degradation process were also examined (as shown in Figure 4.66). The micrographs clearly illustrate a highly rough texture of the coatings, which increases with GO content during degradation. The lighter grey regions in SEM micrographs shows the exposed SS substrate surface from where the coating undergoing degradation has been eroded (Figure 4.66, Column X). A

comparison of the surface morphology of the coatings before and after immersion in SBF can be observed in Figures 4.55 and 4.66, respectively, revealing a noticeable difference in surface texture.

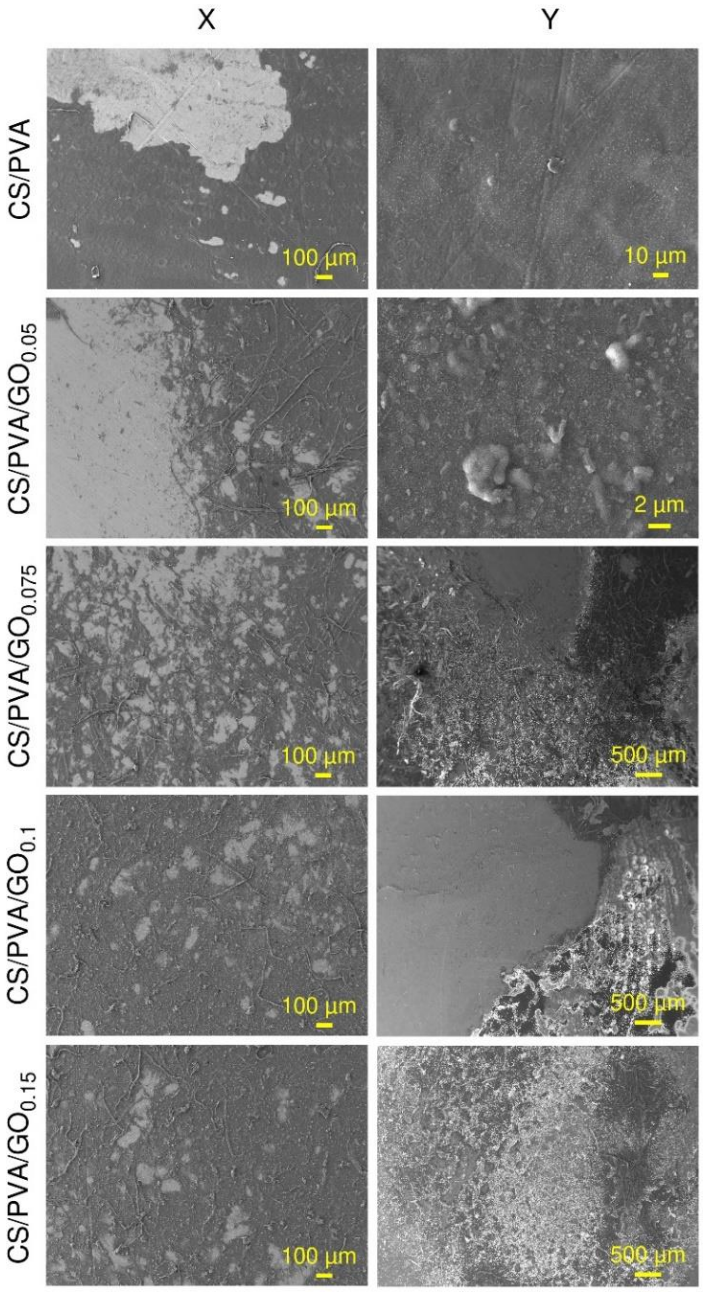

Figure 4.66 FE-SEM micrographs illustrating morphological changes in CS/PVA/GO coatings undergoing degradation after immersion in SBF for 14 days. Column X represents degraded coatings on SS substrate surface after 14 days and Column Y illustrates precipitated whitish layer.

Additionally, a whitish layer that precipitated on the coating surfaces (Figure 4.66, Column Y) could be observed, which is considered suitable as it promotes interaction between the material surface and surrounding tissues (Mokhtari et al. 2018). Energy dispersive spectroscopy (EDS) of test sample revealed the presence of elements such as C, O, and Fe along with small amounts of Na, Cl, K, Cr, Mn, Ca, P, and Ni (Table 4.11). These results provide valuable insights into the degradation behaviour and surface morphology of the polymeric coatings, which are crucial factors in designing reliable and long-lasting biomedical coatings.

Table 4.11 Elemental contents of CS/PVA/$GO_{0.15}$ coating degraded over a time period of 14 days in simulated body fluid (SBF).

Elements	**Mass normal %**
C	24.65
O	5.70
Na	4.23
Cr	12.32
Mn	0.70
Fe	37.23
Ni	4.79
Cl	1.68
Ca	5.83
P	2.42

Chapter 5

Conclusions

The pressing need for hygienic living conditions prompts new challenge for the development of affordable, environmentally friendly, and non-toxic antimicrobial materials. In the realm of resilient bacterial pathogens both in drinking water sources and healthcare facilities, unresolved challenges persisted up to the present day. The effective eradication of bacterial contaminants therefore demands innovative solutions to mitigate allied risks and safeguard public health. The current work is dedicated to develop a polymer-nanoparticles system as 'antibiotic alternatives' offering potent biocidal properties while minimizing the antimicrobial resistance crisis. Three types of polymer nanocomposites, in forms of hydrogels and thin-film coatings containing different biocidal agents (AgNPs or GO) were evaluated for controlling bacterial infections. The antibacterial characteristics, mechanism of action and kinetic modelling of polymeric nanocomposites was done under relevant conditions for water disinfection and biomedical implants coatings. The remarkable versatility of these polymeric nanocomposites, capable of controlling microbial spread in two seemingly unrelated domains, is a testament to their potential. This work serves as a reference point for future research, offering a foundation for the design and implementation of antimicrobial materials across various applications.

"Each achievement is a stepping stone, sufficient for my journey, yet paving the way for others to explore and innovate."

The following conclusions are drawn based on the research work carried out:

5.1 Nano-silver loaded Chitosan-Polyvinyl alcohol (CS/PVA/Ag) Hydrogel for Water Disinfection

- An innovative material was developed to simultaneously eliminate natural and biomedical contaminants from water using a cross-linked chitosan-based hydrogel as an immobilization matrix.
- The nanocomposite was fabricated by immobilizing silver nanoparticles (AgNPs) on to chitosan-PVA hydrogel through *in situ* chemical reduction. The hierarchical network of hydrogel acted as 'miniature nanoreactor' that enabled simultaneous synthesis and immobilization of nanoparticles.
- Structural characterization confirmed the successful loading of AgNPs onto CS/PVA without losing their antimicrobial activity. A high payload of AgNPs did not compromise

the overall structural integrity of CS/PVA hydrogel and remained firmly intercalated within the semi-interpenetrating networks.

- Hydrogel nanocomposites displayed excellent strain-selective biocidal activity under batch process conditions over a broad range of microbial concentrations (10^3-10^6 CFU mL^{-1}). The hydrogels retained ~92% of its disinfection efficiency after 10 reuses and reduced overall ≤ 78% of biofilm within 24 h.

- The correlation of disinfection profile and silver release on multiple reuse, deemed the biocidal action of hydrogel to be 'contact-active', where a higher uptake of microbial cells enabled by macro porous structure of the hydrogel resulted in their instant disruption when in the close vicinity of immobilized AgNPs.

- The hydrogel's affordability, mechanical durability, and long-term disinfection efficacy with a cumulative silver release below 100 ppb indicates its practical employability for point-of-use water treatment purposes.

5.2 Nano-silver loaded Chitosan-Graphene oxide (CS/GO/Ag) Hydrogel for water Disinfection

- The developed nanocomposite hydrogel i.e., chitosan-graphene oxide, served as an immobilization matrix for *in situ* synthesized AgNPs. Optimal GO content, achieved through qualitative cross-linking, ensures structural stability and provides ample anchoring sites for high AgNPs loading.

- The immobilization of small-sized AgNPs increased the surface area by 3-folds to facilitate rapid water permeation with dynamic swelling behaviour and imparted greater thermal and mechanical stability to the hydrogel.

- Chitosan-GO/Ag hydrogel exhibits species-specific disinfection potential under batch conditions with multiple reuse cycles, while adhering to WHO silver release safety limits for drinking water.

- A coupled antibacterial mechanism involving both membrane damage and oxidative stress pathways was envisaged in hydrogel nanocomposites.

- Nanocomposite hydrogels, when formulated into bactericidal column filters, achieve 99% bacterial inactivation within 2.9 minutes in a continuous reactor, following Weibull kinetics as statistically optimized.

- In fixed-bed hydrogel reactors, complete disinfection of real canal and rainwater is achieved within 20 minutes, demonstrating practical water treatment feasibility.
- CS/GO/Ag hydrogel nanocomposites exhibit significant biocompatibility with mammalian cells and biodegradability in soil.
- The implementation of hydrogel reactors with operational simplicity holds immense potential for real-world applications, especially in regions with critical water disinfection infrastructure deficiencies.

5.3 Chitosan-Polyvinyl alcohol/Graphene oxide (CS/PVA/GO) Nanocomposite as Biomedical Coatings

- Graphene oxide, serving as a bacterial growth inhibitor in varying concentrations, was successfully embedded in a chitosan-PVA matrix to create protective coatings on 316L stainless steel substrates through solvent casting and subsequent evaporation.
- This technique yielded smooth, crack-free polymer nanocomposite thin-films on the substrate, demonstrating considerable mechanical strength, thermal stability, and UV-shielding properties.
- Gravimetric drying analysis revealed that thicker coatings (~1400 µm) retained more residual solvent compared to thinner coatings (~700 µm).
- Bioactive coatings exhibited a robust antibacterial response (>82%) within 1 hour and achieved complete inhibition at 6 hours against nosocomial infections causing *Staphylococcus* species.
- The primary antibacterial mechanism of these nanocomposite coatings involved ROS-mediated oxidative stress, supported by morphological damage, intercellular component leakage, and reparatory activity inhibition.
- The coatings demonstrated non-cytotoxicity toward human cell lines and excellent blood compatibility. The addition of GO enhanced coating stability against hydrolytic degradation (69-78%) in simulated body fluids during a 14-day testing period.
- This study's facile and eco-friendly approach opens new avenues for developing an effective strategy to enhance the antibacterial performance and biocompatibility of stainless steel-based implants simultaneously.

Future Scope of the Work

Some key recommendations for future researchers in this field drawn from the insights gained in the current research are given below:

- In addition to the enforcement of stringent guidelines and policies targeting microbial contamination from anthropogenic sources, there's a pressing need for scientific endeavours to explore novel materials and innovative techniques that selectively combat harmful pathogens.
- Extending the hydrogel-based continuous reactor presented in this study with scalable parameters and a comprehensive cost-to-benefit analysis could greatly enhance its adoption in commercial water treatment industries.
- Research into earth-abundant metal-free nanoscale materials such as carbon nitride, red phosphorus, or other natural products, either individually or in synergy with graphene oxide, holds promise for greener nanocomposites, especially in the context of water disinfection.
- Utilizing cross-linking and reducing agents from plant-based sources instead of chemical compounds may enhance the extent of biocompatibility and provide a more suitable microenvironment for optimizing microbe-nanoparticle interactions.
- The potential lies in designing or modifying coatings that permit surface rejuvenation or repair, extending their functional lifespan. Such studies, coupled with a profound understanding of environmental factors, fatigue resistance, and chemical stability, can pave the way for futuristic materials.
- Extensive *in vivo* experimentation to assess long-term biological responses to biomaterials and potential cytotoxicity is of paramount importance. Prioritizing translational research and regulatory compliance through extensive pre-clinical and clinical trials is essential to evaluate the safety and efficacy of these materials in real-world scenarios.

Bibliography

1. Abbasi E, Milani M, Fekri Aval S, Kouhi M, Akbarzadeh A, Tayefi Nasrabadi H, Nikasa P, Joo SW, Hanifehpour Y and Nejati-Koshki K (2016): Silver nanoparticles: synthesis methods, bio-applications and properties. Critical Reviews in Microbiology. 42(2): 173-180.

2. Abberton CL, Bereschenko L, van der Wielen PWJJ and Smith CJ (2016): Survival, biofilm formation, and growth potential of environmental and enteric *Escherichia coli* strains in drinking water microcosms. Applied and Environmental Microbiology. 82(17): 5320-5331.

3. Abboud Y, Saffaj T, Chagraoui A, Bouari AEL, Brouzi K, Tanane O and Ihssane B (2014): Biosynthesis, characterization and antimicrobial activity of copper oxide nanoparticles (CONPs) produced using brown alga extract (*Bifurcaria bifurcata*). Applied Nanoscience. 4: 571-576.

4. Abdal-hay A, Amna T and Lim JK (2013): Biocorrosion and osteoconductivity of PCL/nHAp composite porous film-based coating of magnesium alloy. Solid State Sciences. 18: 131-140.

5. Abdullah ZW, Dong Y, Davies IJ and Barbhuiya S (2017): PVA, PVA blends, and their nanocomposites for biodegradable packaging application. Polymer-Plastics Technology and Engineering. 56(12): 1307-1344.

6. Abid N, Khan AM, Shujait S, Chaudhary K, Ikram M, Imran M, Haider J, Khan M, Khan Q and Maqbool M (2022): Synthesis of nanomaterials using various top-down and bottom-up approaches, influencing factors, advantages, and disadvantages: A review. Advances in Colloid and Interface Science. 300: 1-18.

7. Abubshait HA, Saad M, Iqbal S, Abubshait SA, Bahadur A, Raheel M, Alshammari FH, Alwadai N, Alrbyawi H and Abourehab MA (2023): Co-doped zinc oxide nanoparticles embedded in Polyvinylalcohol Hydrogel as solar light derived photocatalyst disinfection and removal of coloured pollutants. Journal of Molecular Structure. 1271: 1-9.

8. Adibzadeh S, Bazgir S and Katbab AA (2014): Fabrication and characterization of chitosan/poly (vinyl alcohol) electrospun nanofibrous membranes containing silver nanoparticles for antibacterial water filtration. Iranian Polymer Journal. 23: 645-654.

9. Agnihotri S, Bajaj G, Mukherji S and Mukherji S (2015): Arginine-assisted immobilization of silver nanoparticles on ZnO nanorods: an enhanced and reusable antibacterial substrate without human cell cytotoxicity. Nanoscale. 7(16): 7415-7429.

10. Agnihotri S, Mukherji S and Mukherji S (2012): Antimicrobial chitosan–PVA hydrogel as a nanoreactor and immobilizing matrix for silver nanoparticles. Applied Nanoscience. 2: 179-188.

11. Agnihotri S, Mukherji S and Mukherji S (2013): Immobilized silver nanoparticles enhance contact killing and show highest efficacy: elucidation of the mechanism of bactericidal action of silver. Nanoscale. 5(16): 7328-7340.

12. Agnihotri S, Mukherji S and Mukherji S (2019): Impact of background water quality on disinfection performance and silver release of immobilized silver nanoparticles: Modeling disinfection kinetics, bactericidal mechanism and aggregation behavior. Chemical Engineering Journal. 372: 684-696.

13. Agnihotri S, Mukherji S and Mukherji S (2014): Size-controlled silver nanoparticles synthesized over the range 5–100 nm using the same protocol and their antibacterial efficacy. RSC Advances. 4(8): 3974-3983.

14. Agnihotri S, Sillu D, Sharma G and Arya RK (2018): Photocatalytic and antibacterial potential of silver nanoparticles derived from pineapple waste: process optimization and modeling kinetics for dye removal. Applied Nanoscience. 8: 2077-2092.

15. Ahmed A, Adak B, Bansala T and Mukhopadhyay S (2019): Green solvent processed cellulose/graphene oxide nanocomposite films with superior mechanical, thermal, and ultraviolet shielding properties. ACS Applied Materials & Interfaces. 12(1): 1687-1697.

16. Ahmed AESI (2012): Hydrogels for water filters: Characterization and regeneration. Journal of Applied Polymer Science. 123(3): 1889-1895.

17. Ahmed EM (2015): Hydrogel: Preparation, characterization, and applications: A review. Journal of Advanced Research. 6(2): 105-121.

18. Akharame MO, Fatoki OS, Opeolu BO, Olorunfemi DI and Oputu OU (2018): Polymeric nanocomposites (PNCs) for wastewater remediation: an overview. Polymer-Plastics Technology and Engineering. 57(17): 1801-1827.

19. Akhavan O (2009): Lasting antibacterial activities of Ag–TiO_2/Ag/a-TiO_2 nanocomposite thin film photocatalysts under solar light irradiation. Journal of Colloid and Interface Science. 336(1): 117-124.

20. Akhavan O and Ghaderi E (2010): Toxicity of graphene and graphene oxide nanowalls against bacteria. ACS Nano. 4(10): 5731-5736.

21. Akpan E, Gbenebor O, Adeosun S and Cletus O (2020): Solubility, degree of acetylation, and distribution of acetyl groups in chitosan. In: Handbook of Chitin and Chitosan. Elsevier, pp. 131-164.

22. Alexander JW (2009): History of the medical use of silver. Surgical Infections. 10(3): 289-292.

23. Alfuraydi RT, Alminderej FM and Mohamed NA (2022): Evaluation of antimicrobial and anti-biofilm formation activities of novel poly (vinyl alcohol) hydrogels reinforced with crosslinked chitosan and silver nano-particles. Polymers. 14(8): 1-25.

24. Alghamdi HM, Abutalib M, Mannaa MA, Nur O, Abdelrazek E and Rajeh A (2022): Modification and development of high bioactivities and environmentally safe polymer nanocomposites doped by Ni/ZnO nanohybrid for food packaging applications. Journal of Materials Research and Technology. 19: 3421-3432.

25. Ali AE-H, Raafat AI, Mahmoud GA, Badway NA, El-Mottaleb M and Elshahawy M (2016): Photocatalytic decolorization of dye effluent using radiation developed polymeric nanocomposites. Journal of Inorganic and Organometallic Polymers and Materials. 26: 606-615.

26. Alkhouzaam A, Qiblawey H, Khraisheh M, Atieh M and Al-Ghouti M (2020): Synthesis of graphene oxides particle of high oxidation degree using a modified Hummers method. Ceramics International. 46(15): 23997-24007.

27. Alvarez PJ, Chan CK, Elimelech M, Halas NJ and Villagrán D (2018): Emerging opportunities for nanotechnology to enhance water security. Nature Nanotechnology. 13(8): 634-641.

28. Amin Yavari S, Castenmiller SM, van Strijp JA and Croes M (2020): Combating implant infections: shifting focus from bacteria to host. Advanced Materials. 32(43): 1-25.

29. Amro NA, Kotra LP, Wadu-Mesthrige K, Bulychev A, Mobashery S and Liu G-y (2000): High-resolution atomic force microscopy studies of the *Escherichia coli* outer membrane: structural basis for permeability. Langmuir. 16(6): 2789-2796.

30. An J-H and Dultz S (2007): Adsorption of tannic acid on chitosan-montmorillonite as a function of pH and surface charge properties. Applied Clay Science. 36(4): 256-264.

31. Archer NK, Mazaitis MJ, Costerton JW, Leid JG, Powers ME and Shirtliff ME (2011): *Staphylococcus aureus* biofilms: properties, regulation, and roles in human disease. Virulence. 2(5): 445-459.

32. Arciola CR, Campoccia D and Montanaro L (2018): Implant infections: adhesion, biofilm formation and immune evasion. Nature reviews microbiology. 16(7): 397-409.

33. Arukalam IO, Oguzie EE and Li Y (2016): Fabrication of FDTS-modified PDMS-ZnO nanocomposite hydrophobic coating with anti-fouling capability for corrosion protection of Q235 steel. Journal of Colloid and Interface Science. 484: 220-228.

34. Arya RK, Kaur J, Chandra A, Ahuja S, Rawat M and Sharma J (2021): Designing of biodegradable polycaprolactone: Binary and ternary coatings to minimize the defects and cost of solvent(s). Journal of Applied Polymer Science. 138(35): 1-15.

35. Asgari E, Esrafili A, Jafari AJ, Kalantary RR, Nourmoradi H and Farzadkia M (2019): The comparison of ZnO/polyaniline nanocomposite under UV and visible radiations for decomposition of metronidazole: degradation rate, mechanism and mineralization. Process Safety and Environmental Protection. 128: 65-76.

36. Ashbolt NJ (2015): Microbial contamination of drinking water and human health from community water systems. Current Environmental Health Reports. 2: 95-106.

37. Askarnia R, Fardi SR, Sobhani M and Staji H (2021): Ternary hydroxyapatite/chitosan/graphene oxide composite coating on AZ91D magnesium alloy by electrophoretic deposition. Ceramics International. 47(19): 27071-27081.

38. Atmianlu PA, Badpa R, Aghabalaei V and Baghdadi M (2021): A review on the various beds used for immobilization of nanoparticles: Overcoming the barrier to nanoparticle applications in water and wastewater treatment. Journal of Environmental Chemical Engineering. 9(6): 1-25.

39. Awada H and Daneault C (2015): Chemical modification of poly (vinyl alcohol) in water. Applied Sciences. 5(4): 840-850.

40. Ayala-Núñez NV, Lara Villegas HH, del Carmen Ixtepan Turrent L and Rodríguez Padilla C (2009): Silver nanoparticles toxicity and bactericidal effect against methicillin-resistant *Staphylococcus aureus*: nanoscale does matter. Nanobiotechnology. 5: 2-9.

41. Aydemir T, Liverani L, Pastore JI, Ceré SM, Goldmann WH, Boccaccini AR and Ballarre J (2020): Functional behavior of chitosan/gelatin/silica-gentamicin coatings by electrophoretic deposition on surgical grade stainless steel. Materials Science and Engineering: C. 115: 1-10.

42. Azam A, Ahmed AS, Oves M, Khan MS and Memic A (2012): Size-dependent antimicrobial properties of CuO nanoparticles against Gram-positive and-negative bacterial strains. International Journal of Nanomedicine. 3527-3535.

43. Bahcelioglu E, Unalan HE and Erguder TH (2021): Silver-based nanomaterials: A critical review on factors affecting water disinfection performance and silver release. Critical Reviews in Environmental Science and Technology. 51(20): 2389-2423.

44. Bain R, Johnston R and Slaymaker T (2020): Drinking water quality and the SDGs. npj Clean Water. 3(1): 1-3.

45. Baker-Austin C, Oliver JD, Alam M, Ali A, Waldor MK, Qadri F and Martinez-Urtaza J (2018): *Vibrio spp.* infections. Nature Reviews Disease Primers. 4(1): 1-19.

46. Bakhsheshi-Rad HR, Ismail AF, Aziz M, Akbari M, Hadisi Z, Khoshnava SM, Pagan E and Chen X (2020): Co-incorporation of graphene oxide/silver nanoparticle into poly-L-lactic acid fibrous: A route toward the development of cytocompatible and antibacterial coating layer on magnesium implants. Materials Science and Engineering: C. 111: 1-16.

47. Balazs AC, Emrick T and Russell TP (2006): Nanoparticle polymer composites: where two small worlds meet. Science. 314(5802): 1107-1110.

48. Barik B, Nayak PS and Dash P (2020): Nanomaterials in wastewater treatments. In: Nanotechnology in the Beverage Industry. Elsevier, pp. 185-206.

49. Barillo DJ and Marx DE (2014): Silver in medicine: A brief history BC 335 to present. Burns. 40: S3-S8.

50. Barnes HA, Hutton JF and Walters K (1989): An introduction to rheology. Elsevier.

51. Basuki KT, Swantomo D and Sanyoto NT (2015): Characterization of chitosan-acrylamide hydrogels as soil conditioner. Advanced Materials Research. 1112: 414-417.

52. Beg S, Almalki WH, Malik A, Farhan M, Aatif M, Rahman Z, Alruwaili NK, Alrobaian M, Tarique M and Rahman M (2020): 3D printing for drug delivery and biomedical applications. Drug Discovery Today. 25(9): 1668-1681.

53. Bezerra RD, Teixeira PR, Teixeira A, Eiras C, Osajima JA and Silva Filho EC (2015): Chemical functionalization of cellulosic materials—main reactions and applications in the contaminants removal of aqueous medium. In: Cellulose—fundamental aspects and current trends. Intech.

54. Bharathi BS and Stalin T (2019): Cerium oxide and peppermint oil loaded polyethylene oxide/graphene oxide electrospun nanofibrous mats as antibacterial wound dressings. Materials Today Communications. 21: 1-11.

55. Bhargava CK and Arya RK (2015): Design of Binary Polymeric Coatings for Minimizing the Residual Solvent, Part I: Experimentation. Drying Technology. 33(1): 92-102.

56. Bharti S, Agnihotri S, Mukherji S and Mukherji S (2015): Effectiveness of immobilized silver nanoparticles in inactivation of pathogenic bacteria. Journal of Environmental Research And Development. 9(3A): 849-856.

57. Bhatia K, Chauhan K, Attri C and Seth A (2017): Improving stability and reusability of *Rhodococcus pyridinivorans* NIT-36 nitrilase by whole cell immobilization using chitosan. International Journal of Biological Macromolecules. 103: 8-15.

58. Bhattarai N, Gunn J and Zhang M (2010): Chitosan-based hydrogels for controlled, localized drug delivery. Advanced Drug Delivery Reviews. 62(1): 83-99.

59. Bitinis N, Hernández M, Verdejo R, Kenny JM and Lopez-Manchado MA (2011): Recent advances in clay/polymer nanocomposites. Advanced Materials. 23(44): 5229-5236.

60. Bogdanovic U, Vodnik V, Mitric M, Dimitrijevic S, Skapin SD, Zunic V, Budimir M and Stoiljkovic M (2015): Nanomaterial with High Antimicrobial Efficacy • Copper/Polyaniline Nanocomposite. ACS Applied Materials & Interfaces. 7(3): 1955-1966.

61. Bondarenko O, Ivask A, Käkinen A, Kurvet I and Kahru A (2013): Particle-cell contact enhances antibacterial activity of silver nanoparticles. PLoS One. 8(5): 1-12.

62. Borkow G and Gabbay J (2009): Copper, an ancient remedy returning to fight microbial, fungal and viral infections. Current Chemical Biology. 3(3): 272-278.

63. Bree G, Geaney H and Ryan KM (2019): Electrophoretic deposition of tin sulfide nanocubes as high-performance lithium-ion battery anodes. ChemElectroChem. 6(12): 3049-3056.

64. Brodie BC (1859): XIII. On the atomic weight of graphite. Philosophical Transactions of the Royal Society of London. (149): 249-259.

65. Buzrul S (2022): The Weibull model for microbial inactivation. Food Engineering Reviews. 14(1): 45-61.

66. Cacaci M, Martini C, Guarino C, Torelli R, Bugli F and Sanguinetti M (2020): Graphene oxide coatings as tools to prevent microbial biofilm formation on medical device. In: Advances in Microbiology, Infectious Diseases and Public Health. Springer, Cham, pp. 21-35.

67. Cámara M, Green W, MacPhee CE, Rakowska PD, Raval R, Richardson MC, Slater-Jefferies J, Steventon K and Webb JS (2022): Economic significance of biofilms: a multidisciplinary and cross-sectoral challenge. npj Biofilms and Microbiomes. 8(1): 1-8.

68. Camargo PHC, Satyanarayana KG and Wypych F (2009): Nanocomposites: synthesis, structure, properties and new application opportunities. Materials Research. 12: 1-39.

69. Campoccia D, Montanaro L and Arciola CR (2013): A review of the biomaterials technologies for infection-resistant surfaces. Biomaterials. 34(34): 8533-8554.

70. Carotenuto G, Nicolais L, Martorana B and Perlo P (2005): Metal–polymer nanocomposite synthesis: novel *ex situ* and *in situ* approaches. In: Metal–Polymer Nanocomposites. Wiley, pp. 155-181.

71. Carpio IEM, Santos CM, Wei X and Rodrigues DF (2012): Toxicity of a polymer–graphene oxide composite against bacterial planktonic cells, biofilms, and mammalian cells. Nanoscale. 4(15): 4746-4756.

72. Chabot V, Higgins D, Yu A, Xiao X, Chen Z and Zhang J (2014): A review of graphene and graphene oxide sponge: material synthesis and applications to energy and the environment. Energy & Environmental Science. 7(5): 1564-1596.

73. Chae K, Jang WY, Park K, Lee J, Kim H, Lee K, Lee CK, Lee Y, Lee SH and Seo J (2020): Antibacterial infection and immune-evasive coating for orthopedic implants. Science Advances. 6(44): 1-16.

74. Chaloupka K, Malam Y and Seifalian AM (2010): Nanosilver as a new generation of nanoproduct in biomedical applications. Trends in Biotechnology. 28(11): 580-588.

75. Chappell J and Greville G (1954): Effect of silver ions on mitochondrial adenosine triphosphatase. Nature. 174(4437): 930-931.

76. Chatterjee AK, Chakraborty R and Basu T (2014): Mechanism of antibacterial activity of copper nanoparticles. Nanotechnology. 25(13): 1-13.

77. Chen J, Wang J, Zhang X and Jin Y (2008): Microwave-assisted green synthesis of silver nanoparticles by carboxymethyl cellulose sodium and silver nitrate. Materials Chemistry and Physics. 108(2-3): 421-424.

78. Chen X, Wei S, Yadav A, Patil R, Zhu J, Ximenes R, Sun L and Guo Z (2011): Poly (propylene)/Carbon Nanofiber Nanocomposites: *Ex Situ* Solvent-Assisted Preparation and Analysis of Electrical and Electronic Properties. Macromolecular Materials and Engineering. 296(5): 434-443.

79. Chen Y, Chen L, Bai H and Li L (2013): Graphene oxide–chitosan composite hydrogels as broad-spectrum adsorbents for water purification. Journal of Materials Chemistry A. 1(6): 1992-2001.

80. Chen Y, Ding Y and Zheng J (2020): A polymer nanocomposite coating with enhanced hydrophilicity, antibacterial and antibiofouling properties: Role of polymerizable emulsifier/anionic ligand. Chemical Engineering Journal. 379: 122268.

81. Cheng YF, Zhang JY, Wang YB, Li CM, Lu ZS, Hu XF and Xu LQ (2019): Deposition of catechol-functionalized chitosan and silver nanoparticles on biomedical titanium surfaces for antibacterial application. Materials Science and Engineering: C. 98: 649-656.

82. Chong MN, Jin B, Chow CW and Saint C (2010): Recent developments in photocatalytic water treatment technology: a review. Water Research. 44(10): 2997-3027.

83. Chuang W-Y, Young T-H, Yao C-H and Chiu W-Y (1999): Properties of the poly (vinyl alcohol)/chitosan blend and its effect on the culture of fibroblast *in vitro*. Biomaterials. 20(16): 1479-1487.

84. Cloutier M, Mantovani D and Rosei F (2015): Antibacterial coatings: challenges, perspectives, and opportunities. Trends in Biotechnology. 33(11): 637-652.

85. Compton OC and Nguyen ST (2010): Graphene oxide, highly reduced graphene oxide, and graphene: versatile building blocks for carbon-based materials. Small. 6(6): 711-723.

86. Cook B, Tehrani B, Cooper J, Kim S and Tentzeris M (2014): Integrated printing for 2D/3D flexible organic electronic devices. In: Handbook of Flexible Organic Electronics: Materials, Manufacturing and Applications. Woodhead Publishing, Oxford, pp. 199-216.

87. Cornell RJ and Donaruma LG (1965): 2-Methacryloxytropones. Intermediates for the synthesis of biologically active polymers. Journal of Medicinal Chemistry. 8(3): 388-390.

88. Cortés YZ, Valenzuela LM, Peña EAE and Sánchez BLE (2021): Antibacterial activity of electrospun nanocomposites fabricated by *In situ* chitosan/silver nanoparticles. IEEE Transactions on NanoBioscience. 21(1): 89-96.

89. Cui X, Lee JJ and Chen WN (2019): Eco-friendly and biodegradable cellulose hydrogels produced from low cost okara: towards non-toxic flexible electronics. Scientific Reports. 9(1): 1-9.

90. Cunningham A and Bürgi T (2013): Bottom-up organisation of metallic nanoparticles. In: Amorphous nanophotonics. Springer, pp. 1-37.

91. Dai T, Wang C, Wang Y, Xu W, Hu J and Cheng Y (2018): A nanocomposite hydrogel with potent and broad-spectrum antibacterial activity. ACS Applied Materials & Interfaces. 10(17): 15163-15173.

92. Das L, Das P, Bhowal A and Bhattachariee C (2020): Synthesis of hybrid hydrogel nano-polymer composite using Graphene oxide, Chitosan and PVA and its application in waste water treatment. Environmental Technology & Innovation. 18: 1-17.

93. de Oliveira Cruz FS, Nascimento MA, Puiatti GA, de Oliveira AF, Mounteer AH and Lopes RP (2020): Textile effluent treatment using a fixed bed reactor using bimetallic Fe/Ni nanoparticles supported on chitosan spheres. Journal of Environmental Chemical Engineering. 8(5): 1-9.

94. Deng C-H, Gong J-L, Zhang P, Zeng G-M, Song B and Liu H-Y (2017): Preparation of melamine sponge decorated with silver nanoparticles-modified graphene for water disinfection. Journal of Colloid and Interface Science. 488: 26-38.

95. Deng Y, Song G-L, Zheng D and Zhang Y (2021): Fabrication and synergistic antibacterial and antifouling effect of an organic/inorganic hybrid coating embedded with nanocomposite Ag@ TA-SiO2 particles. Colloids and Surfaces A: Physicochemical and Engineering Aspects. 613: 1-14.

96. Depan D, Girase B, Shah J and Misra RDK (2011): Structure–process–property relationship of the polar graphene oxide-mediated cellular response and stimulated growth of osteoblasts on hybrid chitosan network structure nanocomposite scaffolds. Acta Biomaterialia. 7(9): 3432-3445.

97. Depan D, Shah J and Misra R (2013): Degradation mechanism and increased stability of chitosan-based hybrid scaffolds cross-linked with nanostructured carbon:

Process–structure–functional property relationship. Polymer Degradation and Stability. 98(11): 2331-2339.

98. Devi L and Gaba P (2019): Hydrogel: An updated primer. Journal of Critical Reviews. 10: 1-10.

99. Dhanalakshmi M, Thenmozhi S, Devi KM and Kameshwaran S (2013): Silver nanoparticles and its antibacterial activity. International Journal of Pharmaceutical & Biological Archives. 4: 819-826.

100. Dil NN and Sadeghi M (2018): Free radical synthesis of nanosilver/gelatin-poly (acrylic acid) nanocomposite hydrogels employed for antibacterial activity and removal of Cu (II) metal ions. Journal of Hazardous Materials. 351: 38-53.

101. Dimatteo R, Darling NJ and Segura T (2018): *In situ* forming injectable hydrogels for drug delivery and wound repair. Advanced Drug Delivery Reviews. 127: 167-184.

102. Domènech B, Muñoz M, Muraviev D and Macanás J (2013): Polymer-silver nanocomposites as antibacterial materials. In: Microbial pathogens and strategies for combating them: science, technology and education. Formatex, pp. 630-640.

103. Dreyer DR, Park S, Bielawski CW and Ruoff RS (2010): The chemistry of graphene oxide. Chemical Society Reviews. 39(1): 228-240.

104. Duan C, Liu C, Meng X, Gao K, Lu W, Zhang Y, Dai L, Zhao W, Xiong C and Wang W (2020): Facile synthesis of Ag NPs@ MIL-100 (Fe)/guar gum hybrid hydrogel as a versatile photocatalyst for wastewater remediation: Photocatalytic degradation, water/oil separation and bacterial inactivation. Carbohydrate Polymers. 230: 1-9.

105. Dubey SK, Dey A, Singhvi G, Pandey MM, Singh V and Kesharwani P (2022): Emerging trends of nanotechnology in advanced cosmetics. Colloids and surfaces B: Biointerfaces. 214: 1-40.

106. Durán N, Durán M, De Jesus MB, Seabra AB, Fávaro WJ and Nakazato G (2016): Silver nanoparticles: A new view on mechanistic aspects on antimicrobial activity. Nanomedicine: nanotechnology, biology and medicine. 12(3): 789-799.

107. Duval RE, Gouyau J and Lamouroux E (2019): Limitations of recent studies dealing with the antibacterial properties of silver nanoparticles: Fact and opinion. Nanomaterials. 9(12): 1-22.

108. Eivazzadeh-Keihan R, Radinekiyan F, Aliabadi HAM, Sukhtezari S, Tahmasebi B, Maleki A and Madanchi H (2021): Chitosan hydrogel/silk fibroin/Mg $(OH)_2$ nanobiocomposite as a novel scaffold with antimicrobial activity and improved mechanical properties. Scientific Reports. 11(1): 1-13.

109. El Knidri H, Laajeb A and Lahsini A (2020): Chitin and chitosan: chemistry, solubility, fiber formation, and their potential applications. In: Handbook of Chitin and Chitosan. Elsevier, pp. 35-57.

110. Escudero-Oñate C and Martínez-Francés E (2018): A review of chitosan-based materials for the removal of organic pollution from water and bioaugmentation. In: Chitin-Chitosan-Myriad Functionalities in Science and Technology.

111. Esua OJ, Sun D-W, Ajani CK, Cheng J-H and Keener KM (2022): Modelling of inactivation kinetics of *Escherichia coli* and *Listeria monocytogenes* on grass carp treated by combining ultrasound with plasma functionalized buffer. Ultrasonics Sonochemistry. 88: 1-11.

112. Fahlman BD (2023): Nanomaterials. In: Materials Chemistry. Springer, pp. 533-719.

113. Fan JJ, Grande CD and Rodrigues DF (2017): Biodegradation of graphene oxide-polymer nanocomposite films in wastewater. Environmental Science: Nano. 4(9): 1808-1816.

114. Fang Y, Xing C, Zhan S, Zhao M, Li M and Liu H (2019): A polyoxometalate-modified magnetic nanocomposite: a promising antibacterial material for water treatment. Journal of Materials Chemistry B 7(11): 1933-1944.

115. Filipović U, Dahmane RG, Ghannouchi S, Zore A and Bohinc K (2020): Bacterial adhesion on orthopedic implants. Advances in Colloid and Interface Science. 283: 1-12.

116. Fiorani G, Saoncella O, Kaner P, Altinkaya S, Figoli A, Bonchio M and Carraro M (2014): Chitosan-polyoxometalate nanocomposites: synthesis, characterization and application as antimicrobial agents. Journal of Cluster Science. 25: 839-854.

117. Gaaz TS, Sulong AB, Akhtar MN, Kadhum AAH, Mohamad AB and Al-Amiery AA (2015): Properties and applications of polyvinyl alcohol, halloysite nanotubes and their nanocomposites. Molecules. 20(12): 22833-22847.

118. Gandara-Loe J, Souza BE, Missyul A, Giraldo G, Tan J-C and Silvestre-Albero J (2020): MOF-based polymeric nanocomposite films as potential materials for drug delivery devices in ocular therapeutics. ACS Applied Materials & Interfaces. 12(27): 30189-30197.

119. Gao F (2012): Advances in polymer nanocomposites: types and applications. Elsevier.

120. García-Cruz L, Casado-Coterillo C, Irabien Á, Montiel V and Iniesta J (2016): High performance of alkaline anion-exchange membranes based on chitosan/poly (vinyl) alcohol doped with graphene oxide for the electrooxidation of primary alcohols. C. 2(2): 1-19.

121. Gaur M, Misra C, Yadav AB, Swaroop S, Maolmhuaidh FÓ, Bechelany M and Barhoum A (2021): Biomedical applications of carbon nanomaterials: fullerenes, quantum dots, nanotubes, nanofibers, and graphene. Materials. 14(20): 1-35.

122. Geim AK and Novoselov KS (2007): The rise of graphene. Nature Materials. 6(3): 183-191.

123. Ghazzy A, Naik RR and Shakya AK (2023): Metal–Polymer Nanocomposites: A Promising Approach to Antibacterial Materials. Polymers. 15(9): 1-30.

124. Ghodsi S, Esrafili A, Sobhi HR, Rezaei Kalantary R and Gholami M (2021): Synthesis and application of g-C_3N_4/Fe_3O_4/Ag nanocomposite for the efficient photocatalytic inactivation of *Escherichia coli* and *Bacillus subtilis* bacteria in aqueous solutions. AMB Express. 11(1): 1-12.

125. Ghorpade VS, Dias RJ, Mali KK and Mulla SI (2019): Citric acid crosslinked carboxymethylcellulose-polyvinyl alcohol hydrogel films for extended release of water soluble basic drugs. Journal of Drug Delivery Science and Technology. 52: 421-430.

126. Giannousi K, Lafazanis K, Arvanitidis J, Pantazaki A and Dendrinou-Samara C (2014): Hydrothermal synthesis of copper based nanoparticles: antimicrobial screening and interaction with DNA. Journal of Inorganic Biochemistry. 133: 24-32.

127. Gogoi N and Chowdhury D (2014): *In-situ* and *ex-situ* chitosan-silver nanoparticle composite: comparison of storage/release and catalytic properties. Journal of Nanoscience and Nanotechnology. 14(6): 4147-4155.

128. Gogoi SK, Gopinath P, Paul A, Ramesh A, Ghosh SS and Chattopadhyay A (2006): Green fluorescent protein-expressing *escherichia coli* as a model system for investigating the antimicrobial activities of silver nanoparticles. Langmuir. 22(22): 9322-9328.

129. Gondal M, Dastageer M and Khalil A (2009): Synthesis of nano-WO_3 and its catalytic activity for enhanced antimicrobial process for water purification using laser induced photo-catalysis. Catalysis Communications. 11(3): 214-219.

130. Götz F (2002): *Staphylococcus* and biofilms. Molecular Microbiology. 43(6): 1367-1378.

131. Grant JJ, Pillai SC, Hehir S, McAfee M and Breen A (2021): Biomedical applications of electrospun graphene oxide. ACS Biomaterials Science & Engineering. 7(4): 1278-1301.

132. Grass G, Rensing C and Solioz M (2011): Metallic copper as an antimicrobial surface. Applied and Environmental Microbiology. 77(5): 1541-1547.

133. Greulich C, Diendorf J, Gessmann J, Simon T, Habijan T, Eggeler G, Schildhauer T, Epple M and Köller M (2011): Cell type-specific responses of peripheral blood mononuclear cells to silver nanoparticles. Acta Biomaterialia. 7(9): 3505-3514.

134. Gulrez SK, Al-Assaf S and Phillips GO (2011): Hydrogels: methods of preparation, characterisation and applications. In: Progress in molecular and environmental bioengineering-from analysis and modeling to technology applications. InTech, pp. 117-150.

135. Gungordu Er S, Edirisinghe M and Tabish TA (2023): Graphene-Based Nanocomposites as Antibacterial, Antiviral and Antifungal Agents. Advanced Healthcare Materials. 12(6): 1-20.

136. Guo Q, Ghadiri R, Weigel T, Aumann A, Gurevich EL, Esen C, Medenbach O, Cheng W, Chichkov B and Ostendorf A (2014): Comparison of *in situ* and *ex situ* methods for synthesis of two-photon polymerization polymer nanocomposites. Polymers. 6(7): 2037-2050.

137. Guo Y, Dundas CM, Zhou X, Johnston KP and Yu G (2021): Molecular engineering of hydrogels for rapid water disinfection and sustainable solar vapor generation. Advanced Materials. 33(35): 1-8.

138. Gyles DA, Castro LD, Silva Jr JOC and Ribeiro-Costa RM (2017): A review of the designs and prominent biomedical advances of natural and synthetic hydrogel formulations. European Polymer Journal. 88: 373-392.

139. Hajji S, Chaker A, Jridi M, Maalej H, Jellouli K, Boufi S and Nasri M (2016): Structural analysis, and antioxidant and antibacterial properties of chitosan-poly (vinyl alcohol) biodegradable films. Environmental Science and Pollution Research. 23: 15310-15320.

140. Halima NB (2016): Poly (vinyl alcohol): review of its promising applications and insights into biodegradation. RSC Advances. 6(46): 39823-39832.

141. Han DL, Yan LF, Chen WF and Li W (2011): Preparation of chitosan/graphene oxide composite film with enhanced mechanical strength in the wet state. Carbohydrate Polymers. 83(2): 653-658.

142. Hanemann T and Szabó DV (2010): Polymer-nanoparticle composites: from synthesis to modern applications. Materials. 3(6): 3468-3517.

143. Haraguchi K (2011): Synthesis and properties of soft nanocomposite materials with novel organic/inorganic network structures. Polymer Journal. 43(3): 223-241.

144. Hasan A, Waibhaw G, Saxena V and Pandey LM (2018): Nano-biocomposite scaffolds of chitosan, carboxymethyl cellulose and silver nanoparticle modified cellulose nanowhiskers for bone tissue engineering applications. International Journal of Biological Macromolecules. 111: 923-934.

145. Hassan CM and Peppas NA (2000): Structure and applications of poly (vinyl alcohol) hydrogels produced by conventional crosslinking or by freezing/thawing methods. In: Biopolymers· PVA hydrogels, anionic polymerisation nanocomposites, pp. 37-65.

146. He P, Chen L, Shao L, Zhang H and Lü F (2019): Municipal solid waste (MSW) landfill: A source of microplastics?-Evidence of microplastics in landfill leachate. Water Research. 159: 38-45.

147. Hennink WE and van Nostrum CF (2012): Novel crosslinking methods to design hydrogels. Advanced Drug Delivery Reviews. 64: 223-236.

148. Hess PH and Parker Jr PH (1966): Polymers for stabilization of colloidal cobalt particles. Journal of Applied Polymer Science. 10(12): 1915-1927.

149. Hir ZAM, Moradihamedani P, Abdullah AH and Mohamed MA (2017): Immobilization of TiO_2 into polyethersulfone matrix as hybrid film photocatalyst for effective degradation of methyl orange dye. Materials Science in Semiconductor Processing. 57: 157-165.

150. Hoop M, Shen Y, Chen XZ, Mushtaq F, Iuliano LM, Sakar MS, Petruska A, Loessner MJ, Nelson BJ and Pané S (2016): Magnetically driven silver-coated nanocoils for efficient bacterial contact killing. Advanced Functional Materials. 26(7): 1063-1069.

151. Höpfner J, Klein C and Wilhelm M (2010): A novel approach for the desalination of seawater by means of reusable poly (acrylic acid) hydrogels and mechanical force. Macromolecular Rapid Communications. 31(15): 1337-1342.

152. Hosseinzadeh H and Barghi A (2019): Synthesis of poly (AN)/poly (AA-co-AM) hydrogel nanocomposite with electrical conductivity and antibacterial properties. Polymer Composites. 40(7): 2724-2733.

153. Hu Z, Zhang L, Zhong L, Zhou Y, Xue J and Li Y (2019): Preparation of an antibacterial chitosan-coated biochar-nanosilver composite for drinking water purification. Carbohydrate Polymers. 219: 290-297.

154. Huang H, Li M, Tian Y, Xie Y, Sheng X, Jiang X and Zhang X (2020): Exfoliation and functionalization of α-zirconium phosphate in one pot for waterborne epoxy coatings with enhanced anticorrosion performance. Progress in Organic Coatings. 138: 1-10.

155. Huang W, Tao F, Li F, Mortimer M and Guo L-H (2020): Antibacterial nanomaterials for environmental and consumer product applications. NanoImpact. 20: 1-76.

156. Huang X, Bao X, Liu Y, Wang Z and Hu Q (2017): Catechol-functional chitosan/silver nanoparticle composite as a highly effective antibacterial agent with species-specific mechanisms. Scientific Reports. 7(1): 1-10.

157. Hummers Jr WS and Offeman RE (1958): Preparation of graphitic oxide. Journal of the American Chemical Society. 80(6): 1339-1339.

158. Idumah CI, Obele CM, Emmanuel EO and Hassan A (2020): Recently emerging nanotechnological advancements in polymer nanocomposite coatings for anti-corrosion, anti-fouling and self-healing. Surfaces and Interfaces. 21: 1-23.

159. ISO (2009): 10993-5: 2009-Biological evaluation of medical devices-Part 5: Tests for *in vitro* cytotoxicity. International Organization for Standardization.

160. ISO (2021): 10993–12: 2021 Biological evaluation of medical devices-Part 12: Sample preparation and reference materials. International Organization for Standardization.

161. Itoh H, Li Y, Chan KHK and Kotaki M (2016): Morphology and mechanical properties of PVA nanofibers spun by free surface electrospinning. Polymer Bulletin. 73: 2761-2777.

162. Jakus AE (2019): An introduction to 3D printing—past, present, and future promise. In: 3D printing in orthopaedic surgery. Elsevier, pp. 1-15.

163. Jatoi AW (2020): Polyurethane nanofibers incorporated with ZnAg composite nanoparticles for antibacterial wound dressing applications. Composites Communications. 19: 103-107.

164. Jaworski S, Wierzbicki M, Sawosz E, Jung A, Gielerak G, Biernat J, Jaremek H, Łojkowski W, Woźniak B and Wojnarowicz J (2018): Graphene oxide-based nanocomposites decorated with silver nanoparticles as an antibacterial agent. Nanoscale Research Letters. 13(1): 1-17.

165. Jayanthi S, Eswar NK, Singh SA, Chatterjee K, Madras G and Sood A (2016): Macroporous three-dimensional graphene oxide foams for dye adsorption and antibacterial applications. RSC Advances. 6(2): 1231-1242.

166. Jena G, Sofia S, Anandkumar B, Vanithakumari S, George R and Philip J (2021): Graphene oxide/polyvinylpyrrolidone composite coating on 316L SS with superior antibacterial and anti-biofouling properties. Progress in Organic Coatings 158: 1-13.

167. Jeon I-Y and Baek J-B (2010): Nanocomposites derived from polymers and inorganic nanoparticles. Materials. 3(6): 3654-3674.

168. Jian Y, Zhang J, Yang C, Qi L, Wang X, Deng H and Shi X (2023): Biological MWCNT/chitosan composite coating with outstanding anti-corrosion property for implants. Colloids and Surfaces B: Biointerfaces. 225: 1-9.

169. Jiang W, Mashayekhi H and Xing B (2009): Bacterial toxicity comparison between nano-and micro-scaled oxide particles. Environmental pollution. 157(5): 1619-1625.

170. Jiao T, Zhao H, Zhou J, Zhang Q, Luo X, Hu J, Peng Q and Yan X (2015): Self-assembly reduced graphene oxide nanosheet hydrogel fabrication by anchorage of chitosan/silver and its potential efficient application toward dye degradation for wastewater treatments. ACS Sustainable Chemistry & Engineering. 3(12): 3130-3139.

171. Jing G, Wang L, Yu H, Amer WA and Zhang L (2013): Recent progress on study of hybrid hydrogels for water treatment. Colloids and Surfaces A: Physicochemical and Engineering Aspects. 416: 86-94.

172. Jorfi M and Foster EJ (2015): Recent advances in nanocellulose for biomedical applications. Journal of Applied Polymer Science. 132(14): 1-19.

173. Jose J and Athikalam Paulose S (2020): Studies on natural rubber nanocomposites by incorporating zinc oxide modified graphene oxide. Journal of Rubber Research. 23: 311-321.

174. Joseph B, Sagarika V, Sabu C, Kalarikkal N and Thomas S (2020): Cellulose nanocomposites: Fabrication and biomedical applications. Journal of Bioresources and Bioproducts. 5(4): 223-237.

175. Kaew-on N, Katemake P and Prasongsuk S (2020): Primer formulations with antibacterial properties for murals. Progress in Organic Coatings. 138: 1-8.

176. Kajal P, Ghosh K and Powar S (2018): Manufacturing techniques of perovskite solar cells. In: Applications of Solar Energy. Springer Singapore, pp. 341-364.

177. Kakaei K, Esrafili MD and Ehsani A (2019): Graphene and anticorrosive properties. In: Interface science and technology. Elsevier, pp. 303-337.

178. Kang S, Pinault M, Pfefferle LD and Elimelech M (2007): Single-walled carbon nanotubes exhibit strong antimicrobial activity. Langmuir. 23(17): 8670-8673.

179. Kango S, Kalia S, Celli A, Njuguna J, Habibi Y and Kumar R (2013): Surface modification of inorganic nanoparticles for development of organic–inorganic nanocomposites—A review. Progress in Polymer Science. 38(8): 1232-1261.

180. Karak N (2009): Fundamentals of polymers: raw materials to finish products. PHI Learning Pvt. Ltd.

181. Kaur R, Goyal D and Agnihotri S (2021): Chitosan/PVA silver nanocomposite for butachlor removal: Fabrication, characterization, adsorption mechanism and isotherms. Carbohydrate Polymers. 262: 1-13.

182. Khan MUA, Yaqoob Z, Ansari MNM, Razak SIA, Raza MA, Sajjad A, Haider S and Busra FM (2021): Chitosan/Poly Vinyl Alcohol/Graphene Oxide Based pH-Responsive Composite Hydrogel Films: Drug Release, Anti-Microbial and Cell Viability Studies. Polymers (Basel). 13(18): 1-19.

183. Khawaja H, Zahir E, Asghar MA and Asghar MA (2018): Graphene oxide, chitosan and silver nanocomposite as a highly effective antibacterial agent against pathogenic strains. Colloids and Surfaces A: Physicochemical and Engineering Aspects. 555: 246-255.

184. Khude P, Majumdar A, Butola BS and Bhattacharyya R (2023): Multi-objective Optimisation of Antibacterial Activity and Comfort of Knitted Fabrics Made from Polyester-Silver Nanocomposite Fibres. Fibers and Polymers. 24(9): 3163-3173.

185. Kim I, Viswanathan K, Kasi G, Thanakkasaranee S, Sadeghi K and Seo J (2022): ZnO nanostructures in active antibacterial food packaging: Preparation methods, antimicrobial mechanisms, safety issues, future prospects, and challenges. Food Reviews International. 38(4): 537-565.

186. Kim SJ, Shin SR, Shin DI, Kim IY and Kim SI (2005): Synthesis and characteristics of semi-interpenetrating polymer network hydrogels based on chitosan and poly (hydroxy ethyl methacrylate). Journal of Applied Polymer Science. 96(1): 86-92.

187. Kokubo T and Takadama H (2006): How useful is SBF in predicting *in vivo* bone bioactivity? Biomaterials. 27(15): 2907-2915.

188. Konios D, Stylianakis MM, Stratakis E and Kymakis E (2014): Dispersion behaviour of graphene oxide and reduced graphene oxide. Journal of Colloid and Interface Science. 430: 108-112.

189. Koo H, Allan RN, Howlin RP, Stoodley P and Hall-Stoodley L (2017): Targeting microbial biofilms: current and prospective therapeutic strategies. Nature Reviews Microbiology. 15(12): 740-755.

190. Koo JH (2019): Polymer nanocomposites: processing, characterization, and applications. McGraw-Hill Education.

191. Kooshki S, Pareek P, Mentheour R, Janda M and Machala Z (2023): Efficient treatment of bio-contaminated wastewater using plasma technology for its reuse in sustainable agriculture. Environmental Technology & Innovation. 1-28.

192. Kristanti RA, Hadibarata T, Syafrudin M, Yılmaz M and Abdullah S (2022): Microbiological contaminants in drinking water: Current status and challenges. Water, Air, & Soil Pollution. 233(8): 1-17.

193. Kroll A, Pillukat MH, Hahn D and Schnekenburger J (2012): Interference of engineered nanoparticles with *in vitro* toxicity assays. Archives of Toxicology 86(7): 1123-1136.

194. Kubo A-L, Capjak I, Vrček IV, Bondarenko OM, Kurvet I, Vija H, Ivask A, Kasemets K and Kahru A (2018): Antimicrobial potency of differently coated 10

and 50 nm silver nanoparticles against clinically relevant bacteria *Escherichia coli* and *Staphylococcus aureus*. Colloids and Surfaces B: Biointerfaces. 170: 401-410.

195. Kumar AKS, Zhang Y, Li D and Compton RG (2020): A mini-review: How reliable is the drop casting technique? Electrochemistry Communications. 121: 1-10.

196. Kumar G, Chaudhary K, Mogha NK, Kant A and Masram DT (2021): Extended release of metronidazole drug using chitosan/graphene oxide bionanocomposite beads as the drug carrier. ACS omega. 6(31): 20433-20444.

197. Kumar MNR (2000): A review of chitin and chitosan applications. Reactive and Functional Polymers. 46(1): 1-27.

198. Kumar RV, Mastai Y, Diamant Y and Gedanken A (2001): Sonochemical synthesis of amorphous Cu and nanocrystalline Cu_2O embedded in a polyaniline matrix. Journal of Materials Chemistry. 11(4): 1209-1213.

199. Kumar S, Krishnakumar B, Sobral A and Koh J (2019): Bio-based (chitosan/PVA/ZnO) nanocomposites film: Thermally stable and photoluminescence material for removal of organic dye. Carbohydrate Polymers. 205: 559-564.

200. Kumar V, Kumar A, Lee D-J and Park S-S (2021): Estimation of number of graphene layers using different methods: a focused review. Materials. 14(16): 1-22.

201. Kumar V, Mittal H and Alhassan SM (2019): Biodegradable hydrogels of tragacanth gum polysaccharide to improve water retention capacity of soil and environment-friendly controlled release of agrochemicals. International Journal of Biological Macromolecules. 132: 1252-1261.

202. Le Ferrand H, Bolisetty S, Demirörs AF, Libanori R, Studart AR and Mezzenga R (2016): Magnetic assembly of transparent and conducting graphene-based functional composites. Nature Communications. 7(1): 1-9.

203. Lee H-J, Song JY and Kim BS (2013): Biological synthesis of copper nanoparticles using *Magnolia kobus* leaf extract and their antibacterial activity. Journal of Chemical Technology & Biotechnology. 88(11): 1971-1977.

204. Lee J, Kim J, Kim S and Min D-H (2016): Biosensors based on graphene oxide and its biomedical application. Advanced Drug Delivery Reviews. 105: 275-287.

205. Lee J, Mackeyev Y, Cho M, Li D, Kim J-H, Wilson LJ and Alvarez PJ (2009): Photochemical and antimicrobial properties of novel C60 derivatives in aqueous systems. Environmental Science & Technology. 43(17): 6604-6610.

206. Lewis K and Klibanov AM (2005): Surpassing nature: rational design of sterile-surface materials. Trends in Biotechnology. 23(7): 343-348.

207. Li D, Zhang X, Yao J, Simon GP and Wang H (2011): Stimuli-responsive polymer hydrogels as a new class of draw agent for forward osmosis desalination. Chemical Communications. 47(6): 1710-1712.

208. Li J, Wan Y, Li L, Liang H and Wang J (2009): Preparation and characterization of 2, 3-dialdehyde bacterial cellulose for potential biodegradable tissue engineering scaffolds. Materials Science and Engineering: C. 29(5): 1635-1642.

209. Li S, Zhang R, Xie J, Sameen DE, Ahmed S, Dai J, Qin W, Li S and Liu Y (2020): Electrospun antibacterial poly (vinyl alcohol)/Ag nanoparticles membrane grafted with 3, 3′, 4, 4′-benzophenone tetracarboxylic acid for efficient air filtration. Applied Surface Science. 533: 1-13.

210. Li X-F and Mitch WA (2018): Drinking water disinfection byproducts (DBPs) and human health effects: multidisciplinary challenges and opportunities. Environmental Science & Technology. 52(4): 1681-1689.

211. Li X, Sun J, Che Y, Lv Y and Liu F (2019): Antibacterial properties of chitosan chloride-graphene oxide composites modified quartz sand filter media in water treatment. International Journal of Biological Macromolecules. 121: 760-773.

212. Li Y, Zhang H, Ma C, Yin H, Gong L, Duh Y and Feng R (2019): Durable, cost-effective and superhydrophilic chitosan-alginate hydrogel-coated mesh for efficient oil/water separation. Carbohydrate polymers. 226: 1-6.

213. Li YL, Deletic A and McCarthy DT (2014): Removal of *E. coli* from urban stormwater using antimicrobial-modified filter media. Journal of Hazardous Materials. 271: 73-81.

214. Liao KH, Lin YS, Macosko CW and Haynes CL (2011): Cytotoxicity of graphene oxide and graphene in human erythrocytes and skin fibroblasts. ACS Applied Materials & Interfaces. 3(7): 2607-2615.

215. Liao Y, Wang M and Chen D (2018): Preparation of polydopamine-modified graphene oxide/chitosan aerogel for uranium (VI) adsorption. Industrial & Engineering Chemistry Research. 57(25): 8472-8483.

216. Lin M-H, Wang Y-H, Kuo C-H, Ou S-F, Huang P-Z, Song T-Y, Chen Y-C, Chen S-T, Wu C-H and Hsueh Y-H (2021): Hybrid ZnO/chitosan antimicrobial coatings with enhanced mechanical and bioactive properties for titanium implants. Carbohydrate Polymers. 257: 1-10.

217. Liu M, Ishida Y, Ebina Y, Sasaki T and Aida T (2013): Photolatently modulable hydrogels using unilamellar titania nanosheets as photocatalytic crosslinkers. Nature Communications. 4(1): 1-7.

218. Liu P, Man Y and Bao Y (2021): Bioactive porous biocomposites coated magnesium alloy implant for bone rejuvenation using a fracture in rat model. Biotechnology and Bioprocess Engineering. 26: 359-368.

219. Liu R, Liang S, Tang X-Z, Yan D, Li X and Yu Z-Z (2012): Tough and highly stretchable graphene oxide/polyacrylamide nanocomposite hydrogels. Journal of Materials Chemistry. 22(28): 14160-14167.

220. Liu S, Zeng TH, Hofmann M, Burcombe E, Wei J, Jiang R, Kong J and Chen Y (2011): Antibacterial activity of graphite, graphite oxide, graphene oxide, and reduced graphene oxide: membrane and oxidative stress. ACS Nano. 5(9): 6971-6980.

221. Liu Y, Mao J, Guo Z, Hu Y and Wang S (2022): Polyvinyl alcohol/carboxymethyl chitosan hydrogel loaded with silver nanoparticles exhibited antibacterial and self-healing properties. International Journal of Biological Macromolecules. 220: 211-222.

222. Liu Y, Park M, Shin HK, Pant B, Choi J, Park YW, Lee JY, Park S-J and Kim H-Y (2014): Facile preparation and characterization of poly (vinyl alcohol)/chitosan/graphene oxide biocomposite nanofibers. Journal of Industrial and Engineering Chemistry. 20(6): 4415-4420.

223. Liu Y, Wang S and Lan W (2018): Fabrication of antibacterial chitosan-PVA blended film using electrospray technique for food packaging applications. International Journal of Biological Macromolecules. 107: 848-854.

224. Lofrano G, Carotenuto M, Libralato G, Domingos RF, Markus A, Dini L, Gautam RK, Baldantoni D, Rossi M and Sharma SK (2016): Polymer functionalized nanocomposites for metals removal from water and wastewater: an overview. Water Research. 92: 22-37.

225. Lončarević D and Čupić Ž (2019): The perspective of using nanocatalysts in the environmental requirements and energy needs of industry. In: Industrial Applications of Nanomaterials. Elsevier, pp. 91-122.

226. Lü T, Zhang S, Qi D, Zhang D and Zhao H (2016): Thermosensitive poly (N-isopropylacrylamide)-grafted magnetic nanoparticles for efficient treatment of emulsified oily wastewater. Journal of Alloys and Compounds. 688: 513-520.

227. Luo H, Xiong G, Hu D, Ren K, Yao F, Zhu Y, Gao C and Wan Y (2013): Characterization of TEMPO-oxidized bacterial cellulose scaffolds for tissue engineering applications. Materials Chemistry and Physics. 143(1): 373-379.

228. Lyu C, Zhao P, Xie J, Dong S, Liu J, Rao C and Fu J (2021): Electrospinning of nanofibrous membrane and its applications in air filtration: A review. Nanomaterials. 11(6): 1-28.

229. Ma J, Liu C, Li R and Wang J (2012): Properties and structural characterization of chitosan/poly (vinyl alcohol)/graphene oxide nano composites. e-Polymers. 12(1): 1-13.

230. Maes S, Vackier T, Nguyen Huu S, Heyndrickx M, Steenackers H, Sampers I, Raes K, Verplaetse A and De Reu K (2019): Occurrence and characterisation of biofilms in drinking water systems of broiler houses. BMC Microbiology. 19(1): 1-15.

231. Magrez A, Kasas S, Salicio V, Pasquier N, Seo JW, Celio M, Catsicas S, Schwaller B and Forró L (2006): Cellular toxicity of carbon-based nanomaterials. Nano Letters. 6(6): 1121-1125.

232. Maillard J-Y and Pascoe M (2023): Disinfectants and antiseptics: mechanisms of action and resistance. Nature Reviews Microbiology. 1-14.

233. Makvandi P, Wang Cy, Zare EN, Borzacchiello A, Niu Ln and Tay FR (2020): Metal-based nanomaterials in biomedical applications: Antimicrobial activity and cytotoxicity aspects. Advanced Functional Materials. 30(22): 1-40.

234. Marathe SA, Kumar R, Ajitkumar P, Nagaraja V and Chakravortty D (2013): Curcumin reduces the antimicrobial activity of ciprofloxacin against *Salmonella Typhimurium* and *Salmonella Typhi*. Journal of Antimicrobial Chemotherapy. 68(1): 139-152.

235. Marjani A, Nakhjiri AT, Adimi M, Jirandehi HF and Shirazian S (2020): Effect of graphene oxide on modifying polyethersulfone membrane performance and its application in wastewater treatment. Scientific Reports. 10(1): 1-11.

236. Matharu RK, Tabish TA, Trakoolwilaiwan T, Mansfield J, Moger J, Wu T, Lourenço C, Chen B, Ciric L and Parkin IP (2020): Microstructure and antibacterial efficacy of graphene oxide nanocomposite fibres. Journal of Colloid and Interface Science. 571: 239-252.

237. Mathew S and Radhakrishnan E (2019): Polymer nanocomposites: Alternative to reduce environmental impact of non-biodegradable food packaging materials. Composites for Environmental Engineering. 99-133.

238. Matsubayashi T, Tenjimbayashi M, Komine M, Manabe K and Shiratori S (2017): Bioinspired hydrogel-coated mesh with superhydrophilicity and underwater superoleophobicity for efficient and ultrafast oil/water separation in harsh environments. Industrial & Engineering Chemistry Research. 56(24): 7080-7085.

239. Matsumoto K, Sakikawa N and Miyata T (2018): Thermo-responsive gels that absorb moisture and ooze water. Nature Communications. 9(1): 1-7.

240. Matsumoto M, Kaneko K, Hara M, Matsui M, Morita K and Maruyama T (2021): Covalent immobilization of gold nanoparticles on a plastic substrate and subsequent immobilization of biomolecules. RSC Advances. 11(38): 23409-23417.

241. Mauter MS, Zucker I, Perreault F, Werber JR, Kim J-H and Elimelech M (2018): The role of nanotechnology in tackling global water challenges. Nature Sustainability. 1(4): 166-175.

242. Maver T, Mastnak T, Mihelič M, Maver U and Finšgar M (2021): Clindamycin-based 3D-printed and electrospun coatings for treatment of implant-related infections. Materials. 14(6): 1-17.

243. Mazaheri M, Akhavan O and Simchi A (2014): Flexible bactericidal graphene oxide–chitosan layers for stem cell proliferation. Applied Surface Science. 301: 456-462.

244. Medupin RO, Abubakre OK, Abdulkareem AS, Muriana RA and Abdulrahman AS (2019): Carbon nanotube reinforced natural rubber nanocomposite for anthropomorphic prosthetic foot purpose. Scientific Reports. 9(1): 1-11.

245. Melaiye A and Youngs WJ (2005): Silver and its application as an antimicrobial agent. 15(2): 125-130.

246. Merritt JH, Kadouri DE and O'Toole GA (2011): Growing and analyzing static biofilms. Current Protocols in Microbiology. 22(1): 1-18.

247. Mersch-Sundermann V, Knasmüller S, Wu X-j, Darroudi F and Kassie F (2004): Use of a human-derived liver cell line for the detection of cytoprotective, antigenotoxic and cogenotoxic agents. Toxicology. 198(1-3): 329-340.

248. Minh NC, Van Hoa N and Trung TS (2020): Preparation, properties, and application of low-molecular-weight chitosan. In: Handbook of Chitin and Chitosan. Elsevier, pp. 453-471.

249. Mishra SK, Teotia AK, Kumar A and Kannan S (2017): Mechanically tuned nanocomposite coating on titanium metal with integrated properties of biofilm inhibition, cell proliferation, and sustained drug delivery. Nanomedicine: Nanotechnology, Biology and Medicine. 13(1): 23-35.

250. Mohan YM, Lee K, Premkumar T and Geckeler KE (2007): Hydrogel networks as nanoreactors: A novel approach to silver nanoparticles for antibacterial applications. Polymer. 48(1): 158-164.

251. Mohan YM, Vimala K, Thomas V, Varaprasad K, Sreedhar B, Bajpai S and Raju KM (2010): Controlling of silver nanoparticles structure by hydrogel networks. Journal of Colloid and Interface Science. 342(1): 73-82.

252. Mokhtari H, Ghasemi Z, Kharaziha M, Karimzadeh F and Alihosseini F (2018): Chitosan-58S bioactive glass nanocomposite coatings on TiO_2 nanotube: Structural and biological properties. Applied Surface Science. 441: 138-149.

253. Moritz M and Geszke-Moritz M (2013): The newest achievements in synthesis, immobilization and practical applications of antibacterial nanoparticles. Chemical Engineering Journal. 228: 596-613.

254. Morones JR, Elechiguerra JL, Camacho A, Holt K, Kouri JB, Ramírez JT and Yacaman MJ (2005): The bactericidal effect of silver nanoparticles. Nanotechnology. 16(10): 1-9.

255. Morselli D, Iseppi R, Papadopoulou EL, Bolelli G, Sabia C, Degli Esposti M and Fabbri P (2023): Sprayable Thermoset Nanocomposite Coatings Based on Silanized-PEG/ZnO to Prevent Microbial Infections of Titanium Implants. Advanced Materials Interfaces. 1-13.

256. Morsi M, Pashameah RA, Sharma K, Alzahrani E, Farea M and Al-Muntaser A (2023): Hybrid MWCNTs/Ag nanofiller reinforced PVP/CMC blend-based polymer nanocomposites for multifunctional optoelectronic and nanodielectric applications. Journal of Polymers and the Environment. 31(2): 664-676.

257. Morsy A (2015): Adsorptive removal of uranium ions from liquid waste solutions by phosphorylated chitosan. Environmental Technology & Innovation. 4: 299-310.

258. Moulay S (2015): Poly (vinyl alcohol) functionalizations and applications. Polymer-Plastics Technology and Engineering. 54(12): 1289-1319.

259. Mousa HM, Abdal-Hay A, Bartnikowski M, Mohamed IM, Yasin AS, Ivanovski S, Park CH and Kim CS (2018): A multifunctional zinc oxide/poly (lactic acid) nanocomposite layer coated on magnesium alloys for controlled degradation and antibacterial function. ACS Biomaterials Science & Engineering. 4(6): 2169-2180.

260. Moyer CA, Brentano L, Gravens DL, Margraf HW and Monafo WW (1965): Treatment of large human burns with 0.5% silver nitrate solution. Archives of Surgery. 90(6): 812-867.

261. Mukherji S, Ruparelia J and Agnihotri S (2011): Antimicrobial activity of silver and copper nanoparticles: variation in sensitivity across various strains of bacteria and fungi. In: Nano-antimicrobials: Progress and prospects. Springer, pp. 225-251.

262. Müller K, Bugnicourt E, Latorre M, Jorda M, Echegoyen Sanz Y, Lagaron JM, Miesbauer O, Bianchin A, Hankin S and Bölz U (2017): Review on the processing

and properties of polymer nanocomposites and nanocoatings and their applications in the packaging, automotive and solar energy fields. Nanomaterials. 7(4): 1-47.

263. Munir MU, Ahmed A, Usman M and Salman S (2020): Recent advances in nanotechnology-aided materials in combating microbial resistance and functioning as antibiotics substitutes. International Journal of Nanomedicine. 7329-7358.

264. Murai K, Watanabe Y, Saito Y, Nakayama T, Suematsu H, Jiang W, Yatsui K, Shim K and Niihara K (2007): Preparation of copper nanoparticles with an organic coating by a pulsed wire discharge method. Journal of Ceramic Processing Research. 8(2): 114-118.

265. Murphy M, Ting K, Zhang X, Soo C and Zheng Z (2015): Current development of silver nanoparticle preparation, investigation, and application in the field of medicine. Journal of Nanomaterials. 2015: 1-12.

266. Mustapha AT, Zhou C, Amanor-Atiemoh R, Owusu-Fordjour M, Wahia H, Fakayode OA and Ma H (2020): Kinetic modeling of inactivation of natural microbiota and *Escherichia coli* on cherry tomato treated with fixed multi-frequency sonication. Ultrasonics Sonochemistry. 64: 1-9.

267. Muthuchamy M, Govindan R, Shine K, Thangasamy V, Alharbi NS, Thillaichidambaram M, Khaled JM, Wen J-L and Alanzi KF (2020): Anti-biofilm investigation of graphene/chitosan nanocomposites against biofilm producing *P. aeruginosa* and *K. pneumoniae*. Carbohydrate Polymers. 230: 1-13.

268. Muzzarelli RA (2011): Potential of chitin/chitosan-bearing materials for uranium recovery: An interdisciplinary review. Carbohydrate Polymers. 84(1): 54-63.

269. Naffakh M and Díez-Pascual AM (2014): Thermoplastic polymer nanocomposites based on inorganic fullerene-like nanoparticles and inorganic nanotubes. Inorganics. 2(2): 291-312.

270. Nangmenyi G and Economy J (2009): Nanometallic particles for oligodynamic microbial disinfection. In: Nanotechnology applications for clean water. Elsevier, pp. 3-15.

271. Nath J, Chowdhury A and Dolui SK (2018): Chitosan/graphene oxide-based multifunctional pH-responsive hydrogel with significant mechanical strength, self-healing property, and shape memory effect. Advances in Polymer Technology. 37(8): 3665-3679.

272. Nayak S, Prasad SR, Mandal D and Das P (2020): Carbon dot cross-linked polyvinylpyrrolidone hybrid hydrogel for simultaneous dye adsorption, photodegradation and bacterial elimination from waste water. Journal of Hazardous Materials. 392: 1-11.

273. Neacşu IA, Nicoară AI, Vasile OR and Vasile BŞ (2016): Inorganic micro-and nanostructured implants for tissue engineering. In: Nanobiomaterials in hard tissue engineering. Elsevier, pp. 271-295.

274. Negm NA, Hefni HH, Abd-Elaal AA, Badr EA and Abou Kana MT (2020): Advancement on modification of chitosan biopolymer and its potential applications. International Journal of Biological Macromolecules. 152: 681-702.

275. Nikolova MP and Apostolova MD (2022): Advances in Multifunctional Bioactive Coatings for Metallic Bone Implants. Materials. 16(1): 1-53.

276. Ning H, Ma Z, Zhang Z, Zhang D and Wang Y (2021): A novel multifunctional flame retardant MXene/nanosilica hybrid for poly (vinyl alcohol) with simultaneously improved mechanical properties. New Journal of Chemistry. 45(9): 4292-4302.

277. Oliveira W, Silva P, Silva R, Silva G, Machado G, Coelho L and Correia M (2018): *Staphylococcus aureus* and *Staphylococcus epidermidis* infections on implants. Journal of Hospital Infection. 98(2): 111-117.

278. Osswald T and Rudolph N (2015): Polymer rheology.

279. Östergren I, Pourrahimi AM, Darmadi I, da Silva R, Stolaś A, Lerch S, Berke B, Guizar-Sicairos M, Liebi M and Foli G (2021): Highly permeable fluorinated polymer nanocomposites for plasmonic hydrogen sensing. ACS Applied Materials & Interfaces. 13(18): 21724-21732.

280. Ozay O, Aktas N, Inger E and Sahiner N (2011): Hydrogel assisted nickel nanoparticle synthesis and their use in hydrogen production from sodium boron hydride. International Journal of Hydrogen Energy. 36(3): 1998-2006.

281. Padalkar S, Capadona JR, Rowan SJ, Weder C, Won Y-H, Stanciu LA and Moon RJ (2010): Natural biopolymers: novel templates for the synthesis of nanostructures. Langmuir. 26(11): 8497-8502.

282. Paino IMM and Zucolotto V (2015): Poly (vinyl alcohol)-coated silver nanoparticles: Activation of neutrophils and nanotoxicology effects in human hepatocarcinoma and mononuclear cells. Environmental Toxicology and Pharmacology. 39(2): 614-621.

283. Pal S, Tak YK and Song JM (2007): Does the antibacterial activity of silver nanoparticles depend on the shape of the nanoparticle? A study of the gram-negative bacterium *Escherichia coli*. Applied and Environmental Microbiology. 73(6): 1712-1720.

284. Paladini F, Pollini M, Sannino A and Ambrosio L (2015): Metal-based antibacterial substrates for biomedical applications. Biomacromolecules. 16(7): 1873-1885.

285. Palansooriya KN, Yang Y, Tsang YF, Sarkar B, Hou D, Cao X, Meers E, Rinklebe J, Kim K-H and Ok YS (2020): Occurrence of contaminants in drinking water sources and the potential of biochar for water quality improvement: A review. Critical Reviews in Environmental Science and Technology. 50(6): 549-611.

286. Palmara G, Frascella F, Roppolo I, Chiappone A and Chiadò A (2021): Functional 3D printing: Approaches and bioapplications. Biosensors and Bioelectronics. 175: 1-16.

287. Palza H (2015): Antimicrobial polymers with metal nanoparticles. International Journal of Molecular Sciences. 16(1): 2099-2116.

288. Palza H, Quijada R and Delgado K (2015): Antimicrobial polymer composites with copper micro-and nanoparticles: Effect of particle size and polymer matrix. Journal of Bioactive and Compatible Polymers. 30(4): 366-380.

289. Pan C, Liu L, Chen Q, Zhang Q and Guo G (2017): Tough, stretchable, compressive novel polymer/graphene oxide nanocomposite hydrogels with excellent self-healing performance. ACS Applied Materials & Interfaces. 9(43): 38052-38061.

290. Panáček D, Hochvaldová L, Bakandritsos A, Malina T, Langer M, Belza J, Martincová J, Večeřová R, Lazar P and Poláková K (2021): Silver covalently bound to cyanographene overcomes bacterial resistance to silver nanoparticles and antibiotics. Advanced Science. 8(12): 1-8.

291. Panchal SS and Vasava DV (2022): Fabricating approaches for synthesis of miktoarm star-shaped polymers having tailored biodegradability. International Journal of Polymeric Materials and Polymeric Biomaterials. 71(18): 1407-1424.

292. Panda S, Rout TK, Prusty AD, Ajayan PM and Nayak S (2018): Electron transfer directed antibacterial properties of graphene oxide on metals. Advanced Materials. 30(7): 1-10.

293. Pandele AM, Ionita M, Crica L, Dinescu S, Costache M and Iovu H (2014): Synthesis, characterization, and *in vitro* studies of graphene oxide/chitosan–polyvinyl alcohol films. Carbohydrate Polymers. 102: 813-820.

294. Pandele AM, Ionita M, Crica L, Vasile E and Iovu H (2017): Novel Chitosan-poly (vinyl alcohol)/graphene oxide biocomposites 3D porous scaffolds. Composites Part B: Engineering. 126: 81-87.

295. Pandey JK, Nakagaito AN and Takagi H (2013): Fabrication and applications of cellulose nanoparticle-based polymer composites. Polymer Engineering & Science. 53(1): 1-8.

296. Pardo-Yissar V, Gabai R, Shipway AN, Bourenko T and Willner I (2001): Gold nanoparticle/hydrogel composites with solvent-switchable electronic properties. Advanced Materials. 13(17): 1320-1323.

297. Parida VK, Sikarwar D, Majumder A and Gupta AK (2022): An assessment of hospital wastewater and biomedical waste generation, existing legislations, risk assessment, treatment processes, and scenario during COVID-19. Journal of Environmental Management. 308: 1-26.

298. Park JH, Olivares-Navarrete R, Baier RE, Meyer AE, Tannenbaum R, Boyan BD and Schwartz Z (2012): Effect of cleaning and sterilization on titanium implant surface properties and cellular response. Acta Biomaterialia. 8(5): 1966-1975.

299. Park S, Kim H, Choi KS, Ji M-K, Kim S, Gwon Y, Park C, Kim J and Lim H-P (2020): Graphene–Chitosan Hybrid Dental Implants with Enhanced Antibacterial and Cell-Proliferation Properties. Applied Sciences. 10(14): 1-10.

300. Park S and Ruoff RS (2009): Chemical methods for the production of graphenes. Nature Nanotechnology. 4(4): 217-224.

301. Pasqui D, Atrei A, Giani G, De Cagna M and Barbucci R (2011): Metal oxide nanoparticles as cross-linkers in polymeric hybrid hydrogels. Materials Letters. 65(2): 392-395.

302. Pérez-Álvarez L, Ruiz-Rubio L, Lizundia E and Vilas-Vilela J (2019): Polysaccharide-based superabsorbents: synthesis, properties, and applications. In: Cellulose-Based Superabsorbent Hydrogels. Springer, Cham, pp. 1393-1431.

303. Perreault F, de Faria AF, Nejati S and Elimelech M (2015): Antimicrobial Properties of Graphene Oxide Nanosheets: Why Size Matters. ACS Nano. 9(7): 7226-7236.

304. Peters BM, Jabra-Rizk MA, O'May GA, Costerton JW and Shirtliff ME (2012): Polymicrobial interactions: impact on pathogenesis and human disease. Clinical microbiology reviews. 25(1): 193-213.

305. Pieper H, Chercheja S, Eigler S, Halbig CE, Filipovic MR and Mokhir A (2016): Toxicity of graphene oxide: endoperoxides as a cause. Angewandte Chemie. 128(1): 413-416.

306. Pinto RJ, Daina S, Sadocco P, Neto CP and Trindade T (2013): Antibacterial activity of nanocomposites of copper and cellulose. BioMed Research International. 1-7.

307. Poh HL, Šaněk F, Ambrosi A, Zhao G, Sofer Z and Pumera M (2012): Graphenes prepared by Staudenmaier, Hofmann and Hummers methods with consequent thermal exfoliation exhibit very different electrochemical properties. Nanoscale. 4(11): 3515-3522.

308. Ponce AA and Klabunde KJ (2005): Chemical and catalytic activity of copper nanoparticles prepared via metal vapor synthesis. Journal of Molecular Catalysis A: Chemical. 225(1): 1-6.

309. Pooresmaeil M and Namazi H (2020): Application of polysaccharide-based hydrogels for water treatments. In: Hydrogels based on natural polymers. Elsevier, pp. 411-455.

310. Porter GC, Schwass DR, Tompkins GR, Bobbala SK, Medlicott NJ and Meledandri CJ (2021): AgNP/Alginate Nanocomposite hydrogel for antimicrobial and antibiofilm applications. Carbohydrate Polymers. 251: 1-14.

311. Pounraj S, Somu P and Paul S (2018): Chitosan and graphene oxide hybrid nanocomposite film doped with silver nanoparticles efficiently prevents biofouling. Applied Surface Science. 452: 487-497.

312. Prabhu S and Poulose EK (2012): Silver nanoparticles: mechanism of antimicrobial action, synthesis, medical applications, and toxicity effects. International Nano Letters. 2: 1-10.

313. Qi C, Zhao L, Lin Y and Wu D (2018): Graphene oxide/chitosan sponge as a novel filtering material for the removal of dye from water. Journal of Colloid and Interface Science. 517: 18-27.

314. Qu X, Alvarez PJ and Li Q (2013): Applications of nanotechnology in water and wastewater treatment. Water Research. 47(12): 3931-3946.

315. Radwan EK, El-Naggar ME, Abdel-Karim A and Wassel AR (2021): Multifunctional 3D cationic starch/nanofibrillated cellulose/silver nanoparticles nanocomposite cryogel: Synthesis, adsorption, and antibacterial characteristics. International Journal of Biological Macromolecules. 189: 420-431.

316. Rao JP and Geckeler KE (2011): Polymer nanoparticles: Preparation techniques and size-control parameters. Progress in Polymer Science. 36(7): 887-913.

317. Rasoulzadehzali M and Namazi H (2018): Facile preparation of antibacterial chitosan/graphene oxide-Ag bio-nanocomposite hydrogel beads for controlled release of doxorubicin. International Journal of Biological Macromolecules. 116: 54-63.

318. Rathod SG, Bhajantri RF, Ravindrachary V, Naik J and Kumar DJM (2016): High mechanical and pressure sensitive dielectric properties of graphene oxide doped PVA nanocomposites. RSC Advances. 6(81): 77977-77986.

319. Rawashdeh RY, Harb AM and AlHasan AM (2020): Biological interaction levels of zinc oxide nanoparticles; lettuce seeds as case study. Heliyon. 6(5): 1-10.

320. Ray SS and Bousmina M (2007): Polymer nanocomposites and their applications. American Scientific Publishers.

321. Ray SS and Okamoto M (2003): Polymer/layered silicate nanocomposites: a review from preparation to processing. Progress in Polymer Science. 28(11): 1539-1641.

322. Refaee AA, El-Naggar ME, Mostafa TB, Elshaarawy RF and Nasr AM (2022): Nano-bio finishing of cotton fabric with quaternized chitosan Schiff base-TiO_2-ZnO nanocomposites for antimicrobial and UV protection applications. European Polymer Journal. 166: 1-21.

323. Reidy B, Haase A, Luch A, Dawson KA and Lynch I (2013): Mechanisms of silver nanoparticle release, transformation and toxicity: a critical review of current knowledge and recommendations for future studies and applications. Materials. 6(6): 2295-2350.

324. Ren Y, Qin X, Barbeck M, Hou Y, Xu H, Liu L and Liu C (2021): Mussel-inspired carboxymethyl chitosan hydrogel coating of titanium alloy with antibacterial and bioactive properties. Materials. 14(22): 1-11.

325. Ricci ML, Fontana S, Pinci F, Fiumana E, Pedna MF, Farolfi P, Sabattini MAB and Scaturro M (2012): Pneumonia associated with a dental unit waterline. The Lancet. 379(9816): 1.

326. Rikhari B, Mani SP and Rajendran N (2020): Polypyrrole/graphene oxide composite coating on Ti implants: A promising material for biomedical applications. Journal of Materials Science. 55: 5211-5229.

327. Rizeq BR, Younes NN, Rasool K and Nasrallah GK (2019): Synthesis, bioapplications, and toxicity evaluation of chitosan-based nanoparticles. International Journal of Molecular Sciences. 20(22): 1-24.

328. Rodrigues PR and Vieira RP (2019): Advances in atom-transfer radical polymerization for drug delivery applications. European Polymer Journal. 115: 45-58.

329. Rook G, Bäckhed F, Levin BR, McFall-Ngai MJ and McLean AR (2017): Evolution, human-microbe interactions, and life history plasticity. The Lancet. 390(10093): 521-530.

330. Rose S, Prevoteau A, Elzière P, Hourdet D, Marcellan A and Leibler L (2014): Nanoparticle solutions as adhesives for gels and biological tissues. Nature. 505(7483): 382-385.

331. Rosiak JM and Yoshii F (1999): Hydrogels and their medical applications. Nuclear Instruments and Methods in Physics Research Section B: Beam Interactions with Materials and Atoms. 151(1-4): 56-64.

332. Rubinstein M and Colby R (2003): Polymer Physics Oxford University Press.

333. Ruiz S, Tamayo JA, Ospina JD, Navia Porras DP, Valencia Zapata ME, Hernandez JHM, Valencia CH, Zuluaga F and Grande Tovar CD (2019): Antimicrobial Films Based on Nanocomposites of Chitosan/Poly(vinyl alcohol)/Graphene Oxide for Biomedical Applications. Biomolecules. 9(3): 1-17.

334. Sadeghi K and Seo J (2022): Metal–ligand complex copolymer as photocurable antimicrobial coatings for infection-resistant surface. Surf. Interfaces. 28: 1-9.

335. Sahoo SK, Manoharan B and Sivakumar N (2018): Introduction: Why perovskite and perovskite solar cells? In: Perovskite photovoltaics. Elsevier, pp. 1-24.

336. Sahraei R and Ghaemy M (2017): Synthesis of modified gum tragacanth/graphene oxide composite hydrogel for heavy metal ions removal and preparation of silver nanocomposite for antibacterial activity. Carbohydrate Polymers. 157: 823-833.

337. Saini I, Sharma A, Dhiman R, Aggarwal S, Ram S and Sharma PK (2017): Grafted SiC nanocrystals: For enhanced optical, electrical and mechanical properties of polyvinyl alcohol. Journal of Alloys and Compounds. 714: 172-180.

338. Sajjad S, Khan Leghari SA and Iqbal A (2017): Study of graphene oxide structural features for catalytic, antibacterial, gas sensing, and metals decontamination environmental applications. ACS Applied Materials & Interfaces. 9(50): 43393-43414.

339. Salazar H, Martins P, Santos B, Fernandes M, Reizabal A, Sebastián V, Botelho G, Tavares CJ, Vilas-Vilela JL and Lanceros-Mendez S (2020): Photocatalytic and antimicrobial multifunctional nanocomposite membranes for emerging pollutants water treatment applications. Chemosphere. 250: 1-15.

340. Sani IK, Masoudpour-Behabadi M, Sani MA, Motalebinejad H, Juma AS, Asdagh A, Eghbaljoo H, Khodaei M, Rhim J-W and Mohammadi F (2022): Value-added utilization of fruit and vegetable processing by-products for the manufacture of biodegradable food packaging films. Food Chemistry. 1-16.

341. Sankar MU, Aigal S, Maliyekkal SM, Chaudhary A, Anshup, Kumar AA, Chaudhari K and Pradeep T (2013): Biopolymer-reinforced synthetic granular nanocomposites for affordable point-of-use water purification. Proceedings of the National Academy of Sciences. 110(21): 8459-8464.

342. Saravanakumar K, Sathiyaseelan A, Mariadoss AVA, Xiaowen H and Wang M-H (2020): Physical and bioactivities of biopolymeric films incorporated with cellulose, sodium alginate and copper oxide nanoparticles for food packaging application. International Journal of Biological Macromolecules. 153: 207-214.

343. Saravanan P, Raju MP and Alam S (2007): A study on synthesis and properties of Ag nanoparticles immobilized polyacrylamide hydrogel composites. Materials Chemistry and Physics. 103(2-3): 278-282.

344. Saunders KJ (2012): Organic polymer chemistry: an introduction to the organic chemistry of adhesives, fibres, paints, plastics and rubbers. Springer Science & Business Media.

345. Shamszadeh S, Akrami M and Asgary S (2022): Size-dependent bioactivity of electrosprayed core–shell chitosan-alginate particles for protein delivery. Scientific Reports. 12(1): 1-14.

346. Shankar S and Rhim J-W (2014): Effect of copper salts and reducing agents on characteristics and antimicrobial activity of copper nanoparticles. Materials Letters. 132: 307-311.

347. Shanmugam BK, Rangaraj S, Subramani K, Srinivasan S, Aicher WK and Venkatachalam R (2020): Biomimetic TiO_2-chitosan/sodium alginate blended nanocomposite scaffolds for tissue engineering applications. Materials Science and Engineering: C. 110: 1-13.

348. Sharma J, Arya RK, Ahuja S and Bhargava CK (2017): Residual solvent study in polymer− Polymer—Solvent coatings: Poly (styrene)—Poly (methyl methacrylate)—Tetrahydrofuran coatings. Progress in Organic Coatings. 113: 200-206.

349. Shi S, Peng Z, Jing J, Yang L and Chen Y (2020): 3D printing of delicately controllable cellular nanocomposites based on polylactic acid incorporating graphene/carbon nanotube hybrids for efficient electromagnetic interference shielding. ACS Sustainable Chemistry & Engineering. 8(21): 7962-7972.

350. Shukla SK, Mishra AK, Arotiba OA and Mamba BB (2013): Chitosan-based nanomaterials: A state-of-the-art review. International Journal of Biological Macromolecules. 59: 46-58.

351. Siciliano V, Passerotto RA, Chiuchiarelli M, Leanza GM and Ojetti V (2023): Difficult-to-Treat Pathogens: A Review on the Management of Multidrug-Resistant *Staphylococcus epidermidis*. Life. 13(5): 1-14.

352. Silva-Leyton R, Quijada R, Bastías R, Zamora N, Olate-Moya F and Palza H (2019): Polyethylene/graphene oxide composites toward multifunctional active packaging films. Composites Science and Technology. 184: 1-10.

353. Singh P, Pandit S, Jers C, Joshi AS, Garnæs J and Mijakovic I (2021): Silver nanoparticles produced from *Cedecea sp.* exhibit antibiofilm activity and remarkable stability. Scientific Reports. 11(1): 1-13.

354. Singh S, Singh G and Bala N (2021): Synthesis and characterization of iron oxide-hydroxyapatite-chitosan composite coating and its biological assessment for biomedical applications. Progress in Organic Coatings. 150: 1-10.

355. Sivaselvam S, Selvakumar R, Viswanathan C and Ponpandian N (2021): Rapid one-pot synthesis of PAM-GO-Ag nanocomposite hydrogel by gamma-ray irradiation for remediation of environment pollutants and pathogen inactivation. Chemosphere. 275: 1-15.

356. Smith AT, LaChance AM, Zeng S, Liu B and Sun L (2019): Synthesis, properties, and applications of graphene oxide/reduced graphene oxide and their nanocomposites. Nano Materials Science. 1(1): 31-47.

357. Solanki JN, Sengupta R and Murthy Z (2010): Synthesis of copper sulphide and copper nanoparticles with microemulsion method. Solid State Sciences. 12(9): 1560-1566.

358. Somayajula D, Agarwal A, Sharma AK, Pall AE, Datta S and Ghosh G (2019): *In situ* synthesis of silver nanoparticles within hydrogel-conjugated membrane for enhanced antibacterial properties. ACS Applied Bio Materials. 2(2): 665-674.

359. Sondi I and Salopek-Sondi B (2004): Silver nanoparticles as antimicrobial agent: a case study on *E. coli* as a model for Gram-negative bacteria. Journal of Colloid and Interface Science. 275(1): 177-182.

360. Song Y, Hu Q, Li T, Sun Y, Chen X and Fan J (2018): Fabrication and characterization of phosphorylated chitosan nanofiltration membranes with tunable surface charges and improved selectivities. Chemical Engineering Journal. 352: 163-172.

361. Stankovich S, Dikin DA, Piner RD, Kohlhaas KA, Kleinhammes A, Jia Y, Wu Y, Nguyen ST and Ruoff RS (2007): Synthesis of graphene-based nanosheets via chemical reduction of exfoliated graphite oxide. Carbon. 45(7): 1558-1565.

362. Staudenmaier L (1898): Method for the preparation of graphitic acid. Reports of the German Chemical Society. 31(2): 1481-1487.

363. Stelzig SH, Menneking C, Hoffmann MS, Eisele K, Barcikowski S, Klapper M and Müllen K (2011): Compatibilization of laser generated antibacterial Ag-and Cu-nanoparticles for perfluorinated implant materials. European Polymer Journal. 47(4): 662-667.

364. Su Z, Sun D, Zhang L, He M, Jiang Y, Millar B, Douglas P, Mariotti D, Maguire P and Sun D (2021): Chitosan/silver nanoparticle/graphene oxide nanocomposites with multi-drug release, antimicrobial, and photothermal conversion functions. Materials. 14(9): 1-17.

365. Suflet DM, Popescu I, Pelin IM, Ichim DL, Daraba OM, Constantin M and Fundueanu G (2021): Dual cross-linked chitosan/pva hydrogels containing silver nanoparticles with antimicrobial properties. Pharmaceutics. 13(9): 1-18.

366. Sultan M, Nagieb ZA, El-Masry HM and Taha GM (2022): Physically-crosslinked hydroxyethyl cellulose-g-poly (acrylic acid-co-acrylamide)-Fe^{3+}/silver nanoparticles for water disinfection and enhanced adsorption of basic methylene blue dye. International journal of biological macromolecules. 196: 180-193.

367. Sun X, Huang C, Wang L, Liang L, Cheng Y, Fei W and Li Y (2021): Recent progress in graphene/polymer nanocomposites. Advanced Materials. 33(6): 1-28.

368. Surkatti R and El-Naas MH (2014): Biological treatment of wastewater contaminated with p-cresol using Pseudomonas putida immobilized in polyvinyl alcohol (PVA) gel. Journal of Water Process Engineering. 1: 84-90.

369. Tabesh E, Salimijazi H, Kharaziha M, Mahmoudi M and Hejazi M (2019): Development of an *in-situ* chitosan-copper nanoparticle coating by electrophoretic deposition. Surface and Coatings Technology. 364: 239-247.

370. Taghizadeh MT, Siyahi V, Ashassi-Sorkhabi H and Zarrini G (2020): ZnO, AgCl and AgCl/ZnO nanocomposites incorporated chitosan in the form of hydrogel beads

for photocatalytic degradation of MB, *E. coli* and *S. aureus*. International Journal of Biological Macromolecules. 147: 1018-1028.

371. Taka AL, Klink MJ, Mbianda XY and Naidoo EB (2021): Chitosan nanocomposites for water treatment by fixed-bed continuous flow column adsorption: a review. Carbohydrate Polymers. 255: 1-15.

372. Tamayo L, Azócar M, Kogan M, Riveros A and Páez M (2016): Copper-polymer nanocomposites: An excellent and cost-effective biocide for use on antibacterial surfaces. Materials Science and Engineering: C. 69: 1391-1409.

373. Tamayo Marín JA, Londoño SR, Delgado J, Navia Porras DP, Valencia Zapata ME, Mina Hernandez JH, Valencia CH and Grande Tovar CD (2019): Biocompatible and antimicrobial electrospun membranes based on nanocomposites of chitosan/poly (vinyl alcohol)/graphene oxide. International Journal of Molecular Sciences. 20(12): 1-14.

374. Tang C, Sun W and Yan W (2014): Green and facile fabrication of silver nanoparticles loaded activated carbon fibers with long-lasting antibacterial activity. RSC Advances. 4(2): 523-530.

375. Thakur I, Verma A and Örmeci B (2021): Mathematical modeling of *E. coli* inactivation in water using Fe-TiO_2 composite in a fixed bed reactor. Seperation and Purification Technology. 260: 1-11.

376. Thandapani G, Radha E, Jayashri J, Florence JAK and Sudha P (2018): Bioactive metallic surfaces for bone tissue engineering. In: Fundamental Biomaterials: Metals. Elsevier, pp. 79-110.

377. Theng B (1970): Interactions of clay minerals with organic polymers. Some practical applications. Clays and Clay Minerals. 18: 357-362.

378. Thomas V, Yallapu MM, Sreedhar B and Bajpai S (2007): A versatile strategy to fabricate hydrogel–silver nanocomposites and investigation of their antimicrobial activity. Journal of Colloid and Interface Science. 315(1): 389-395.

379. Tiller JC, Liao C-J, Lewis K and Klibanov AM (2001): Designing surfaces that kill bacteria on contact. Proceedings of the National Academy of Sciences. 98(11): 5981-5985.

380. Timofeeva L and Kleshcheva N (2011): Antimicrobial polymers: mechanism of action, factors of activity, and applications. Applied Microbiology and Biotechnology. 89: 475-492.

381. Tiwari JN, Tiwari RN and Kim KS (2012): Zero-dimensional, one-dimensional, two-dimensional and three-dimensional nanostructured materials for advanced electrochemical energy devices. Progress in Materials Science. 57(4): 724-803.

382. Tyliszczak B, Drabczyk A, Kudłacik-Kramarczyk S, Bialik-Wąs K, Kijkowska R and Sobczak-Kupiec A (2017): Preparation and cytotoxicity of chitosan-based hydrogels modified with silver nanoparticles. Colloids and Surfaces B: Biointerfaces. 160: 325-330.

383. Ullah F, Othman MBH, Javed F, Ahmad Z and Akil HM (2015): Classification, processing and application of hydrogels: A review. Materials Science and Engineering: C. 57: 414-433.

384. United-Nations (2015): The millennium development goals report. United Nations. 72: 1-75.

385. Urzedo AL, Goncalves MC, Nascimento MH, Lombello CB, Nakazato G and Seabra AB (2020): Cytotoxicity and antibacterial activity of alginate hydrogel containing nitric oxide donor and silver nanoparticles for topical applications. ACS Biomaterials Science & Engineering. 6(4): 2117-2134.

386. Usuki A, Kojima Y, Kawasumi M, Okada A, Fukushima Y, Kurauchi T and Kamigaito O (1993): Synthesis of nylon 6-clay hybrid. Journal of Materials Research. 8(5): 1179-1184.

387. Valliammai A, Selvaraj A, Mathumitha P, Aravindraja C and Pandian SK (2021): Polymeric antibiofilm coating comprising synergistic combination of citral and thymol prevents methicillin-resistant *Staphylococcus aureus* biofilm formation on titanium. Materials Science and Engineering: C 121: 1-12.

388. Váradi L, Luo JL, Hibbs DE, Perry JD, Anderson RJ, Orenga S and Groundwater PW (2017): Methods for the detection and identification of pathogenic bacteria: past, present, and future. Chemical Society Reviews. 46(16): 4818-4832.

389. Varaprasad K, Reddy GSM, Jayaramudu J, Sadiku R, Ramam K and Ray SS (2014): Development of microbial resistant Carbopol nanocomposite hydrogels via a green process. Biomaterials Science. 2(2): 257-263.

390. Vatanpour V, Keskin B, Mehrabani SAN, Karimi H, Arabi N, Behroozi AH, Shokrollahi-far A, Gul BY and Koyuncu I (2022): Investigation of boron nitride/silver/graphene oxide nanocomposite on separation and antibacterial improvement of polyethersulfone membranes in wastewater treatment. Journal of Environmental Chemical Engineering. 10(1): 107035.

391. Vilela D, Stanton MM, Parmar J and Sánchez S (2017): Microbots decorated with silver nanoparticles kill bacteria in aqueous media. ACS Applied Materials & Interfaces. 9(27): 22093-22100.

392. Wahid F, Zhong C, Wang H-S, Hu X-H and Chu L-Q (2017): Recent advances in antimicrobial hydrogels containing metal ions and metals/metal oxide nanoparticles. Polymers. 9(12): 1-27.

393. Wan A, Xu Q, Sun Y and Li H (2013): Antioxidant activity of high molecular weight chitosan and N, O-quaternized chitosans. Journal of Agricultural and Food Chemistry. 61(28): 6921-6928.

394. Wang G and Fakhri A (2020): Preparation of CuS/polyvinyl alcohol-chitosan nanocomposites with photocatalysis activity and antibacterial behavior against G+/G-bacteria. International Journal of Biological Macromolecules. 155: 36-41.

395. Wang J and Chen C (2014): Chitosan-based biosorbents: modification and application for biosorption of heavy metals and radionuclides. Bioresource technology. 160: 129-141.

396. Wang K and Liu Q (2013): Adsorption of phosphorylated chitosan on mineral surfaces. Colloids and Surfaces A: Physicochemical and Engineering Aspects. 436: 656-663.

397. Wang L, He J, Zhu L, Wang Y, Feng X, Chang B, Karahan HE and Chen Y (2019): Assembly of pi-functionalized quaternary ammonium compounds with graphene hydrogel for efficient water disinfection. Journal of Colloid and Interface Science. 535: 149-158.

398. Wang T, Kuttappan D, Amalaradjou MA, Luo Y and Luo Y (2021): Polydopamine-coated chitosan hydrogel beads for synthesis and immobilization of silver nanoparticles to simultaneously enhance antimicrobial activity and adsorption kinetics. Advanced Composites and Hybrid Materials. 4: 696-706.

399. Wang T, Li Y, Liu Y, Xu Z, Wen M, Zhang L, Xue Y and Shang L (2023): Highly biocompatible Ag nanocluster-reinforced wound dressing with long-term and synergistic bactericidal activity. Journal of Colloid and Interface Science. 633: 851-865.

400. Wang Y, Li B, Zhou Y and Jia D (2008): Chitosan-induced synthesis of magnetite nanoparticles via iron ions assembly. Polymers for Advanced Technologies. 19(9): 1256-1261.

401. Wang Y, Yang Y, Shi Y, Song H and Yu C (2020): Antibiotic-free antibacterial strategies enabled by nanomaterials: progress and perspectives. Advanced Materials. 32(18): 1-21.

402. Wang YJ, Tian MW, Qu LJ, Zhu SF, Sun YN and Han GT (2015): Enhanced Thermal, UV Blocking and Dye Absorptive Properties of Chitosan/poly(vinyl alcohol)/Graphene Oxide Fibers. Fibers and Polymers. 16(9): 2011-2020.

403. White RJ (2001): An historical overview of the use of silver in wound management. British Journal of Community Nursing. 6(Sup1): 3-8.

404. WHO (2016): Decontamination and reprocessing of medical devices for health-care facilities. World Health Organization. https://apps.who.int/iris/bitstream/handle/10665/250232/9789241549851-eng.pdf?sequence=1

405. WHO (2011): Guidelines for drinking-water quality. World Health Organization. https://iris.who.int/bitstream/handle/10665/44584/9789241548151_eng.pdf?sequence=1

406. WHO (2018): Health-care waste fact sheet. World Health Organization. https://www.who.int/news-room/fact-sheets/detail/health-care-waste

407. WHO (2015): Health Care Associated Infections Fact Sheet. World Health Organization. https://www.convatec.at/media/1286/gpsc_ccisc_fact_sheet_en.pdf

408. WHO (2021): Silver in drinking water: Background document for development of WHO Guidelines for Drinking-water Quality.

409. WHO (2019): Water, sanitation, hygiene and health: a primer for health professionals. World Health Organization. https://apps.who.int/iris/bitstream/handle/10665/330100/WHO-CED-PHE-WSH-19.149-eng.pdf

410. WHO (2022): WHO global water, sanitation and hygiene: annual report 2020. World Health Organization.

https://apps.who.int/iris/bitstream/handle/10665/354462/9789240033085-eng.pdf?sequence=1

411. Wu D, Wang Y, Li Y, Wei Q, Hu L, Yan T, Feng R, Yan L and Du B (2019): Phosphorylated chitosan/$CoFe_2O_4$ composite for the efficient removal of Pb (II) and Cd (II) from aqueous solution: adsorption performance and mechanism studies. Journal of Molecular Liquids. 277: 181-188.

412. Wu H, Yu G, Pan L, Liu N, McDowell MT, Bao Z and Cui Y (2013): Stable Li-ion battery anodes by *in-situ* polymerization of conducting hydrogel to conformally coat silicon nanoparticles. Nature Communications. 4(1): 1-6.

413. Wu S, Su F, Dong X, Ma C, Pang L, Peng D, Wang M, He L and Zhang Z (2017): Development of glucose biosensors based on plasma polymerization-assisted nanocomposites of polyaniline, tin oxide, and three-dimensional reduced graphene oxide. Applied Surface Science. 401: 262-270.

414. Wu X, Ye L, Liu K, Wang W, Wei J, Chen F and Liu C (2009): Antibacterial properties of mesoporous copper-doped silica xerogels. Biomedical Materials. 4(4): 1-7.

415. Wypij M, Trzcińska-Wencel J, Golińska P, Avila-Quezada GD, Ingle AP and Rai M (2023): The strategic applications of natural polymer nanocomposites in food packaging and agriculture: Chances, challenges, and consumers' perception. Frontiers in Chemistry. 10: 1-18.

416. Xie M, Gao M, Yun Y, Malmsten M, Rotello VM, Zboril R, Akhavan O, Kraskouski A, Amalraj J and Cai X (2023): Antibacterial nanomaterials: mechanisms, impacts on antimicrobial resistance and design principles. Angewandte Chemie International Edition. 62(17): 1-25.

417. Xie M, Huang K, Yang F, Wang R, Han L, Yu H, Ye Z and Wu F (2020): Chitosan nanocomposite films based on halloysite nanotubes modification for potential biomedical applications. International Journal of Biological Macromolecules. 151: 1116-1125.

418. Xie S, Zhao J, Zhang B, Wang Z, Ma H, Yu C, Yu M, Li L and Li J (2015): Graphene Oxide Transparent Hybrid Film and Its Ultraviolet Shielding Property. ACS Applied Materials & Interfaces. 7(32): 17558-17564.

419. Xing C, Chang J, Ma M, Ma P, Sun L and Li M (2022): Ultrahigh-efficiency antibacterial and adsorption performance induced by copper-substituted polyoxomolybdate-decorated graphene oxide nanocomposites. Journal of Colloid and Interface Science. 612: 664-678.

420. Xing Z, Guo J, Wu Z, He C, Wang L, Bai M, Liu X, Zhu B, Guan Q and Cheng C (2023): Nanomaterials-Enabled Physicochemical Antibacterial Therapeutics: Toward the Antibiotic-Free Disinfections. Small. 1-33.

421. Xiong Z, Sun Z-B, Zheng M-L, Cao Y-Y, Jin F, Chen W-Q, Zhao Z-S and Duan X-M (2011): A facile method for the room-temperature synthesis of water-soluble magnetic Fe_3O_4 nanoparticles: Combination of *in situ* synthesis and decomposition of polymer hydrogel. Materials Chemistry and Physics. 130(1-2): 72-78.

422. Xu L, Wang C, Cui Y, Li A, Qiao Y and Qiu D (2019): Conjoined-network rendered stiff and tough hydrogels from biogenic molecules. Science Advances. 5(2): 1-10.

423. Xu L, Zhao K, Miao J, Yang Z, Li Z, Zhao L, Su H, Lin L and Hu Y (2022): High-strength and anti-bacterial BSA/carboxymethyl chitosan/silver nanoparticles/calcium alginate composite hydrogel membrane for efficient dye/salt separation. International Journal of Biological Macromolecules. 220: 267-279.

424. Xu M, Luo H, Rong H, Wu S, Zheng Z and Chen B (2023): Calcium alginate gels-functionalized polyurethane foam decorated with silver nanoparticles as an antibacterial agent for point-of-use water disinfection. International Journal of Biological Macromolecules. 231: 1-11.

425. Xue B, Qin M, Wu J, Luo D, Jiang Q, Li Y, Cao Y and Wang W (2016): Electroresponsive supramolecular graphene oxide hydrogels for active bacteria adsorption and removal. ACS Applied Materials & Interfaces. 8(24): 15120-15127.

426. Yadav M, Rhee KY, Park SJ and Hui D (2014): Mechanical properties of Fe_3O_4/GO/chitosan composites. Composites Part B: Engineering. 66: 89-96.

427. Yadav N, Dubey A, Shukla S, Saini CP, Gupta G, Priyadarshini R and Lochab B (2017): Graphene oxide-coated surface: inhibition of bacterial biofilm formation due to specific surface–interface interactions. ACS Omega. 2(7): 3070-3082.

428. Yadollahi M, Farhoudian S and Namazi H (2015): One-pot synthesis of antibacterial chitosan/silver bio-nanocomposite hydrogel beads as drug delivery systems. International Journal of Biological Macromolecules. 79: 37-43.

429. Yallappa S, Manjanna J, Sindhe M, Satyanarayan N, Pramod S and Nagaraja K (2013): Microwave assisted rapid synthesis and biological evaluation of stable copper nanoparticles using *T. arjuna* bark extract. Spectrochimica Acta Part A: Molecular and Biomolecular Spectroscopy. 110: 108-115.

430. Yang D, Liu Q, Gao Y, Wan S, Meng F, Weng W and Zhang Y (2023): Characterization of silver nanoparticles loaded chitosan/polyvinyl alcohol antibacterial films for food packaging. Food Hydrocolloids. 136: 1-9.

431. Yang JM, Su WY and Yang MC (2004): Evaluation of chitosan/PVA blended hydrogel membranes. Journal of Membrane Science. 236(1-2): 39-51.

432. Yang M-C, Tseng Y-Q, Liu K-H, Cheng Y-W, Chen W-T, Chen W-T, Hsiao C-W, Yung M-C, Hsu C-C and Liu T-Y (2019): Preparation of amphiphilic chitosan–graphene oxide–cellulose nanocrystalline composite hydrogels and their biocompatibility and antibacterial properties. Applied Sciences. 9(15): 1-10.

433. Yang Y, Xu Y, Wei S and Shan W (2021): Oral preparations with tunable dissolution behavior based on selective laser sintering technique. International Journal of Pharmaceutics. 593: 1-12.

434. Yao H, Zhang P, Huang Y, Cheng H, Li C and Qu L (2020): Highly efficient clean water production from contaminated air with a wide humidity range. Advanced Materials. 32(6): 1-8.

435. Ye M, Mohanty P and Ghosh G (2014): Morphology and properties of poly vinyl alcohol (PVA) scaffolds: impact of process variables. Materials Science and Engineering: C. 42: 289-294.

436. Ying Y, Wu Y and Huang J (2020): Preparation and characterization of chitosan/poly (vinyl alcohol)/graphene oxide films and studies on their antibiofilm formation activity. Journal of Biomedical Materials Research - Part A. 108(10): 2015-2022.

437. Yu H, Zhang B, Bulin C, Li R and Xing R (2016): High-efficient synthesis of graphene oxide based on improved hummers method. Scientific Reports. 6(1): 1-7.

438. Yuan Y, Liu F, Xue L, Wang H, Pan J, Cui Y, Chen H and Yuan L (2016): Recyclable *escherichia coli*-specific-killing AuNP–polymer (ESKAP) nanocomposites. ACS Applied Materials & Interfaces. 8(18): 11309-11317.

439. Zain NM, Stapley AG and Shama G (2014): Green synthesis of silver and copper nanoparticles using ascorbic acid and chitosan for antimicrobial applications. Carbohydrate Polymers. 112: 195-202.

440. Zaïri F, Gloaguen J-M, Naït-Abdelaziz M, Mesbah A and Lefebvre J-M (2011): Study of the effect of size and clay structural parameters on the yield and post-yield response of polymer/clay nanocomposites via a multiscale micromechanical modelling. Acta Materialia. 59(10): 3851-3863.

441. Zakia M, Koo JM, Kim D, Ji K, Huh P, Yoon J and Yoo SI (2020): Development of silver nanoparticle-based hydrogel composites for antimicrobial activity. Green Chemistry Letters and Reviews. 13(1): 34-40.

442. Zare Y and Shabani I (2016): Polymer/metal nanocomposites for biomedical applications. Materials Science and Engineering: C. 60: 195-203.

443. Zarghami V, Ghorbani M, Bagheri KP and Shokrgozar MA (2021): Prevention the formation of biofilm on orthopedic implants by melittin thin layer on chitosan/bioactive glass/vancomycin coatings. Journal of Materials Science: Materials in Medicine. 32(7): 1-9.

444. Zeng X, Xing X, Gupta M, Keber FC, Lopez JG, Lee Y-CJ, Roichman A, Wang L, Neinast MD and Donia MS (2022): Gut bacterial nutrient preferences quantified *in vivo*. Cell. 185(18): 3441-3456.

445. Zhang D, Yang S, Chen Y, Liu S, Zhao H and Gu J (2018): ^{60}Co γ-ray irradiation crosslinking of chitosan/graphene oxide composite film: Swelling, thermal stability, mechanical, and antibacterial properties. Polymers. 10(3): 1-14.

446. Zhang G, Li W, Chen S, Zhou W and Chen J (2020): Problems of conventional disinfection and new sterilization methods for antibiotic resistance control. Chemosphere. 254: 1-12.

447. Zhang J, Yang H, Shen G, Cheng P, Zhang J and Guo S (2010): Reduction of graphene oxide via L-ascorbic acid. Chemical Communications. 46(7): 1112-1114.

448. Zhang R, Wang Y, Ma D, Ahmed S, Qin W and Liu Y (2019): Effects of ultrasonication duration and graphene oxide and nano-zinc oxide contents on the properties of polyvinyl alcohol nanocomposites. Ultrasonics sonochemistry. 59: 1-15.

449. Zhang S, Liang X, Gadd GM and Zhao Q (2021): A sol–gel based silver nanoparticle/polytetrafluorethylene (AgNP/PTFE) coating with enhanced antibacterial and anti-corrosive properties. Applied Surface Science. 535: 1-10.

450. Zhang T, Zuo T, Hu D and Chang C (2017): Dual physically cross-linked nanocomposite hydrogels reinforced by tunicate cellulose nanocrystals with high toughness and good self-recoverability. ACS Applied Materials & Interfaces. 9(28): 24230-24237.

451. Zhang W, Huang H and Bernstein R (2022): Zwitterionic hydrogel modified reduced graphene oxide/ZnO nanocomposite blended membrane with high antifouling and antibiofouling performances. Journal of Colloid and Interface Science. 613: 426-434.

452. Zhang X, Yan S, Chen J, Tyagi R and Li J (2020): Physical, chemical, and biological impact (hazard) of hospital wastewater on environment: presence of pharmaceuticals, pathogens, and antibiotic-resistance genes. In: Current Developments in Biotechnology and Bioengineering. Elsevier, pp. 79-102.

453. Zhang Y, Ping Y, Zhou R, Wang J and Zhang G (2018): High throughput sequencing-based analysis of microbial diversity in dental unit waterlines supports the importance of providing safe water for clinical use. Journal of Infection and Public Health. 11(3): 357-363.

454. Zhang Z, van Kleunen M, Becks L and Thakur MP (2020): Towards a general understanding of bacterial interactions. Trends in Microbiology. 28(10): 783-785.

455. Zhao C, Pandit S, Fu Y, Mijakovic I, Jesorka A and Liu J (2016): Graphene oxide based coatings on nitinol for biomedical implant applications: effectively promote mammalian cell growth but kill bacteria. RSC Advances. 6(44): 38124-38134.

456. Zhao D, Shen Z and Shen X (2021): Dual-functional calcium alginate hydrogel beads for disinfection control and removal of dyes in water. International Journal of Biological Macromolecules. 188: 253-262.

457. Zhao F, Zhou X, Liu Y, Shi Y, Dai Y and Yu G (2019): Super moisture-absorbent gels for all-weather atmospheric water harvesting. Advanced Materials. 31(10): 1-7.

458. Zhao H, Li X, Zhang L, Hu Z, Zhong L and Xue J (2021): Preparation and bacteriostatic research of porous polyvinyl alcohol/biochar/nanosilver polymer gel for drinking water treatment. Scientific Reports. 11(1): 1-11.

459. Zhao J, Wang Z, White JC and Xing B (2014): Graphene in the aquatic environment: adsorption, dispersion, toxicity and transformation. Environmental Science & Technology. 48(17): 9995-10009.

460. Zhao Y, Guo L, Shen W, An Q, Xiao Z, Wang H, Cai W, Zhai S and Li Z (2020): Function integrated chitosan-based beads with throughout sorption sites and inherent diffusion network for efficient phosphate removal. Carbohydrate Polymers. 230: 1-9.

461. Zheng K and Xie J (2021): Cluster materials as traceable antibacterial agents. Accounts of Materials Research. 2(11): 1104-1116.

462. Zhou X, Guo Y, Zhao F and Yu G (2019): Hydrogels as an emerging material platform for solar water purification. Accounts of Chemical Research. 52(11): 3244-3253.

463. Zhou X, Zhao F, Guo Y, Zhang Y and Yu G (2018): A hydrogel-based antifouling solar evaporator for highly efficient water desalination. Energy & Environmental Science. 11(8): 1985-1992.

464. Zhu Y, Murali S, Cai W, Li X, Suk JW, Potts JR and Ruoff RS (2010): Graphene and graphene oxide: synthesis, properties, and applications. Advanced Materials. 22(35): 3906-3924.

465. Ziani K, Fernández-Pan I, Royo M and Maté JI (2009): Antifungal activity of films and solutions based on chitosan against typical seed fungi. Food Hydrocolloids. 23(8): 2309-2314.

Appendix

Appendix-A

Details of instruments used

- **Autoclave:** Equitron, India.
- **Centrifuge:** Himac 22G, Hitachi, Japan; Sorvall Legend XFR, Thermo Scientific, USA.
- **ELISA plate reader:** Multiskan Spectrum, Thermo Scientific, USA; BioRad, USA
- **Field emission-scanning electron microscopy:** Hitachi SU8010, Japan; Carl-Zeiss Sigma 500 FEG-SEM, Germany.
- **Fourier Transform Infrared Spectroscopy:** Nicklet 380 Thermo Fisher, USA; Perkin Elmer-Spectrum RX-IFTIR, USA.
- **Differential Scanning Calorimetry:** DSC131 evo, SETARAM Instrumentation, France
- **Inductively Coupled Plasma-Atomic Emission spectrometer:** ARCOS- simultaneous ICP Spectrometer, Germany
- **Raman Spectroscopy:** LabRam HR800 Raman spectroscope, Horiba Jobin-Yvon, France
- **Transmission electron microscopy:** Jeol JEM-F200, Japan.
- **Fluorescence microscope:** Nikon Eclipse50i, Japan.
- **Mechanical strength:** Shimadzu Autograph AG100KNG universal testing machine (UTM), Japan.
- **Thermogravimetric analysis:** Setsys, Setaram Instrumentation, France
- **Brunauer-Emmett-Teller analysis**: NOVA touch 4L, Quantachrome Instruments, USA
- **Microwave Plasma-Atomic Emission spectrometry:** MP-AES, Agilent 4100, USA.
- **Incubator:** Calton® BOD incubator, NSW India.
- **CO_2 incubator:** Thermo Fisher Forma™, USA.
- **Automated cell counter:** Curiosis Facscope™ B, Korea.
- **Rotational Rheometer:** Anton Paar RheolabQC, Austria.
- **Laminar flow cabinet:** Thermadyne Biosafety Cabinet Class-I, India.
- **Oven:** NSW India.
- **pH meter:** Adwa AD1030, Hungary.
- **Scanning electron microscopy:** Hitachi S-3400N, Japan.
- **Shaking incubator:** Excella® E25 Incubator shaker, New Brunswick Scientific, USA.
- **Thermogravimetric Analyzer:** EXSTAR TG/DTA 6300, Seiko Instruments Inc., Japan.

- **Ultrasonic bath:** PCI analytics-9L, India.
- **UV-Viz spectrophotometer:** UV-2600, Shimadzu Corp., Japan.
- **Vortex:** Tarson Spinix 3002, India.
- **Water bath:** Precision Reciprocal Shaking Bath, Thermo Scientific, USA; NSW India.
- **Weighing balance:** ME 104 Mettler Toledo, USA; Precisa ES225SM-D, Switzerland.
- **X-ray diffractometer**: PANalytical X-pert Pro, The Netherlands.
- **X-ray photoelectron spectroscopy:** ESCALAB, Thermo Fischer Scientific, USA.

Appendix-B

List of materials used

All chemicals and reagents used for the experiments were of the highest analytical grade. Glassware and plasticware were procured from Borosil, JSGW and Tarsons, India. All experiments were conducted using either deionized or double distilled water. Glassware used were treated with Aqua Regia (3:1 solution of hydrochloric acid and nitric acid) to remove all the accumulated metals and salts, followed by washing with distilled water. Sterilization of the media components, buffers, saline solutions were done in an autoclave at 121°C (15 psi) for 15 minutes unless otherwise specified.

Loba-Chemie Pvt. Ltd, India: Sodium hydroxide, sulphuric acid, graphite powder (purity 98%, particle size -60 mesh), sodium nitrate, potassium permanganate, nitro blue tetrazolium chloride, lithium lactate, 30% hydrogen peroxide, and 3-(4,5-Dimethylthiazol-2-yl)-2,5-diphenyltetrazolium bromide), sodium chloride, potassium chloride, sodium phosphate dibasic, potassium phosphate monobasic, magnesium chloride hexahydrate, sodium sulphate, sodium carbonate, sodium hydrogen carbonate, di-potassium hydrogen phosphate trihydrate.

Hi Media Laboratories Pvt. Ltd. (Mumbai, India): Poly (vinyl alcohol), calcium chloride, bovine serum albumin, glutaraldehyde, nutrient agar, nutrient broth, luria broth, tris Buffer, β-Nicotinamide adenine dinucleotide sodium salt, Phenazine methosulfate, Iodonitrotetrazolium chloride, Tris-HCl, Tris-base, L-glutathione, 5, 5′-dithiobis- (2-nitrobenzoic acid), RPMI-1640, Fetal bovine serum, Coomassie Brilliant Blue G-250, and DMEM.

Merck, USA: Acetic acid**,** ethanol**,** hydrochloric acid**,** nitric acid, phosphoric acid, and sodium hydroxide.

Nano Wings Pvt. Ltd., India: Chitosan (>99% pure, 85% deacetylated, MW 100–300 kD).

Jindal Steel Corporation, India: Surgical grade stainless steel (AISI 316L).

Sigma Aldrich (USA): Silver nitrate and sodium borohydride.

National Collection of Industrial Microorganisms (CSIR-NCL, Pune, India): Bacterial slant cultures of *Enterobacter aerogenes* NCIM 5139 (ATCC 13048), *Staphylococcus aureus* NCIM 2127 (ATCC 9144) and *Staphylococcus epidermidis* NCIM 2493 (ATCC 12228).

Microbial Type Culture Collection and Gene Bank (CSIR-IMTECH, Chandigarh, India): *Escherichia coli* MTCC 739 (ATCC 10536) culture (freeze-dried).

National Centre for Cell Science, Pune (India): Human hepatocellular carcinoma cells (HepG2) and African green monkey kidney cells (Vero).

Appendix-C

Details of reagents prepared

1. *Phosphate buffer saline (PBS)*

Designated amount of sodium chloride, potassium chloride, potassium phosphate monobasic and sodium phosphate dibasic were mixed in 80 mL of distilled water. Solution was adjusted to desired pH ~7.2 and final volume was made 100 mL with addition of distilled water.

For 1X (100 mL), pH ~7.2	
Components	**Amount**
Sodium chloride (NaCl)	800 mg
Potassium chloride (KCl)	20 mg
Sodium phosphate dibasic (Na_2HPO_4)	144 mg
Potassium phosphate monobasic (KH_2PO_4)	24.5 mg

2. *Bicarbonate buffer*

0.72g of sodium carbonate (Na_2CO_3) and 1.89g of sodium bicarbonate ($NaHCO_3$) were added to 400 mL of distilled water. Solution was adjusted to desired pH ~8.6 and final volume was made to 500 mL with addition of distilled water.

3. *Bradford reagent*

Reagent was prepared by adding 0.01% (w/v) Coomassie Brilliant Blue G-250, 4.7% (w/v) ethanol, and 8.5% (w/v) phosphoric acid.

4. *LDH assay reagent*

Solution A: Mixture of 1.175 mM phenazine methosulfate (PMS in distilled water), 2.610 mM iodonitrotetrazolium chloride (INT in dimethyl sulfoxide), and 5.185 mM β-nicotinamide adenine dinucleotide sodium (NAD in distilled water)

Solution B: 50mM lithium lactate in distilled water

Solution C: 200 mM TRIS in distilled water with pH 8

Reagent preparation: 50 µL each of solution A, solution B, and solution C.

5. Simulated body fluid

The container with 700 mL of distilled water was placed in a constant temperature water bath at 36.5 ± 0.5 ◦C, the reagents were completely dissolved in the order listed in the table below, and the pH value of the SBF was adjusted to 7.45 with Tris and HCl. Finally, the volume was made to 1000 mL with addition of distilled water.

For 1000 mL, pH ~7.45	
Components	**Amount**
Sodium chloride (NaCl)	8.035 g
Sodium hydrogen carbonate ($NaHCO_3$)	0.355 g
Di-potassium hydrogen phosphate trihydrate (K_2HPO_4. $3H_2O$)	0.231 g
Magnesium chloride hexahydrate ($MgCl_2$. $6H_2O$)	0.311 g
1.0 M Hydrochloric acid (HCl)	39 mL
Calcium chloride ($CaCl_2$)	0.292 g
Sodium sulphate (Na_2SO_4)	0.072 g

Appendix-D

Standard Curves

1. *Standard curve of Bovine Serum Albumin (BSA) using Bradford method*

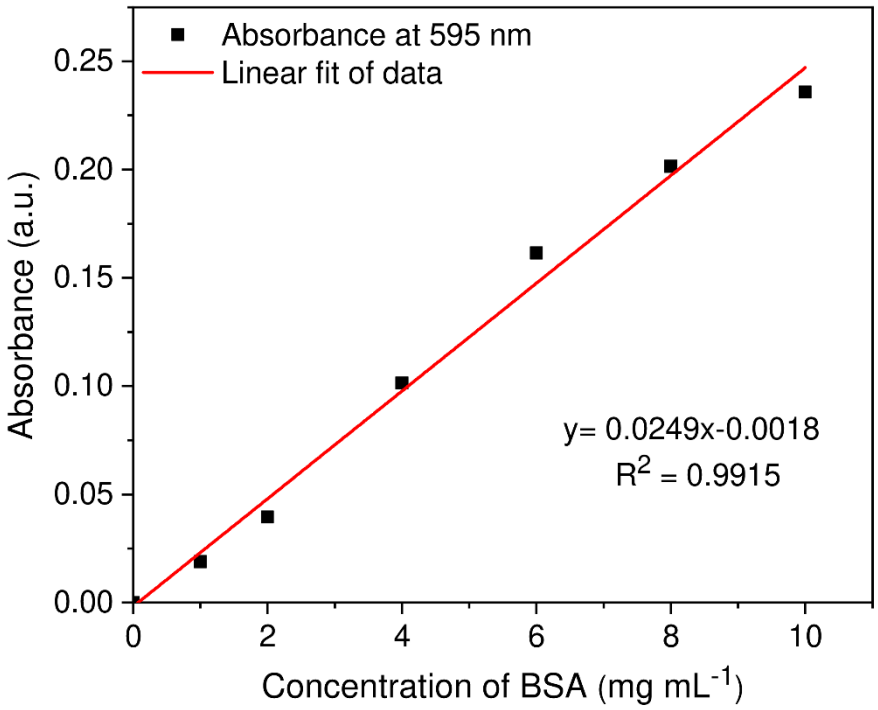

Raw Data

Table A1 Raw data used for calculating folds increase in intracellular ROS in graph of figure 4.37(a).

Sample	***E. aerogenes***	***E. coli***	***S. aureus***	***S. epidermidis***
	OD_{575}			
Control	0.1209	0.1339	0.1325	0.1311
CS/GO	0.1618	0.1757	0.1751	0.1637
CS/GO/Ag	0.4749	0.4303	0.4158	0.3509

Table A2 Raw data used for calculating folds increase in intracellular ROS in graph of figure 4.61(a).

Sample	***S. epidermidis***	***S. aureus***
	OD_{575}	
Control	0.0635	0.0377
CS/PVA	0.0666	0.0490
$CS/PVA/GO_{0.05}$	0.1133	0.0807
$CS/PVA/GO_{0.075}$	0.1183	0.1061
$CS/PVA/GO_{0.1}$	0.1310	0.1199
$CS/PVA/GO_{0.15}$	0.1591	0.1295

SPRINGER NATURE LICENSE
TERMS AND CONDITIONS

Aug 17, 2023

This Agreement between Thapar University -- Navneet Dhiman ("You") and Springer Nature ("Springer Nature") consists of your license details and the terms and conditions provided by Springer Nature and Copyright Clearance Center.

License Number	5611250805876
License date	Aug 17, 2023
Licensed Content Publisher	Springer Nature
Licensed Content Publication	Springer eBook
Licensed Content Title	Graphene Oxide Coatings as Tools to Prevent Microbial Biofilm Formation on Medical Device
Licensed Content Author	Margherita Cacaci, Cecilia Martini, Cinzia Guarino et al
Licensed Content Date	Jan 1, 2019
Type of Use	Thesis/Dissertation
Requestor type	academic/university or research institute
Format	print and electronic
Portion	figures/tables/illustrations
Number of figures/tables/illustrations	1

Will you be translating?	no
Circulation/distribution	1 - 29
Author of this Springer Nature content	no
Title	Development of polymeric hydrogel nanocomposites for antibacterial application
Institution name	Thapar Institute of Engg. & Technology
Expected presentation date	Mar 2024
Portions	Fig.1
Requestor Location	Thapar University Navneet Kaur c/o Biotech Lab 2, TIFAC-CO Bhadson Road PATIALA, Punjab 147004 India Attn: Thapar University
Total	0.00 USD

Terms and Conditions

Springer Nature Customer Service Centre GmbH Terms and Conditions

The following terms and conditions ("Terms and Conditions") together with the terms specified in your [RightsLink] constitute the License ("License") between you as Licensee and Springer Nature Customer Service Centre GmbH as Licensor. By clicking 'accept' and completing the transaction for your use of the material ("Licensed Material"), you confirm your acceptance of and obligation to be bound by these Terms and Conditions.

1. Grant and Scope of License

1. 1. The Licensor grants you a personal, non-exclusive, non-transferable, non-sublicensable, revocable, world-wide License to reproduce, distribute, communicate to the public, make available, broadcast, electronically transmit or create derivative works using the Licensed Material for the purpose(s) specified in your RightsLink Licence Details only. Licenses are granted for the specific use requested in the order

Environmental Science Nano

ROYAL SOCIETY OF CHEMISTRY

PAPER

Check for updates

Cite this: *Environ. Sci.: Nano*, 2020, 7, 2337

Hierarchically aligned nano silver/chitosan–PVA hydrogel for point-of-use water disinfection: contact-active mechanism revealed†

Navneet Kaur Dhiman [a] and Shekhar Agnihotri *[abc]

Received 19th April 2020,
Accepted 11th June 2020

DOI: 10.1039/d0en00405g

rsc.li/es-nano

The unsafe disposal of biomedical waste poses hazardous consequences to natural water resources, which may get contaminated through several means of leakage into waterways. Herein, the disinfection potential of nano-silver loaded chitosan–PVA hydrogel to completely eradicate biomedical contaminants coexisting with natural contaminants in environmental samples was successfully demonstrated for the first time. The polymeric network of the hydrogel served a dual role for *in situ* synthesis and immobilization of silver nanoparticles (AgNPs) simultaneously. Porous Ag-loaded hydrogels displayed a temperature-dependent swelling behavior and exhibited an improved mechanical strength (Young's modulus, 12.36 ± 0.29 MPa; elongation at break, 180%) by effectively distributing the external stress and restored its structural integrity. Complete disinfection (100% killing) could be achieved within 4 h against all the four tested contaminants, demonstrating a distinct strain-specific biocidal activity. Being a diffusion-controlled process, the oxidative dissolution of AgNPs deeply buried in the interiors of the hydrogel architectures was adversely affected on repeated use and restricted the maximum silver release to 38.8 ± 5.6 μg g^{-1} hydrogel in an aqueous suspension over 7 days. Correlating the reusability and silver release kinetics, a predominant contact-active role of the hydrogel was envisaged *via* 'capture and kill' over leaching of silver ions for rapid water disinfection. The Ag-loaded hydrogels also severely inhibited the biofilm formation of *Escherichia coli* and *Staphylococcus aureus* till 48 h. Finally, the hydrogels could completely disinfect the natural water samples, *i.e.*, river, ground, and tap water with inherited microbiota and biomedical contaminants in 2 h under the real conditions.

Environmental significance

This study accounts for the possibilities of biomedical contamination coexisting with natural contaminants in our water resources and their complete removal through hydrogel-based disinfection systems, thus mitigating their hazardous consequences. The concentration range of each water quality parameter was selected so as to represent the practical water chemistry conditions prevailing in various regions around the globe. The semi-interpenetrating networks of the hydrogel performed a dual role, acting both as a nanoreactor for *in situ* AgNP synthesis and a support matrix for their subsequent immobilization. The hydrogel appeared to be robust, reusable with anti-biofilm characteristics, and achieved 100% disinfection with only ~74 ppb of silver release in the water samples through the 'contact-active' mode of bactericidal action; thus, it poses no hazards associated with silver leaching.

1. Introduction

The recent interventions in nanotechnology have created new paradigms of using functional nanomaterials for water purification purposes.[1,2] Several coinage metals (copper, silver, gold) and metal oxides at the nanoscale have demonstrated excellent capabilities to purify contaminated water owing to their high aspect ratio along with unique physicochemical characteristics.[3] Silver nanoparticles (AgNPs) possess the most striking attributes among such nanomaterials for myriad of water based applications such as the removal of emerging contaminants,[4] photocatalytic water-splitting,[5] wastewater treatment,[6] biomedical coatings,[7] and potable water purification.[8–12] Despite this, the use of AgNPs for water purification still lacks practical affordability for three main reasons.[13] First, colloidal AgNPs are more prone to get aggregated under different chemical conditions of

[a] *Department of Biotechnology, Thapar Institute of Engineering and Technology, Bhadson Road, Patiala-147004, Punjab, India*
[b] *TIFAC Centre of Relevance and Excellence (CORE) in Agro and Industrial Biotechnology, Thapar Institute of Engineering and Technology, Bhadson Road, Patiala-147004, Punjab, India*
[c] *Department of Agriculture and Environmental Sciences, National Institute of Food Technology Entrepreneurship and Management, Kundli, Sonepat-131028, Haryana, India. E-mail: agnish@niftem.ac.in; Tel: +91 99200 32558*

† Electronic supplementary information (ESI) available. See DOI: 10.1039/d0en00405g

water and eventually lose their original efficacy at the time of application.[10] Second, in the absence of any carrier support or matrix, AgNPs cannot be reused/retrieved further, which make such systems uneconomical and unrealistic.[8] Most importantly, an inevitable release of colloidal AgNPs into the waterways after every single use would adversely affect aquatic life forms and eventually, humans.[14] Few recent progresses in immobilizing AgNPs on to various support materials such as silica,[9] granular activated carbon,[15] graphene oxide,[16,17] electrospun cellulose membrane,[18] and polymeric gels[12,19] have overcome the aforementioned limitations, establishing silver-based nanocomposites as promising materials to treat contaminated water/wastewater.

While selecting an ideal material for immobilization, the porous morphology of the support matrix allows a dense, stable localization of biomolecules/nanomaterials through suitable surface functionalization approaches.[20–22] Polymeric chitosan hydrogels bear such characteristics where the presence of semi-interpenetrating networks facilitate maximum AgNP–water interactions within the hydrogel without getting dissolved in it. Being innately antimicrobial, non-cytotoxic, and biodegradable, chitosan hydrogel-based nanocomposites have recently been utilized for several biomedical purposes.[7,23] Moreover, poor mechanical strength of the chitosan hydrogel can be minimized either by adding certain crosslinker(s) or introducing another compatible polymer such polyvinyl alcohol (PVA). In contrast to this, many studies rely on the modification of chitosan polymers using either harsh chemicals and/or crosslinkers, which pose even more hazardous implications to the ecosystem.[24] A few studies have demonstrated the incorporation of pre-synthesized AgNPs over the nanocomposite *via* surface functionalization, which requires an additional step of chemical processing, making this approach unworthy.[25] Interestingly, a diverse range of nanoparticle-hydrogel systems have recently been reported following our strategy,[19] wherein *in situ* synthesis of nanoparticles could be achieved within the polymeric network of bulk hydrogel, which simultaneously acted as an immobilizing matrix for AgNPs.[26–28] The underlying limitations in such reports further prompted us to develop nano-silver loaded hydrogel for point-of-use water disinfection purposes under natural water quality conditions.

Within the Indian subcontinent, rivers, canals, ponds, and aquifers are considered as the major natural resources of clean water, which reach urban communities through municipal supply after preliminary treatments. The inherent chemical conditions of natural waters (alkalinity, hardness, organic matter), however, may make these treatments ineffective,[10] thus allowing microbial contaminants to grow before they get consumed in our homes. In addition, the unsafe garbage/waste disposal practices through landfills, septic tanks, and sewers have emerged as the major conduits of surface and groundwater contamination. Although there have been several reports on purifying water using silver-based nanocomposites, most of the disinfection studies are confined due to the use of distilled/deionized water as the medium.[29–32] This might be a major hurdle for the successful application of hydrogels in water purification purposes under practically relevant conditions. As a step ahead, it is imperative to testify the applicability of nanocomposites in real, natural waters under various water quality parameters. Moreover, it is of great public health concern to elucidate the fate of microbial contaminants that may enter into drinking water systems (DWS) through various means.

Herein, we have attempted to investigate a facile and eco-friendly approach for synthesizing chitosan–PVA hydrogel with *in situ* immobilized AgNPs for water disinfection purposes. The disinfection studies were tested against four bacterial strains under simulated potable water conditions. *Escherichia coli* (*E. coli*) and *Enterobacter aerogenes* (*E. aerogenes*) are well known indicators of water contamination, while *Staphylococcus aureus* (*S. aureus*) and *Staphylococcus epidermidis* (*S. epidermidis*) are associated with health infections and are considered as the representatives of unsafe biomedical waste disposal activities. Experiments were conducted against real water sources (canal, groundwater, and tap water) collected from local regions to further validate the efficacy of the method. A distinct strain-specific disinfection potential of AgNPs/chitosan–PVA hydrogel was observed under various test conditions. Minimum leaching of silver from the hydrogel indicated its potential safety towards the environment, apart from achieving 100% disinfection after every use. AgNPs immobilized over the hydrogel further prevented biofilm formation. The AgNP-laden hydrogel could completely disinfect three environmental samples river water, ground water and tap water under real conditions without manipulating their inherent water quality parameters and microbial communities.

2. Materials and methods

2.1 Materials required

Chitosan (>99% pure, 85% deacetylated, MW 100–300 kD) was procured from Nano Wings Pvt. Ltd., Telangana, India. Silver nitrate, sodium borohydride, and phosphate buffer solution (PBS) were obtained from Sigma Aldrich Pvt. Ltd., USA, while polyvinyl alcohol (PVA, MW 85–124 kD) was purchased from HiMedia Pvt. Ltd., India. Sodium hydroxide pellets were obtained from SD Fine Chemicals Ltd. Acetic acid, glutaraldehyde (25% v/v, >98% purity), and ethanol were purchased from Merck Life Science Pvt. Ltd., India. All other solvents were obtained from Loba Chemie Pvt. Ltd., Mumbai, India and used as received. For antibacterial experiments, non-pathogenic strains of *E. coli* MTCC 739 (ATCC 10536) were procured from Microbial Type Culture Collection and Gene Bank, CSIR-IMTECH, Chandigarh (India), while *E. aerogenes* NCIM 5139 (ATCC 13048), *S. aureus* NCIM 2127 (ATCC 9144), and *S. epidermidis* NCIM 2493 (ATCC 12228) were procured from National Collection of Industrial Microorganisms (CSIR-NCL, Pune, India) as stock

 This journal is © The Royal Society of Chemistry 2020

cultures. All the experiments were conducted using either deionized (for nanoparticle synthesis) or double distilled (for disinfection studies) water. The disinfection experiments were also done in water samples from natural sources without any purification steps at their natural microbial contaminants level and spiked externally with the aforementioned strains at $\sim 10^3$–10^4 CFU mL^{-1} as the initial cell concentration.

2.2 Synthesis of nano-Ag loaded chitosan–PVA hydrogels

As described earlier,[19] a 2% w/v chitosan suspension was prepared in 2% v/v acetic acid solution while stirring overnight at 40 °C. A clear chitosan solution, devoid of any insoluble impurities, was obtained through centrifugation and filtration. Similarly, a 4% w/v PVA solution was prepared in distilled water at 90 °C under vigorous stirring for 4 h. Chitosan and PVA solutions were added in equal ratios (1 : 1) in a beaker and stirred at 60 °C initially for 2 h and then at 25 °C over the next 12 h to obtain a homogeneous blend suspension. To this solution, 100 μL 25% v/v glutaraldehyde was added dropwise under constant stirring at 25 °C. The solution was then casted in test tubes/Petri plates and cured at 45 °C in a hot air oven for gelation. The formed hydrogels were removed from the molds through precipitation with 12% w/v NaOH solution at room temperature for 8 h. The hydrogels were then washed repeatedly with distilled water to remove the residual alkali. The hydrogels were subjected to five repeated freeze/thaw cycles, with each cycle comprising of a freezing step (16 h at −20 °C), followed by a thawing step (3 h at 25 °C) to develop porous network structures within the hydrogel system.

The hydrogel was sliced into cylindrical discs (10 mm × 6 mm) and introduced into a vial containing 10 mM $AgNO_3$ aq. solution for one day under dark conditions. After the required incubation, the discs were washed thrice with DI water to remove any unbound silver ions. The Ag^+ loaded hydrogels were immersed in 10 mM $NaBH_4$ solution for 10 min for carrying out the reduction of silver ions to AgNPs. These hydrogel discs were again rinsed with DI water, dried under vacuum, and sealed in plastic bags till further use. The chitosan–PVA hydrogel discs with loaded silver nanoparticles is designated as Ag/CS–PVA hydrogel in later sections.

2.3 Material characterization

The optical spectra of the hydrogel films were recorded on a UV-vis spectrometer (Shimadzu 2600, Japan) with a diffuse reflectance accessory over the 200–600 nm wavelength range in triplicate. Fourier-transform infrared spectroscopic (FTIR, Nicolet 380 Thermo Fisher, USA) analyses were carried out in the 500–4000 cm^{-1} range after lyophilizing the samples for 48 h so as to remove all the moisture/adsorbed water vapors and their characteristic peaks were compared. The thermal degradation studies were done using differential scanning calorimetry (DSC 131 evo, SETARAM Instrumentation, France). For this, the lyophilized specimens were analyzed at a heating/cooling rate of 20 K min^{-1} under N_2 atmosphere. The surface morphology of pristine and Ag/CS–PVA hydrogels was compared using a field emission scanning electron microscope (FE-SEM, Hitachi SU-8010, Japan). A thin specimen of the hydrogel samples was sputtered with gold and pasted over the sample stubs using a carbon tape. Elemental analyses and the composition of the hydrogel samples were also investigated through energy-dispersive X-ray spectroscopy (EDX). The mechanical performance of the hydrogels, before and after immobilizing the AgNPs, was determined using a dynamic mechanical analyzer (DMA RSA3, TA instruments, USA) in their swollen state with a crosshead speed of 3 mm min^{-1} at room temperature (25 °C). At least three specimens with similar dimensions (15 mm × 10 mm × 0.15 mm) were tested for each set of hydrogels.

2.4 Swelling studies

The initial dry weight of the lyophilized hydrogel discs (10 mm diameter) was calculated and designated as W_1. The hydrogels were then soaked in distilled water at 25 °C and the swollen weight (W_2) of the corresponding hydrogel discs was determined at regular time interval over a span of 2 h after wiping the surface. The swelling ratio (S%) is defined as the ratio of the water content retained within the swollen hydrogel ($W_2 - W_1$) to its initial dry weight (W_1). The impact of temperature on the swelling studies was also evaluated for the Ag/CS–PVA hydrogel over a broad range from 15–45 °C by following eqn (1).

$$S(\%) = \frac{W_2 - W_1}{W_1} \times 100 \quad (1)$$

2.5 Strain specific disinfection and reusability studies

The antibacterial activity of the as-synthesized pristine and Ag/CS–PVA hydrogels was primarily tested in both solid and liquid medium through disc diffusion and viable cell count methods, respectively, against four bacterial strains, namely, *E. coli*, *E. aerogenes*, *S. aureus*, and *S. epidermidis*. In the disc diffusion method, nutrient agar plates were spread with 100 μL of the chosen microbial solution having a count of $\sim 10^6$–10^7 CFU mL^{-1}. The sample discs were then placed on the surface of the inoculated agar plates and kept at 37 °C in an incubation chamber. The experiments were performed in duplicate and the diameters of the inhibition zones were measured after 18–20 h of incubation.

Quantitative assays for determining bacterial killing were performed by adopting the standard pour plate culture method. Briefly, sterilized flasks containing the nutrient media were inoculated with 10 μL of the repeatedly sub-cultured microbial strain and kept in a rotary shaker at 37 °C at 120 rpm for 14–16 h. At the end of the log phase of microbial growth, the grown cultures were isolated in pellets through centrifugation, washed thrice, and resuspended in PBS. The disinfection studies were performed at a fixed

initial bacterial concentration (N_0 = 10^3–10^5 CFU mL^{-1}) of each strain, diluting their respective harvested suspension (1×10^9 CFU mL^{-1}) through optical density measurements using a spectrophotometer. For instance, the hydrogel discs were introduced into the flasks with $\sim 10^3$ CFU mL^{-1} microbial contamination (diameter 10 mm, pristine and Ag-loaded), incubated at 37 °C, 120 rpm in a rotary shaker; aliquots were withdrawn from the flasks at stipulated time intervals (0, 15, 30, 60, 90, 120, and 240 minutes) and plated on agar plates. The numbers of viable bacterial colonies were counted in triplicate after incubating for a period of 18–24 h.

The long-term affordability of the Ag-loaded CS/PVA hydrogel was tested by evaluating its disinfection potential over multiple uses. For this, hydrogel discs (15 mm × 10 mm) were immersed in a 100 mL batch reactor having 10^3 CFU mL^{-1} microbial suspension for a period of 4 h. After the required incubation, the hydrogels were immediately removed from the microbial suspension, washed with deionized water, and completely dried (nitrogen purging) so as to prepare it for next use. Similar experiments were repeated over 10 similar cycles by incubating the same hydrogel disc and the corresponding residual antibacterial activities (R_{ab}%) were estimated (eqn (2)). The disinfection efficacy of the Ag/CS–PVA hydrogel was tested separately against two microbes, namely, *E. coli* and *S. aureus*.

$$R_{ab}\% = \left(\frac{N_0 - N_t}{N_0}\right) \times 100 \quad (2)$$

where, N_0 = initial viable counts; N_t = viable counts after the completion of each cycle.

2.6 Biofilm assays

Pre-grown cultures of both *E. coli* and *S. aureus* were diluted in the 1 : 100 ratio in a freshly prepared LB media and assayed separately. The CS–PVA hydrogel films (pristine and AgNPs loaded) were introduced in each well containing 100 μL of the diluted bacterial suspension in a 96-well micro-titer plate and were incubated at 37 °C for 48 h. The wells containing only the unsterilized media (*i.e.*, devoid of both microbes and hydrogel) were taken as negative controls, while bacteria inoculated media without any hydrogel were taken as the positive control. After the required time period, the media were removed and the cells were thoroughly washed with 1× PBS buffer under brisk shaking so as to remove the possible planktonic bacteria, if they remain in each well of the microtiter plate. 125 μL 0.1% (w/v) crystal violet dye was then added to all the wells and stained for 20 min at room temperature. Excess crystal violet was removed by washing with 1× PBS twice under vigorous shaking and was allowed to dry in air. For quantification of the adherent cells, cell-bound crystal violet was dissolved in the respective solvents (200 μL 30% acetic acid for *S. aureus*; 80% ethanol for *E. coli*), as specified earlier[33] by covering the plates and incubated for 10–15 min at room temperature. The biofilm growth of both the species was finally monitored at 570 nm using a micro plate reader (BioRad, USA). All the data are expressed as the mean ± standard deviation (SD) of the triplicate experimental data. A two-tailed Student's *t*-test was used to determine the differences in the biofilm formation between the control and each group. The P value of <0.005 was taken as significant.

3. Results and discussion

The schematic representation of synthesizing chitosan–PVA hydrogel is shown in Fig. 1. With repeated freeze–thaw treatments, a porous network structure was developed on the precipitated chitosan–PVA (CS–PVA) hydrogel, as is evident from change in the colour of the hydrogel from golden yellow to opaque yellow (Fig. S1, ESI†). An *in situ* approach was employed for immobilizing AgNPs, where most of the silver ions from the solution were anchored on to hydrogel network through ion-exchange mechanism while remaining silver ions were occupied within the semi-interpenetrating network of the CS–PVA hydrogel. The amine and hydroxyl functional moieties naturally present within the CS/PVA hydrogel acted as nucleation sites that allowed stable anchoring of silver ions, which were progressively reduced into AgNPs through a suitable reducing agent.[19] The yellow color hydrogel turned into brownish black, indicating the *in situ* formation of AgNPs, which were subsequently immobilized within the porous hydrogel network of the hydrogel (Fig. S1c, ESI†). The polymeric network of CS–PVA thus served a dual role, both as a reactor for synthesizing AgNPs along with providing a template for their subsequent immobilization.

3.1 Characterization of the Ag/chitosan–PVA hydrogel

The *in situ* immobilization of AgNPs on to the CS–PVA hydrogel was evaluated through diffuse reflectance spectroscopy (Fig. 2a). It is evident that while the AgNP-immobilized hydrogel displayed a distinct surface plasmon resonance at 421 nm, which confirmed the successful loading of nano-silver, no such extinction peak was observed in pristine CS–PVA hydrogel. A full width at half maximum (FWHM) value of 122 indicated that silver would have uniformly distributed throughout the surface of the CS–PVA hydrogel in its nanoparticulate form. Further, the stability of the Ag/CS–PVA hydrogel was evaluated over a period of five months where no significant variation in its original SPR or FWHM value was observed.

The FTIR spectra of chitosan–PVA hydrogel before and after immobilizing AgNPs were also compared (Fig. 2b). An absorption peak at 3280 cm^{-1} corresponds to the characteristic OH and/or NH stretching vibrations, which appeared in both the variants of CS–PVA hydrogel due to intermolecular hydrogen bonding between the two polymeric residues. Besides, a new vibrational band that appeared at 3450 cm^{-1} in the Ag/CS–PVA hydrogel confirms that AgNPs were firmly bonded to the hierarchical network of the CS–PVA hydrogel during their synthesis and growth stages.

 This journal is © The Royal Society of Chemistry 2020

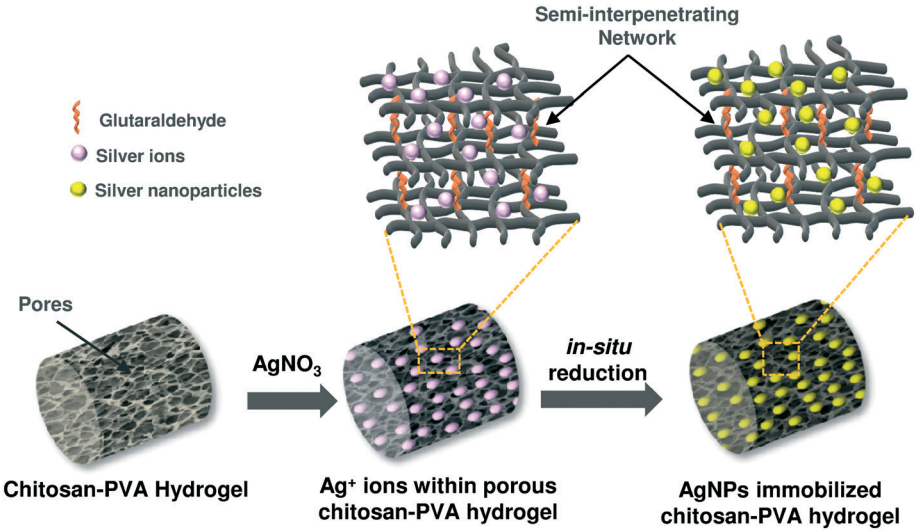

Fig. 1 Schematic representation of chitosan–PVA hydrogel acting as nano reactor for synthesizing silver nanoparticles and their subsequent immobilization within the semi interpenetrating network of hydrogel.

Similarly, a few other characteristic peaks at 2925 cm^{-1} (CH stretching), 1453 cm^{-1} (CH bending), and 1323 cm^{-1} (CN stretching) appeared in both the hydrogel forms and remain unaltered even after loading AgNPs. Interestingly, a peak at 1674 cm^{-1} in pristine chitosan–PVA, attributed to carbonyl (–C═O) bond stretching,[34] not only appeared with reduced intensity in the Ag/CS–PVA hydrogel but also shifted to a lower frequency, *i.e.*, 1638 cm^{-1}. This clearly indicates that although there exists a stronger intermolecular interaction between hydroxyl groups of PVA and hydroxyl/amine groups of chitosan while forming the hydrogel, many free –OH and $–NH_2$ moieties would still be available as nucleation sites to Ag^+ ions for *in situ* synthesis of AgNPs and concurrently, their immobilization. It is worth noting that the absorption band at ~1100 cm^{-1}, referring to crystallization sensitive peak of PVA, appeared in both pristine and Ag/CS–PVA hydrogels with the same intensity. This validates that the incorporation of AgNPs did not alter the overall crystallinity of PVA in the blend polymer.

The dried hydrogels were investigated using differential scanning calorimetry to determine their miscibility and water retention characteristics (Fig. 2c). The thermogram profile of pure chitosan exhibited a typical dissociation peak at 150 °C, which noticeably reduced to 144 °C after blending with PVA. This was a clear indication of the strong hydrogen-bonding between chitosan and PVA polymeric residues. In contrast, immobilizing AgNPs on to the CS–PVA hydrogel resulted in a significant loss in thermal characteristics (dissociation peak 80 °C), which occurred due to the reduced chances of interaction among water moieties and polymeric chains in the presence of AgNPs. Nevertheless, a good miscibility between AgNPs and CS–PVA blend composites were in good agreement with our previous study[19] where the incorporation of the nanoparticles reduced the overall hydrophilicity of the nanocomposite hydrogel.

The optical characteristics corroborated with the FE-SEM analyses, wherein the hydrogel nanocomposites depicted a distinct variation in surface topography after immobilizing AgNPs (Fig. 2d and e). The *in situ* immobilized AgNPs existed in the aggregated form, uniformly distributed over the entire surface of CS–PVA with a high density (15.8% by weight), as depicted through EDX analyses. The characteristic peaks of carbon (C), sodium (Na), and oxygen (O) elements appeared due to the chitosan/PVA polymeric blend and a peak at ~2.93 keV further validated the existence of silver as AgNPs. It is clear that such a uniform dispersion of AgNPs did not affect the overall structural integrity of the CS–PVA hydrogel and yielded a stable intercalation of AgNPs within their semi-interpenetrating network.

A hydrogel-based system employed for water purification purposes should possess both strong and flexible characteristics so as to be able to bear harsh processing conditions with the required durability. A preliminary validation of the improved mechanical performance of the Ag/CS–PVA hydrogel was noticed when it could withstand a load up to 50 g and regained its original shape without any deformation (Fig. 2f). We further evaluated the mechanical properties of the CS–PVA hydrogel blends before and after immobilizing the AgNPs using tensile-compression tests (Fig. 2g). The Young's modulus of rigidity and % elongation at break were selected as the two mechanical parameters for comparing the rigidity/hardness and flexibility of the hydrogels, respectively. The hydrogel exhibited an extraordinary self-recovery and fatigue resistance ability, where the value of Young's modulus was marginally improved after immobilizing AgNPs (12.36 ± 0.29 MPa) compared to its pure form (10.52 ± 0.56 MPa). This indicated that a homogenous reinforcement of AgNPs within the hydrogel network could behave cooperatively to dissipate the energy while distributing the external stress and thus could effectively restore its structural integrity.[35]

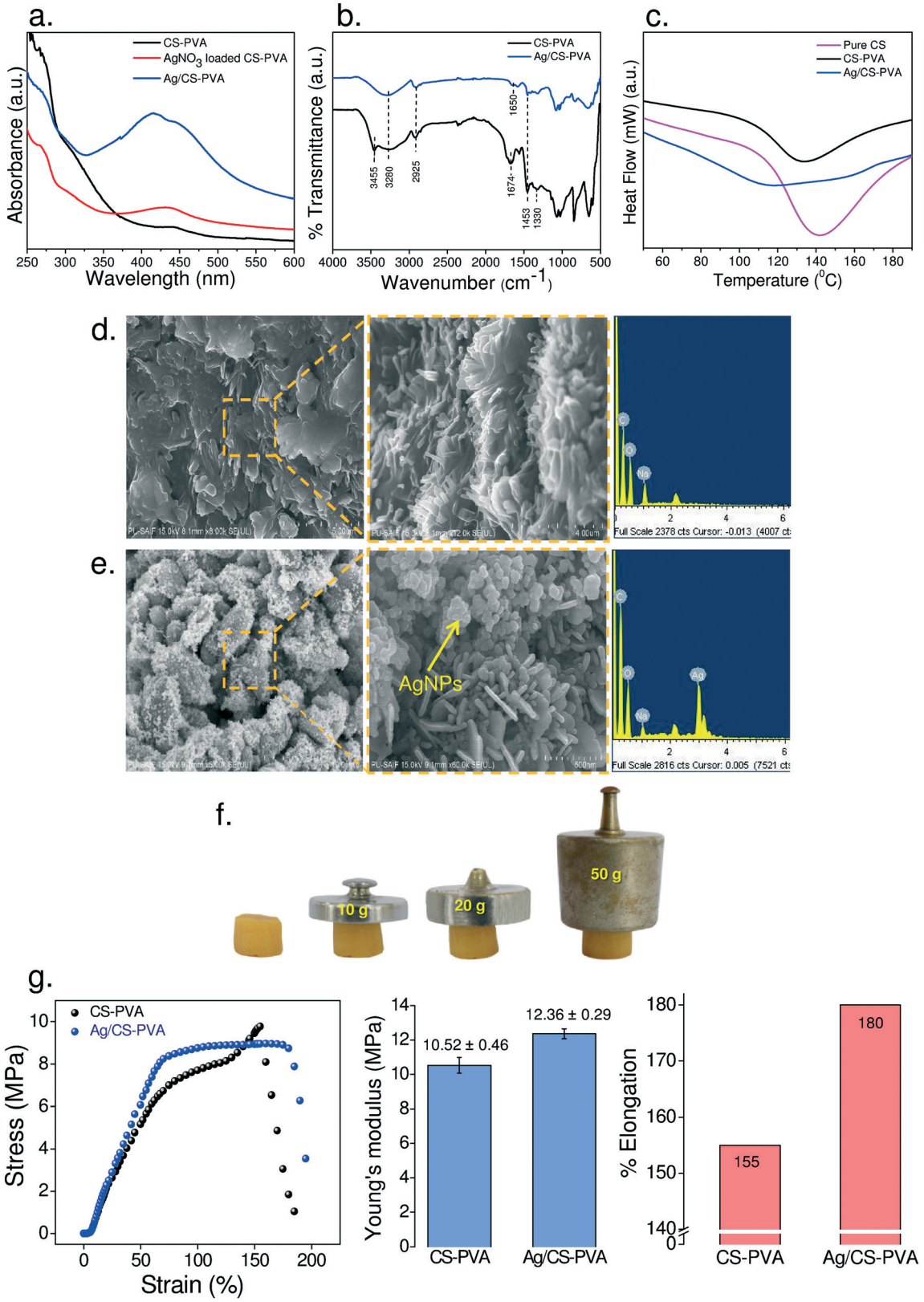

Fig. 2 Characterization of pristine, ionic silver and nano-Ag loaded CS–PVA hydrogels through (a) diffuse reflectance spectroscopy (b) FTIR (c) differential scanning calorimetry. Through SEM micrographs, the two hydrogel forms *i.e.* (d) pristine and (e) *in situ* synthesized AgNPs showed surface morphology distinctions as a result of localized, dense immobilization of nano-silver. The mechanical performance of Ag/CS–PVA hydrogel was evaluated through (f) its load-bearing capacity up to 50 g and regaining the original shape without any noticeable deformation and (g) compressive tensile strength curves, depicting Young's modulus of rigidity (MPa) and elongation at break (%) as compared to its pristine form (CS–PVA). The error bars represent standard error (±SE); sample size n = 3.

This journal is © The Royal Society of Chemistry 2020

In addition, the elongation at break (%) values of the pure and Ag/CS–PVA hydrogels were obtained as 155% and 180%, respectively, which could be ascribed to a higher flexibility of the inter-twined polymeric network within the hydrogel after immobilizing AgNPs. We evidenced a unique combination of high compressive strength and elasticity at the same time in the Ag/CS–PVA hydrogel. This unusual behavior could be explained by a unique property of the AgNPs, which might act as a cross-linker between polymeric chains of the hydrogel, if suitably dispersed.[36,37] Unlike the organic cross-linkers, the silver nanoparticles can crosslink both the short and long polymeric chains to a much greater extent owing to their higher surface area/volume ratio and thus could effectively restrain the mechanical deformation of the hydrogel under external stimuli. A recent few studies[36–38] have also demonstrated similar features in hybrid nano-polymeric gels, wherein the presence of two or more polymeric chains with varying chain lengths effectively distributed the stress in the entire system, thus contributing towards high compressive toughness concomitantly with maintaining the elasticity of their network.

The results of the time-dependent and temperature-dependent swelling kinetics are summarized in Fig. 3. Both pristine and Ag/CS–PVA hydrogels swelled rapidly and attained maximum swelling within 60 min under the tested conditions (25 °C, pH 7). The swelling behavior of both the hydrogel forms indicated that it could carry a large volume of water while maintaining its structural integrity and strength. The Ag/CS–PVA hydrogel demonstrated a remarkable reduction in the swelling capacity (52.5 ± 3.6%) than its pristine form (67.2 ± 3.9%). This could be ascribed to the reduction in the surface functional-moieties of CS–PVA polymer after incorporating AgNPs, which became less available for water molecules to form stable hydrogen bonding such that the diffusion of water inside the hydrogel was critically hindered. The temperature-dependent swelling kinetics of the Ag/CS–PVA hydrogel was also evaluated at pH 7 under a broad temperature range (15–45 °C), typically manifested within the Indian subcontinent in a year (Fig. 3b). The results indicate that the swelling ratios increased with increasing temperature in both the hydrogel variants. In particular, Ag/CS–PVA hydrogels exhibited a temperature-responsive swelling behaviour due to the reversible association/dissociation of hydrogen bonds within the semi-interpenetrating networks.

3.2 Disinfection studies of the nano-silver loaded chitosan–PVA hydrogel

The biocidal effects of the Ag/CS–PVA hydrogels were primarily tested against four bacterial strains with diverse pathogenicity in solid agar medium. As reported earlier,[14,19] the antibacterial activity of the Ag/CS–PVA hydrogel was compared with its pristine form using disc diffusion methods (Fig. 4a) and the data is summarized in Table S1, ESI.† It is evident that the pure CS–PVA hydrogel did not elicit any visible zone of inhibition (ZoI) and even the presence of chitosan having inherent antimicrobial characteristics could not contribute towards the biocidal activity. On the contrary, the Ag/CS–PVA hydrogel showed a distinct antibacterial activity against all the four tested microorganisms, exhibiting ZoI ranging from 13 to 21 mm. A clear ZoI in the solid agar media is indicative of the mobility of Ag^{+}/AgNPs from the hydrogel in an amount sufficient to inhibit the growth of microbes present in the surrounding regions. Out of the selected strains, *E. coli* and *S. epidermidis* appeared to be the least and most sensitive bacterial species against the Ag-reinforced hydrogel, respectively.

The disinfection performance of the hydrogels was further evaluated in a liquid medium at a fixed initial bacterial concentration of 10^3 CFU mL^{-1} in a 100 mL batch reactor (Fig. 4b–e). Regardless of the strain type, Ag/CS–PVA hydrogel appeared to be bactericidal against all microbial species and achieved 100% disinfection within 2–3 h (Fig. S2, ESI†). On the other hand, although pristine CS–PVA hydrogel manifested a variable bacterial killing (%) against similar species, it could not achieve complete disinfection even after 4 h under similar test conditions (Fig. 4f and S3, ESI†). Interestingly, Ag/CS–PVA hydrogel elicited a distinct strain-specific disinfection potential on the basis of the 'extent of disinfection' (*i.e.*, time to achieve complete disinfection)

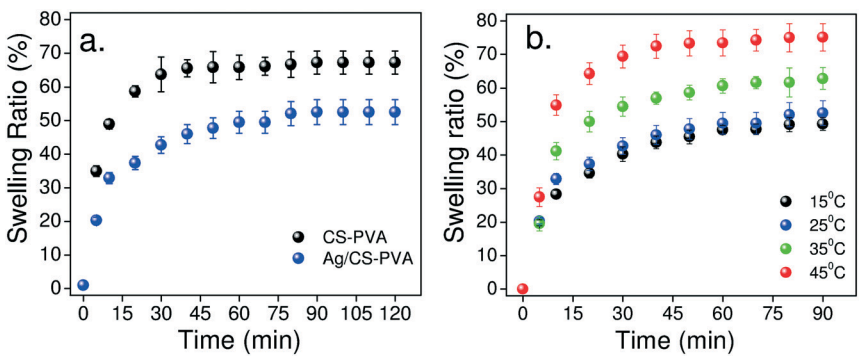

Fig. 3 (a) Dynamic swelling behaviour of two hydrogel variants under ambient conditions (20% relative humidity, pH 7, 25 °C) and (b) temperature dependent swelling kinetics of Ag-loaded chitosan–PVA hydrogel at wide temperature range typically manifested in Indian subcontinent.

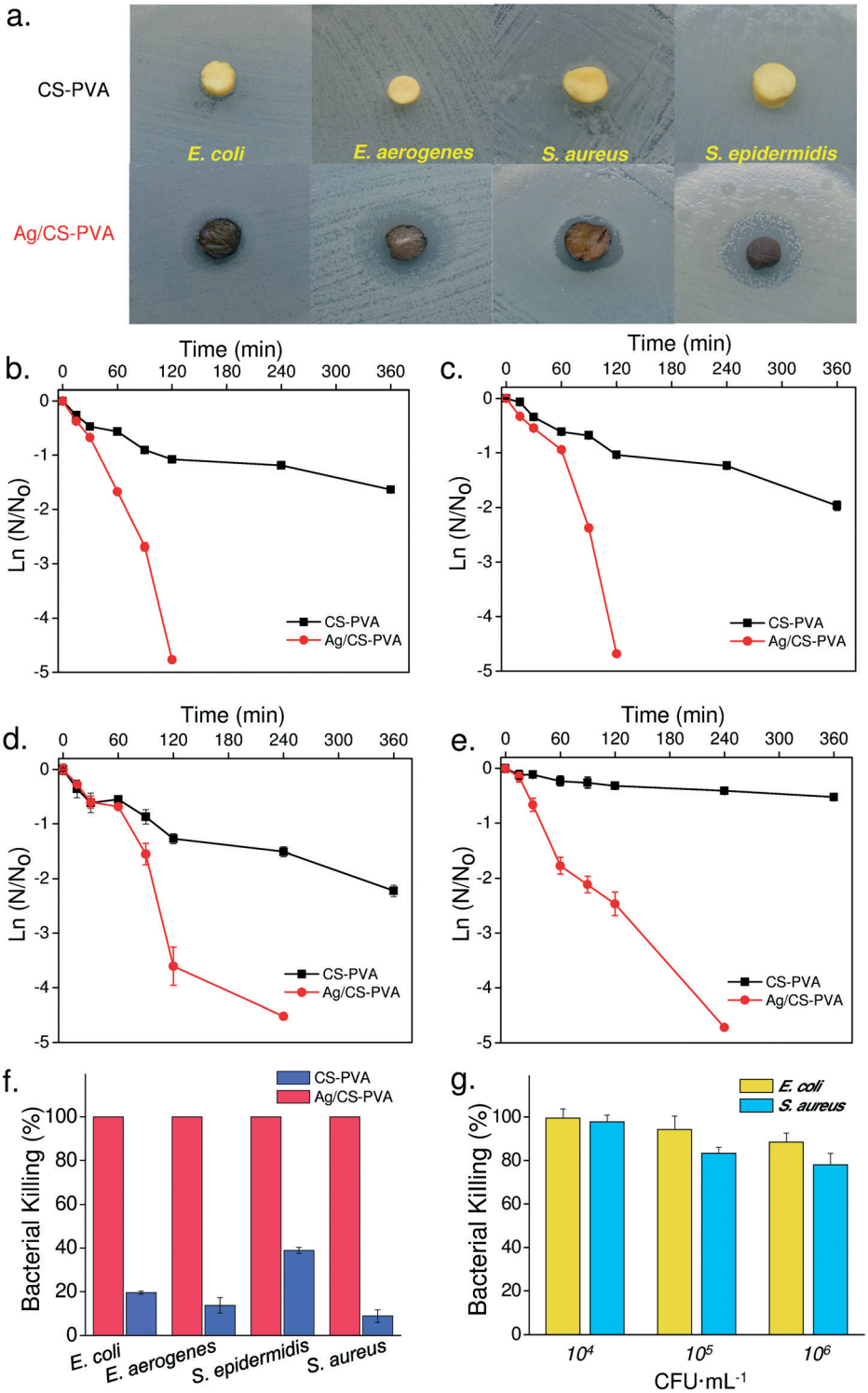

Fig. 4 (a) Disc diffusion tests for comparing the antibacterial activity of hydrogel before and after immobilizing silver nanoparticles (Ag/CS–PVA) in solid media. The strain-specific disinfection potential of hydrogels was evaluated in liquid suspension against four strains (b) *E. coli* MTCC 739 (c) *E. aerogenes* NCIM 5139 (d) *S. aureus* NCIM 2127 and (e) *S. epidermidis* NCIM 2493 as representatives for water and biomedical contamination. (f) A comparative disinfection ability of hydrogels was tested under ambient physico-chemical conditions (g). The disinfection performance of Ag-loaded CS–PVA hydrogel was evaluated at higher initial bacterial concentration (10^4–10^6 CFU ml^{-1}) against *E. coli* and *S. aureus*.

where the susceptibility of various bacterial species followed the order: *E. coli* ~ *E. aerogenes* > *S. aureus* > *S. epidermidis*. Comparing all bacterial strains, Ag/CS–PVA hydrogel appeared to be more effective against natural water contaminants, *i.e.*, *E. coli* and *E. aerogenes* but it was equally biocidal towards the bacterial species associated with

 This journal is © The Royal Society of Chemistry 2020

biomedical infections, *i.e.*, *S. aureus* and *S. epidermidis* with a marginal delay of 60 min in the extent of disinfection. Even at a higher bacterial concentration (10^4–10^6 CFU mL^{-1}), >90% microbial killing could be achieved against *E. coli* using Ag/CS–PVA hydrogel and ~80% *S. aureus* cells were inhibited at similar initial bacterial counts (Fig. 4g). Although similar extent of disinfection could be achieved within 120 min against *E. coli* and *S. aureus*, it was prolonged to 4 h for both *S. aureus* and *S. aureus* microbial strains. These results, therefore, suggest the excellent disinfection performance of the Ag/CS–PVA hydrogel for a wide range of bacterial populations.

3.3 Reuse potential of the hydrogel

The capacity to reuse a hydrogel is an important feature to claim its sustainable affordability in water disinfection purposes. As shown in Fig. 5a, Ag/CS–PVA hydrogel could retain ≥99.5% of its biocidal activity against *E. coli* after 8 repeated uses, which was marginally reduced to ~92% after the next two cycles. The Ag-loaded hydrogel appeared to be less effective against *S. aureus*, where the residual activity of the hydrogel was progressively reduced after every use. The disinfection performance of the hydrogel at 6th usage attained its threshold value, after which the biocidal activity sharply declined to ~32%. At first instance, a higher retention of the antibacterial activity of the hydrogels against Gram-negative bacteria (*E. coli*) than Gram-positive bacteria (*S. aureus*) appeared to be the result of their strain-selective biocidal performance. However, a thorough analysis justifying the variation in the disinfection performance against different strains may provide some useful insights about the mechanism of bactericidal action of the hydrogel during disinfection.

It is well known that the presence of the peptidoglycan layer on the cell wall of *S. aureus* makes them more resistant to harsh environments, toxins, chemicals, and even antibacterial agents, as compared to *E. coli* cells.[20] Moreover, *S. aureus* belong to sessile, adherent microbial communities that rapidly form multilayer biofilm virtually over all surfaces, thus making them resistant towards contact-active antibacterial action.[7] We also speculated that after 6 repeated uses, the formation of a similar stagnant biofilm of *S. aureus* over the hydrogel could be the responsible cause for the reduction in its biocidal activity. Possibly, the establishment of the *S. aureus* biofilm could adversely affect the outer exposed surface of the porous hydrogel such that water along with microbial contaminants could not get diffused in the interior of the hydrogel causing a lower direct-contact between *S. aureus* and the immobilized AgNPs. Such results are in agreement with our recent study,[10] wherein immobilized AgNPs over silica surfaces have shown a significant reduction in the disinfection performance.

3.4 Silver release and mechanism of action of disinfection

The practical viability of silver nanocomposites for potable water applications is greatly linked to the extent of release of silver into aqueous systems. Due to its adverse eco-toxicological effects, we analyzed the silver content of treated water in two different conditions: first when incubated in aqueous environment over a longer period of time (Fig. S4, ESI†) and second, after every reuse (Fig. 5b). The total amount of silver content in the Ag/CS–PVA hydrogel was measured to be 9.47 mg g^{-1} hydrogel through ICP-AES. As predicted, the release characteristics of the hydrogel exposed for long duration (up to 7 days) to deionized water indicated a strong anchoring of the *in situ* synthesized AgNPs within the hydrogel networks, wherein the amount of silver released was determined to be 0.08 ± 0.01% and 0.41 ± 0.07% of the total loaded Ag after the 2nd and 7th day of incubation, respectively (Fig. S4, ESI†). Further, we evaluated the corresponding silver release from the hydrogel after each reuse. The maximum amount of silver in the effluent was measured to be 74.3 ± 4.2 ppb after 10th use, which falls below the permissible limit of Ag in drinking water (100 ppb) as per USEPA and WHO guidelines.[39] Although the amount of Ag released in the suspension increased after every use,

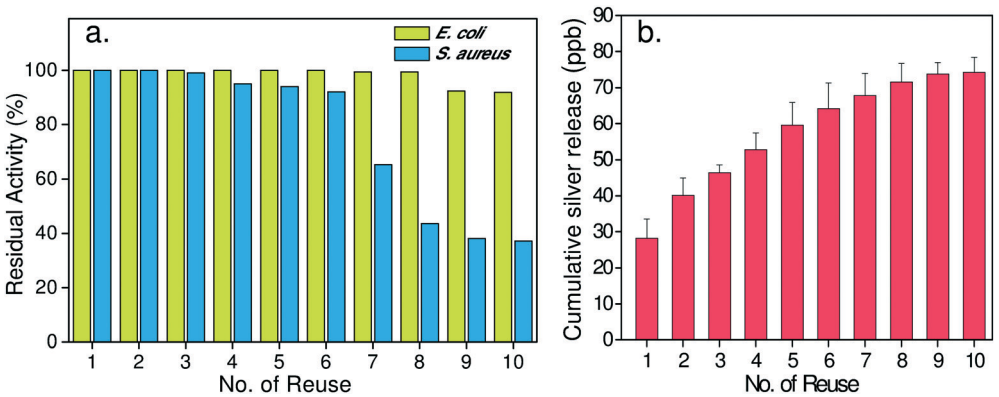

Fig. 5 (a) The disinfection potential of Ag-loaded chitosan–PVA hydrogel on multiple reuses was determined over 10 cycles against *E. coli* and *S. aureus* as representatives of water and biomedical contaminants, respectively. (b) Corresponding silver release profile was investigated under identical conditions in deionized water, devoid of any contaminants.

the rate of silver release profile was progressively reduced after repeated usage and reached a plateau after 8th reuse.

We hypothesize that silver release kinetics is mediated *via* a two-step process involving the oxidative dissolution of immobilized AgNPs under ambient conditions. First, a rapid diffusion of water inside the porous hydrogel inevitably facilitates reaction between the surface exposed silver atoms (Ag^0 as AgNPs) with dissolved oxygen. This results in the formation of silver(I) oxide, Ag_2O layer as surface passivation over the AgNPs at sub-nanoscale level. The silver oxide layer acts as a reservoir of silver ions, which get released into the system till the oxidative dissolution of Ag_2O continues, as shown below:

$$4Ag_{(s)}^{0} + O_{2(aq)} \xrightarrow{\text{Oxidation}} 2Ag_2O_{(s)} \quad (3)$$

$$2Ag_2O_{(s)} + 4H_3O_{(aq)}^{+} \xrightarrow{\text{Dissolution}} 4Ag_{(aq)}^{+} + 6H_2O_{(aq)} \quad (4)$$

Therefore, an overall high rate of release of silver during the early stages of the hydrogel use can be explained through diffusion-limited process, in which AgNPs lying at the surface of the hydrogel were preferentially solvated due to the short-diffusion pathways. It is imperative that water diffusion within the interiors of the hydrogel networks was adversely affected upon repeated usage. This might result in an increasingly tortuous pathway for water molecules to reach the rest of the deeply buried AgNPs and carrying their oxidative dissolution. As a result, water molecules would be slowly-diffused inside the more compact, denser regions of polymeric hydrogel and elicited a reduced rate of silver release in subsequent use, as evidenced in this study.

The silver-release profile suggested a strong AgNP retention capacity of the CS–PVA hydrogel, wherein silver leaching from hydrogel either in the form of silver ions/nanoparticles or both could not solely dictate its disinfection potential. In fact, the presence of the hierarchical macroporous structure of the hydrogel appeared to be conducive for higher uptake of the microbial cells owing to its large surface area and confined environment.[40] Moreover, an extremely slow oxidative dissolution of immobilized AgNPs contributed to maintain a highly-localized antimicrobial environment within the porous hydrogel, wherein the microbial cells get 'trapped and killed' instantly. Our reusability study supported these observations wherein a decline in the disinfection potential was observed after each reuse, which could be possible only in the case with a lower surface area available for direct contact with the microbial cells and hence, elicited a diminished biocidal response (Fig. 5a). Further, correlating the disinfection profile and silver release kinetics on repeated usage also suggested that the extent of disinfection remained unaffected by varying silver release into the system. This surface-dependent disinfection performance of the Ag/CS–PVA hydrogel appeared to be highly effective as compared to other routinely claimed mechanisms of AgNPs, such as the release of silver ions and reactive oxygen species (ROS) generation.[23] A recent few studies from various research groups[8–10,40–42] have proven that the surface immobilized AgNPs perform more effectively in water disinfection due to their predominant contact-active role of 'capture and kill' compared to the contribution of Ag release, even if it occurs to an amount that is just sufficient to elicit biocidal effects. All these findings provide compelling evidences to elucidate the mechanism of disinfection of the Ag/CS–PVA hydrogel, which is predominantly contact-killing driven.[43,44]

3.5 Anti-biofilm activities of the hydrogel

The inherent characteristics of drinking water systems (DWS) in urban communities may sometimes make the conditions favorable for a few opportunistic microbes to grow, attach, and eventually form a biofilm.[45] This situation becomes even worse if the DWS gets contaminated with healthcare-associated microbes due to the unsafe disposal of biomedical waste. These contaminants may enter the drinking water supplies either through broken pipelines at nearby waste dumping sites or the leaching of microbes in the surrounding environment. Under such water quality conditions, faecal contaminants persist longer in DWS and become resilient towards conventional disinfectants using the attached biofilm as a shelter for their survival and regrowth.[46]

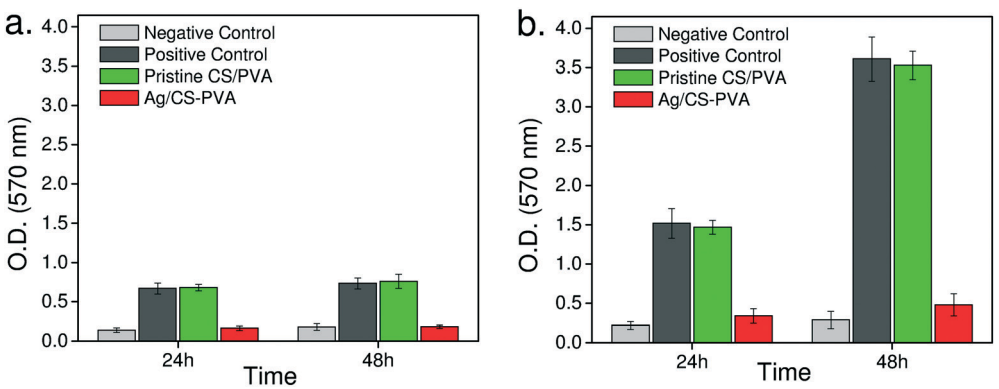

Fig. 6 Anti-biofilm characteristics of pristine and Ag loaded CS–PVA hydrogel against (a) *E. coli* and (b) *S. aureus* over a period of 48 h.

This journal is © The Royal Society of Chemistry 2020

Table 1 Physicochemical characteristics of three water sources in Patiala district, Punjab, India

Characteristics	Water samples		
Water sources	Bhakra canal	Tube well	Urban supply
Water type	River water	Ground water	Tap water
Locations	30.299° N 76.326° E	30.289° N 76.416° E	30.356° N 76.367° E
Odour	Odourless	Odourless	Odourless
pH	7.98 ± 0.11	7.18 ± 0.04	7.45 ± 0.18
Alkalinity (mg L^{-1} as $CaCO_3$)	98	327	292
TDS (mg L^{-1})	138	448	500
TSS (mg L^{-1})	10	12	16
BOD (mg L^{-1})	<5	<5	<5
COD (mg L^{-1})	<5	<5	<5
Total hardness (mg L^{-1} as $CaCO_3$)	56.4	332	227
Microbial colony counts (CFU mL^{-1})	240 ± 11	55 ± 7	255 ± 31

Henceforth, we investigated the ability of the CS–PVA hydrogel to inhibit the biofilm formation of two bacterial strains, *E. coli* and *S. aureus*, before and after incorporating silver nanoparticles (Fig. 6). In the case with *E. coli*, the Ag/CS–PVA hydrogel depicted 75% reduction in bacterial biofilm as compared to the positive control after 24 h and worked effectively with a similar extent of biofilm inhibition after 48 h as well. Besides, the presence of the chitosan polymer with inherent antimicrobial characteristics could not contribute towards any reduction in bacterial biofilm for pristine CS/PVA hydrogel. With *S. aureus*, the Ag/CS–PVA hydrogel demonstrated ~78% reduction in bacterial biofilm after 24 h and achieved even greater anti-biofilm features (87%) after 48 h, as compared to the positive control. On the contrary, pristine CS–PVA showed an increase in biofilm formation after 48 h. We conclude that a variation in biofilm formation among two different microbial strains did not affect the anti-biofilm characteristics of the Ag/CS–PVA hydrogel. In fact, the Ag/CS–PVA hydrogel impeded biofilm formation of both *E. coli* and *S. aureus* till 48 h and hence, we could predict the disinfection behavior of this hydrogel for natural ecosystem under controlled conditions.

3.6 Disinfection of natural water resources

Very recently, we reported the impact of water quality parameters (alkalinity, hardness, and natural organic matter)

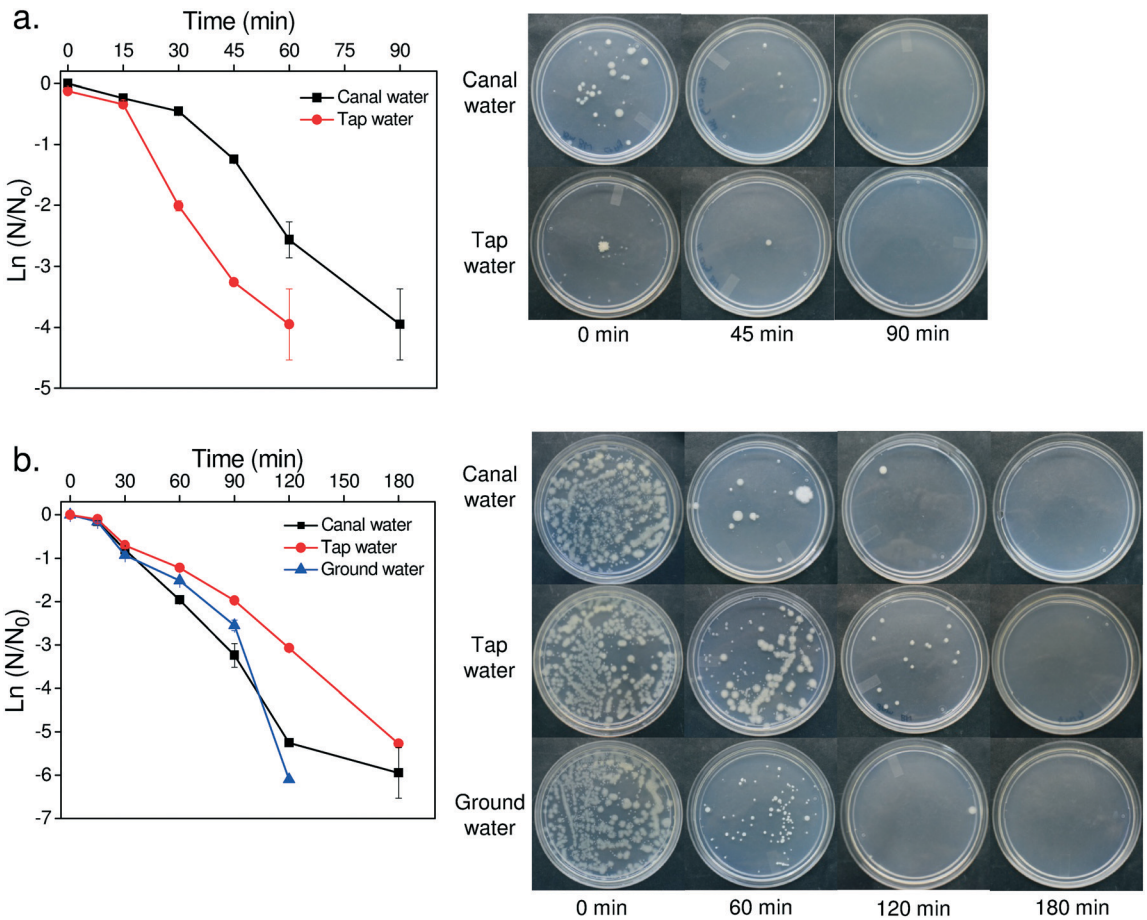

Fig. 7 Disinfection performance of nano-silver loaded chitosan–PVA hydrogel against natural samples *i.e.*, canal water, groundwater and tap water with (a) inherent microbiota and (b) externally spiked contaminants, *S. aureus* tested at 10^3–10^4 CFU ml^{-1}. Corresponding images depict a distinct reduction in bacterial population with the duration of treatment.

on the disinfection performance of immobilized AgNPs for simulated lake water.[10] Herein, we extended our efforts to demonstrate the disinfection efficacy of the Ag/CS–PVA hydrogel in environmental samples systematically collected from three water sources, *i.e.*, Bhakra canal, ground water, and tap water within Patiala district, Punjab, India and their physicochemical parameters are summarized in Table 1. The chosen water samples include vast and complex habitats for diverse microbial communities, wherein groundwater and canal water samples were found to have the least and highest microbial counts, respectively. However, no fecal indicator bacteria and endotoxins were detected in the environmental samples of tap water. The disinfection studies in the environmental samples with intrinsic micro biota depicted complete killing of the contaminants within 60 and 90 min in tap water and canal water, respectively (Fig. 7a). It is imperative that tap water, supplied through municipal supply, is primarily treated with disinfectants and could thus possibly get contaminated during the water distribution process. No disinfection studies were conducted for ground water samples due to the insignificant microbial counts.

Later, a few experiments were conducted for similar water sources with externally spiked *S. aureus* (initial bacterial counts $\sim 10^5$ CFU mL^{-1}), simulating conditions for the leakage of biomedical contaminants into potable water from nearby dumping sites (Fig. 7b). It was observed that the Ag/CS–PVA hydrogel could disinfect all natural water samples with 100% efficacy even at higher initial bacterial counts, where the time to achieve disinfection was observed to be 180 min for canal and/or tap water and 90 min for ground water. It seems that the inherent background chemical conditions of all water samples were responsible for such a variation in the disinfection performance of the Ag/CS–PVA hydrogels. Such results are consistent with the fact that different water resources with variable physicochemical characteristics greatly influence the disinfection efficacy of silver nanocomposites other than just pH and temperature.[10,47]

It is observed that contaminated water supplies from municipal reservoirs, groundwater, canals/lakes, and rivers exhibit various levels of contamination, which may pose serious health risks. However, little is understood about the consequences pertaining to the leakage of biomedical contaminants from waste disposal sites in nearby areas of water reservoirs. These biomedical contaminants are likely to be translocated through sewage and surface runoff and subsequently percolate to aquifers, which are the major sources of washing and irrigation, other than drinking water in India. Since developing countries cannot afford expensive technologies for eradicating or managing biomedical waste, we presented the employability of the Ag/CS–PVA hydrogel as one of the feasible solutions for mitigating biomedical contaminants in natural water systems and improving the potable water quality.

4. Conclusions

The unsafe disposal of biomedical waste along with the presence of inherent contaminants may pose hazardous impacts on the quality of local water bodies. In this work, we could successfully demonstrate the disinfection efficacy of nano-silver loaded chitosan–PVA hydrogel to eradicate biomedical and natural contaminants together, wherein the hierarchical network of the hydrogel acted both as a nanoreactor and an immobilizing matrix for AgNPs. Apart from a rapid, strain-selective biocidal activity of the Ag/CS–PVA hydrogel against four bacterial strains, it also exhibited a good disinfection efficacy over a broad microbial concentration range (10^3–10^6 CFU mL^{-1}) typically manifested in water/wastewater treatments. The fabricated hydrogel is cheap, affordable, and mechanically durable, which can be reused multiple times with a cumulative silver release below 100 ppb, enabling treated water safe for drinking purposes. Correlating disinfection profile and silver release on multiple use, the biocidal action of the hydrogel appeared to be 'contact-active', wherein the hierarchical macroporous structure of the hydrogel enabled a higher uptake of the microbial cells, which get attached and are disrupted instantly when they come in the close vicinity of immobilized AgNPs. A long-term anti-biofilm activity and disinfection efficacy of the Ag/CS–PVA hydrogel without much silver release indicates its long-term employability for practical water treatment purposes and addresses a feasible solution for the complete removal of natural contaminants and nosocomial pathogens simultaneously.

Conflicts of interest

The authors declare that they have no known competing financial interests or personal relationships that could have appeared to influence the work reported in this paper.

Acknowledgements

This work was financially supported through Institute seed grant (TIET/DORSP/57/474, dated 28.03.2017) and DST-SERB, Govt. of India under the project grant YSS/2015/001599 (Engineering Sciences, dated 23.03.2016). NKD is thankful to UGC-Maulana Azad National Fellowship, Govt. of India (201718-MANF-2017-18-PUN-83207) for granting junior research fellowship.

References

1 P. J. J. Alvarez, C. K. Chan, M. Elimelech, N. J. Halas and D. Villagrán, Emerging opportunities for nanotechnology to enhance water security, *Nat. Nanotechnol.*, 2018, **13**, 634–641.

2 F. Yu, X. Ming, Y. Xu, Z. Chen, D. Meng, H. Cheng, Z. Shi, P. Shen and X. Wang, Quasimetallic molybdenum carbide–based flexible polyvinyl alcohol hydrogels for enhancing solar water evaporation, *Adv. Mater. Interfaces*, 2019, **6**, 1901168.

 This journal is © The Royal Society of Chemistry 2020

3 M. S. Mauter, I. Zucker, F. Perreault, J. R. Werber, J.-H. Kim and M. Elimelech, The role of nanotechnology in tackling global water challenges, *Nat. Sustain.*, 2018, **1**, 166–175.

4 S. Agnihotri, D. Sillu, G. Sharma and R. K. Arya, Photocatalytic and antibacterial potential of silver nanoparticles derived from pineapple waste: process optimization and modeling kinetics for dye removal, *Appl. Nanosci.*, 2018, **8**, 2077–2092.

5 A. Chauhan, D. Sillu and S. Agnihotri, Removal of pharmaceutical contaminants in wastewater using nanomaterials: A comprehensive review, *Curr. Drug Metab.*, 2019, **20**, 483–505.

6 D. Jassby, T. Y. Cath and H. Buisson, The role of nanotechnology in industrial water treatment, *Nat. Nanotechnol.*, 2018, **13**, 670–672.

7 N. K. Dhiman, S. Agnihotri and R. Shukla, in *Nanotechnology in Modern Animal Biotechnology*, Springer, 2019, pp. 115–171.

8 S. Agnihotri, G. Bajaj, S. Mukherji and S. Mukherji, Arginine-assisted immobilization of silver nanoparticles on ZnO nanorods: an enhanced and reusable antibacterial substrate without human cell cytotoxicity, *Nanoscale*, 2015, **7**, 7415–7429.

9 S. Agnihotri, S. Mukherji and S. Mukherji, Immobilized silver nanoparticles enhance contact killing and show highest efficacy: elucidation of the mechanism of bactericidal action of silver, *Nanoscale*, 2013, **5**, 7328–7340.

10 S. Agnihotri, S. Mukherji and S. Mukherji, Impact of background water quality on disinfection performance and silver release of immobilized silver nanoparticles: Modeling disinfection kinetics, bactericidal mechanism and aggregation behavior, *Chem. Eng. J.*, 2019, **372**, 684–696.

11 D. Chakraborty, V. Sharma, S. Agnihotri, S. Mukherji and S. Mukherji, Disinfection of water in a batch reactor using chloridized silver surfaces, *J. Water Process. Eng.*, 2017, **16**, 41–49.

12 M. Fan, L. Gong, Y. Huang, D. Wang and Z. Gong, Facile preparation of silver nanoparticle decorated chitosan cryogels for point-of-use water disinfection, *Sci. Total Environ.*, 2018, **613**, 1317–1323.

13 S. Bharti, S. Agnihotri, S. Mukherji and S. Mukherji, Effectiveness of immobilized silver nanoparticles in inactivation of pathogenic bacteria, *J. Environ. Res. Dev.*, 2015, **9**, 849–856.

14 S. Agnihotri, S. Mukherji and S. Mukherji, Size-controlled silver nanoparticles synthesized over the range 5–100 nm using the same protocol and their antibacterial efficacy, *RSC Adv.*, 2014, **4**, 3974–3983.

15 P. Biswas and R. Bandyopadhyaya, Water disinfection using silver nanoparticle impregnated activated carbon: Escherichia coli cell-killing in batch and continuous packed column operation over a long duration, *Water Res.*, 2016, **100**, 105–115.

16 X. Zeng, D. T. McCarthy, A. Deletic and X. Zhang, Silver/reduced graphene oxide hydrogel as novel bactericidal filter for point-of-use water disinfection, *Adv. Funct. Mater.*, 2015, **25**, 4344–4351.

17 Z. Chen, J. Wang, X. Duan, Y. Chu, X. Tan, S. Liu and S. Wang, Facile fabrication of 3D ferrous ion crosslinked graphene oxide hydrogel membranes for excellent water purification, *Environ. Sci.: Nano*, 2019, **6**, 3060–3071.

18 J. Ding, J. Zhang, J. Li, D. Li, C. Xiao, H. Xiao, H. Yang, X. Zhuang and X. Chen, Electrospun polymer biomaterials, *Prog. Polym. Sci.*, 2019, **90**, 1–34.

19 S. Agnihotri, S. Mukherji and S. Mukherji, Antimicrobial chitosan-PVA hydrogel as a nanoreactor and immobilizing matrix for silver nanoparticles, *Appl. Nanosci.*, 2012, **2**, 179–188.

20 S. Agnihotri and N. K. Dhiman, in *Advances in Biomaterials for Biomedical Applications*, ed. A. Tripathi and J. S. Melo, Springer, Singapore, 2017, ch. 12, pp. 479–545, DOI: 10.1007/978-981-10-3328-5_12.

21 S. Agnihotri, N. K. Dhiman and A. Tripathi, in *Handbook of Antimicrobial Coatings*, ed. A. Tiwari, Elsevier, 2018, ch. 20, pp. 435–486, DOI: 10.1016/B978-0-12-811982-2.00020-2.

22 D. Sillu and S. Agnihotri, Cellulase immobilization onto magnetic halloysite nanotubes: Enhanced enzyme activity and stability with high cellulose saccharification, *ACS Sustainable Chem. Eng.*, 2020, **8**, 900–913.

23 S. Li, S. Dong, W. Xu, S. Tu, L. Yan, C. Zhao, J. Ding and X. Chen, Antibacterial hydrogels, *Adv. Sci.*, 2018, **5**, 1700527.

24 S. S. Silva, J. F. Mano and R. L. Reis, Ionic liquids in the processing and chemical modification of chitin and chitosan for biomedical applications, *Green Chem.*, 2017, **19**, 1208–1220.

25 H. Wu, J. Zheng, A.-L. Kjøniksen, W. Wang, Y. Zhang and J. Ma, Metallogels: Availability, applicability, and advanceability, *Adv. Mater.*, 2019, **31**, 1806204.

26 J. Liu, C. Hong, X. Shi, S. Nawar, J. Werner, G. Huang, M. Ye, D. A. Weitz, A. A. Solovev and Y. Mei, Hydrogel microcapsules with photocatalytic nanoparticles for removal of organic pollutants, *Environ. Sci.: Nano*, 2020, **7**, 656–664.

27 D. A. Berillo, J. L. Caplin, A. B. Cundy and I. N. Savina, A cryogel-based bioreactor for water treatment applications, *Water Res.*, 2019, **153**, 324–334.

28 D. K. Nandakumar, Y. Zhang, S. K. Ravi, N. Guo, C. Zhang and S. C. Tan, Solar energy triggered clean water harvesting from humid air existing above sea surface enabled by a hydrogel with ultrahigh hygroscopicity, *Adv. Mater.*, 2019, **31**, 1806730.

29 X. Wang, W. Sun, W. Yang, S. Gao, C. Sun and Q. Li, Mesoporous silica-protected silver nanoparticle disinfectant with controlled Ag+ ion release, efficient magnetic separation, and effective antibacterial activity, *Nanoscale Adv.*, 2019, **1**, 840–848.

30 S. C. Motshekga, S. Sinha Ray and A. Maity, Synthesis and characterization of alginate beads encapsulated zinc oxide nanoparticles for bacteria disinfection in water, *J. Colloid Interface Sci.*, 2018, **512**, 686–692.

31 Y. Liu, F. Li, Z. Guo, Y. Xiao, Y. Zhang, X. Sun, T. Zhe, Y. Cao, L. Wang, Q. Lu and J. Wang, Silver nanoparticle-embedded hydrogel as a photothermal platform for combating bacterial infections, *Chem. Eng. J.*, 2020, **382**, 122990.

32 D. V. Quang, P. B. Sarawade, S. J. Jeon, S. H. Kim, J.-K. Kim, Y. G. Chai and H. T. Kim, Effective water disinfection using silver nanoparticle containing silica beads, *Appl. Surf. Sci.*, 2013, **266**, 280–287.

33 J. H. Merritt, D. E. Kadouri and G. A. O'Toole, Growing and analyzing static biofilms, *Curr. Protoc. Microbiol.*, 2005, **22**, 1B.1.

34 J. M. Yang, W. Y. Su, T. L. Leu and M. C. Yang, Evaluation of chitosan/PVA blended hydrogel membranes, *J. Membr. Sci.*, 2004, **236**, 39–51.

35 L. Xu, C. Wang, Y. Cui, A. Li, Y. Qiao and D. Qiu, Conjoined-network rendered stiff and tough hydrogels from biogenic molecules, *Sci. Adv.*, 2019, **5**, eaau3442.

36 K. Haraguchi and T. Takehisa, Nanocomposite hydrogels: A unique organic–inorganic network structure with extraordinary mechanical, optical, and swelling/de-swelling properties, *Adv. Mater.*, 2002, **14**, 1120–1124.

37 B. Xu, H. Li, Y. Wang, G. Zhang and Q. Zhang, Nanocomposite hydrogels with high strength cross-linked by titania, *RSC Adv.*, 2013, **3**, 7233–7236.

38 Q. Wang and Z. Gao, A constitutive model of nanocomposite hydrogels with nanoparticle crosslinkers, *J. Mech. Phys. Solids*, 2016, **94**, 127–147.

39 WHO, *Guidelines for drinking-water quality*, World Health Organization, Geneva, 4th edn, 2011.

40 S. J. Shirbin, S. J. Lam, N. J.-A. Chan, M. M. Ozmen, Q. Fu, N. O'Brien-Simpson, E. C. Reynolds and G. G. Qiao, Polypeptide-based macroporous cryogels with inherent antimicrobial properties: The importance of a macroporous structure, *ACS Macro Lett.*, 2016, **5**, 552–557.

41 D. A. Salick, J. K. Kretsinger, D. J. Pochan and J. P. Schneider, Inherent antibacterial activity of a peptide-based beta-hairpin hydrogel, *J. Am. Chem. Soc.*, 2007, **129**, 14793–14799.

42 D. A. Salick, D. J. Pochan and J. P. Schneider, Design of an injectable β-Hairpin peptide hydrogel that kills methicillin-resistant Staphylococcus aureus, *Adv. Mater.*, 2009, **21**, 4120–4123.

43 M. Hoop, Y. Shen, X. Z. Chen, F. Mushtaq, L. M. Iuliano, M. S. Sakar, A. Petruska, M. J. Loessner, B. J. Nelson and S. Pané, Magnetically driven silver-coated nanocoils for efficient bacterial contact killing, *Adv. Funct. Mater.*, 2015, **26**, 1063–1069.

44 D. Vilela, M. M. Stanton, J. Parmar and S. Sánchez, Microbots decorated with silver nanoparticles kill bacteria in aqueous media, *ACS Appl. Mater. Interfaces*, 2017, **9**, 22093–22100.

45 S. Maes, T. Vackier, S. Nguyen Huu, M. Heyndrickx, H. Steenackers, I. Sampers, K. Raes, A. Verplaetse and K. De Reu, Occurrence and characterisation of biofilms in drinking water systems of broiler houses, *BMC Microbiol.*, 2019, **19**, 77.

46 C. L. Abberton, L. Bereschenko, P. W. J. J. van der Wielen and C. J. Smith, Survival, biofilm formation, and growth potential of environmental and enteric Escherichia coli strains in drinking water microcosms, *Appl. Environ. Microbiol.*, 2016, **82**, 5320–5331.

47 L.-J. A. Ellis, M. Baalousha, E. Valsami-Jones and J. R. Lead, Seasonal variability of natural water chemistry affects the fate and behaviour of silver nanoparticles, *Chemosphere*, 2018, **191**, 616–625.

 This journal is © The Royal Society of Chemistry 2020

Colloids and Surfaces B: Biointerfaces 227 (2023) 113362

Contents lists available at ScienceDirect

Colloids and Surfaces B: Biointerfaces

journal homepage: www.elsevier.com/locate/colsurfb

Graphene oxide reinforced chitosan/polyvinyl alcohol antibacterial coatings on stainless steel surfaces exhibit superior bioactivity without human cell cytotoxicity

Navneet Kaur Dhiman [a], M. Sudhakara Reddy [a], Shekhar Agnihotri [b,c,*]

[a] Department of Biotechnology, Thapar Institute of Engineering and Technology, Bhadson Road, Patiala 147004, Punjab, India
[b] Department of Agriculture and Environmental Sciences, National Institute of Food Technology Entrepreneurship and Management, Kundli, Sonepat, Haryana 131028, India
[c] Centre for Advanced Translational Research in Food Nano-Biotechnology (CATR-FNB), National Institute of Food Technology Entrepreneurship and Management, Kundli, Sonepat, Haryana 131028, India

ARTICLE INFO

Keywords:
Antibacterial mechanism
Biomedical coatings
Metal implants
Surface modification
Degradation behaviour

ABSTRACT

The study proposes an alternative therapeutics to diminish bacterial attachment in biomedical implants by modifying their surface with passive coatings. A uniform, thin-film of chitosan/polyvinyl alcohol/graphene oxide (CS/PVA/GO) was coated on 316 L stainless steel (SS) surface through spread casting followed by solvent evaporation. The abundant anchoring sites available at macromolecular interfaces of chitosan/PVA matrix facilitated a smooth, dense loading of GO. The effect of GO content on physicochemical features, antibacterial potential, and biocompatibility of coatings was thoroughly studied. The hybrid films displayed good adhesion behavior, and UV-protection ability with desired mechanical and thermal stability when coated on SS surface. Coatings manifested a 1.5–1.7 fold rise in antibacterial efficacy against *Staphylococcus epidermidis* and *Staphylococcus aureus* and exhibited a permanent biocidal response after 6 h of contact-active behaviour. We investigated a 3-fold generation of reactive oxygen species as the predominant antibacterial mechanism, which diminishes bacterial integrity by inducing protein leakage (8.5–9 fold higher) and suppressing respiratory chain activity as two secondary mechanisms. All coatings with varying GO content appeared non-haemolytic (<2%) with ultra-low cytotoxicity (<29.08%) against human hepatocellular carcinoma (HepG2) and peripheral blood mononuclear cells. The degradation rate of coatings in simulated body fluid exhibited a higher stability, indicated by a lower weight loss (69–78%) and a decrease in pH values as the GO content in coatings increased from 0.05 to 0.15 wt%. Such anti-infective coating is a step forward in inhibiting bacterial colonization on SS surfaces to extend its lifespan.

1. Introduction

Regenerative healthcare therapies aim to restore the mobility and function of damaged tissues by utilizing biomedical implants as substitutes. The rising post-operative complications in these implants however, call for superior biomaterials that offer required biocompatibility, mechanical durability, and corrosion resistance along with intended functions [1–3]. Biomedical devices and implants based on stainless steel (SS) and its alloys are acknowledged for such characteristics [4]. Without exception, these materials cannot completely eradicate bacterial adhesion and proliferation thus, are prone to be attacked with biomaterial-associated infections [5,6]. Besides, the undesired leaching of a few elements, viz. iron, chromium, and nickel from SS implants manifests adverse effects on surrounding tissues [7]. The development of antibacterial biomaterial via surface modification has emerged as one of the viable strategies to handle antibiotic resistance and serious post-clinical consequences while combating bacterial infections.

Among various approaches for imparting antimicrobial features onto implant surfaces, surface coating of biomaterials through incorporating the antibacterial component is still considered the most feasible and effective [8]. Recent advancements in functional antimicrobial coatings

* Corresponding author at: Department of Agriculture and Environmental Sciences, National Institute of Food Technology Entrepreneurship and Management, Kundli, Sonepat, Haryana 131028, India.
E-mail address: agnish@niftem.ac.in (S. Agnihotri).

https://doi.org/10.1016/j.colsurfb.2023.113362
Received 4 March 2023; Received in revised form 11 May 2023; Accepted 19 May 2023
Available online 20 May 2023
0927-7765/© 2023 Elsevier B.V. All rights reserved.

emphasize effectiveness via incorporating nanomaterials with biocidal characteristics like copper, zinc-oxide, silver, and titania for mitigating the severity of bacterial infections [8–11]. However, coating systems often fall short of their intended use because of toxicity, biocompatibility, and environmental issues caused by the leaching of inorganic metal ions [12]. Finding new-generation biomaterials that can effectively combat against bacterial infections is under the quest. Graphene and its derivatives, since their discovery in 2004 have been at the forefront of biomedical research because of their unique physicochemical attributes [13,14]. Graphene oxide (GO), in particular has invoked scientific interest due to its easy functionalization, remarkable mechanical strength, biocidal nature, and limited cytotoxicity [15,16].

Graphene oxide (GO) is a two-dimensional structure consisting of hexagonally packed carbon atoms with various functional groups such as hydroxyl, epoxy, and carboxyl, which facilitate its application as an antibacterial agent [17,18]. The antibacterial action of GO through physical interaction with bacteria is too complex and depends on sharp edges and their orientation on the deposited surface [4,19]. A direct-contact and ROS-dependant oxidative stress are hypothesized to be leading mechanisms of GO for disrupting bacterial cells [20,21]. Further, the combination of GO and polymers have become progressively popular, as it results in nanocomposites that are robust and biocompatible [22,23]. Moreover, GO-based polymer composite coatings have been found to effectively increase substrate adhesion, prevent crack formation, and improve the overall antibacterial performance of coatings [24,25].

Various polymers (natural/synthetic) such as chitosan, poly (ethylene glycol), poly(vinyl pyrrolidone), and poly(vinyl alcohol) have been employed synergistically with GO in coating systems that render the metallic implant with coveted antimicrobial interface [26]. Among biopolymers, chitosan (CS), which is a cationic polyaminosaccharide of β-(1,4)-linked N-acetyl-2-amino-2-deoxy-D-glucopyranose and 2-amino-2-deoxy-β-D-glucopyranose is widely employed in biomedical applications as a surface modifier due to its prominent film-forming ability, complexing capability, biocompatibility, and biodegradability [27]. However, chitosan alone has a limited use for developing biomedical coatings due to its weak mechanical strength and antibacterial properties [28]. PVA, a synthetic water-soluble polymer with excellent mechanical, biocompatible, biodegradable and nontoxic properties has been widely used in biomedical applications as a tuneable plasticizer [3, 29,30]. The incorporation of PVA with biopolymeric blends can improve their processability and mechanical properties via intermolecular hydrogen bonding [30]. Thus, the vital characteristics of PVA can be integrated with CS to form a mechanically stable polymer composite which could provide a durable support matrix for GO as an antimicrobial filler and form a strong film on metallic implants.

Several recent studies have investigated the antimicrobial potential of CS/PVA/GO nanocomposites in biomedical applications (Table S1). For instance, Ruiz et al. [3] and Tamayo Marin et al. [31] prepared well-dispersed composites of CS/PVA with 0.25–1.0 wt% graphene oxide by drop-casting and freeze-drying methods, respectively. They reported strong activity against Gram-positive and Gram-negative bacteria and desired biocompatibility in Wistar rats. Yang et al. [32] produced CS/PVA electrospun membranes using a relatively higher GO content i.e., 1–5 wt% and demonstrated high antibacterial efficacy against *E. coli* and *S. aureus*. Additionally, conjugating CS/PVA nanofibers with allicin and GO (0.1–0.5 wt%) also exhibited strong antibacterial activity with sustained release character [33]. These studies provide compelling evidences that the proportion of GO in CS/PVA matrices is crucial while dictating antibacterial efficacy of a nanocomposite. The optimization of GO content, is therefore necessary while designing chitosan/PVA-based antimicrobial coatings without posing any significant cytotoxic implications.

The present work demonstrates as how a bioactive coating material on stainless steel implants can effectively eradicate nosocomial infections without evoking toxicological implications on human cells. Several thin-films composed of chitosan/polyvinyl alcohol varying graphene oxide content were fabricated and characterized through physicochemical and biological studies. The antimicrobial efficacy of coatings was evaluated at clinically relevance conditions against *Staphylococcus aureus* and *Staphylococcus epidermidis* strains, the two most common strains responsible for causing hospital-acquired infections. The underlying mechanisms of antibacterial action of coatings causing severe damage to bacterial biofilms were thoroughly examined and verified. Furthermore, coatings were undergone through *in vitro* hemocompatibility and cytocompatibility tests to envisage their wide applicability as antibacterial coatings for biomedical surfaces, especially stainless steel implants.

2. Materials and methods

All details regarding materials used, material characterizations, and live/dead bacterial staining assay are provided in supporting information (S1, S2 and S3).

2.1. Preparation of chitosan/poly(vinyl alcohol)/graphene oxide coatings

Graphene oxide was synthesized using graphite flakes through modified Hummers method [34]. A 3% w/v chitosan suspension (2.5% v/v acetic acid: water) and aqueous PVA (4% w/v) solution were each separately prepared. Next, a 1:1 ratio blend of CS and PVA was prepared by stirring at 500 rpm for 2 h at 60°C. A predetermined amount of GO was added to achieve a final concentration of 0.05%, 0.075%, 0.1% and 0.15% w/v in the resulting CS/PVA/GO nanocomposites. The CS/PVA blend without GO was used as an experimental control. All solutions were ultrasonicated for 2 h and then mechanically homogenized at 40°C, 150 rpm for 12 h. Finally, these nanocomposites were coated onto stainless steel surfaces.

2.2. Coating stainless steel substrates with CS/PVA/GO nanocomposites

Initially, 316 L SS substrates (15 mm × 15 mm × 2 mm) were cleaned using a series of ultrasonic treatments. First, they were kept in 70% acetone for 15 min, followed by 70% ethanol and deionized water for an equal duration. Afterward, the substrates were dried in an ambient environment and stored in a sealed container to prevent surface contamination until further use. A simple spread casting method followed by solvent evaporation was used to coat the substrates. To achieve this, 100 μL of composite coating solutions were uniformly spread onto SS substrates and dried at room temperature for 24 h. The samples were labeled according to their final GO concentration (% w/v) in the coating suspensions as follows: CS/PVA, CS/PVA/$GO_{0.05}$, CS/PVA/$GO_{0.075}$, CS/PVA/$GO_{0.1}$, and CS/PVA/$GO_{0.15}$. All coated substrates were kept under ambient conditions, shielded from direct sunlight, until subsequent analysis. Five sets of independent experiments were also performed to evaluate the reproducibility of coating fabrication process.

2.3. Evaluation of antimicrobial activity of coatings

2.3.1. Antibacterial contact assay

The surface decontamination of coated 316 L surgical SS substrates was performed through UV exposure for 30 min in a sterilized laminar airflow chamber. In a separate experiment, a 100 μL bacterial suspension (*S. aureus* or *S. epidermidis*, ~10^6 CFU mL^{-1}) was spread onto petri plates containing nutrient agar. The coated SS substrates were carefully placed onto the surface of petri plates and incubated at 37°C. The coated substrates were periodically removed from plates after a contact time interval of 1 h, 2 h, 4 h, and 6 h, respectively. After 24 h, the plates were monitored and again kept in incubator for 30 days.

2.3.2. Antibacterial drop test

The antibacterial efficacy of thin-film coatings was further examined

using an antibacterial drop test. In brief, bacteria were inoculated into the nutrient broth and cultured at 37°C for 18–20 h under vigorous shaking. Cultured bacteria were harvested and diluted with phosphate buffer saline (PBS) to attain ~10^6 CFU mL^{-1} as initial count for studies. A 100 μL bacterial suspension was evenly spread over the surface of solid agar media. Once dried, coated SS substrates were carefully placed onto solid media surface and incubated at 37°C. After 1 h incubation, bacteria attached on SS substrates were washed with 1 mL PBS, a 100 μL of which was re-spread on a fresh nutrient agar plate and incubated at 37°C for 24 h and thereafter, used for counting bacterial colonies. The remaining washed-out bacterial suspension was immediately used for live/dead bacterial staining assay.

2.4. Mechanism(s) of antibacterial action of coatings

2.4.1. Assessment of morphological damage

Bacterial strains (*S. aureus* and *S. epidermidis* each, 10^6 CFU mL^{-1}) were exposed to CS/PVA/GO coated SS substrate (15 × 15 mm^2) for 6 h at 37°C to investigate any ultra-structural changes in bacterial cells, after direct contact with antibacterial coatings. Bacteria exposed to pristine SS substrate were used as positive control. After the required treatment, bacterial pellet was harvested by centrifugation at 5000 rpm for 10 min and washed twice with PBS solution. The cells were fixed in PBS suspension containing 2.5% glutaraldehyde (500 μL) for 3 h. After primary fixation, cells were centrifuged at 5000 rpm and rinsed twice with PBS. Cells were completely dehydrated with a graded ethanol series (30%, 50%, 70%, 90%, and 100%) for 15 min each [35]. A 10 μL aliquot was drop casted on a SS surface (5 mm × 5 mm), dried under laminar air-flow and immediately analysed using field emission gun scanning electron microscopy (FEG-SEM, ZEISS Sigma 500, Germany).

2.4.2. Determination of reactive oxygen species (ROS)

The level of ROS generation in bacterial cells was determined using nitro-blue tetrazolium (NBT) reduction assay with slight modifications [36]. *S. aureus* and *S. epidermidis* suspensions (10^6 CFU mL^{-1}) were initially cultured at 37°C for 6 h in the presence of CS/PVA/GO coatings. Bacterial cells incubated in the absence of any material was taken as negative control. Thereafter, 375 μL of NBT solution (1 mg mL^{-1}) was added to the cell suspensions and incubated at 37°C for 30 min. The reaction was terminated by adding 75 μL of 0.1 M HCL and bacterial suspensions were recovered by centrifugation at 5000 rpm for 10 min. The obtained bacterial pellets were treated with 300 μL dimethyl sulfoxide (DMSO) to extract the reduced NBT. Finally, the extracted solutions were diluted with 300 μL PBS and the optical density of bluish-violet formazan was recorded at 575 nm.

2.4.3. Protein leakage assay

The quantitative estimation of intracellular protein leakage from bacterial cells was carried out using Bradford's assay [37]. The coating substrates were incubated with bacterial cells (10^6 CFU mL^{-1}) at 37°C for 6 h in an incubator shaker. From each test vial, 1 mL of treated culture aliquot was withdrawn and centrifuged at 6000 rpm, 4°C for 30 min. The supernatant was treated with Bradford's reagent (0.01% w/v Coomassie Brilliant Blue G-250, 4.7% w/v ethanol, 8.5% w/v phosphoric acid) and the corresponding absorbance was measured at 595 nm.

2.4.4. Lactate dehydrogenase (LDH) release assay

The release of LDH caused by cytosolic leakage resulting from poor membrane integrity is often used to quantify cell death. The intensity of LDH release was determined by the stoichiometric conversion of iodonitrotetrazolium chloride to iodonitrotetrazolium formazan at 490 nm spectrophotometrically, due to the formation of NADH [38].

For microplate assay, an assay reagent was prepared by adding 50 μL each of PIN (1.175 mM PMS, 2.610 mM INT, 5.185 mM NAD) solution, 50 mM lithium lactate and 200 mM TRIS (pH-8). Bacterial cells (~10^6 CFU mL^{-1}) were exposed to coating samples for 6 h at 37°C. After this duration, samples were transferred to microcentrifuge tubes and centrifuged at 1200 rpm for 5 min. A 60 μL supernatant was transferred to a 96-well plate onto which 180 μL assay mixture was added to each well and incubated for 30 min at 25°C. After incubation, the optical density of each well was recorded at 490 nm on an ELISA reader (Thermo-Scientific Multiskan® spectrum). A 0.85% saline suspension and 0.1% Triton X-100 were taken as negative and positive controls, respectively. The % LDH release was calculated using OD_{490} values in Eq. (1). The LDH activity of positive control was considered 100% and activity of all other test samples was calculated relatively.

$$\%\mathrm{LDH}\,release = \left(\frac{\mathrm{Mean\,OD\,of\,test\,sample} - \mathrm{Mean\,OD\,of\,negative\,control}}{\mathrm{Mean\,OD\,of\,positive\,control} - \mathrm{Mean\,OD\,of\,negative\,control}}\right) \times 100 \quad (1)$$

2.5. Biocompatibility analyses

2.5.1. Hemocompatibility

To assess the biocompatibility of the coatings with blood, a hemolytic assay was performed using human red blood cells (RBCs), following a previously reported method with minor modifications [39,40]. In brief, RBCs were isolated from fresh human blood by centrifugation (4000 rpm, 5 min), washed three times with PBS buffer, and diluted to a final concentration of 5% (v/v) in PBS. A 500 μL RBC suspension was added to each vial containing coating samples (10 ×10 mm^2; 6.83 mg). Positive and negative controls were prepared using 0.1% Triton X-100 and sterile PBS solutions, respectively. All samples were incubated in a shaking incubator (100 rpm) at 37°C for 1 h. After incubation, the coatings were physically removed and the remaining contents in the vials were centrifuged (2000 rpm, 10 min). The extent of hemolysis in the samples was calculated by measuring the absorbance (540 nm) of the supernatant using Eq. (2). The degree of hemolysis (%) in the coatings was determined by using the biomaterial hemolytic index values (H) established in the guidelines of the American Society of Testing and Materials (ASTM) F756–00.

$$\mathrm{Hemolysis}\% = \left(\frac{\mathrm{Mean\,OD\,of\,test\,sample} - \mathrm{Mean\,OD\,of\,negative\,control}}{\mathrm{Mean\,OD\,of\,positive\,control} - \mathrm{Mean\,OD\,of\,negative\,control}}\right) \times 100 \quad (2)$$

2.5.2. Cytocompatibility in human peripheral blood mononuclear cells

The MTT assay was used to determine the cytotoxicity and cell viability human peripheral blood mononuclear cells (PBMCs). PBMCs were isolated from a healthy human blood through density gradient centrifugation with HiSep™ LSM 1077 [41]. First, EDTA-stabilized blood was diluted in 1:1 ratio with sterile PBS (pH 7.2), then overlaid carefully on HiSep™ solution and was centrifuged (400×g, 20°C) for 30 min. After centrifugation, the intermediate buffy layer containing PBMCs was harvested and washed twice with sterile PBS before suspending cells in RPMI-1640. The number of viable cells were determined by trypan blue dye exclusion technique on an automated cell counter (Curiosis Facscope™ B).

For MTT assay, ~1 × 10^6 cells/well were seeded along with the suspensions, soaked with various coated films and incubated at 37°C with 5% CO_2 for 24 h in a CO_2 incubator (Thermo-Fisher Forma™). At this point, any changes in morphology were viewed and recorded under an inverted microscope. After required treatments, the supernatants were discarded and MTT reagent (5 mg mL^{-1} in PBS solution) was added to each well and again kept further at 37°C for 4 h. The MTT solution was then removed, and DMSO was added to each well to dissolve the formazan crystals. The absorbance of the solubilized formazan was measured at 570 nm using a microplate reader. Cell viability was expressed as a percentage of viable cells in comparison to the

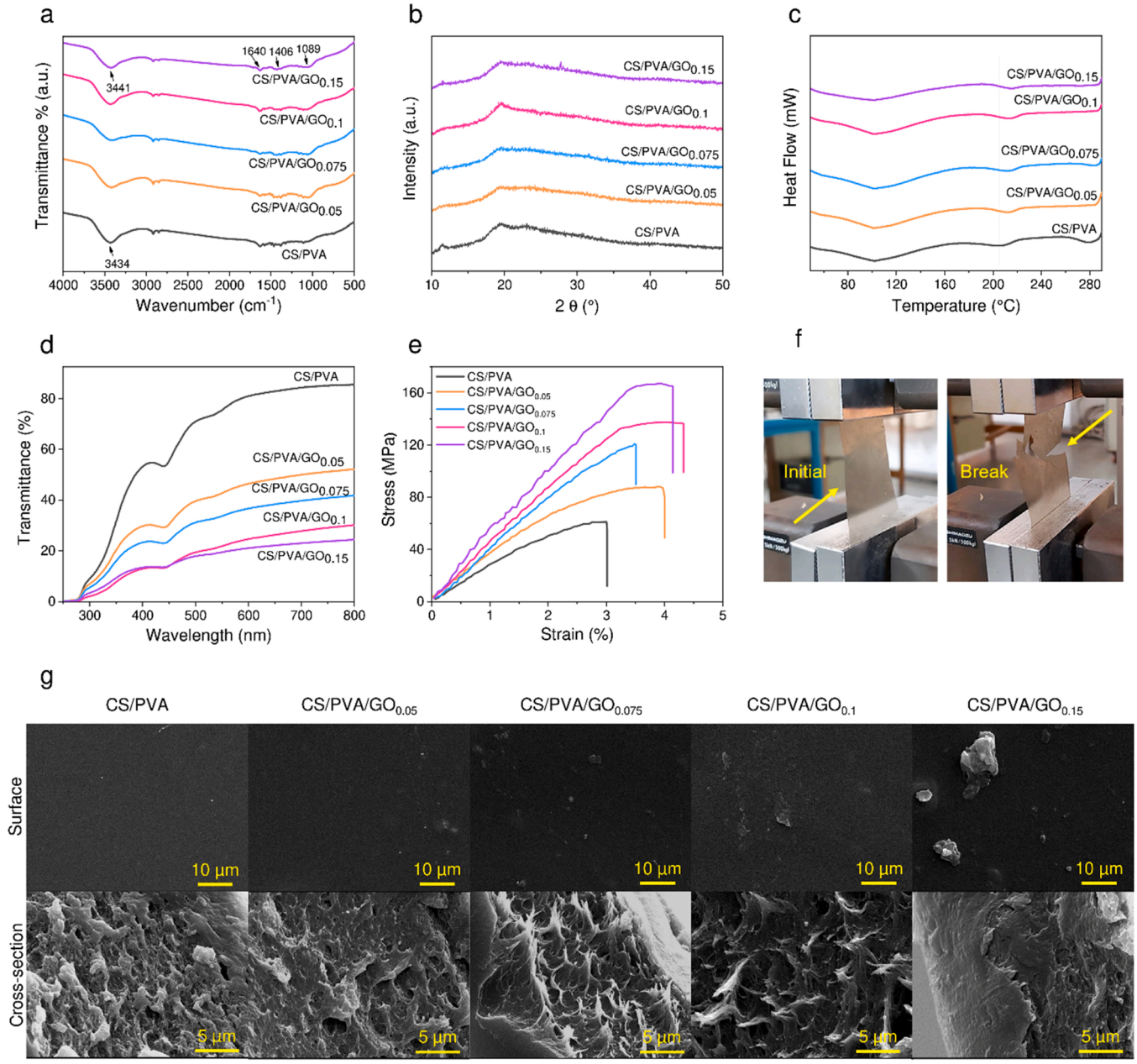

Fig. 1. : (a) FTIR spectra (b) X-ray diffraction patterns (c) DSC thermograms (d) Optical transmittance spectra (e) Stress-strain curve of various CS/PVA composites after reinforcing GO with varying content (0.05–0.15 wt%). (f) Digital images of coating film at initial moment (left) and at breakpoint (right) (g) SEM micrographs showing surface topography and cross-sectional microstructures of pure CS/PVA and CS/PVA/GO.

untreated control cells Eq. (3).

$$\text{Cell } viability\% = \left(\frac{\text{Mean OD of test sample}}{\text{Mean OD of negative control}}\right) \times 100 \quad (3)$$

2.5.3. Cytocompatibility in human hepatocellular carcinoma cells (HepG2)

The HepG2 cells were cultured in a seeding flask at 37°C in 5% CO_2 in Dulbecco's Modified Eagle's Medium supplemented with 10% (v/v) fetal bovine serum and 1% (v/v) penicillin-streptomycin. The cell culture was monitored after every 2–3 days and adherent cells were detached by trypsinization in between sub-cultures. After attaining 60–80% confluency, HepG2 cells were harvested and prepared for MTT assay. The viable cells were counted and plated at a density of 1×10^4 cells/well in a 96-well plate. Cell viability and cytotoxicity were assessed similarly, as described for PBMCs.

2.6. Degradation of coatings in simulated biological fluid

The coated substrates were subjected to hydrolytic degradation analysis in a simulated biological fluid (SBF) in compliance with ASTM F1635–16 standards. The SBF was prepared using an established procedure [42]. The coated samples were immersed in 15 mL of SBF and incubated at 37°C for the desired time periods (1, 3, 7, 10, and 14 days). Prior to immersion, the initial dry weight of each sample (W_0) was determined while weight after immersion was designated as 'W'. The dry weight of uncoated SS substrate was recorded as 'W_b'. SBF was replaced every 24 h and its pH value was measured every day. The degradation rate was then calculated as the percentage weight loss after specific period using Eq. (4). Finally, the dried coatings were analysed through FE-SEM to evaluate the extent of degradation and its effects on their morphology.

$$\text{Weight } loss\% = \left(\frac{W_0 - W}{W_0 - W_b}\right) \times 100 \quad (4)$$

2.7. Statistical analyses

All experiments were performed in triplicates and results were expressed as mean ± standard deviation values. Data were evaluated for statistical significance by analysis of variance (ANOVA), followed by Tukey's Multiple Comparison Test, $p < 0.05$ using GraphPad Prism 8.0.1 software.

3. Results and discussion

Stainless steel (SS) implants, despite providing several advantages such as durability, appearance, and corrosion resistance, are more prone to bacterial colonization than other metal-based implants [43,44]. Surface modification of SS implants with biocidal coatings is an effective strategy to design novel biomaterials with tuneable functionalities. Modulating surface characteristics of implants with antimicrobial coatings aim to avoid post-surgery infections, improve cell interactions, tissue growth and biocompatibility [45]. As a step forward, we attempted to develop passive coatings on 316 L stainless steel that would minimizes bacterial adhesion onto its surface and prevent further bacterial colonization without releasing any bactericidal agent in surrounding tissues. The nanocomposite coatings were fabricated by incorporating graphene oxide in chitosan/PVA matrix through green chemistry, where positively charged chitosan moieties electrostatically interacted with negatively-charged GO sheets, and hydroxyl groups on PVA chains formed stable intermolecular hydrogen bonds with oxygen groups of GO [46]. A strong hydrogen-bonding between amino groups of chitosan and oxygen functionalities of GO was also prevalent. We chose a spread casting and solvent evaporation strategy to fabricate CS/PVA/GO thin-film coatings on 316 L SS implant surfaces, which is a cost-effective method compared to other expensive techniques such as sputtering, pulsed laser-deposition, electrophoretic deposition, plasma spray [47,48].

3.1. Material characterization

FTIR spectrum of pure GO exhibited a strong peak at 3411 cm^{-1} due to stretching vibrations of hydroxyl (-OH) groups (Fig. S1a). Other characteristics bands at 1726 cm^{-1} (stretching vibrations of C═O from carboxylic groups), 1401 cm^{-1} (O-H deformation vibrations), 1215 cm^{-1} (epoxy rings), 1052 cm^{-1} (C-OH bending) were also manifested. A peak at 1629 cm^{-1} due to C═C stretching modes validate its sp^2 configuration [49]. All these analyses confirmed the successful synthesis of graphene oxide. In chitosan, the vibrational peak at 1653 cm^{-1} was assigned to carbonyl (C═O) stretching of acetylated amino (-NHCO-) group (Fig. S1a). A few other peaks at 3421 cm^{-1}, 2884 cm^{-1}, 1602 cm^{-1}, and 1382 cm^{-1} can be ascribed to -OH stretching, C-H stretching vibrations and N-H bending of amino groups, respectively present in chitosan polymer [46]. The FTIR spectra of CS/PVA/GO coatings (Fig. 1a) displayed a relatively broader absorption band at 3441 cm^{-1} due to combined stretching effects of amine and hydroxyl groups contributed from chitosan and graphene oxide, respectively. As compared to pristine chitosan and GO, corresponding peaks at 1602 cm^{-1} (-NH_2 vibrations) and 1726 cm^{-1} (C═O stretching vibration of carboxylic groups) disappeared. Besides, the appearance of a new peak at 1640 cm^{-1} clearly indicates a stable association between CS/PVA polymeric blend and the oxygenated groups of GO via hydrogen bonding and electrostatic interactions [3]. A slight decrease in the intensities of the OH-bands in CS/PVA/GO coatings than pristine CS/PVA (without GO) is consistent with the formation of intermolecular hydrogen bonds between GO and PVA, as witnessed before [50–52]. Further, no significant difference in the -OH band intensities was observed among the CS/PVA/GO coatings with varying GO content (Fig. S1). This suggests that adding such a low proportionate of GO to CS/PVA matrix did not alter the hydrogen bonding already existed between the CS and PVA components.

The XRD pattern of GO (Fig. S2b) shows a characteristic 2θ peak at 10.9° (d-spacing, 0.816 nm) indicating the existence of oxygen containing moieties [53]. The XRD pattern of chitosan at 2θ= 10° reflects the hydrated crystalline structure and a broad peak 2θ= 20° indicated the existence of amorphous structure [49]. The addition of GO to CS/PVA coatings led to an increase in the intensity of PVA lattice peak at 19.8° contributing towards an enhanced crystallinity of the PVA component (Fig. 1b). On the other hand, the absence of a distinct GO peak at 10.9° may be attributed to the complete exfoliation of GO sheets and their integration within the hierarchical matrices of CS/PVA polymers [46]. Furthermore, given the low proportion of GO (0.05–0.15 wt%) in the CS/PVA/GO nanocomposites, it is possible that the characteristic diffraction peak of GO was too weak and overshadowed by the chitosan peak. These findings corroborate to similar studies done with CS/PVA/GO nanocomposites [52,54]. Though the GO concentrations used in those studies were much higher (~10–47 folds) than the current work. XRD results also indicate a significant enhancement in polymer crystallinity after incorporating GO, which is likely to enhance mechanical strength of the coatings.

Differential scanning colorimetry (DSC) was used to examine thermal stability of CS/PVA polymeric networks while varying GO loading. The thermograms of all coating samples showed broad endothermic peaks in the temperature range of 100–140°C, which is due to the evaporation of adsorbed water. Sharp peaks at higher temperatures were observed, which were attributed to crystalline melting transition (Fig. 1c). Pure PVA sample showed endothermic peaks at 108°C and 227°C, which were assigned to the evaporation of adsorbed moisture and melting transition, respectively [55]. The thermogram analysis revealed that the CS/PVA coating exhibited peak broadening and a shift towards a lower temperature i.e., from 227°C to 205°C, indicating stable interactions between the polymer moieties. After the incorporation of GO in the coatings, DSC curves showed red shifts in the peaks in the range of 211–214°C. This red shift resulted from the crosslinking of CS/PVA and GO through hydrogen bonds, which restricted the motion of molecular chains and increased the melting temperature of the coatings [56]. It indicates that both CS/PVA and GO were compatible while coating fabrication, which improved the overall thermal characteristics of nanocomposites.

The development of UV-protective materials is crucial while designing bioactive coatings, as they must remain protected against radiation-induced damage while maintaining their appearance and avoiding cracks for extended periods [57,58]. We analysed the UV-light shielding behaviour of CS/PVA films varying GO content through light transmittance (Fig. 1d). Pristine CS/PVA films exhibited poor UV-absorption capability having 53.2% transmittance and high transparency in UV region (200–400 nm). A proportionate rise in GO content however, significantly enhanced the UV-shielding effect of CS/PVA films. This was manifested through a drastic reduction in transmittance in CS/PVA/$GO_{0.05}$ (29.7%), CS/PVA/$GO_{0.075}$ (23.3%), CS/PVA/$GO_{0.1}$ (13.4%), and CS/PVA/$GO_{0.15}$ (12.9%) films. An increased GO content appeared responsible for such UV-blocking ability of organic coatings where planar structure and high C/O ratio of GO nanosheets imparted an effective barrier to UV light [34]. Besides, GO sheets are well known UV-absorbers which potentially transform the adsorbed energy to less damaging thermal energy via photo-physical process. The incorporation of GO sheets onto CS/PVA based composite coatings prevent unsolicited UV-induced protein degradation at implants site [34] and thus improve tissue regeneration.

The mechanical properties of thin-film coatings on stainless steel surface were studied (Fig. 1e). Stress–strain curve in all samples depicts a typical modulus and tensile strength at fracture behaviour of coatings. The curves exhibited a linear regime depicting maximum hydrogen-

Table 1
Tensile strength and Young's Modulus of composite coatings.

Sample	Tensile strength (σ) (MPa)	Young's Modulus (E) (MPa)
CS/PVA	61.22 ± 1.58	24.40 ± 2.23
CS/PVA/$GO_{0.05}$	87.88 ± 0.64	29.15 ± 0.52
CS/PVA/$GO_{0.075}$	120.92 ± 1.21	30.84 ± 1.79
CS/PVA/$GO_{0.1}$	137.56 ± 1.13	34.24 ± 0.85
CS/PVA/$GO_{0.15}$	167.13 ± 0.72	42.28 ± 0.41

bond content during elastic stress until hydrogen-bonding network was severely ruptured. We analysed that incorporation of minute amount of GO (0.05 wt%) intensified tensile strength and Young's modulus of CS/PVA coatings by 43% and 20% respectively. The tensile strength at break of CS/PVA/GO composite films was enhanced from 87.88 to 167.13 MPa while increasing the GO content from 0.05 to 0.15 wt% (Table 1). The strong dependency of tensile strength on GO content is ascribed to great dispersion of GO into hierarchical networks of CS-PVA, which augments a strong hydrogen bonding and electrostatic interactions at molecular level. As a result, under mechanical stress, energy released while forming hydrogen bond between CS/PVA matrix and GO always remains higher than energy loss during matrix deformation. Thus, better interactions among GO and CS/PVA provide better load transfer which ultimately leads to mechanical strength enhancement [49,59]. Fig. 1f demonstrates the breaking of composite thin-films at break point during tensile tests.

SEM micrographs unveiled the surface structure and interfacial interactions of coatings. The unusual tangentially curved morphologies in pristine CS/PVA surface were indicative of chitosan susceptibility to self-aggregation [49]. This was further verified after incorporating graphene oxide into chitosan/PVA matrix which resulted in better surface smoothness due to great dispersion, miscibility and strong interactions of GO with CS/PVA. The surface morphology of CS/PVA/$GO_{0.05}$ and CS/PVA/$GO_{0.075}$ coatings did not deviate much from their pristine form. Whereas, incorporating a higher GO content imparted slightly rough features on CS/PVA/$GO_{0.1}$ and CS/PVA/$GO_{0.15}$ film surfaces accompanied by larger artefacts. The cross-sectional images of coating films showed fractured surface along with grooves and rough edges (Fig. 1g and S3a). The polymeric blends appear denser after incorporating GO sheets thanks to synergistic charge carriers, complementary microstructures and superior chain entanglement among chitosan, PVA and GO. SEM micrographs did not show any individual exfoliated multi-layered GO (as also deduced from Raman spectra, S4, Fig. S3b) and envisages a great adhesion as if they were well wrapped between layers of CS/PVA blends. Further, EDX spectra (Table S2, Fig. S3c) confirmed the presence of characteristic elements and revealed a proportional increase in oxygen content with increasing GO content in the coatings.

3.2. Antibacterial efficacy of coatings

S. aureus and *S. epidermidis* are one of the most reported microbial species causing biomaterial associated infections [8]. Hence, the antimicrobial efficacy of CS/PVA/GO coatings on SS surfaces were examined against these clinically relevant strains at various test conditions.

3.2.1. Antibacterial contact assay

The uncoated SS substrates did not show any inhibitory effect on bacterial growth, regardless of the bacterial species and incubation time (Fig. 2). In contrast, CS/PVA/GO-coated substrates exhibited a significant inhibition of bacterial growth, forming a clear zone of inhibition (ZoI). Although increasing the GO content in CS/PVA coatings did not produce any noticeable changes in bacterial growth, the duration of the initial contact time certainly had a profound impact. Coatings that were in contact with bacteria for 1–3 h displayed only a bacteriostatic response since a permanent ZoI could not be established in the exposed area and was eventually replaced by bacterial growth from neighbouring areas over 10 days of aging (Fig. S4). However, a 6 h contact duration was sufficient to impart a permanent antibacterial (bactericidal) response onto the coated surface, where no signs of bacterial growth were observed on the formed ZoI even after aging the plates for a month. This suggests that the biomedical coatings exhibit a contact-active behaviour, which sometimes provides a higher antibacterial response than materials that prefer release-mediated antibacterial action, as reported earlier [60,61].

3.2.2. Antibacterial drop test

The drop test results indicate that both *S. epidermidis* and *S. aureus*

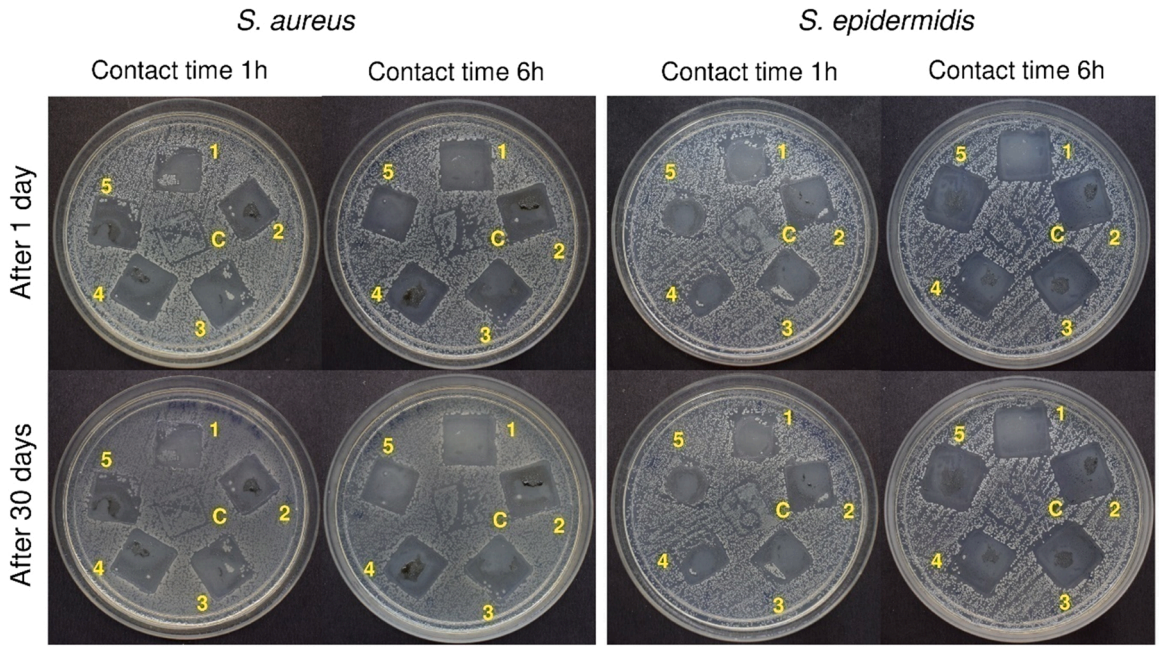

Fig. 2. : Contact bacterial growth inhibition of *S. aureus* and *S. epidermidis* by coatings where, C=control; 1 =CS/PVA; 2 =CS/PVA/$GO_{0.05}$; 3 =CS/PVA/$GO_{0.075}$; 4 =CS/PVA/$GO_{0.1}$; 5 =CS/PVA/$GO_{0.15}$ at 1 h & 6 h contact time after 1 day and its progression after 30 days.

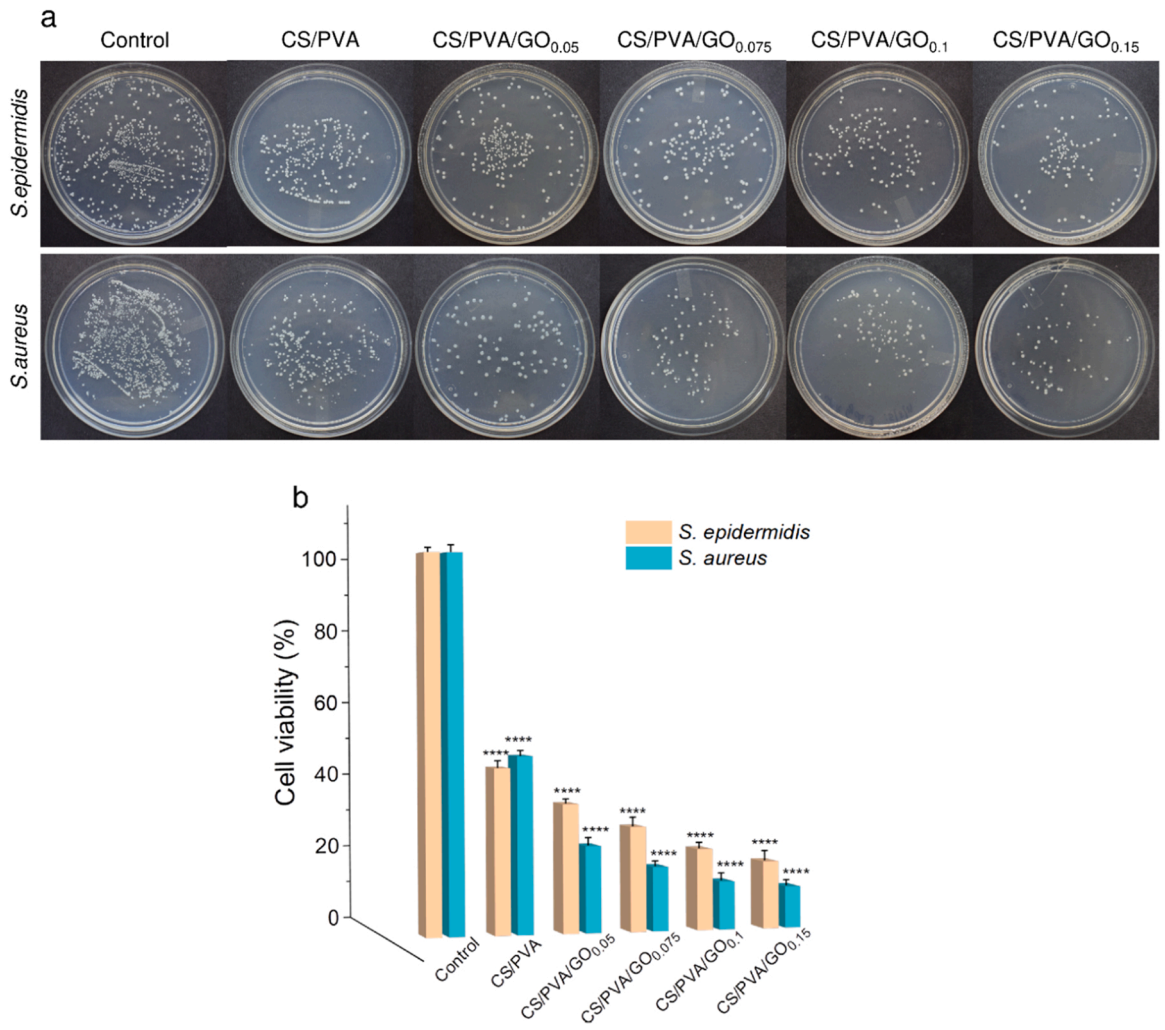

Fig. 3. : (a) Digital images of colony-forming unit of *S. epidermidis* and *S. aureus* incubated for 1 h on the control (pristine SS) and CS/PVA/GO coated SS surfaces. (b) Drop test for the quantitative analysis of bacterial cell viability (%) against CS/PVA/GO coatings for *S. aureus* and *S. epidermidis*. Asterisk- statistically different compared to control (****$p < 0.0001$).

grew well on uncoated SS surface forming bacterial biofilm in 10 days. However, fewer bacterial colonies were propagated in CS/PVA/GO coatings revealing a significant antibacterial activity against both strains (Fig. 3a). The cell viability (%) data of pure CS/PVA coating also indicated bacterial growth viz. 43.6% and 46.7% for *S. epidermidis* and *S. aureus*, respectively (Fig. 3b). With increasing GO concentration (0.05–0.15 wt%) in coatings, the cell viability reduced from 33.9% to 17.7% (*S. epidermidis)* and 22.8–10.9% (*S. aureus)* in just 1 h of incubation exhibiting an intense biocidal nature of the coatings. Furthermore, increasing the incubation time to 6 h resulted in complete eradication of bacterial cells at higher GO concentrations (≥0.1 wt%, Fig. S5). The results obtained in this study demonstrate a superior antibacterial efficacy compared to previously reported literature, where comparatively higher GO concentrations were required to induce effective bactericidal activity (Table S1). The reproducibility of coatings' fabrication was evaluated using a drop test, which revealed excellent replicability in terms of bioactivity, thus validating the efficacy of our procedure (Table S3).

3.2.3. *LIVE/DEAD assay*

A live/dead bacterial staining assay was conducted to assess the membrane permeability of bacteria following exposure to the coatings. The results, presented in Fig. 4, show dominant green and negligible red fluorescence signals for the control groups, indicating that the untreated cells maintained a normal membrane. Compared to the negative control, the CS/PVA coating displayed some bacterial inhibition, likely due to the inherent bactericidal properties of chitosan moieties. The cationic moieties present in this polysaccharide are known to compromise the cellular framework of bacteria, leading to their death [62]. In contrast, the GO-based coatings showed varied degrees of red fluorescence. As the GO content in coatings was increased from 0.05 to 0.15 wt%, there was a significant enhancement in red fluorescence as the number of non-viable bacterial cells increased and only a few sporadic live bacteria cells survived. These results were attributed to the synergistic effect of GO and CS, which could more efficiently disrupt the bacterial cell membrane in contact with CS/PVA/GO coatings, leading to bacterial inactivation as a consequence of the leakage of intracellular metabolites through permeable membranes. Further, the fluorescent images showed a higher number of non-viable cells in case of *S. aureus* than *S. epidermidis*, which were in good agreement with the antibacterial drop test results.

3.3. *Antibacterial mechanism of bioactive coatings*

Other than analysing the quantitative data for antibacterial analyses, it is equally important to understand the mechanistic insights into the functioning of antibacterial coatings while designing anti-biofouling surfaces for biomedical purposes. This can be understood well by

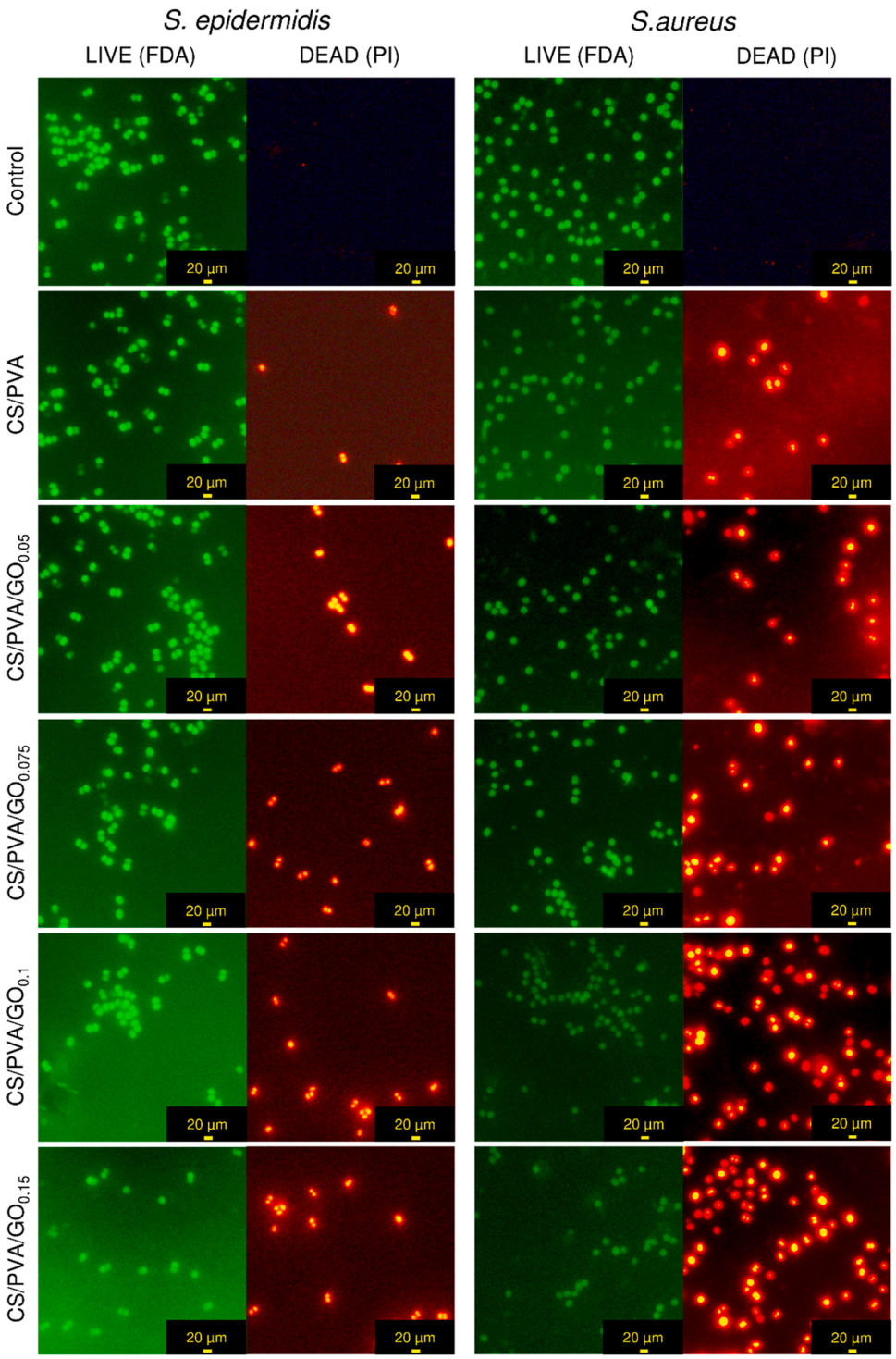

Fig. 4. Fluorescent images showing the comparative distribution of live and dead cell of *S. epidermidis* and *S. aureus* bacteria when come in direct contact to CS/PVA/GO coatings.

elucidating the underlying mechanism of antibacterial action of these coatings.

3.3.1. *Bacterial morphology through SEM*

The SEM images of untreated (control) cells revealed a typical glossy, circular, and grape-shaped morphology of *S. epidermidis* colonies with intact and smooth cell membranes (Fig. 5a). However, when treated with CS/PVA/GO coatings, significant morphological abnormalities were observed in *S. epidermidis*. The majority of bacterial cells appeared wrinkled with shrunken cell membranes, and perforated with pronounced breakages, indicating severe damage to cellular integrity. Similar findings were observed in *S. aureus* cells, which exhibited lysed cells and distorted shapes after exposure to CS/PVA/GO coatings. The exterior surface morphology analysis revealed irreversible damage to the cell membrane due to direct contact with immobilized GO sheets within CS/PVA matrices, as confirmed through material characterization. As previously reported, graphene oxide, when dispersed in a polymeric matrix, exhibits a much more lethal antibacterial action than

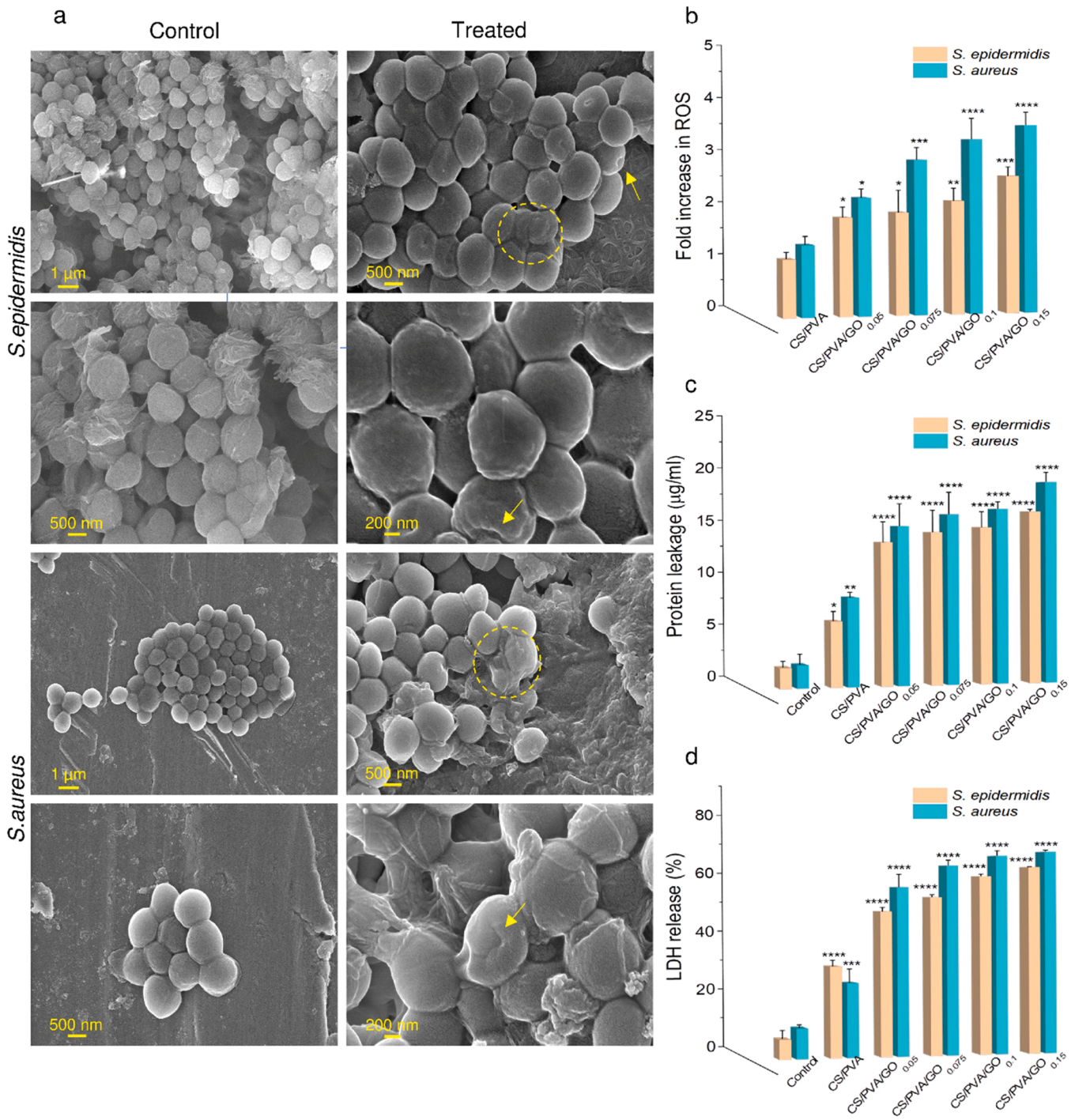

Fig. 5. : (a) FE-SEM micrographs of *S. epidermidis* and *S. aureus* untreated (control) and treated with CS/PVA/GO coating. (b) Fold increase in intracellular ROS of *S. epidermidis* & *S. aureus* cells exposed to CS/PVA/GO composites, leakage of (c) cytoplasmic proteins, (d) respiratory chain lactate dehydrogenases from *S. epidermidis* & *S. aureus* cells exposed to various CS/PVA/GO coatings. Asterisk- statistically different from control and CS/PVA (*$p < 0.05$, **$p < 0.001$, ***p & ****$p \leq 0.0001$).

its colloidal form [56]. GO triggers ROS generation, causing severe membrane damage, forming pits/holes and enhancing membrane permeability [60,61,63].

3.3.2. Membrane damage through ROS-triggered oxidative stress

The mechanism of antibacterial action via oxidative stress generation is evident in GO-based coatings. Our observations reveal a 2–3 fold increase in ROS production in *S. epidermidis* and *S. aureus* cells when treated with CS/PVA/GO coatings (Fig. 5b). The ROS production was consistent with an increase in GO content in the antibacterial coatings. This highlights the role of CS/PVA/GO coating as an electron donor on the bacterial surface, which reacts with oxygen molecules to generate superoxide radicals ($O_2^{\bullet-}$). Such an abrupt rise in ROS at bacterial surface could not be handled by their defence mechanism and get accumulated, resulting in an antibacterial response. Excessive levels of ROS may propel adverse events to bacteria furthermore viz. enhanced membrane permeability, diminished enzymes activity and destruction of cellular proteins/nucleic acids, leading to bacterial death [64].

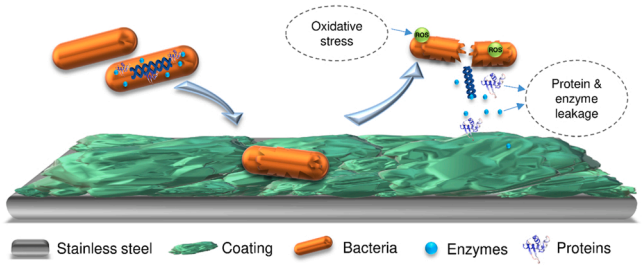

Fig. 6. : Schematic representation of plausible mechanism behind antibacterial potential of CS/PVA/GO coatings.

3.3.3. Leakage of cytoplasmic proteins

The release of intracellular proteins was evaluated to determine membrane leakage in treated bacterial cells (Fig. 5c). No significant release of proteins was observed in untreated *S. epidermidis* (1.87 μg mL^{-1}) and *S. aureus* (2.08 μg mL^{-1}) cells. However, upon introducing CS/PVA/GO coated SS substrates to both bacterial suspensions, the amount of released protein drastically enhanced by 8.5–9 folds. The increase in protein leakage was also dependent on GO-content (0.05–0.15 wt%) in the final CS/PVA coatings. This confirms our hypothesis that a GO-induced rise in ROS levels would have severely compromised membrane permeability of pathogenic bacteria resulting in the release of all intracellular components including proteins.

3.3.4. Suppression of respiratory chain activity

LDH release assay was further employed to test bacterial cell membrane integrity (Fig. 5d). SS substrates coated with CS/PVA/GO disrupted cellular respiration with significant difference among controls, CS/PVA and CS/PVA/GO coatings. The LDH release (%) in control and pristine CS/PVA were 6.4% and 29.6% (*S. epidermidis*) and 9.8%, 24.2% (*S. aureus*), respectively. As discussed earlier, introducing GO in bioactive coatings caused more release of LDH. For instance, CS/PVA/$GO_{0.05}$, CS/PVA/$GO_{0.075}$, CS/PVA/$GO_{0.1}$, and CS/PVA/$GO_{0.15}$ showed LDH release of 47.3%, 51.8%, 58.6%, and 61.5% for *S. epidermidis* while 55.2%, 62.1%, 65.2%, 66.6% for *S. aureus* respectively. An increase in LDH release in culture supernatants clearly indicates more lysed bacterial cells [65]. Therefore, CS/PVA coatings having 0.15% GO disrupted the bacterial membrane most severely. These results indicated that following LDH release, an important enzyme in cellular respiration, CS/PVA/GO coatings are capable to suppress cellular respiration and reproduction by inhibiting respiratory chain activity.

Analysing results, a coupled mechanism of bacterial inhibition with CS/PVA/GO coatings was envisaged. We observed that both structural and chemical characteristics of GO, which often work synergistically, dictate its lethal action towards pathogens. A few studies claimed that direct contact of GO sheets with bacterial surface through their sharp edges can likely cause deep penetration and puncture membranes, often leading to cellular deformation [3,66]. However, such penetration of GO sheets onto bacterial suspension was difficult to predict as GO exists in immobilized state within CS/PVA matrix. Even during coating process, slow water evaporation forms a self-assembled surface where majority of GO sheets would lie flat in basal plane of the substrate surface. This observation aligned well to SEM micrographs where no signs of sharp edges of GO sheets were found. Therefore, in contrast to earlier reports, we eliminated the "nano-knife" behaviour of immobilized GO as its primary antibacterial action mechanism. As reported recently [28], while a contact-active CS/PVA hydrogel had shown remarkable biocidal effects, the inclusion of GO would only augment its action, which cannot be ignored. Besides, cell rupturing, protein leakage and respiratory dehydrogenases disruption via CS/PVA/GO coatings could have also been triggered by lipid peroxidation due to the oxidative nature of GO [67]. Therefore, being passive in nature (non-releasing antimicrobial), the predominant mechanism of GO-based coatings was mediated through oxidative stress (ROS generation) [4]. Damaged cell membrane further weakened the cellular integrity inhibiting its respiratory chain activity and promoting cytoplasmic leakage as the two main secondary mechanisms, leading to antibacterial response (Fig. 6).

3.4. Evaluation of biocompatibility

In-vitro hemolytic assays were performed to evaluate the compatibility of blood-contacting coatings. Percentage hemolysis of pristine CS/PVA, CS/PVA/$GO_{0.05}$, CS/PVA/$GO_{0.075}$, CS/PVA/$GO_{0.1}$, and CS/PVA/$GO_{0.15}$ coatings were recorded as 1.15%, 1.84%, 1.87%, 3.21% and 3.43%, respectively (Fig. 7a). While a consistent increase in hemolysis was observed with increasing GO content, the extent of RBC rupture also became prominent which is attributed to surface-linked toxicological response of GO against RBCs. The RBC disruption occurs due to strong electrostatic interactions between negatively-charged GO surface and positively-charged phosphatidylcholine lipids on RBC's outer membrane [53]. Coatings having GO concentration < 0.1% were classified as non-hemolytic (H<2%) as per the hemolysis grade defined by ASTM F756–00 standard (H= 0–2%, non-hemolytic; H= 2–5%, slightly hemolytic; H=>5%, hemolytic). Fig. 7b represents an apparent difference in colour between the test samples, positive and negative control. Positive control causing 100% RBC lysis demonstrated bright red colour while the negative control was pale yellow. The test samples were observed having an incremental change in pink colour.

3.5. Cytotoxicity towards PBMCs and HepG2 cells

Human peripheral blood mononuclear cells (PBMCs) represent one of the major population of cells that gather at the first line of immune defence during biomaterial implantation in human body [68]. Therefore, the impact of coatings on PBMCs was investigated first (Fig. 7c). We demonstrated that none of the coatings induced any cytotoxicity effects, where all test samples (CS/PVA/GO coatings) resulted in an average cell viability of 77.1% under the test concentration range of 2–6 mg mL^{-1}. HepG2 cells are employed as *in vitro* model for determining materials' cytotoxicity [60,69]. As shown in Fig. 7d, all bioactive coatings including the highest GO concentration (0.15 wt%) demonstrated > 70% cell viability under similar test conditions.

Microscopic analysis demonstrated virtually no significant change in shape of cells upon exposure to CS/PVA/GO coatings. Both, treated PBMCs and HepG2 cells exhibited well defined and extended morphologies, similar to untreated ones (Fig. 7e). All coatings with GO displayed statistically significant decrease in survival of PBMCs and HepG2 cells compared to control. However, the difference between cell viability of coatings on account of increase in GO concentration was non-significant in both cell groups.

Additionally, when GO concentration in coating films was increased from 2 to 4 mg mL^{-1}, cell viability concomitantly decreased from 82.4% to 77.4% (PBMCs) and 80.9–78.3% (HepG2 cells). At 6 mg mL^{-1} GO concentration, mammalian cell viability further reduced to 72.22% (HepG2) and 70.92% (PBMCs). As per the biocompatibility guidance, ISO 10993–5, 2009, 'Biological evaluation of medical devices', ≥ 70% cell viability obtained in test method is regarded as the cytotoxicity safety limit [70]. Thus, we conclude that CS/PVA/GO coatings when coated on SS implants appear as non-cytotoxic against the targeted mammalian cells.

3.6. Degradation behaviour of CS/PVA/GO coatings

The purpose of evaluating extent of degradation in simulated body fluid over 14 days period was to determine coating's durability and estimate its longevity *in vivo* (Fig. 8a). This would enable us to design a more reliable and long-lasting biomedical coatings. Following the 14-day testing period, pure CS/PVA coatings exhibited a final degradation of 87%, while CS/PVA/GO coatings displayed declining

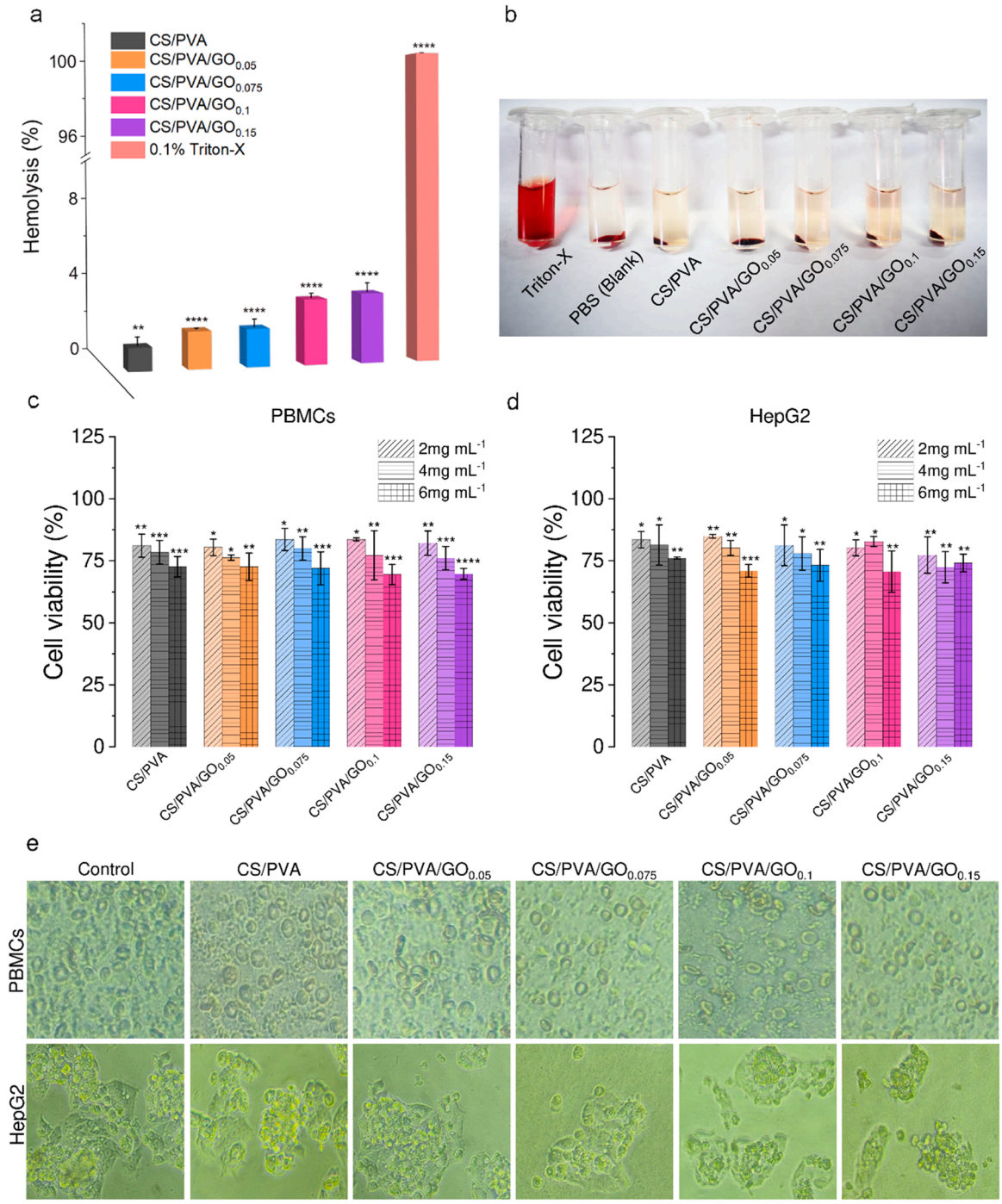

Fig. 7. : (a) Hemolysis of human erythrocytes by CS/PVA/GO composite coatings. (b) Photographs from hemolytic activity test where PBS and Triton X-100 stand as negative and positive controls respectively. Cytotoxicity analysis of soak solutions obtained from CS/PVA/GO coatings at concentration range of 2–6 mg mL^{-1} on (c) PBMCs, and (d) HepG2 cells as determined by MTT assay. Results reported in terms of % cell viability and in controls cells (unexposed) 100% cell viability (0% cytotoxicity) was taken. (e) Bright-field microscopic images displaying morphology of PBMCs and HepG2 after treatment with 6 mg mL^{-1} soak solution of CS/PVA/GO coatings. Asterisk- statistically significant from control (*$p < 0.05$, **$p < 0.001$, ***p & ****$p < 0.0001$).

deterioration from 78% to 69% as the GO content increased from 0.05 to 0.15 wt%. It is well-established that degradation of polymers in a body fluid occurs due to a complex series of events, including water absorption, molecule hydration, hydrogen bond rupture, and eventual hydrolysis of unstable bonds [31,71]. Our results indicate that increasing the GO content in Chitosan/PVA blends restrained the entry of SBF into the polymeric matrices, resulting in lower weight loss and consequently lower degradation [3]. This finding underscores the strong adhesion and improved stability of CS/PVA/GO-based coatings [31]. We hypothesize that the extensive hydrogen bonding network between the polymer matrix and GO provides the CS/PVA/GO composite with high-energy links and immense chemical stability.

In addition, a gradual decline in solution pH was observed during the degradation processes of coatings (Fig. 8b). This observation is an indicative of coating hydrolysis-led dissolution of a more susceptible and acidic moieties available in amorphous phases of the polymer matrix. As a result, the release of residual acetic acid and other harmless degradation by-products, typically present in chitosan polymer may have

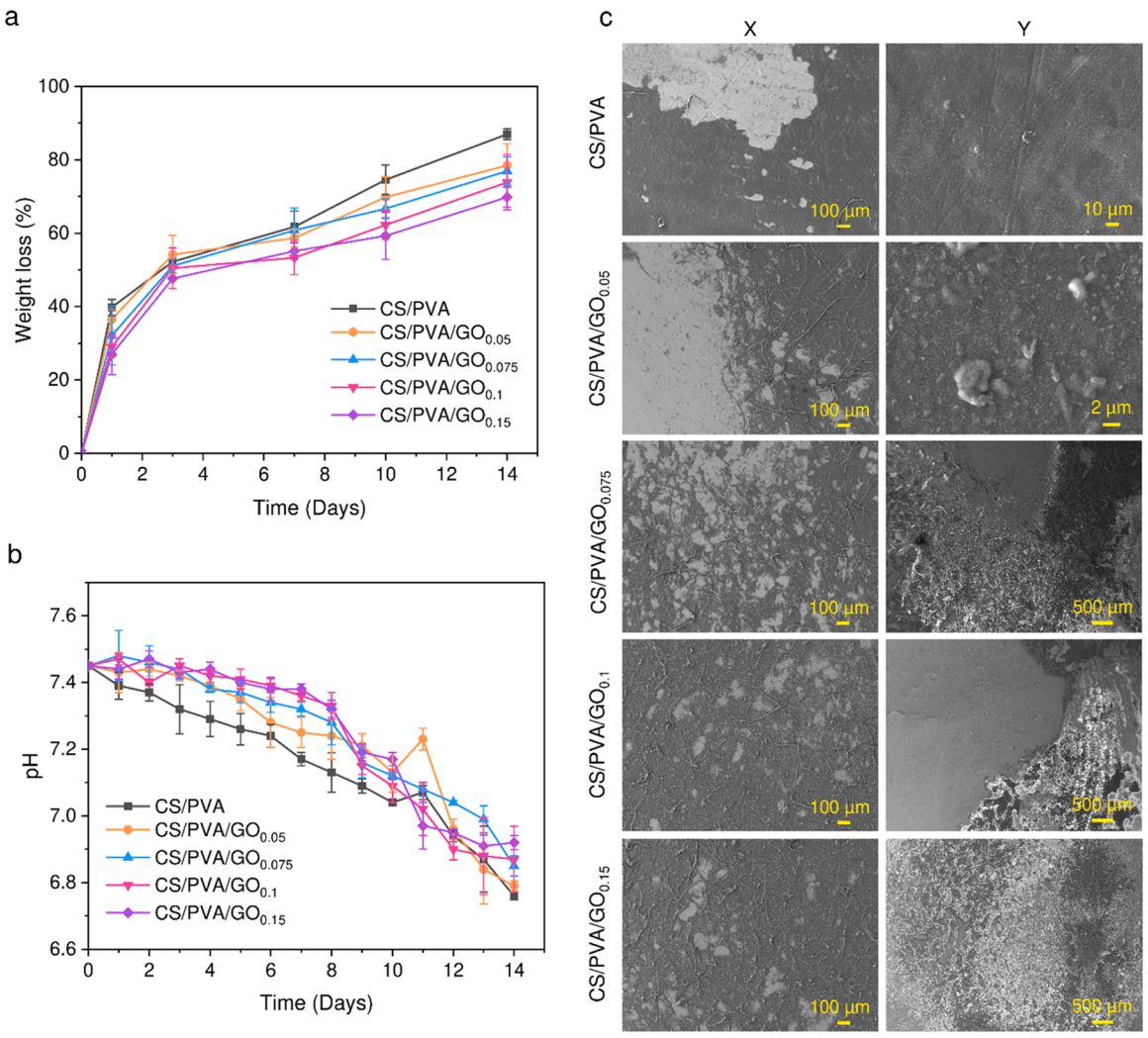

Fig. 8. : (a) Weight loss of CS/PVA/GO nanocomposite coatings and (b) Changes in pH of simulated body fluid, SBF at different time intervals over the span of 14 days. (c) FE-SEM micrographs illustrating morphological changes in CS/PVA/GO coatings undergoing degradation after immersion in SBF for 14 days. Column X represents degraded coatings on SS substrate surface after 14 days and Column Y illustrates precipitated whitish layer.

contributed to the lowering of the pH of SBF [72]. As determined by ASTM F1635 standard, the admissible pH scales that promote and maintain vital functions in human body lie between 6 and 8. This indicates that the values obtained in 6.7–7.5 range during coating degradation in this study lie within the reference domain of biological processes.

The topographical changes in CS/PVA/GO coatings that might occur during the degradation process were also examined (as shown in Fig. 8c). The micrographs clearly illustrate a highly rough texture of the coatings, which increases with GO content during degradation. The lighter grey regions in SEM micrographs shows the exposed SS substrate surface from where the coating undergoing degradation has been eroded (Fig. 8c, Column X). A comparison of the surface morphology of the coatings before and after immersion in SBF can be observed in Figs. 1g and 8c, respectively, revealing a noticeable difference in surface texture. Additionally, a whitish layer that precipitated on the coating surfaces (Fig. 8c, Column Y) could be observed, which is considered suitable as it promotes interaction between the material surface and surrounding tissues [73]. Energy dispersive spectroscopy (EDS) of test sample revealed the presence of elements such as C, O, and Fe along with small amounts of Na, Cl, K, Cr, Mn, Ca, P, and Ni (Table S4). These results provide valuable insights into the degradation behaviour and surface morphology of the polymeric coatings, which are crucial factors in designing reliable and long-lasting biomedical coatings.

4. Conclusion

We propose a new prophylactic coating composed of chitosan/polyvinyl-alcohol/graphene oxide that could reduce bacterial challenge during tissue repair surgeries. A simple, facile method of solvent casting at room temperature using polymeric blend of chitosan and PVA with varying GO content resulted in CS/PVA/GO coatings on 316 L SS substrate. SEM surface morphological analysis indicated a smooth and crack-free surface of polymer film on substrate yielding an increase in mechanical strength with increasing GO content. The bioactive coatings displayed a well-recognized (>82%) antibacterial action against nosocomial infections causing bacteria *S. aureus* and *S. epidermidis*. The detailed analyses of antibacterial action mechanism revealed ROS-mediated oxidative stress as the leading cause, which primarily induces membrane damage followed by the leakage of intercellular proteins and inhibition of reparatory activity. Further, coatings with GO content < 0.1 wt% demonstrated an outstanding blood compatibility. The cell viability through MTT assay indicated the as-developed coatings to be non-cytotoxic towards human cells lines PBMCs and HepG2. The addition of GO provided excellent stability against degradation in simulated body fluids. In conclusion, the present study may seek new avenues for developing an effective strategy modifying stainless steel-based implants to improve their antibacterial performance and biocompatibility simultaneously.

CRediT authorship contribution statement

Navneet Kaur Dhiman: Investigation, Methodology, Formal analysis, Data curation, Writing – original draft. **M. Sudhakara Reddy:** Supervision, Writing – review & editing. **Shekhar Agnihotri**: Conceptualization, Funding acquisition, Project administration, Resources, Supervision, Validation, Writing – review & editing.

Declaration of Competing Interest

The authors declare that they have no known competing financial interests or personal relationships that could have appeared to influence the work reported in this paper.

Data availability

Data will be made available on request.

Acknowledgements

This work was financially supported through Institute seed grant (TIET/DORSP/57/474, 28.03.2017) and DST-SERB grant, Govt. of India (YSS/2015/001599, 23.03.2016). NKD gratefully acknowledges UGC-Maulana Azad National Fellowship, Govt. of India (201718-MANF-2017–18-PUN-83207) while carrying out this work. NKD is also thankful to Sr. Parvinder Singh for shape modulation of SS substrates and Mr. Devendra Sillu for assistance in live/dead cell assay.

Appendix A. Supplementary data

Supplementary data includes Materials used (S1), Material characterization (S2), LIVE/DEAD bacterial staining assay (S3), Raman spectroscopy of GO (S4), Comparative details of antibacterial efficacy of CS/PVA/GO composites (Table S1), Elemental composition of CS/PVA/GO coatings (Table S2), Cell viability % of *S. aureus* and *S. epidermidis* against CS/PVA/GO coatings (Table S3), Elemental composition of degraded coating (Table S4), Magnified FTIR region (3030–3790 cm^{-1}) of coatings (Fig. S1), FTIR and XRD of chitosan and graphene oxide (Fig. S2), SEM micrographs of CS/PVA/GO coatings (Fig. S3a), Raman spectra of GO (Fig. S3b), EDS spectra of CS/PVA/GO coatings (Fig. S3c), contact bacterial growth inhibition at 2 h and 4 h (Fig. S4), and the antibacterial drop test at 6 h (Fig. S5).

Appendix A. Supporting information

Supplementary data associated with this article can be found in the online version at doi:10.1016/j.colsurfb.2023.113362.

References

[1] K. Chae, W.Y. Jang, K. Park, J. Lee, H. Kim, K. Lee, C.K. Lee, Y. Lee, S.H. Lee, J. Seo, Antibacterial infection and immune-evasive coating for orthopedic implants, Sci. Adv. 6 (44) (2020) 1–15, https://doi.org/10.1126/sciadv.abb0025.

[2] P. Herman-Bausier, Y.F. Dufrêne, Force matters in hospital-acquired infections, Science 359 (6383) (2018) 1464–1465, https://doi.org/10.1126/science.aat3764.

[3] S. Ruiz, J.A. Tamayo, J.D. Ospina, D.P. Navia Porras, M.E. Valencia Zapata, J.H. M. Hernandez, C.H. Valencia, F. Zuluaga, C.D.Grande Tovar, Antimicrobial films based on nanocomposites of chitosan/poly(vinyl alcohol)/graphene oxide for biomedical applications, Biomolecules 9 (3) (2019) 1–17, https://doi.org/10.3390/biom9030109.

[4] F. Perreault, A.F. de Faria, S. Nejati, M. Elimelech, Antimicrobial properties of graphene oxide nanosheets: why size matters, ACS Nano 9 (7) (2015) 7226–7236, https://doi.org/10.1021/acsnano.5b02067.

[5] E. Zhang, X. Zhao, J. Hu, R. Wang, S. Fu, G. Qin, Antibacterial metals and alloys for potential biomedical implants, Bioact. Mater. 6 (8) (2021) 2569–2612, https://doi.org/10.1016/j.bioactmat.2021.01.030.

[6] W. Xi, V. Hegde, S.D. Zoller, H.Y. Park, C.M. Hart, T. Kondo, C.D. Hamad, Y. Hu, A. H. Loftin, D.O. Johansen, Point-of-care antimicrobial coating protects orthopaedic implants from bacterial challenge, Nat. Commun. 12 (1) (2021) 1–15, https://doi.org/10.1038/s41467-021-25383-z.

[7] X. Yue, L. Zhang, X. He, D. Kong, Y. Hua, Hypo-toxicity and prominent passivation characteristics of 316 L stainless steel fabricated by direct metal laser sintering in a simulated inflammation environment, J. Mater. Sci. Technol. 93 (2021) 205–220, https://doi.org/10.1016/j.jmst.2021.03.053.

[8] N.K. Dhiman, S. Agnihotri, R. Shukla, Silver-based polymeric nanocomposites as antimicrobial coatings for biomedical applications. Nanotechnology in Modern Animal Biotechnology, Springer,, 2019, pp. 115–171, https://doi.org/10.1007/978-981-13-6004-6_4.

[9] Y. Lin, X. Liu, Z. Liu, Y. Xu, Visible-light-driven photocatalysis-enhanced nanozyme of TiO_2 nanotubes@ MoS_2 nanoflowers for efficient wound healing infected with multidrug-resistant bacteria, Small 17 (39) (2021) 1–14, https://doi.org/10.1002/smll.202201184.

[10] N. Tripathy, R. Ahmad, S.H. Bang, J. Min, Y.-B. Hahn, Tailored lysozyme–ZnO nanoparticle conjugates as nanoantibiotics, ChemComm 50 (66) (2014) 9298–9301, https://doi.org/10.1039/C4CC03712J.

[11] N. Tripathy, R. Ahmad, S.H. Bang, G. Khang, J. Min, Y.-B. Hahn, Outstanding antibiofilm features of quanta-CuO film on glass surface, ACS Appl. Mater. Interfaces 8 (24) (2016) 15128–15137, https://doi.org/10.1021/acsami.6b04494.

[12] S. Soroldoni, F. Abreu, Í.B. Castro, F.A. Duarte, G.L.L. Pinho, Are antifouling paint particles a continuous source of toxic chemicals to the marine environment? J. Hazard. Mater. 330 (2017) 76–82, https://doi.org/10.1016/j.jhazmat.2017.02.001.

[13] Y. Yang, A.M. Asiri, Z. Tang, D. Du, Y. Lin, Graphene based materials for biomedical applications, Mater. Today 16 (10) (2013) 365–373, https://doi.org/10.1016/j.mattod.2013.09.004.

[14] S. Akash, B. Sivaprakash, N. Rajamohan, M. Govarthanan, B.T. Elakiya, Remediation of pharmaceutical pollutants using graphene-based materials-A review on operating conditions, mechanism and toxicology, Chemosphere (2022) 1–37, https://doi.org/10.1016/j.chemosphere.2022.135520.

[15] M.D. Rojas-Andrade, G. Chata, D. Rouholiman, J. Liu, C. Saltikov, S. Chen, Antibacterial mechanisms of graphene-based composite nanomaterials, Nanoscale 9 (3) (2017) 994–1006, https://doi.org/10.1039/C6NR08733G.

[16] D.J. Joshi, J.R. Koduru, N.I. Malek, C.M. Hussain, S.K. Kailasa, Surface modifications and analytical applications of graphene oxide: a review, Trends Anal. Chem. 144 (2021) 1–25, https://doi.org/10.1016/j.trac.2021.116448.

[17] Z.M. Marković, S.P. Jovanović, P.Z. Mašković, M. Danko, M. Mičušík, V. B. Pavlović, D.D. Milivojević, A. Kleinová, Z. Špitalský, B.M.T. Marković, Photo-induced antibacterial activity of four graphene based nanomaterials on a wide range of bacteria, RSC Adv. 8 (55) (2018) 31337–31347, https://doi.org/10.1039/C8RA04664F.

[18] O.C. Compton, S.T. Nguyen, Graphene oxide, highly reduced graphene oxide, and graphene: versatile building blocks for carbon-based materials, Small 6 (6) (2010) 711–723, https://doi.org/10.1002/smll.200901934.

[19] T. Pulingam, K.L. Thong, J.N. Appaturi, C.W. Lai, B.F. Leo, Mechanistic actions and contributing factors affecting the antibacterial property and cytotoxicity of graphene oxide, Chemosphere 281 (2021) 1–11, https://doi.org/10.1016/j.chemosphere.2021.130739.

[20] Y. Liu, J. Wen, Y. Gao, T. Li, H. Wang, H. Yan, B. Niu, R. Guo, Antibacterial graphene oxide coatings on polymer substrate, Appl. Surf. Sci. 436 (2018) 624–630, https://doi.org/10.1016/j.apsusc.2017.12.006.

[21] O. Akhavan, E. Ghaderi, Toxicity of graphene and graphene oxide nanowalls against bacteria, ACS Nano 4 (10) (2010) 5731–5736, https://doi.org/10.1021/nn101390x.

[22] A. Saadati, B.N. Khiarak, A.A. Zahraei, A. Nourbakhsh, H. Mohammadzadeh, Electrochemical characterization of electrophoretically deposited hydroxyapatite/chitosan/graphene oxide composite coating on Mg substrate, Surf. Interfaces 25 (2021) 1–12, https://doi.org/10.1016/j.surfin.2021.101290.

[23] G. Jena, S. Sofia, B. Anandkumar, S. Vanithakumari, R. George, J. Philip, Graphene oxide/polyvinylpyrrolidone composite coating on 316L SS with superior antibacterial and anti-biofouling properties, Prog. Org. Coat. 158 (2021) 1–13, https://doi.org/10.1016/j.porgcoat.2021.106356.

[24] X. Li, P. Bandyopadhyay, T.T. Nguyen, O.-K. Park, J.H. Lee, Fabrication of functionalized graphene oxide/maleic anhydride grafted polypropylene composite film with excellent gas barrier and anticorrosion properties, J. Membr. Sci. 547 (2018) 80–92, https://doi.org/10.1016/j.memsci.2017.10.031.

[25] M. Muthuchamy, R. Govindan, K. Shine, V. Thangasamy, N.S. Alharbi, M. Thillaichidambaram, J.M. Khaled, J.-L. Wen, K.F. Alanzi, Anti-biofilm investigation of graphene/chitosan nanocomposites against biofilm producing *P. aeruginosa* and *K. pneumoniae*, Carbohydr. Polym. 230 (2020) 1–13, https://doi.org/10.1016/j.carbpol.2019.115646.

[26] K. Sadeghi, J. Seo, Metal–ligand complex copolymer as photocurable antimicrobial coatings for infection-resistant surface, Surf. Interfaces 28 (2022) 1–9, https://doi.org/10.1016/j.surfin.2021.101573.

[27] I. Aranaz, A.R. Alcántara, M.C. Civera, C. Arias, B. Elorza, A. Heras Caballero, N. Acosta, Chitosan: an overview of its properties and applications, Polymers 13 (19) (2021) 1–27, https://doi.org/10.3390/polym13193256.

[28] N.K. Dhiman, S. Agnihotri, Hierarchically aligned nano silver/chitosan–PVA hydrogel for point-of-use water disinfection: contact-active mechanism revealed, Environ. Sci. Nano 7 (8) (2020) 2337–2350, https://doi.org/10.1039/D0EN00405G.

[29] H. Shagholani, S.M. Ghoreishi, M. Mousazadeh, Improvement of interaction between PVA and chitosan via magnetite nanoparticles for drug delivery application, Int. J. Biol. Macromol. 78 (2015) 130–136, https://doi.org/10.1016/j.ijbiomac.2015.02.042.

[30] S.K. Mishra, S. Kannan, Development, mechanical evaluation and surface characteristics of chitosan/polyvinyl alcohol based polymer composite coatings on

titanium metal, J. Mech. Behav. Biomed. Mater. 40 (2014) 314–324, https://doi.org/10.1016/j.jmbbm.2014.08.014.
[31] J.A. Tamayo Marín, S.R. Londoño, J. Delgado, D.P. Navia Porras, M.E. Valencia Zapata, J.H. Mina Hernandez, C.H. Valencia, C.D.Grande Tovar, Biocompatible and antimicrobial electrospun membranes based on nanocomposites of chitosan/poly (vinyl alcohol)/graphene oxide, Int. J. Mol. Sci. 20 (12) (2019) 1–14, https://doi.org/10.3390/ijms20122987.
[32] S. Yang, P. Lei, Y. Shan, D. Zhang, Preparation and characterization of antibacterial electrospun chitosan/poly (vinyl alcohol)/graphene oxide composite nanofibrous membrane, Appl. Surf. Sci. 435 (2018) 832–840, https://doi.org/10.1016/j.apsusc.2017.11.191.
[33] Y. Liu, R. Song, X. Zhang, D. Zhang, Enhanced antimicrobial activity and pH-responsive sustained release of chitosan/poly (vinyl alcohol)/graphene oxide nanofibrous membrane loading with allicin, Int. J. Biol. Macromol. 161 (2020) 1405–1413, https://doi.org/10.1016/j.ijbiomac.2020.08.051.
[34] S. Xie, J. Zhao, B. Zhang, Z. Wang, H. Ma, C. Yu, M. Yu, L. Li, J. Li, Graphene oxide transparent hybrid film and its ultraviolet shielding property, ACS Appl. Mater. Interfaces 7 (32) (2015) 17558–17564, https://doi.org/10.1021/acsami.5b04231.
[35] X. Huang, X. Bao, Y. Liu, Z. Wang, Q. Hu, Catechol-functional chitosan/silver nanoparticle composite as a highly effective antibacterial agent with species-specific mechanisms, Sci. Rep. 7 (1) (2017) 1–10, https://doi.org/10.1038/s41598-017-02008-4.
[36] S.A. Marathe, R. Kumar, P. Ajitkumar, V. Nagaraja, D. Chakravortty, Curcumin reduces the antimicrobial activity of ciprofloxacin against *Salmonella typhimurium* and *Salmonella typhi*, J. Antimicrob. Chemother. 68 (1) (2013) 139–152, https://doi.org/10.1093/jac/dks375.
[37] Y. Fang, C. Xing, S. Zhan, M. Zhao, M. Li, H. Liu, A polyoxometalate-modified magnetic nanocomposite: a promising antibacterial material for water treatment, J. Mater. Chem. B 7 (11) (2019) 1933–1944, https://doi.org/10.1039/C8TB03331E.
[38] A. Kroll, M.H. Pillukat, D. Hahn, J. Schnekenburger, Interference of engineered nanoparticles with in vitro toxicity assays, Arch. Toxicol. 86 (7) (2012) 1123–1136, https://doi.org/10.1007/s00204-012-0837-z.
[39] R. Eivazzadeh-Keihan, F. Radinekiyan, H.A.M. Aliabadi, S. Sukhtezari, B. Tahmasebi, A. Maleki, H. Madanchi, Chitosan hydrogel/silk fibroin/Mg $(OH)_2$ nanobiocomposite as a novel scaffold with antimicrobial activity and improved mechanical properties, Sci. Rep. 11 (1) (2021) 1–13, https://doi.org/10.1038/s41598-020-80133-3.
[40] S. Shamszadeh, M. Akrami, S. Asgary, Size-dependent bioactivity of electrosprayed core–shell chitosan-alginate particles for protein delivery, Sci. Rep. 12 (1) (2022) 1–14, https://doi.org/10.1038/s41598-022-24389-x.
[41] A. Valliammai, A. Selvaraj, P. Mathumitha, C. Aravindraja, S.K. Pandian, Polymeric antibiofilm coating comprising synergistic combination of citral and thymol prevents methicillin-resistant *Staphylococcus aureus* biofilm formation on titanium, Mater. Sci. Eng. C. 121 (2021) 1–12, https://doi.org/10.1016/j.msec.2021.111863.
[42] T. Kokubo, H. Takadama, How useful is SBF in predicting in vivo bone bioactivity? Biomaterials 27 (15) (2006) 2907–2915, https://doi.org/10.1016/j.biomaterials.2006.01.017.
[43] S. Majhi, V.C. Peddiraju, A. Mishra, Effect of antimicrobial peptide (AMP)–tethered stainless steel surfaces on the bacterial membrane, Mater. Today Chem. 21 (2021) 1–10, https://doi.org/10.1016/j.mtchem.2021.100541.
[44] A.B. Tesler, P. Kim, S. Kolle, C. Howell, O. Ahanotu, J. Aizenberg, Extremely durable biofouling-resistant metallic surfaces based on electrodeposited nanoporous tungstite films on steel, Nat. Commun. 6 (1) (2015) 1–10, https://doi.org/10.1038/ncomms9649.
[45] X. Shen, Y. Zhang, P. Ma, L. Sutrisno, Z. Luo, Y. Hu, Y. Yu, B. Tao, C. Li, K. Cai, Fabrication of magnesium/zinc-metal organic framework on titanium implants to inhibit bacterial infection and promote bone regeneration, Biomaterials 212 (2019) 1–16, https://doi.org/10.1016/j.biomaterials.2019.05.008.
[46] Y.J. Wang, M.W. Tian, L.J. Qu, S.F. Zhu, Y.N. Sun, G.T. Han, Enhanced thermal, UV blocking and dye absorptive properties of chitosan/poly(vinyl alcohol)/graphene oxide fibers, Fiber Polym. 16 (9) (2015) 2011–2020, https://doi.org/10.1007/s12221-015-5279-9.
[47] D. Sivaraj, K. Vijayalakshmi, Enhanced antibacterial and corrosion resistance properties of Ag substituted hydroxyapatite/functionalized multiwall carbon nanotube nanocomposite coating on 316L stainless steel for biomedical application, Ultrason. Sonochem. 59 (2019) 1–11, https://doi.org/10.1016/j.ultsonch.2019.104730.
[48] M. Kurakula, N.R. Naveen, Electrospraying: a facile technology unfolding the chitosan based drug delivery and biomedical applications, Eur. Polym. J. 147 (2021) 1–18, https://doi.org/10.1016/j.eurpolymj.2021.110326.
[49] D.L. Han, L.F. Yan, W.F. Chen, W. Li, Preparation of chitosan/graphene oxide composite film with enhanced mechanical strength in the wet state, Carbohydr. Polym. 83 (2) (2011) 653–658, https://doi.org/10.1016/j.carbpol.2010.08.038.
[50] Y. Liu, M. Park, H.K. Shin, B. Pant, J. Choi, Y.W. Park, J.Y. Lee, S.-J. Park, H.-Y. Kim, Facile preparation and characterization of poly (vinyl alcohol)/chitosan/graphene oxide biocomposite nanofibers, J. Ind. Eng. Chem. 20 (6) (2014) 4415–4420, https://doi.org/10.1016/j.jiec.2014.02.009.
[51] Y. Ying, Y. Wu, J. Huang, Preparation and characterization of chitosan/poly (vinyl alcohol)/graphene oxide films and studies on their antibiofilm formation activity, J. Biomed. Mater. Res. -A 108 (10) (2020) 2015–2022, https://doi.org/10.1002/jbm.a.36961.
[52] A.M. Pandele, M. Ionita, L. Crica, S. Dinescu, M. Costache, H. Iovu, Synthesis, characterization, and in vitro studies of graphene oxide/chitosan–polyvinyl alcohol films, Carbohydr, Polym 102 (2014) 813–820, https://doi.org/10.1016/j.carbpol.2013.10.085.
[53] K.H. Liao, Y.S. Lin, C.W. Macosko, C.L. Haynes, Cytotoxicity of graphene oxide and graphene in human erythrocytes and skin fibroblasts, ACS Appl. Mater. Interfaces 3 (7) (2011) 2607–2615, https://doi.org/10.1021/am200428v.
[54] A.M. Pandele, M. Ionita, L. Crica, E. Vasile, H. Iovu, Novel Chitosan-poly (vinyl alcohol)/graphene oxide biocomposites 3D porous scaffolds, Compos. B. Eng. 126 (2017) 81–87, https://doi.org/10.1016/j.compositesb.2017.06.010.
[55] S. Kumar, B. Krishnakumar, A. Sobral, J. Koh, Bio-based (chitosan/PVA/ZnO) nanocomposites film: thermally stable and photoluminescence material for removal of organic dye, Carbohydr. Polym. 205 (2019) 559–564, https://doi.org/10.1016/j.carbpol.2018.10.108.
[56] J. Ma, C. Liu, R. Li, J. Wang, Properties and structural characterization of chitosan/poly (vinyl alcohol)/graphene oxide nano composites, e-Polym. 12 (1) (2012) 1–13, https://doi.org/10.1515/epoly.2012.12.1.386.
[57] A. Ahmed, B. Adak, T. Bansala, S. Mukhopadhyay, Green solvent processed cellulose/graphene oxide nanocomposite films with superior mechanical, thermal, and ultraviolet shielding properties, ACS Appl. Mater. Interfaces 12 (1) (2019) 1687–1697, https://doi.org/10.1021/acsami.9b19686.
[58] A.A. Refaee, M.E. El-Naggar, T.B. Mostafa, R.F. Elshaarawy, A.M. Nasr, Nano-bio finishing of cotton fabric with quaternized chitosan Schiff base-TiO_2-ZnO nanocomposites for antimicrobial and UV protection applications, Eur. Polym. J. 166 (2022) 1–21, https://doi.org/10.1016/j.eurpolymj.2022.111040.
[59] S.G. Rathod, R.F. Bhajantri, V. Ravindrachary, J. Naik, D.J.M. Kumar, High mechanical and pressure sensitive dielectric properties of graphene oxide doped PVA nanocomposites, RSC Adv. 6 (81) (2016) 77977–77986, https://doi.org/10.1039/C6RA16026C.
[60] S. Agnihotri, G. Bajaj, S. Mukherji, S. Mukherji, Arginine-assisted immobilization of silver nanoparticles on ZnO nanorods: an enhanced and reusable antibacterial substrate without human cell cytotoxicity, Nanoscale 7 (16) (2015) 7415–7429, https://doi.org/10.1039/C4NR06913G.
[61] S. Agnihotri, S. Mukherji, S. Mukherji, Immobilized silver nanoparticles enhance contact killing and show highest efficacy: elucidation of the mechanism of bactericidal action of silver, Nanoscale 5 (16) (2013) 7328–7340, https://doi.org/10.1039/C3NR00024A.
[62] M.U.A. Khan, Z. Yaqoob, M.N.M. Ansari, S.I.A. Razak, M.A. Raza, A. Sajjad, S. Haider, F.M. Busra, Chitosan/poly vinyl alcohol/graphene oxide based pH-responsive composite hydrogel films: drug release, anti-microbial and cell viability studies, Polymers 13 (18) (2021) 1–19, https://doi.org/10.3390/polym13183124.
[63] S. Liu, T.H. Zeng, M. Hofmann, E. Burcombe, J. Wei, R. Jiang, J. Kong, Y. Chen, Antibacterial activity of graphite, graphite oxide, graphene oxide, and reduced graphene oxide: membrane and oxidative stress, ACS Nano 5 (9) (2011) 6971–6980, https://doi.org/10.1021/nn202451x.
[64] S. Panda, T.K. Rout, A.D. Prusty, P.M. Ajayan, S. Nayak, Electron transfer directed antibacterial properties of graphene oxide on metals, Adv. Mater. 30 (7) (2018) 1–10, https://doi.org/10.1002/adma.201702149.
[65] S. Jaworski, M. Wierzbicki, E. Sawosz, A. Jung, G. Gielerak, J. Biernat, H. Jaremek, W. Łojkowski, B. Woźniak, J. Wojnarowicz, Graphene oxide-based nanocomposites decorated with silver nanoparticles as an antibacterial agent, Nanoscale Res. Lett. 13 (1) (2018) 1–17, https://doi.org/10.1186/s11671-018-2533-2.
[66] N. Yadav, A. Dubey, S. Shukla, C.P. Saini, G. Gupta, R. Priyadarshini, B. Lochab, Graphene oxide-coated surface: inhibition of bacterial biofilm formation due to specific surface–interface interactions, ACS Omega 2 (7) (2017) 3070–3082, https://doi.org/10.1021/acsomega.7b00371.
[67] J.J. Fan, C.D. Grande, D.F. Rodrigues, Biodegradation of graphene oxide-polymer nanocomposite films in wastewater, Environ. Sci. Nano 4 (9) (2017) 1808–1816, https://doi.org/10.1039/C7EN00396J.
[68] C. Greulich, J. Diendorf, J. Gessmann, T. Simon, T. Habijan, G. Eggeler, T. Schildhauer, M. Epple, M. Köller, Cell type-specific responses of peripheral blood mononuclear cells to silver nanoparticles, Acta Biomater. 7 (9) (2011) 3505–3514, https://doi.org/10.1016/j.actbio.2011.05.030.
[69] V. Mersch-Sundermann, S. Knasmüller, X.-J. Wu, F. Darroudi, F. Kassie, Use of a human-derived liver cell line for the detection of cytoprotective, antigenotoxic and cogenotoxic agents, Toxicology 198 (1–3) (2004) 329–340, https://doi.org/10.1016/j.tox.2004.02.009.
[70] A.L. Urzedo, M.C. Goncalves, M.H. Nascimento, C.B. Lombello, G. Nakazato, A. B. Seabra, Cytotoxicity and antibacterial activity of alginate hydrogel containing nitric oxide donor and silver nanoparticles for topical applications, ACS Biomater. Sci. Eng. 6 (4) (2020) 2117–2134, https://doi.org/10.1021/acsbiomaterials.9b01685.
[71] D. Depan, B. Girase, J. Shah, R.D.K. Misra, Structure–process–property relationship of the polar graphene oxide-mediated cellular response and stimulated growth of osteoblasts on hybrid chitosan network structure nanocomposite scaffolds, Acta Biomater. 7 (9) (2011) 3432–3445, https://doi.org/10.1016/j.actbio.2011.05.019.
[72] D. Depan, J. Shah, R. Misra, Degradation mechanism and increased stability of chitosan-based hybrid scaffolds cross-linked with nanostructured carbon: process–structure–functional property relationship, Polym. Degrad. Stab. 98 (11) (2013) 2331–2339, https://doi.org/10.1016/j.polymdegradstab.2013.08.007.
[73] H. Mokhtari, Z. Ghasemi, M. Kharaziha, F. Karimzadeh, F. Alihosseini, Chitosan-58S bioactive glass nanocomposite coatings on TiO_2 nanotube: Structural and biological properties, Appl. Surf. Sci. 441 (2018) 138–149, https://doi.org/10.1016/j.apsusc.2018.01.314.